UNIVERSITAT DE BARCELONA

Substructure in the phase-space of the Galaxy with Gaia

Pau Ramos

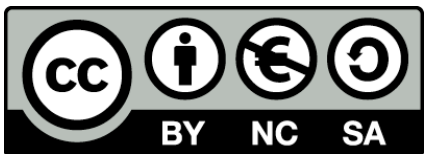

TESI DOCTORAL

SUBSTRUCTURE IN THE PHASE-SPACE OF THE GALAXY WITH GAIA

PAU RAMOS

DIRECTOR:
Dr. Ma. Teresa Antoja Castelltort

UNIVERSITAT DE
BARCELONA

Pau Ramos, *Substructure in the phase-space of the Galaxy with Gaia*,
PhD Thesis
Barcelona, 29 de maig de 2020

Image: Milky Way over Nanga Parbat - fairy meadows, by Shahbaz Aslam.
Composition: Pau Ramos.

Substructure in the phase-space of the Galaxy with Gaia

Memòria presentada per optar al grau de doctor per la

Universitat de Barcelona

Programa de doctorat en Física

Autor:
Pau Ramos

Directora de la tesi:
Dr. Ma. Teresa Antoja Castelltort

Tutor de la tesi:
Dr. Alberto Manrique Oliva

UNIVERSITAT DE
BARCELONA

「近づくたびにきらめき
目の前に広がる
僕らのための景色」

— Galileo Galilei

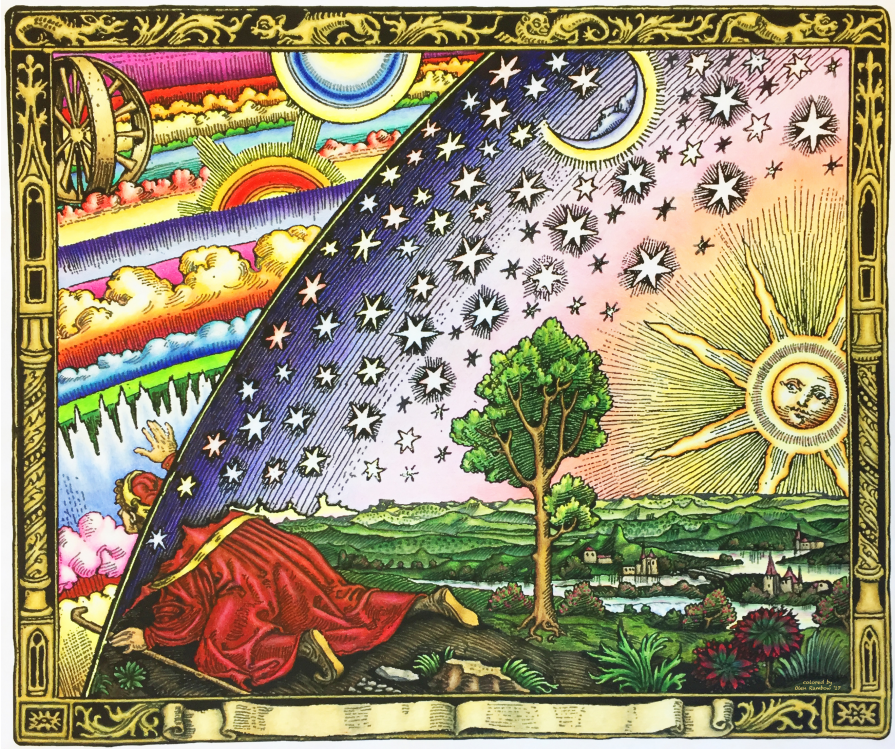

ABSTRACT

The *Gaia* mission and its extensive catalogue of stars has marked the beginning of the Golden Age of Galactic dynamics. We have now access to the kinematics of more than a billion stars with which we can start deciphering the history of our Galaxy. Before *Gaia*, we knew that the phase-space of the Milky Way (MW) contained a wealth of substructure created by the different dynamical processes and components of the Galaxy, but we did not have enough kinematical data with which to characterise it with precision outside the Solar neighbourhood (SN).

In this thesis we set out to detect and describe the kinematic substructure of the MW, not only near the Sun but to the very limit of the *Gaia* sphere. Our goal is to characterise the phase-space features of our Galaxy, introducing novel empirical measurements that can help us understand the structure of the MW and its evolution, together with the dynamics of its different components (bar, spiral arms, halo, satellites), and the interactions among them over time. We will focus on the disc and the structures of the halo, in particular, the Sagittarius (Sgr) dwarf spheroidal, a galaxy undergoing full tidal disruption and most likely a significant perturber in the recent history of our Galaxy.

Our methodology is centred on the analysis of the *Gaia* DR2 data mostly using the wavelet transformation (WT) that is a robust statistical tool to reveal the substructure present in the velocity maps. We apply it on the plane of Galactocentric radial velocity (v_R) against rotational velocity (v_ϕ), venturing into regions beyond the SN, but also, and for the first time, to the proper motion histograms of distant stars all around the sky.

As a result, we find that the velocity field of the MW disc is highly structured not only at the SN but, at least, up to distances of $\sim$3 kpc. We have characterised the shape of each structure and described their changes with position in the Galaxy. We report that the v_ϕ of each structure decreases with Galactocentric radius in a different way, which allows us to associate tentatively each structure with a different dynamical mechanism, namely, the phase-mixing process most likely initiated by the last pericentre passage of Sgr, and the resonances with the non-axisymmetric components of the MW (bar and/or spiral arms).

Additionally, we detect two arch-like structures towards the anticentre corresponding to Monoceros and Anticentre stream (ACS). Thanks to our method, we are able to observe their morphology

sharper than ever and produce a kinematic selection of member stars. From this, we obtain a precise characterisation of Monoceros and ACS that can be now used to compare quantitatively the models proposed to explain their origin. Based on our preliminary analysis, we favour the scenario in which they were caused by the repeated perturbations induced by Sgr, as opposed to being disrupted satellites as some authors propose.

We respect to Sgr, we have detected the kinematic signature of its stream across the whole sky, and measured the proper motion along a large portion of the tidal tails, which was not possible before Gaia. We have shown also that the predictions of the models do not match our observations, and thus require revision. The resulting sample of candidate stars represents a vast catalogue of stars of different stellar types that can be used to model the orbit of Sgr, as well as their distribution along the stream and its link to the star formation history.

Finally, we complement this sample with the largest list of RR Lyrae in Sgr. In doing so, we have obtained a precise characterisation of the 3D distribution of its tidal debris as well as its tangential velocities, mostly unexplored until now as these require distances and proper motions simultaneously.

All together, we have provided a detailed characterisation of the kinematic substructure present throughout the MW that we can now use to study and model the evolution of our Galaxy and its components in a global, transverse manner which takes into account the coupling between the Sgr stream and the disc.

But it's been no bed of roses.
No pleasure cruise.
I consider it a challenge before the whole human race.
And I ain't gonna lose.

— Queen

ACKNOWLEDGMENTS

I write this lines from isolation, in my house, where I have been confined for more than two months now, because someone at the other side of the world decided that it was a good idea to cook a Pangolin. In the room next to mine, my dear flatmate is practising Karate via Zoom, my personal trainer is looking at me, disappointed, as I slowly turn into a walking dumpling, all these while my neighbours cheer for me from their windows, which they always do at 8pm for reasons that escape my comprehension. The days that I have spent working on my thesis from home could have been a real hell on earth if it were not for all the good people that care for me, and to which I want to dedicate the following lines.

First and foremost, I want to thank my supervisor. Teresa, I feel so lucky to have been your student. You have taught me what it means to do research, to face the challenges with illusion, and how to properly write a part... Damn it! Thank you for your patience and for always having a moment to listen.

I also want to dedicate an especial thanks to Cesca, as she gave me the chance to turn my life around the day she asked in class if someone wanted to postulate for a PhD grant. Her positive energy and dedication to Astronomy are commendable.

I am very grateful to all the people in the Gaia team as well. Working with you these three years, during which many things happened, has been really enjoyable. Just to mentioned a few, I would like to thank Mercè for guiding me successfully through my spaghettified master thesis, and to Fede, for being such a great and crazy (in the good way) guy. I could not forget the amazing technical and administrative team that we have, backing us all the time, specially Dani (you always know who to fix my problems) and JR... JR, going to your office is always a pleasure, as I know that I will find there with a smile and a honest predisposition to help in whatever way you can.

I also thank all the people at Planta 7, my colleagues but, more importantly, my friends. I will miss my office-mate, one of the first persons I meet here and whose company has been both instructive and enjoyable. Also the three (sometimes more) people next door, for giving my so many great moments, inside and outside the University, and for being there when Alfred and I want to bother someone with

our little game of "frontón". With them, I have learned about the deep lore of Star Wars, the unforgettable taste of "Lechazo" hamburgers, the value of late night talks, and... you know... the value of friendship (ooooh). I want to thank the Cosmoboys (plus Katie) as well for being such great people. They make my coffee breaks feel like I am inside a real life sitcom. I know that, even in the distance, some of they will still force me to read One Piece and Saga, which I appreciate. A special mention to Nico for helping me with all the administrative nuances.

No puc acabar sense primer agrair a la gent que m'acompanya en la vida fora de l'àmbit acadèmic. Als Baby-sharks, presi inclosa, i a Sun-praisers, jojo-posers i fans de los aviones varios. Als meus amics de tota la vida de Badalona, així com a "Los de always y Aleix", y a tota la gent que m'he anat trobant pel camí i que m'han fet ser qui sóc.

Por último, pero no por ello menos importante, quiero agradecer a mi madre por haberme criado con tanto amor y apoyarme en (casi) todo lo que me he propuesto. También a mi padre, que siempre me recuerda que la realidad se pueden mirar de muchas maneras. Por supuesto, al resto de mi familia también les agradezco su cariño y que, a pesar de mis excentricidades, me quieran como lo hacen.

Tinc mil amics perfectes,
Tinc un amor atòmic.
I no, no em diguis que no perquè m'ho vull creure.
Tothom es creu especial i tots som pardals.
Tothom es creu especial i tots som bestials.
Tothom es creu especial.... i no ens fa cap mal.

— Oques grasses

RESUMEN EN ESPAÑOL

La astronomía Galáctica comenzó su época dorada el día 25 de abril de 2018, coincidiendo con los inicios de esta tesis, al hacerse públicos los datos de los primeros 22 meses de observación del satélite *Gaia* de la Agencia Espacial Europea. Dichos datos contienen posiciones y movimientos propios para más de 1.3 miles de millones de estrellas de nuestra Galaxia, la Vía Láctea (VL). Para una porción de estas, las más brillantes y cercanas, *Gaia* también proporciona distancias precisas y velocidades radiales, lo cual supone la muestra 6D (posiciones y velocidades) más grande hasta la fecha con alrededor de 7 millones de estrellas. El objetivo de esta tesis es usar todo el potencial de estos datos para estudiar en detalle la sub-estructura cinemática de las estrellas que forman la VL, tanto en el disco como en el halo y sus satélites. Se cree que dicha sub-estructura está inducida en su mayoría por elementos internos como la barra o los brazos espirales, o bien por interacciones con galaxias enanas que, al ser devoradas por nuestra Galaxia, perturban gravitacionalmente el disco. En este sentido, debemos fijarnos en la galaxia enana de Sagitario (Sgr), actualmente en pleno proceso de disrupción, claramente visible en forma de corriente estelar (producido por las estrellas que ha ido perdiendo con el tiempo) que da, al menos, una vuelta entera en el cielo. Estudios recientes demuestran que esta galaxia satélite fue lo suficientemente masiva en el pasado como para perturbar significativamente la VL.

Primero, usamos la muestra 6D para detectar la sub-estructura cinemática presente en los mapas de velocidad, tanto cerca del Sol, como en regiones inexploradas del disco de la VL. El resultado es la lista más completa de estructuras cinemáticas y su precisa caracterización morfológica. Al poder explorar regiones alejadas del Sol, hemos sido capaces de seguir las estructuras a medida que nos movíamos por la Galaxia y medir sus cambios de localización en el plano de las velocidades. Esto ha llevado al descubrimiento de que las estructuras cambian con el radio Galactocéntrico de formas distintas, algunas manteniendo un momento angular común (lo cual podríamos asociar con resonancias de la barra/brazos espirales) y otras compartiendo energías/frecuencias orbitales (posiblemente vinculadas con perturbaciones inducidas por la galaxia enana de Sgr).

Luego expandimos nuestra búsqueda a las partes más lejanas de la Galaxia usando un método novedoso que permite procesar de forma rápida toda la muestra de *Gaia* al completo. Para ello, buscamos sobre-densidades en los histogramas de movimientos propios

(ya no usamos la velocidad radial) de todas las estrellas lejanas que encontramos en cada uno de los HEALpix de nivel 5 en que hemos dividido el cielo. Como resultado, hemos detectado dos estructuras en forma de arco en el hemisferio norte Galáctico, en la dirección del anticentro. Dichas estructuras corresponden a Monoceros y ACS, siendo esta la primera vez que han sido detectadas únicamente por su cinemática y sin limitarse a un tipo de estrellas concreto, como había sido siempre el caso hasta ahora. Tras caracterizar su morfología, cinemática y la distribución de sus estrellas en los diagramas de color-magnitud, concluimos que estas estructuras parecen estar asociadas al disco tal como algunos estudios apuntan, en lugar de al halo como otros trabajos defendían. Así pues, la causa más probable para explicar sus propiedades observadas es que Sgr, al interactuar gravitatoriamente con la VL, impulsó las estrellas que habitan en el borde del disco separándolas así de este.

Aplicando la misma metodología usada para detectar Monoceros y ACS, hemos sido capaces de producir la muestra más grande existente de estrellas pertenecientes al corriente estelar de Sgr. Dicha muestra aporta movimientos propios a lo largo de la mayor parte de las colas de marea, lo cual hasta ahora no había sido posible al nivel de precisión actual, y que permite conocer con precisión los cambios en la cinemática que la corriente experimenta a lo largo de su órbita. Igual que antes, nuestra muestra no se restringe a una población estelar concreta, lo cual nos posibilitará estudiar con detalle la composición a lo largo de las colas de marea. Esto, unido a la precisa caracterización de su cinemática, permitirá modelar con gran precisión la historia de formación de Sgr.

Finalmente, expandimos la muestra de estrellas de Sgr con la lista más grande de RR Lyrae hasta la fecha. A pesar de ser una muestra pequeña en comparación a la anterior, debido básicamente a la baja proporción de este tipo de estrellas, el hecho de ser candelas estándar permite calcular su distancia con gran precisión. De esta manera, somos capaces de determinar la distribución espacial en 3D de las estrellas que forman la corriente y, al añadir los movimientos propios, obtener por primera vez las velocidades tangenciales a lo largo de las colas de Sgr. Con esta muestra y la anterior, hemos demostrado que la cinemática de modelos ampliamente usados hasta ahora no se ajusta a las observaciones, lo cual nos lleva a la necesaria revisión del potencial gravitatorio de la VL. Los nuevos datos aportados en esta tesi servirán para ajustar de forma más precisa que nunca la órbita de Sgr al poder contar de finalmente con los movimientos propios, a la vez que distancias precisas, para una gran cantidad de estrellas.

Los tres aspectos estudiados en esta tesis (sub-estructura cinemática en el disco, Monoceros-ACS, y la órbita de Sgr) están, muy probablemente, estrechamente ligados entre sí. El potencial gravitatorio de la VL da forma y moldea la cinemática de cada uno de ellos in-

dividualmente pero, al mismo tiempo, es Sgr a través de su órbita la responsable, probablemente, de la aparición de algunas de las estructuras observadas. Se crea así una conexión entre los tres elementos que, gracias a los datos aportados en esta tesis, permitirá realizar por primera vez un ajuste híbrido a los parámetros que definen las características de nuestra Galaxia así como su evolución en el tiempo.

PUBLICATIONS

Complete list of publications at the moment of thesis deposit.

Published articles in this thesis

- Teresa Antoja, **Pau Ramos**, Cecilia Mateu, Amina Helmi, Friedrich Anders, Carme Jordi, and Julio A. Carballo-Bello. "An all-sky proper-motion map of the Sagittarius stream using *Gaia* DR2". In: *Astronomy and Astrophysics*, March 2020, 635, L3. DOI: 10.1051/0004-6361/201937145.
- **Pau Ramos**, Teresa Antoja, Francesca Figueras. "Riding the kinematic waves in the Milky Way disk with *Gaia* ". In: *Astronomy and Astrophysics*, November 2018, 619, A72. DOI: 10.1051/ 0004-6361/201833494.

Other published articles

- Anders, F.; Khalatyan, A.; Chiappini, C.; Queiroz, A. B.; Santiago, B. X.; Jordi, C.; Girardi, L.; Brown, A. G. A.; Matijevič, G.; Monari, G.; Cantat-Gaudin, T.; Weiler, M.; Khan, S.; Miglio, A.; Carrillo, I.; Romero-Gómez, M.; Minchev, I.; de Jong, R. S.; Antoja, T.; **Ramos, P.**; Steinmetz, M.; Enke, H. "Photo-astrometric distances, extinctions, and astrophysical parameters for *Gaia* DR2 stars brighter than G = 18". In: *Astronomy and Astrophysics*, August 2019, 628, A94. DOI: 10.1051/0004-6361/201935765.
- Cantat-Gaudin, T.; Jordi, C.; Wright, N. J.; Armstrong, J. J.; Vallenari, A.; Balaguer-Núñez, L.; **Ramos, P.**; Bossini, D.; Padoan, P.; Pelkonen, V. M.; Mapelli, M.; Jeffries, R. D. "Expanding associations in the Vela-Puppis region. 3D structure and kinematics of the young population". In: *Astronomy and Astrophysics*, June 2019, 626, A17. DOI: 10.1051/0004-6361/201834957.

Other articles submitted

- **Pau Ramos**, Cecilia Mateu, Teresa Antoja, Amina Helmi, Alfred Castro-Ginard, Eduardo Balbinot, Josep Maria Carrasco. "Full 5D characterisation of the Sagittarius stream with Gaia DR2 RR Lyrae". Accepted for publication in: *Astronomy and Astrophysics*, DOI: 10.1051/0004-6361/202037819.

Conference proceedings

- **Pau Ramos**, Teresa Antoja, Francesca Figueras. "Riding the kinematic waves in the Milky Way disk with *Gaia* ". In: *53rd ESLAB Symposium: The Gaia Universe, held 8-12 April, 2019 at ESTEC/ESA, Noordwijk, The Netherlands.*, April 2019. DOI: 10.5281/ zenodo. 2636392.
- **Pau Ramos**, Teresa Antoja, Francesca Figueras. "Kinematic structure in the Solar Neighbourhood and surroundings with *Gaia* : a vast richness to explore". In: *Highlights on Spanish Astrophysics X, Proceedings of the XIII Scientific Meeting of the Spanish Astronomical Society held on July 16-20, 2018, in Salamanca, Spain.*, July 2018.

CONTENTS

INTRODUCTION

1

The Universe is a complex system and, as such, it is by nature intertwined. Ever since the smallest of the asymmetries created a tinny imbalance that made the cosmos start rolling, like a snowball, it has grown to become a marvellous mesh of galaxies, always evolving, interacting, looking for an Utopian equilibrium. Thus came humanity, perpetually mesmerised by complexity, who once gazed upon the skies and since then never ceased to wonder, meditate and deliberate on what could possibly be the origin of such beauty. With time, we managed to developed the tools necessary to study, measure and, ultimately, gain knowledge. Building up from the incipient science conceived in Mesopotamia, we now understand, at least partially, how come we even exist.

Our current view of the history of the Universe is one where the mutual influence and interplay between its different constituents has played a key role. The most accepted narrative describes the evolution of these "star schools" that we call galaxies as a hierarchical process (Press & Schechter, 1974; White & Rees, 1978; Springel et al., 2006; De Lucia & Blaizot, 2007): smaller galaxies feed the big ones, inducing stellar formation and reshaping them as a response to the changes brought to the gravitational potential. The process by which an infalling satellite galaxy losses mass is called tidal stripping and is characterised by the appearance of streams – rivers of stars that emerge from their progenitor as they are no longer gravitationally bound to it. Dozens of streams are now known, both in far away galaxies (Martínez-Delgado et al., 2010) as well as in our own (e.g., Belokurov et al., 2006). With enough time, the stripped stars drift away from their birth place, mix-up with their host, and can no longer be easily associated to a particular satellite.

Only recently it became possible to unearth the fossil records left behind by said encounters, either because we can now identify extragalactic stars based on their precise chemical compositions and kinematics provided by several all-sky surveys, or because we have enough high quality data to "hear" the echoes of long past encounters through the perturbations exerted on the host galaxy. The branch of astrophysics addressing these topics is known as Galactic Archaeology[1], a blooming field now that the work of the astronomers has become more like that of a palaeontologist.

1 While the term was already being used in the 1980's, it was not until 2010 that it began to take root.

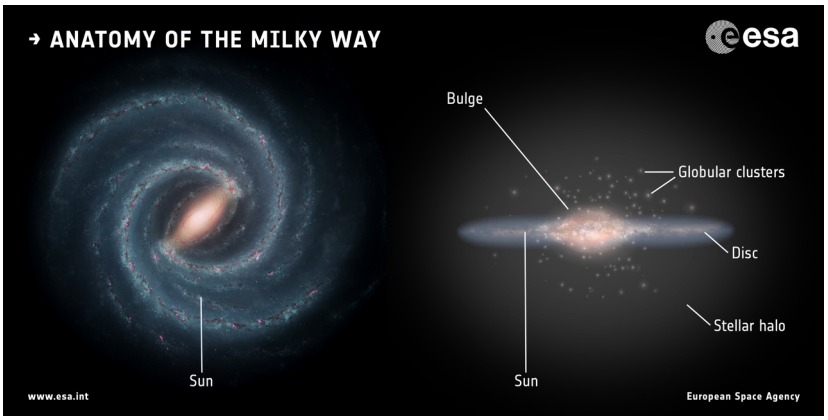

Figure 1: Artistic impression of the MW depicting its different components. Copyright: Left: NASA/JPL-Caltech; right: ESA; layout: ESA/ATG medialab

The focus of this thesis is our Galaxy, the Milky Way (MW), just another barred-spiral galaxy in this galactic zoo. Being part of it, we can study its dynamics from the inside in great detail to test our astrophysical and cosmological models. Its particular history has made it so that it is composed by an extended, low-density, almost non-rotating and rather spherical stellar halo, probably embedded in an invisible self-gravitating fluid called dark matter that dominates the gravitational potential; a boxy/peanut bulge sitting at the middle; and a very crowded, flattened ensemble of stars orbiting in a disc shape that forms the starry band that we can see at night (Mihalas & Binney, 1981; Binney & Tremaine, 2008; Freeman & Bland-Hawthorn, 2002; Bland-Hawthorn & Gerhard, 2016). It also has several spiral arms, and a group of stars forming a bar which rotates like a solid-rigid body about the centre of the Galaxy (Bissantz & Gerhard, 2002; Gerhard, 2011), where the super massive black hole Sagittarius A* sits.

All this mixture of orbits, depicted in Fig. 1, can be accounted for with the Distribution function (DF): a 6-dimensional probability distribution that quantifies the expected number of stars at a given position and with a given velocity. The different components of the Galaxy mentioned above coexist in phase-space, the domain of the DF, as they interact among themselves through time and space. Nevertheless, the large time-scales of the evolution of these systems, compared to our lives, mean that we can only access one snap-shot of phase-space and we have to rely on our theories to correctly interpret the relation between the history of the MW and the incomplete observation of its present state.

The dynamics of the DF are governed by a system of differential equations formed by the Poisson equation, which relates the curvature of space-time with how the mass is distributed in a galaxy, and the Boltzmann equation, a continuity equation that in this context relates

the internal evolution of the DF with a particular gravitational potential. Solving these two equations together would result in a complete understanding and characterisation of the DF – the Holy Grail of Galactic dynamics. However, analytical solutions are only available for highly symmetric systems which, by Noether's theorem (Noether, 1971), have sufficient conserved quantities to make the problem simple enough.

The MW is certainly not one of these ideal cases and, nevertheless, it is still useful to think in terms of quantities that should be conserved along the orbits of the stars. For instance, the energy and the angular momentum (only in the direction perpendicular to the disc) are conserved in any time-independent and axisymmetric potential. In this context, a proper base for the phase-space (instead of positions and velocities) are the so-called action-angle[2] coordinates that are constituted by i) actions, integrals of motion that act like labels uniquely identifying the orbit, each having an associated angular frequency, and ii) angles, which tell us the phase within said orbit (Binney & Tremaine, 2008). In a Keplerian set-up, where the radial and the azimuthal periods are equal, as is the case for our Solar system, there is only one significant frequency to zero-order approximation: $\sim \frac{1}{365.24}\,\text{days}^{-1}$ in the case of the Earth. In general, though, all three frequencies are important for stars in a galaxy like our own as they travel on eccentric orbits and oscillate up and down the disc.

The interaction between different components (bar, disc, halo) produce secular changes in said frequencies, can populate (deplete) certain trajectories based on their frequencies due to resonance trapping (scattering) and even introduce peculiar signatures in phase-space when a group of stars are taken out of equilibrium (either caused by an internal or external perturbation), switching on a phase-mixing process. All these dynamical mechanisms imprint conspicuous features in the distribution of velocities, and even positions, which we can observe and relate with the shape and evolution of our Galaxy.

1.1 THE MILKY WAY BEFORE GAIA

More than 100 years ago, Schwarzschild imagined the MW disc as a stacking of stars in orbits that oscillate both in Galactocentric radius (R) and perpendicular to the plane (Z). Assuming that the Galaxy was axisymmetric and that the density fell with R exponentially, he described the velocity distribution at the Solar neighbourhood (SN) as a triaxial Gaussian (Schwarzschild, 1907), with a long tail towards

2 In the cases when the gravitational potential does not have enough symmetries, such base can still be constructed. Nevertheless, a simpler potential must be used, usually a Stäckel potential. This means that the action-angles assigned to one star/orbit are not the true ones, since in general they do not longer exist, and are instead an approximation based on the observed position and velocity.

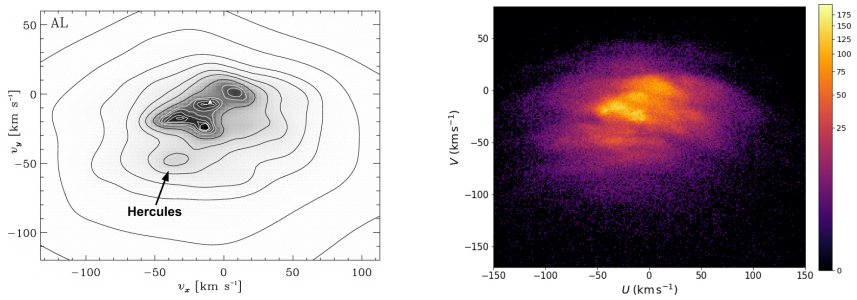

(a) (b)

Figure 2: Galactocentric radial velocity (v_R, horizontal axis) against azimuthal velocity (v_ϕ, vertical axis). Left: results obtained with the *Hipparcos* satellite (From Dehnen, 1998). Right: same projection but with the *Gaia* DR2 data (From Gaia Collaboration et al., 2018d).

lower azimuthal velocities[3] (v_ϕ). While the scarce data available at the time could seem to favour this description, there were already some hints of substructure in velocity space (e.g, Proctor, 1869; Eggen, 1958), implying a more complex distribution of orbits. Initially, it was thought that this complexity could be related to the disruption of Open Clusters, too young still to be relaxed in the Galactic potential (Eggen, 1996). It was not until we gained access to a large data set of stars with measured proper motions that we had the opportunity to explore Schwarzschild's prediction reliably. Using the observations from the *Hipparcos* satellite (ESA, 1997), the predecessor of *Gaia*, Dehnen (1998) produced a detailed map of the velocities at the SN that revealed a wealth of substructure (see Fig. 2.a).

With the fact that these over-densities, also known as *moving groups*, contained stars with different ages and metallicities (Skuljan et al., 1999; Famaey et al., 2005; Antoja et al., 2008), the dynamical origin proposed by Kalnajs (1991), Dehnen (2000), Fux (2001) and De Simone et al. (2004) became the favoured explanation. In this scenario, the appearance of substructure is related to a break of symmetry in the system: either the Galaxy is not axisymmetric like Schwarzschild assumed or the potential varies with time. In reality, the combined contribution of the spiral arms and the Galactic bar implies that both conditions are most likely meet simultaneously. Many of the features observed in velocity space were naturally explained by a short and fast bar whose Outer Lindblad Resonance (OLR) is close to the Sun, causing a significant resonant scattering/trapping. This has been the preferred model for a long time (e.g., Kalnajs, 1991; Dehnen, 2000; Minchev et al., 2007; Monari et al., 2017a; Quillen et al., 2018a). In particular, Antoja et al. (2012) used the RAVE data (Steinmetz et al.,

3 This effect is known as asymmetric drift and it is caused by a combination of i) having more stars closer to the centre of the potential well (i.e., a density profile that decreases with angular momentum) and ii) the inner stars having a greater probability of visiting far away regions of the disc (they are kinematically hotter).

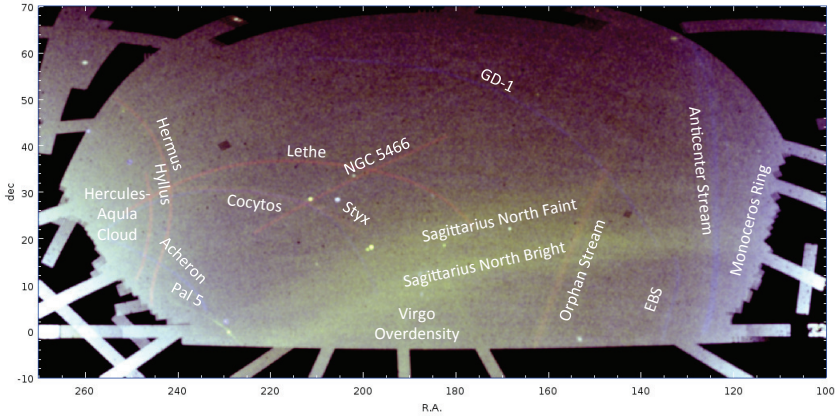

Figure 3: Field of streams in the North Galactic hemisphere as seen by SDSS (From Grillmair & Carlin (2016)).

2006) to demonstrate that the azimuthal velocity of the *moving groups* changed with Galactocentric radius to, later, relate the gradients of some of them (in particular, the so-called Hercules *moving group*) with the OLR and use that information to estimate the pattern speed of the bar (Antoja et al., 2014). Still, these pioneer studies could only explore regions near the Sun, up to ~1 kpc, due to the restrictions of the available samples. Recently, it has been shown that a long and slow bar can also explain reasonably well the morphology and location in velocity space of the Hercules *moving group*: Pérez-Villegas et al. (2017) proposed that the stars orbiting near the Lagrangian points of the co-rotation resonance could visit the SN and create substructure, whereas, in the case of Hunt & Bovy (2018), the main source of substructure is the resonance 4:1 of the slow bar.

In parallel, Minchev et al. (2009) showed that some of the substructure, specifically that with an arch shape in the plane of radial velocity (v_R) against azimuthal velocity, can be related to phase-mixing. Gómez et al. (2012) explored the idea even deeper by using N-body models of a MW-like galaxy accreting a small satellite. They found that these arches are expected to change with azimuth across the disc, and that the information encoded in the kinematics could reveal details about the mass and orbit of the perturber. This added another layer of complexity in the interpretation of the observed phase-space. The major shortcoming to distinguish among the available models was that they predicted similar results at the SN and the lack of data, restricted at the time to the surroundings of the Sun and limited to ~300 000 stars, prevented almost any attempt of venturing beyond.

Tangential to that discussion, the study of the halo of the MW was revealing more and more substructure, in this case related to the satellites and their disruption, first in the form of Dwarf Spheroidal galaxies like the Sagittarius (Sgr) dwarf detected by Ibata et al. (1994), then

by discovering the first Ultra Faint Dwarf galaxies (see the introduction by Simon & Geha, 2007). As more and more data for these systems became available thanks to several high-quality photometric and spectroscopic surveys like the Sloan Digital Sky Survey (SDSS York et al., 2000) and PanSTARRS-1 (PS1 Chambers et al., 2016), we started detecting prominent streams of stars spanning several degrees in the sky, like the ones shown in Fig. 3 (see Grillmair & Carlin, 2016, for a review on the topic), or even wrapping around it entirely in the case of the Sgr stream (Majewski et al., 2003).

The formation of stellar streams is a natural consequence of the tidal stripping that all satellites suffer while being cannibalised by the MW. The stars that manage to escape the gravitational pull of their progenitor, mostly the ones with enough energy (i.e., the kinematically hottest population), become bound to the host's potential with an orbital frequency that decreases with Galactocentric distance. This introduces a difference in the velocities between stars ejected close to the centre of the host and those ejected farther away from it. As a result, the tidal debris "fans out", delineating reasonably well the orbit of their progenitor (but see Sanders & Binney, 2013) and thus enabling the estimation of the shape and mass of our Galaxy (e.g., Johnston et al., 1999; Eyre & Binney, 2009).

The Sgr stream (Mateo et al., 1996; Totten & Irwin, 1998), being the most prominent, long and massive of them all, has been extensively used to study the profile of the MW's potential. The first attempt to it was done by Helmi (2004), where she argued that the kinematics of the leading arm (the tidal debris that, having a higher orbital frequency than the Dwarf, orbits ahead of it) constrains the dark matter halo to be prolate[4]. Later, several studies attempting to fit the stream's observed distance and radial velocities reached contradicting conclusions, from oblate halos (Johnston et al., 2005) to a triaxial one with the short axis almost parallel to the galactic plane (Law & Majewski, 2010b), in principle an unstable configuration (Debattista et al., 2013). Nonetheless, none of them has been able to reproduce successfully observed features like a bifurcation in the leading arm (Belokurov et al., 2006), clearly appreciable in Fig. 3, later detected also in the trailing (Koposov et al., 2012; Navarrete et al., 2017). Peñarrubia et al. (2010) showed that a rotating progenitor could create such features but later demonstrated that the Sgr Dwarf probably never hosted a disc (Peñarrubia et al., 2011). To aggravate the situation, the observational studies where performed with only some hundreds or thousands of stars, usually of a very specific population. Only recently it was possible to reach one order of magnitude more stars by using the extensive optical/near-infrared catalogue of RR-Lyrae stars of PS1 (Sesar et al., 2017b). This type of variable stars are standard candles for which em-

4 Prolate: spheroid with one axis longer than the other two, similar to a Rugby ball. Oblate: spheroid with one axis shorter than the other two, similar to a pancake.

pirical relations have been constructed that allow the estimation of their distance from the apparent magnitude and metallicity with an accuracy of 5% (Vivas & Zinn, 2006). In Hernitschek et al. (2017), they modelled the spatial distribution of the stream in 3D but could not give a list of candidates since removing the contamination from the disc and halo is not trivial. To do it properly, the kinematic data is necessary. The radial velocities, though, were only available for a small sample of stars in Sgr and the other two components of the velocity were missing due to the almost absolute lack of proper motions measured at those distances (but see Sohn et al., 2015, for an application with the Hubble Space Telescope data).

1.2 GAIA ENTERS THE SCENE

Right after *Hipparcos*, the European Space Agency (ESA) started working on its successor. Originally thought as an interferometer, *Gaia* was conceived back in the early '90s (Battrick, 1994), but it was not until the 2000s when the science plan finally crystallised (Perryman et al., 2001). Then, all the hopes of engineers and scientists alike were placed inside a Soyuz spacecraft and launched into the sky the 19th of December 2013. Almost a month later, on the 8th of January, on its way to the Lagrange point L2, *Gaia* observed the Universe for the first time.

The *Gaia* satellite rotates about its axis with a six hours period, capturing the light of all the sources (stars, unresolved binares, quasars, far away galaxies, and others) that reach the focal plane through its two telescopes, and measures their position with a precision at the level of μas (Gaia Collaboration et al., 2016b). After sending the data to the ground facilities and processing it, firsts by grouping individual transits into sources and then by modelling their movement in the sky, parallaxes and proper motion are obtained for almost any object brighter than ~21 mag with the Astrometric Global Iterative Solution (AGIS, Lindegren et al., 2016). With a vast amount of astrometric data, expected to be orders of magnitude larger than any previous sample available, complemented by the photometry and low-resolution spectra obtained other two on-board instruments provide, *Gaia* was set to revolutionise all fields of astrophysics. As I am writing this words, the satellite continues to acquire data and has already produced more than 70 Petabytes of information during its ~2 000 days (~66 months) of operation, already beyond the nominal mission (5 years) and with enough fuel to last at least another 3 or 4 years.

It has not been necessary to wait until the end of the mission to start feeling its impact – on the 25th of April 2018, shortly after the beginning of this thesis, the second data release (DR2, Gaia Collaboration et al., 2018b) was made public. With only 22 months of data, it brought positions and magnitudes (G) for nearly 1.7 billion stars,

and parallaxes, proper motions and magnitudes in the red (RP filter) and blue (BP filter) bands (Riello et al., 2018; Evans et al., 2018) for 1.3 billion of them (Gaia Collaboration et al., 2018b). Combined with the radial velocities for cool stars up to magnitude G ~13 obtained from the RVS instrument (Cropper et al., 2018; Soubiran et al., 2018), this represents the largest 6D sample of stars in history: 7.2 million stars with full phase-space information! In the following months we experienced a flood of articles, with more than 5 papers a day using DR2 data being submitted to peer-reviewed journals and touching almost every branch of astrophysics: from solar system objects to extragalactic studies, even testing the predictions of General relativity, and, of course, also Galactic astrophysics. As a part of the *Gaia* community, I lived those first weeks with great excitement, a period that will be surely remembered as the beginning of the Golden Age of Galactic Astronomy.

1.3 RECENT DEVELOPMENTS IN GALACTIC ARCHAEOLOGY

The reduction of the uncertainties in velocities by an order of magnitude allowed to explore the kinematics of the disc with an unprecedented precision within a large volume, of the order of several kiloparsecs (Gaia Collaboration et al., 2018d). Figure 2.b shows the v_R-v_ϕ plane at the SN which, thanks to *Gaia*, was observed at a level of detail never seen before. With just a histogram, the *moving groups* can be spotted without any effort while, until then, advanced techniques were required to reveal them. With a simple visual inspection, it becomes obvious that the whole kinematic plane is populated by several structures, some of which now appear to have well defined arch-like shapes, including a new structure at large v_ϕ that went undetected for decades due to the lack of statistics. This figure was presented in the science demonstration paper published together with the DR2 data, and established the power of *Gaia* to resolve the phase-space substructure of the MW.

Shortly after, several authors used this same data to make other major contributions to Galactic Archaeology. For instance, Helmi et al. (2018) proved that, hidden in our disc, there are ancient stars native to another galaxy (Gaia-Enceladus) that collided with our own ~10 Gyr ago (see also Belokurov et al., 2018). These stars now dominate the inner halo, in good agreement with the hierarchical formation models (e.g., Bullock & Johnston, 2005), giving yet another proof that the halo of our Galaxy was not formed *in-situ*. Such massive interaction must have heated the primordial MW, possibly in the shape of a proto-disk at the time, and lunched most of its stars into halo-like orbits (Di Matteo et al., 2019; Gallart et al., 2019). As a result, the local halo is dominated by two different components, the debris of Gaia-Enceladus (more metal poor) and the heated disc (more metal rich),

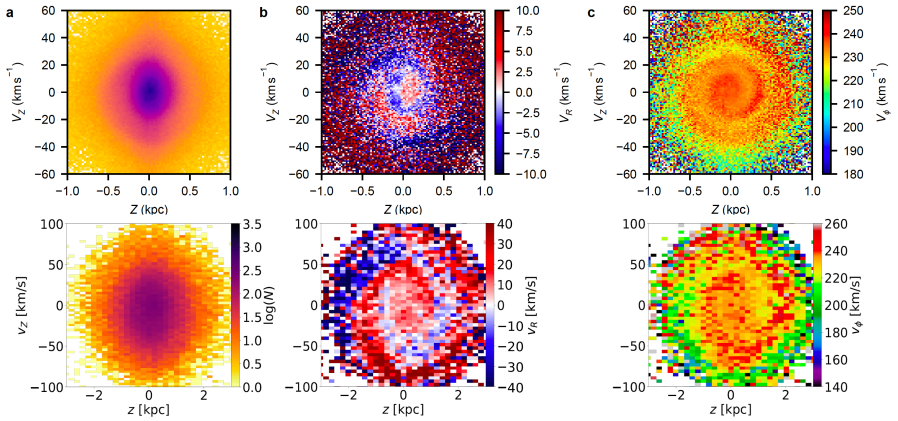

Figure 4: Velocity perpendicular to the disc (vertical axis) against height above/below the plane (horizontal axis) coloured by density (a), azimuthal velocity (b) and radial velocity (c). Top: observations from *Gaia* DR2 (from Antoja et al. 2018). Bottom: simulation of the interaction between a MW-like host galaxy and a Sgr-like satellite (from Laporte et al. 2019a).

producing the double sequence in the Hertzsprung–Russell diagram observed with DR2 (Gaia Collaboration et al., 2018a).

Another crucial revelation was that our Galaxy was out of equilibrium. Antoja et al. (2018) demonstrated that the disc is undergoing a phase-mixing process, as some authors hinted before (e.g., Minchev et al., 2009; Gómez et al., 2012), and that the cause was most likely the interaction with a satellite: the Sgr dwarf galaxy. Alternative explanations were proposed, like the buckling of the bar (Khoperskov et al., 2019) or the continuous interaction of the disc with dark matter sub-halos (Chequers et al., 2018), an idea partially supported by the discovery of gaps in some well-known streams (e.g., Bonaca et al., 2019b). Still, Sgr remained the best candidate since its existence is undeniable and the modelling of its interaction with the MW reproduces the observations more accurately. Most notably, Laporte et al. (2019a,b) showed with an N-body simulation that is was possible to simultaneously reproduce, at least qualitatively, the phase-space spiral (see Fig. 4), some of the features seen in the kinematic maps (Gaia Collaboration et al., 2018d), as well as a pair of diffuse overdensities in the Galactic anticentre at a distance ~10 kpc known as Monoceros (Newberg et al., 2002; Crane et al., 2003) and the ACS (Grillmair, 2006), for which alternative origins – such as being disrupted satellites – are still being considered (e.g., Ibata et al., 2003; Peñarrubia et al., 2005; Kazantzidis et al., 2008; Slater et al., 2014; Xu et al., 2015).

Inspite of the reinvigorated interest on Sgr for its link with the disc dynamics, there has been little advance in the understanding of its orbit as the main issues with its modelling remained almost untouched, that is, as we discussed in Sect. 1.1, the kinematics of the leading arm

and the bifucartion/s. Some attempts to study the proper motions of the stream with *Gaia* used already known members (Yang et al., 2019). However, a study that would take advantage of the full power of the satellite was still missing.

1.4 GOALS OF THE THESIS

This thesis began right before the DR2 release, when the community was expectantly waiting for the superb quality and extent of the *Gaia* data that was promised to help us answer some of the questions that could not be addressed before. We devoted the period previous to the publication to test and refine our pipelines to quickly process the new observations and be the first to explore a Galaxy that was now being unfolded right in front of our eyes. The methods developed had to be automatic and fast in order to deal with the vast amount of data available, and should allow for the robust detection of new kinematic substructure across the whole MW in order to quantify its variations and gradients.

The ultimate goal of this thesis is to provide a thorough characterisation of the phase-space features of our Galaxy, introducing novel empirical measurements that are an essential clue to decipher the structure of the MW and its past, together with the modelling of its different components – from the pattern speed of the bar and spiral arms to the shape of the halo and the chronology of its interactions with satellite galaxies. More specifically:

- Characterise the substructures in velocity space for the disc stars, track each of them individually across the MW and quantify their changes with position across the Galaxy.
- Extend the search for phase-space substructure to the edge of the disc, describe the morphology and investigate their kinematics.
- Investigate the different agents that can cause the phase-space substructure found in the disc: non-axisymmetries of the potential and/or perturbations (internal or external).
- Detect the kinematic substructure in the halo of the MW and, in particular, provide a precise description of the Sgr stream regarding its proper motions, distance and distribution on the sky.

Despite being apparently disconnected subjects, in the light of the new observations we have learned that these are actually closely related. Thus, we want to provide a link between the kinematics of the disc and the orbit of Sgr that future works will need to consider in order to fully understand the structure and history of our Galaxy.

1.5 THESIS OVERVIEW

This thesis is organised as follows:

- In Chapter 2, we study the kinematic substructure of the MW disc, in particular, the v_R-v_ϕ plane. This is the most informative projection when studying the dynamical effects of non-axisymmetric components like the bar. One of the goals is to explore the changes of the *moving groups* as a function of Galactocentric radius and azimuth since, as mentioned before, it helps to break the degeneracies among the possible mechanisms that could formed them.

  We started running our codes on the same day that the DR2 data was made public, and we immediately realised the level of complexity that *Gaia* was revealing. Thanks to the use of the Wavelet Transformation (WT Starck & Murtagh, 2002), we successfully detected and classified the hundreds of *moving groups* present, not only at the SN, but also at other Galactic neighbourhoods. These regions, until now almost completely unexplored, contain a wealth of kinematic substructure as well. By connecting the different regions, we have found that most of the moving groups are actually structures in phase-space that can span several kiloparsecs both in radius and azimuth. We have also measured their gradients and offer, for the first time, a tentative separation between the different structures based on their dynamical origin, associating them with resonances (when the angular momentum is roughly preserved along the track) or with phase-mixing (when it is the energy/frequency).

- In Chapter 3, we set out to detect the kinematic substructure in the halo and at the edge of the disc using only proper motions. By not requiring the radial velocity, we increase the magnitude limit of our sample from roughly <13 mag to <21 mag, resulting in a list of $\sim 7\times10^8$ stars once we remove the ones that are close to the Sun with a cut in parallax. In order to deal with the vast size of the sample, we apply the WT to the proper motion histogram that we obtain at each patch in the sky (HEALpix level 5), and focus on the properties of the dominant structure.

  With this strategy we have revealed, among other things, known external galaxies and Globular clusters, as well as a complex Galactic anticentre, especially in the north Galactic hemisphere where we have detected Monoceros and ACS with an unprecedented level of detail. Their arch-like shape and disc-like kinematics, together with their Herzprung-Russel diagrams, make us favour a perturbative origin in which their stars were once part of the disc. The characterisation of these structures, both morphological and kinematical, provides the required empirical data

to model their orbits accurately for the first time, and compare quantitatively the different theories proposed for their origin. Furthermore, the stars that we have associated with Monoceros and ACS can also be used to test the different models using their chemistry and ages (combined with data from future *Gaia* releases and other surveys).

- In Chapter 4, we take the results from the previous chapter but focus instead on a particular system: the Sgr stream. We are interested on it for its impact on the MW and we aim to provide a vast sample of stars with which to study the proper motion trends along the stream.

  By selecting the dominant over-densities in the proper motion plane that have been found to lay near the orbital plane of Sgr, and then removing those that are seen to follow the kinematics of the disc, we have been able to isolate its contribution. As a result, we show for the first time the proper motion variations along the whole stream as it wraps around the sky. Moreover, we have produced the largest sample of Sgr stars ever compiled encompassing different stellar type: turn-off, red clump, horizontal branch and even (in the nearer parts of the stream) main sequence stars. Finally, comparing these new observations with one of the most popular models of the stream (Law & Majewski, 2010b) we note significant discrepancies that are most likely related to the use of a wrong gravitational potential.

- In Chapter 5, once we have proven the capabilities of *Gaia* for studying even distant objects such as Sgr, we decide to go one step further and examine in depth the 5D distribution of the tidal debris along its tails. The study of its tangential velocities has never been attempted befor because it requires both proper motions and distances. Nevertheless, it is important in order to have access to its full phase-space, together with the radial velocities that can be obtain with spectroscopy if one has a reliable sample of stars.

  For that, we used the *Gaia* RR Lyrae stars (Holl et al., 2018; Clementini et al., 2019), standard candles for which photometric distances can be derived with a precision of ~5%. We started by selecting probable members based on their trends in distance and proper motions. With the resulting sample, the largest ever obtained in 5D, we then measured the changes in Galactocentric distance, tangential velocities and metallicity along the stream, and provided new apocentres, mean metalicities and empirical trends for the RR Lyrae stars that can be used to model the old population of the stream. Additionally, we found new observational constrains on the bifurcation, a poorly understood feature whose origin still eludes us.

- Finally, in Chapter 6 we summarise the main results of the thesis and discuss their implications in the light of the coetaneous work, as well as proposing future avenues that our research has open up.

KINEMATIC SUBSTRUCTURE IN THE MILKY WAY DISC

2

Abstract

Context: Gaia DR2 has delivered full-sky 6-D measurements for millions of stars, and the quest to understand the dynamics of our Galaxy has entered a new phase.

Aims: Our aim is to reveal and characterise the kinematic substructure of the different Galactic neighbourhoods, to form a picture of their spatial evolution that can be used to infer the Galactic potential, its evolution and its components.

Methods: We take ~5 million stars in the Galactic disk from the *Gaia* DR2 catalogue and build the velocity distribution at different Galactic Neighbourhoods distributed along 5 kpc in Galactic radius and azimuth. We decompose their distribution of stars in the V_R-V_ϕ plane with the wavelet transformation and asses the statistical significance of the structures found.

Results: We detect distinct kinematic sub-structures (arches and more rounded groups) that diminish their azimuthal velocity as a function of Galactic radius in a continuous way, connecting volumes up to 3 kpc apart in some cases. The decrease rate is, on average, of ~23 $\mathrm{km\,s^{-1}\,kpc^{-1}}$. In azimuth, the variations are much smaller. We also observe different behaviours: some approximately conserve their vertical angular momentum with radius, while some seem to have nearly constant kinetic energy. These two trends are consistent with the approximate predictions of resonances and of phase mixing, respectively. In addition, we detect new kinematic structures that only appear at inner/outer Galactic radius, different from the Solar Neighbourhood.

Conclusions: The strong and distinct variation observed for each kinematic sub-structure with position in the Galaxy, along with the characterisation of extrasolar moving groups, will allow to better model the dynamical processes affecting the velocity distributions.

This chapter has been published as: P. Ramos, T. Antoja and F. Figueras, 2018, A&A 619, A72

2.1 INTRODUCTION

The velocity distribution of the stars in our Galaxy has been thoroughly studied over recent decades (e.g. Eggen 1996; Dehnen 1998; Skuljan et al. 1999; Famaey et al. 2005; Antoja et al. 2008), in an attempt to understand the Galactic potential and its components. Models of the orbital effects of the Galactic bar and the spiral arms have shown that they create substructures and gaps in the velocity distribution, and that these are sensitive to position in the Galaxy (Dehnen 2000; Fux 2001; Bovy 2010; Antoja et al. 2011; Quillen et al. 2011; McMillan 2013; Hunt & Bovy 2018). All these studies also demonstrate that only the exploration of regions outside the Solar neighbourhood (SN) would yield a proper constraint on the potential.

The first studies that investigated Galactic regions relatively distant from the Sun, even with the limitations in the number of stars and precision of their samples, already presented relevant results. For instance, Wilson (1990) was able to trace the Hyades and Sirius streams up to 1.3 and 0.8 kpc away from the Sun, respectively, using K giants. Later, Antoja et al. (2012) was the first study showing that the kinematic substructures in the SN change their velocities when observed in other volumes of the RAVE data (Steinmetz et al., 2006). In a follow-up of that work, Antoja et al. (2014) demonstrated that the azimuthal velocity of the Hercules stream decreases with Galactic radius consistently with the effects of the Outer Lindblad Resonance (OLR) of the Galactic bar, as proposed by the models of Dehnen (2000) and Fux (2001). With data from RAVE, LAMOST (Cui et al., 2012), APOGEE (Majewski et al., 2017) and GALAH De Silva et al. (2015), later studies have also shown that the kinematic groups are position dependent (Xia et al., 2015; Liang et al., 2017; Monari et al., 2017b; Kushniruk et al., 2017; Quillen et al., 2018b; Hunt & Bovy, 2018; Monari et al., 2018).

Now, the *Gaia* mission (Gaia Collaboration et al., 2016b), which allowed astrophysicists to gain considerable scientific insight with only a year of observation time (*Gaia* DR1, Gaia Collaboration et al. 2016a), has the chance to show its unparalleled scientific value once more with the second data release (*Gaia* DR2, Gaia Collaboration et al. 2018b). After 668 days of surveying, the unprecedented quantity, quality, and extension of the *Gaia* data has already uncovered a new configuration of the velocity distribution in the SN. This includes stars organised in multiple thin arches that have never been seen before (Gaia Collaboration et al., 2018d) as well as the beautiful continuity of these substructures through the Galactic disk (Antoja et al., 2018). All these new findings force us to re-evaluate the hypotheses behind the existence of kinematic substructure in the disk, an undertaking that requires a more detailed characterisation of the velocity distribution.

In this work, we use ~5 million sources in *Gaia* DR2 with positions, radial velocity, proper motions and parallaxes to study the known and the new main features of the velocity distribution of the SN, as well as to examine the most remote regions in the disk explored thus far. For this, we use the wavelet transformation (WT) to detect overdensities in the velocity distributions and draw their evolution with Galactic radius and azimuth.

This Chapter is organised as follows. In Section 2.2, we describe the observational data used and its partition into sub-samples. Section 2.3 presents the formalism of the WT and the methodology used to detect structures. Section 2.4 characterises the kinematic distribution of the SN and Sect. 2.5 explores the evolution of these in different Galactic neighbourhoods. Then, in Sect. 2.6 we discuss the implications of our findings and propose possible future lines of research. Finally, we present the main conclusions of this work in Sect. 2.7.

2.2 DATA AND SAMPLE SELECTION

Gaia is an all-sky astrometric satellite from which we can now obtain positions in the sky (α, δ), parallaxes (ϖ), and proper motions ($\mu_{\alpha*}$, μ_δ), along with the estimated uncertainties (σ) and correlations, for ~1.3 billion sources. Also, line of sight velocities (v_{los}) are available for >7.2 million stars with an effective temperature between 6900K and 3550K (Katz et al., 2019), corresponding roughly to spectral types from F2 to M2 (Pecaut & Mamajek, 2013).

Our goal to study the kinematic structure required all six phase-space coordinates, which means that our sample consists only of stars with observed radial velocity. On top of that, we limited ourselves to sources with "good" parallax ($\varpi/\sigma_\varpi > 5$) in order to use the estimator $1/\varpi$ as distance (this choice and its effects are discussed in Appendix A). Additionally, we focus on disk stars by selecting the heights (Z) between $\pm$0.5 kpc, which corresponds roughly to the 10th and 90th percentile of the whole sample. As a result, our sample is composed of 5,136,533 stars. A significant fraction of red giants over dwarfs for the most distant sub-samples is expected, with a more homogeneous mix near the Sun's position. We note, however, that the youngest stars are missing due to the restriction in effective temperature.

For simplicity, we adopted a cylindrical Galactocentric coordinate system since it is better suited for systems with rotational symmetry, as is roughly the case for the Milky Way (MW) disk. We fixed the reference at the Galactic centre (GC) with the radial direction (R) pointing outwards from it, the azimuthal (ϕ) negative in the direction of rotation, and the vertical component (Z) positive towards the north Galactic pole. In this scenario, we took the Sun to be at $R_\odot = 8.34$ kpc (Reid et al., 2014), $\phi_\odot = 0°$ and $Z_\odot = 14$ pc (Binney et al., 1997). Following from the choice of coordinate system, we studied

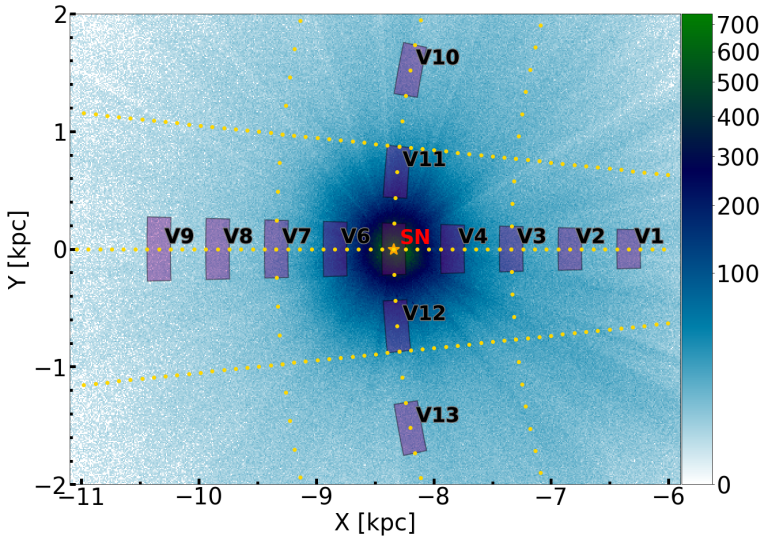

Figure 5: Distribution of the sample in configuration space. We show the histogram of the 5,136,533 stars (see text) with a binning of 10x10 pc. The Sun is shown as an orange star and the GC is located at $(X, Y) = (0, 0)$. The golden dots indicate the centres of the volumes used for the exploration in different Galactic neighbourhoods. Each radial line contains 51 volumes, and each arch at fixed radius has 21 volumes. The purple patches correspond to the subsamples from the wider grid for which we perform a detailed study of their velocity distribution. The properties of these subsamples are summarised in Table 1.

the stars in the $\dot{R} = V_R$, $R\dot{\phi} = V_\phi$ velocity plane. To compute these from the *Gaia* observables, we adopted a circular velocity for the Sun of 240 $\mathrm{km\,s^{-1}}$as in Reid et al. (2014), and a peculiar velocity with respect to the local standard of rest (LSR) in Cartesian coordinates of $(U_\odot, V_\odot, W_\odot) = (11.1, 12.24, 7.25)$ $\mathrm{km\,s^{-1}}$from Schönrich et al. (2010). The uncertainty in velocities was computed by error propagation with the Jacobian matrix of the transformation, including the correlations, from ICRS to Galactocentric cylindrical coordinates.

Figure 5 displays the distribution of the sample in the disk plane, highlighting the isotropy of the *Gaia* data except for the radial features related to extinction. Superposed, we plot the 13 sub-samples that we used to study the variation of the velocity distribution with radius and azimuth. The properties of these sub-samples are shown in Table 1. The SN has the largest number of stars and the smallest uncertainties, allowing for a detailed study of the kinematic structures. Then V1 to V9 along R let us explore the changes with Galactocentric distance and the effects of the sample size. Finally, we used V10 to V13, located at mirrored azimuths with respect to the Sun, to investigate variations in azimuth. All these volumes are part of a wider grid of sub-samples, whose centres are represented by the golden dots in Fig.5. Their sizes are kept constant, with 200 pc in radius and 3 deg

Table 1: Properties of the main sub-samples in our study. In the first column, the name of the volume is shown according to Fig.5. Columns 2 and 3 contain the ranges of the radial and azimuthal coordinates. The last two columns show the summary statistics *Counts* and $\tilde{\sigma}_{vel}$ that are, respectively, the number of stars in the sub-sample and the square root of the trace of the median velocity error covariance matrix in cylindrical coordinates.

Volume	R [kpc]	ϕ [°]	Counts	$\tilde{\sigma}_{vel}$ [km/s]
SN	8.24-8.44	-1.5~1.5	435,801	0.83
V1	6.24-6.44	-1.5~1.5	6,920	3.45
V2	6.74-6.94	-1.5~1.5	10,959	2.53
V3	7.24-7.44	-1.5~1.5	20,743	1.93
V4	7.74-7.94	-1.5~1.5	88,184	1.99
V6	8.74-8.94	-1.5~1.5	77,457	1.95
V7	9.24-9.44	-1.5~1.5	13,006	1.94
V8	9.74-9.94	-1.5~1.5	5,994	2.39
V9	10.24-10.44	-1.5~1.5	3,340	2.79
V10	8.24-8.44	-12~-9	10,579	1.63
V11	8.24-8.44	-6~-3	72,524	1.75
V12	8.24-8.44	3~6	64,849	1.71
V13	8.24-8.44	9~12	9,753	1.62

in azimuth, resulting in an area of ~0.18 kpc^2 (smaller towards the GC and larger in the opposite direction). Overall, we explored the Galaxy disk with 216 volumes divided into three sweeps along R (at $\phi = \{-6, 0, 6\}$ deg.) and three along ϕ (at $R = \{R_\odot - 1, R_\odot, R_\odot + 1\}$ kpc). To produce smooth results, we had to balance the step size and overlapping of the volumes with the range of exploration: we decided to layout the centres every 100 pc between 6.04 and 11.04 kpc, and every 1.5 degrees between -15 and 15 degrees. This translates into an overlapping such that each area is covered completely by half of the two adjacent areas.

2.3 METHODS

In order to detect substructures in the velocity plane (V_R, V_ϕ), we used the WT (Starck & Murtagh, 2002). Particularly, we used the *à trous* algorithm, which allows the treatment of discrete data, like time series or images, without reducing the number of pixels (in our case, a 2D histogram). The WT decomposes the signal into several layers, or scales, of the same dimensions as the original, each comprising a

range of frequencies (in case of time) or sizes (in the case of space). In practice, the WT returns a map of coefficients for every scale such that zero means that the signal is constant in a neighbourhood whose size is determined by the scale (as we shall see below), whereas positive coefficients correspond to overdensities and negative ones are related to underdensities. The algorithm works by successive application of smoothing filters that, when subtracting one from the previous, results in the mentioned maps of wavelet coefficients. A more detailed explanation can be found in Antoja et al. (2008, 2015b) and Kushniruk et al. (2017) and references therein, where the WT is applied to similar and other cases. Here we used the multiresolution analysis (MRA) software, developed by CEA (Saclay, France) and Nice Observatory (Starck et al., 1998).

By construction, in the *à trous* algorithm, structures found at scale j have sizes between approximately 2^j and 2^{j+1} pixels. The conversion from pixels to physical units ($km\,s^{-1}$in this case) is given simply by the bin size (Δ) of the initial 2D histogram. For our work, we chose $\Delta = 0.5\ km\,s^{-1}pixel^{-1}$. Structures of a certain diameter D produce the highest wavelet coefficient at a scale j such that $\Delta 2^j \leqslant D \leqslant \Delta 2^{j+1}$. However, they also produce positive (negative) coefficients at other scales, especially if the overdensity (underdensity) is very significant or isolated. Other authors have focused on the upper scales (e.g. Antoja et al. 2012; Kushniruk et al. 2017), motivated not only by the typical sizes of the structures they were looking for, but also by limitations imposed by the measurement uncertainties. Now the quality of the data allows the study of smaller scales and for this work we investigated the scales j=2, 3, 4, and 5, corresponding roughly to the velocity ranges of 2-4 $km\,s^{-1}$, 4-8 $km\,s^{-1}$, 8-16 $km\,s^{-1}$, and 16-32 $km\,s^{-1}$, respectively.

Once the WT was computed, we performed a search for local maxima at each scale. To that end, we used the method `peak_local_max` from the *Python* package `Scikit-image` (van der Walt S et al., 2014), which returns a list of peaks separated by at least d pixels. To filter fluctuations that would correspond to a smaller scale, we used a minimum distance $d = 2^j$ pixels to retain only structures of diameters between approximately 2^j and 2^{j+1}. We note that with this approach elongated features will manifest as a trail of peaks, their precise location being along the line mostly determined by fluctuations.

Subsequently, to asses the significance of a peak, we acknowledge that the source of uncertainty in our data (the histogram) is Poisson noise. As in previous work (e.g. Antoja et al. 2008, 2012), we selected in the software the option of "Poisson with few events", which is based on the autoconvolution histogram method (Slezak et al., 1993) and which enables the study of the low-density regions in the velocity plane without loosing precision at the centre of the distribution. In short, the method evaluates the probability (P_p) that a given coeffi-

cient is not due to Poisson noise. Since it works in the wavelet space, it takes into account the number of stars not only at the peak, but also in a vicinity whose size, again, depends on the scale. Once we specify a significance threshold, the method returns a binary value signifying whether that peak is real or not, at that level of confidence (CL). For this work, we use a CL of 4, coded as:

- 0: $P_p < \epsilon_{1\sigma}$
- 1: $\epsilon_{1\sigma} \leqslant P_p < \epsilon_{2\sigma}$
- 2: $\epsilon_{2\sigma} \leqslant P_p < \epsilon_{3\sigma}$
- 3: $P_p \geqslant \epsilon_{3\sigma,}$

where $\epsilon_{n-\sigma}$ corresponds to the area $P[N(0,1) \geqslant n]$, N(0,1) being the Normal distribution, for instance, $\epsilon_{1\sigma} \approx 0.841$.

Additionally, we coded an alternative metric for the significance of the peaks that is the percentage of times the peak appears in a bootstrap (BS) of the data. We produced N=1,000 BS of the sample, computed the WT, and searched for all the peaks. Afterwards, and for each scale, we counted how many peaks had fallen inside a circle of radius 2^j pixels around the peak detected in the data[1]. Subsequently, the ratio between this number and the number of BS N, gives a value between 0 (the re-sampling failed to reproduce the peak every time) and 1 (the local maximum is always reproduced). We refer to this quantity as P_{BS} and is a measure of the probability we had of observing a particular peak in the data.

The output of the method described is a list of local maxima detected at each scale, along with the value of the WT coefficient, and the two measures of significance. We then consider a peak significant either if CL$\geqslant 2$ or $P_{BS} \geqslant 0.8$. In addition, we counted the number of stars closer to the peak than the minimum distance of $d = 2^j$ pixels, since those are the source of the positive (negative) wavelet coefficient. For these stars, we also computed their median error in V_R and V_ϕ to quantify the data uncertainty.

2.4 SOLAR NEIGHBOURHOOD

In this section, we study the kinematic substructure of the SN sample described in Sect. 2.2. The starting point is the 2D histogram of the cylindrical velocity coordinates V_R and V_ϕ, which is very similar to Fig. 22 from Gaia Collaboration et al. (2018d). After applying the methodology presented in Sect. 2.3 we obtain the wavelet planes (Fig. 6) and a list of significant peaks at the scales of $j = 2, 3, 4, 5$, corresponding to 2-4, 4-8, 8-16, and 16-32 $\mathrm{km\,s^{-1}}$, respectively. The colours in Fig.

1 Here, we assume that all local maxima correspond to structures of the upper size limit.

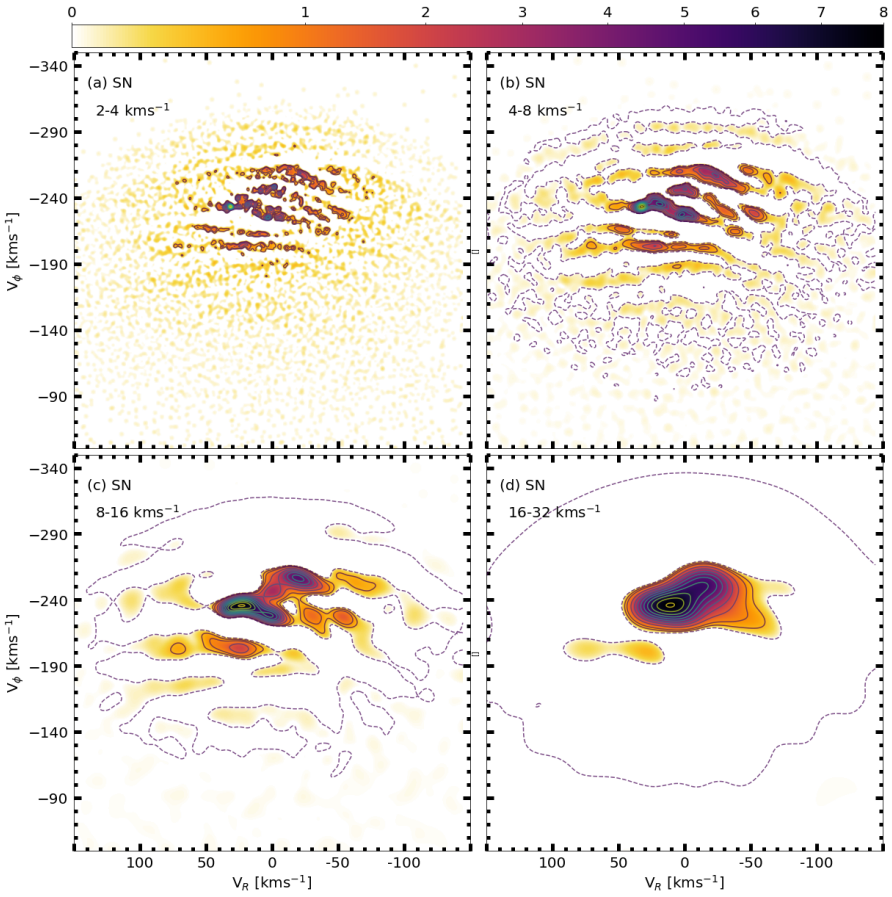

Figure 6: Wavelet planes highlighting the velocity substructure in the SN at different scales. The panels correspond to scales from $j = 2$ (a) to $j = 5$ (d). The colour bar shows only the positive coefficients, just like the solid-line contours, which are shown for different percentages of the maximum coefficient at levels from 10 to 90% every 10%, plus 5% and 99%. Additionally, the negative coefficients are represented by the dashed-line contour at the -1% level. With the values used (see text), the Sun would be located at (-11,-252) km s^{-1}.

6 correspond to the positive WT coefficients, while the contours are presented in two styles: solid lines delimit the positive coefficients at different levels (see caption) and dashed lines mark the negative coefficients at a single level. The negative contours help track the valleys and highlight the elongated features, but we did not plot them for the scale j=2 to ease visualization.

Panels (c) and (d) in Fig. 6 show a bi-modality and an asymmetric yet structured central distribution formed by several large-scale kinematic groups, similarly to previous studies (e.g. Dehnen, 1998; Antoja et al., 2012). However, at lower scales (panels (a) and (b)) we see the recently discovered thin arches (Gaia Collaboration et al., 2018d) crossing the velocity space in an almost horizontal direction. Imme-

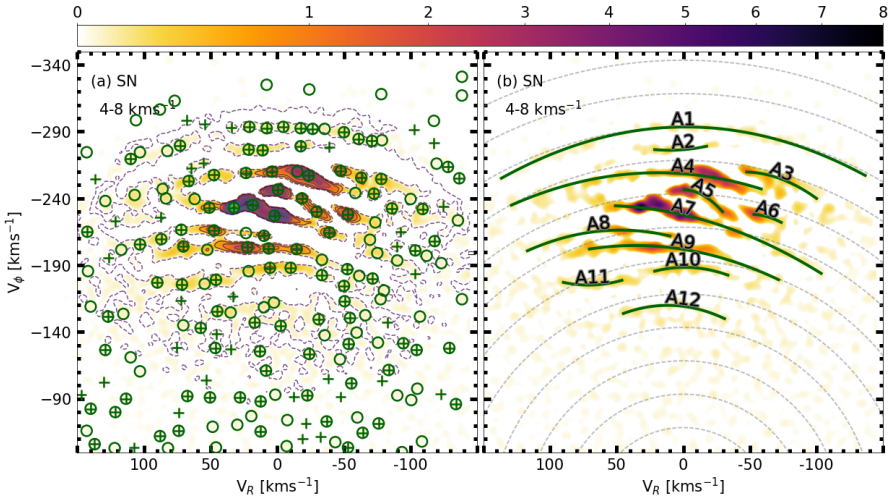

Figure 7: Wavelet plane at small scale (j=3) with the peaks and arches found. The circles correspond to those local maxima with a Poisson significance greater or equal to 2 ($P_p \geqslant \epsilon_{2\sigma}$), whereas crosses correspond to those with $P_{BS} \geqslant 0.8$. In both cases, the diameter corresponds to $\Delta 2^{j+1}$, indicating the highest size expected for the structures at this scale. On the right, we have associated the peaks into arches and fitted a parabola (dark green lines). The dashed grey lines then correspond to constant kinetic energy tracks.

diately below, we analyse these thin arches (Section 2.4.1) and the larger-scale kinematic groups (Section 2.4.2) in more detail.

2.4.1 *Thin arches in the velocity distribution*

The precision of the *Gaia* data, with uncertainties in the measurements well below 1 km s^{-1}, and the large number of stars in the SN sample (Table 1) allow us for the first time to appreciate the unprecedented detail of the velocity plane at small scales. The existence of thin arches in the *Gaia* DR2 data was first discovered by simple inspection of the 2D histograms of the velocity distribution. Here, the WT gives us a new representation of the data, allowing for a characterisation of the arches and, more importantly, the evaluation of their statistical significance.

Panels (a) and (b) in Fig. 6 clearly show wavelet coefficients that appear connected and organised in the above-mentioned thin arches, either composed of overdensities (positive coefficients) or underdensities (negative coefficients). The scales at which these elongated features appear indicate that they are intrinsically thin, at the level of 2-8 km s^{-1}. Another advantage of the WT is that it highlights overdensities that are otherwise hard to discern by direct inspection of the histogram, like the arches at high $|V_\phi|$. Although panels (a) and (b) unveil similar kinematic substructure, some of the arches appear to be split into two at the lower scale; for example, the structure passing

Table 2: Arches found at small scale j=3 (4-8 km s^{-1}). The arches are those appearing in Fig. 7, ordered by increasing V_ϕ. For each arch we give a label in the first column, the Classical MGs that it contains (if any) in the second column, and three of its points in the velocity plane in columns 3, 4, and 5, that is, the coordinates of the first and last peak of the line, and the expected azimuthal velocity corresponding to zero radial velocity, respectively. The last column shows a reduced χ^2 between the arch and the corresponding track of constant kinetic energy.

n.	Contains	Start (V_R,V_ϕ)	End (V_R,V_ϕ)	o-cross	Reduced χ^2
A1	-	136.5, -254.5	-136.5, -255.0	-293.4	4.09
A2	-	21.5, -276.5	-17.5, -279.0	-276.4	1.20
A3	γLeo	-47.5, -260.5	-100.0, -239.5	-246.5	335.05
A4	Sirius	129.0, -238.0	-58.5, -244.0	-258.4	25.52
A5	Coma,Dehnen98-6	-0.5, -246.5	-29.5, -230.0	-246.5	44.96
A6	Dehnen98-14	-53.0, -228.0	-73.5, -222.0	-200.4	1290.04
A7	Hyades,Pleiades	51.0, -233.0	-103.5, -183.5	-227.7	111.01
A8	-	117.0, -201.5	10.0, -212.0	-209.1	297.48
A9	Hercules, ϵInd	70.5, -204.0	-71.5, -180.0	-201.9	42.84
A10	HR1614	21.5, -185.5	-33.5, -182.5	-188.3	1.14
A11	Bobylev16-22	90.0, -177.0	46.0, -179.0	-203.7	260.49
A12	Arcturus	45.0, -155.5	-31.0, -149.5	-159.2	5.50

through (V_R, V_ϕ)=(0,-270) km s^{-1}. However, for the sake of simplicity, the remainder of this subsection is devoted to the scale j=3 alone.

Figure 7a shows the peaks detected at a scale of 4-8 km s^{-1}. Their coordinates and characteristics are listed in Table B.1 (available at the CDS, see Appendix B). Peaks signalled with a circle are significant in terms of the Poisson noise (significance greater or equal to 2, $P_p \geqslant \epsilon_{2\sigma}$); those marked with a cross are those that appeared in more than 80% of the bootstraps. As already discussed in Sect. 2.3, in the case of elongated structures, our peak finder procedure yields a trail of peaks. Although this method is suboptimal in detecting entire arches, we can nonetheless indirectly detect them as well as define their shape in the following manner. We selected as members of each arch the significant peaks, according either to their CL or their P_{BS}, that show continuity in the WT coefficient. With this definition, an arch ends when the significance of the peaks we detect drops below the threshold. We note that in some cases where the connectivity of the wavelet coefficients is not clear, this grouping is slightly conjectural, yet our global conclusions do not vary. Once the peaks were selected and grouped, we fitted a second-order polynomial, $\tilde{V}_\phi(V_R)$, to each arch between its minimum and maximum V_R.

The arches obtained are plotted in Fig. 7b with solid dark green lines and their characteristics are given in Table 2, including the coordinates in velocity space of the first and last peaks, as well as the

zero-order term of the polynomial (which corresponds to $\tilde{V}_\phi(V_R = 0)$). In the table we also include, for reference, the name of previously known kinematic groups (discussed in Sect. 2.4.2) that are contained within the arches. However, it is important to note that, since past studies dealt with more circular moving groups (MGs) – due mostly to the lack of precision in the astrometry–, the classical MGs and our arches are morphologically different entities.

We detected 12 arches, 6 of which cover a large range of radial velocities (A1,4,7,8,9,12). All of them are roughly constant in azimuthal velocity. We also see that, while some parabolas are symmetrical with respect to $V_R = 0$, others are inclined and/or present the maximum at $V_R \neq 0$, as already noted by Gaia Collaboration et al. (2018d). We confirm the existence of A1 already reported by Gaia Collaboration et al. (2018d) while A8 and A9 would correspond to the two branches of Hercules described in the same study.

From all the underdensities seen in this velocity space, the most prominent known one (the gap separating Hercules from the central part) is now clearly seen running between A7 and A8-9. Another gap, just below A12, hints to a thirteenth arch, although the small number of peaks in panel (b) does not allow us to constrain it. In contrast, we see a well organised trail of peaks above A1, at $V_\phi \sim -320$ km s^{-1}, but these only have one star each and therefore we refrain from connecting them as an arch.

Several models have shown that dynamical processes like phase mixing can imprint "arc-like features" of constant radial frequency, ω_R (Minchev et al., 2009; Gómez et al., 2012). Since this quantity is basically dependent on the energy for almost circular orbits, (also on angular momentum for more eccentric orbits, but not so strongly, see Dehnen 1999), these arches can be dubbed as structures of nearly constant energy. For this, we included constant energy profiles in Fig. 7b as grey dashed lines. We see how some of the arches found, such as A1 for example, are clearly compatible with having a constant kinetic energy along their trails. To quantify this similarity, we compared each parabola (evaluated with a step size of 0.1 km s^{-1}) to the corresponding constant kinetic energy line, using the energy of the parabola at zero radial velocity, that is, $\frac{1}{2}\tilde{V}_\phi^2(V_R = 0)$, and calculated a reduced χ^2 statistic (last column in Table 2). For the short arches, based on the few peaks used for their fit, this quantity may not be representative.

For the remaining arches, according to the reduced χ^2 , arches 1, 10 and 12 are the most compatible, while A3, 7, and 8 show the largest discrepancy with a constant energy line.

2.4.2 *Classic and new kinematic groups*

From the wavelet planes shown in panels (c) and (d) of Fig. 6, we can see the dominance of more rounded structures as the elongated

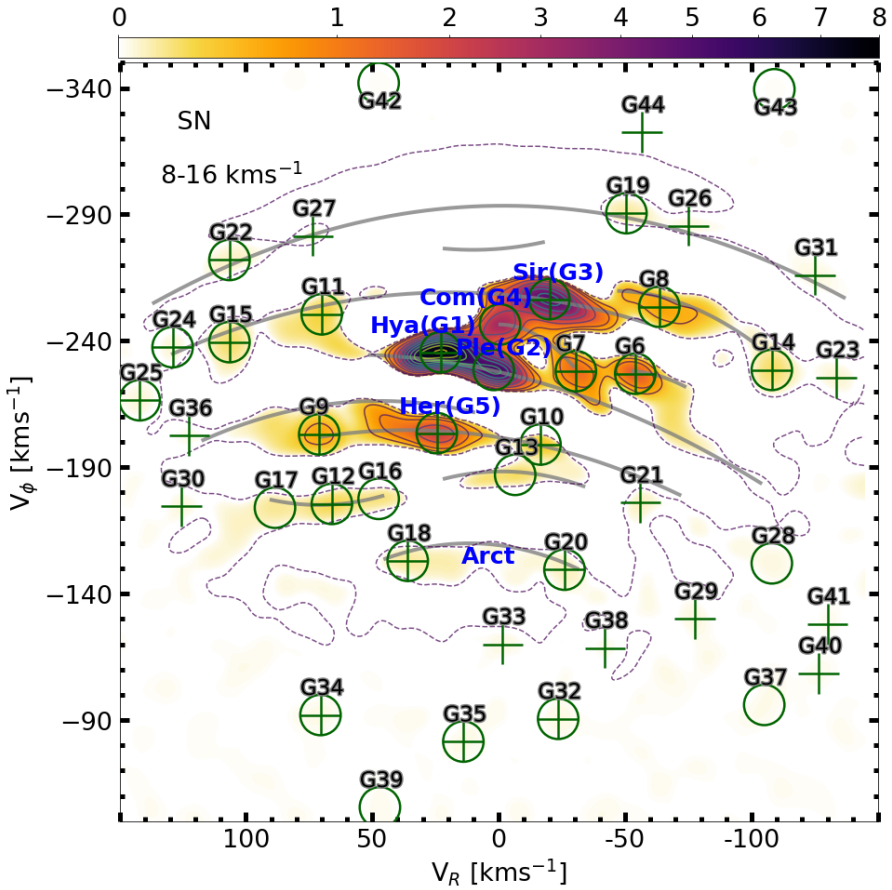

Figure 8: Wavelet plane (j=4) with the peaks found. The circles and crosses are defined as in Fig. 7. Also, solid grey lines represent the arches found in that same figure.

features merge or fade away. Nonetheless, in panel (c) we can still appreciate some imprints of elongated structures. From both panels, we can clearly recognise a bi-modality formed by the centre of the distribution and the Hercules MG. Yet, in panel (d) the latter presents a peanut-shape, which is in fact related to two different structures, while the central over-density contains the classical MGs.

In Fig. 8 we show the significant peaks found at j=4 where, as before, circles are related to Poisson, and crosses to bootstraps. For reference, we also plot the arches from Fig. 7b as grey lines. It becomes obvious that most of the peaks sit on top of an arch. Some of the known MGs are therefore expected to belong to the same arch, as we shall see below. All the detections in Fig. 8 are listed in Table 3, ranked according to their wavelet coefficient, that is, their relative strength at that scale. The list also contains the coordinates of the peak and the two measures of significance. The names of the objects are given according to the name in the literature that is most commonly assigned to the group (see Appendix C for details). Finally, if no match is found, we assign a new name composed of the letters

'GMG' (*Gaia* Moving Group) and a number according to their position on the list. The table also contains the number of stars contributing to the peak, along with their median errors in the radial and azimuthal velocities.

As can be seen, the known MGs (listed from selected literature in Table 5) are among the peaks with higher coefficients, consistent with previous samples. Indeed, we confirm 22 previously known objects from Table 5, including the most common ones. Regarding those that we do not observe, after studying each case individually we identify three reasons for this: i) we detect the MGs at a smaller scale (Fig. 7a), for example HR1614 or Hercules I; ii) the over-density is tracing an elongated feature and, as a consequence, the same structure can present the peaks at different locations depending on the sample used, for example Liang17-12 or Antoja12-15; and iii) in the case of the MGs described in Dehnen (1998), their positions were later determined with higher accuracy and renamed, for example Dehnen98-9 (Hercules II) or Dehnen98-12 (ϵInd). Therefore, we can say that all peaks are confirmed in a certain way[2]. The most noticeable differences with previous studies are the wavelet coefficients and peaks at the less dense regions on the velocity plane, which *Gaia* samples now with significantly better statistics. For instance, the Bobylev16-22 (G16, or Arifyanto05) appears to be elongated and matches one of the found arches (A11), plotted in grey beneath. Its relation to groups II and III from Helmi et al. (2006), however, is still not clear. Also, Arcturus (associated to G18 and G20) is very conspicuous, while before it was only detected in specially selected samples (Williams et al., 2009). The larger wavelet coefficients for G18 compared to G20 are consistent with previous findings that Arcturus has a preferential positive V_R (negative U). Besides, ϵInd (G9) appears to be more connected to Hercules than in previous studies (Liang et al., 2017), and similarly for Liang17-9 (G10). Regarding Hercules, in contrast with other studies of the SN, we detect a single peak between the two reported previously (e.g. Antoja et al., 2012; Bobylev & Bajkova, 2016).

A further point of interest is the connection between γLeo (G8) and Antoja12-12 (G14), which was not observed in Antoja et al. (2012), following one of the arches (A3).

Another change with respect to past work, however, is that approximately 30 candidates MGs are found, roughly half of which have CL$\geqslant$2. The increase in the number of stars and the decrease in the uncertainties are the main reasons behind this findings, along with the fact that we are looking for peaks in an elongated structure (see Sect. 2.3). A more exhaustive cross-match with the literature is required to find previously detected groups among them and their definitive existence needs to be confirmed since the significance is

2 Except for NGC 1901 from Dehnen (1998) which is out of the SN sample (Kos et al., 2018).

Table 3: Groups detected at scale j=4 (~8-16 km s^{-1}). We ordered the objects by decreasing order of wavelet coefficient (column 5), as indicated by the index in column 1. For each object, we show the velocity coordinates of the peak (columns 3 and 4), as well as the two significance statistics (see Sect. 2.3) in columns 6 and 7. In addition, columns 8 to 10 contain the number of stars inside a circle of diameter 16 km s^{-1} along with the associated median error. To assign a name to each peak, we compare their position in velocity space with the known MGs we have compiled from selected literature (Table 5). Since some of the known objects have been reported by more than one author, the last column informs of how many unique MGs are close to our peak. In cases with more than one match, the name in column 2 is chosen according to the criteria given in Appendix C. We found four cases of multiple-matching: the Pleiades with a MGs from Xia et al. (2015) called "Hyades-Pleiades"; Hercules II with Dehnen98-8; γLeo with is Dehnen98-13; and with Dehnen98-6 overlapping with Wolf 630. Finally, we have a double match between Arifyanto05 and Bobylev16-22, the latter being closer to our peak.

n.	Name	V_R	V_ϕ	Wavelet	C.L.	P_{BS}	Stars	σ_{VR}	$\sigma_{V\phi}$	Matches
G1	Hyades	23.0	-235.5	7.6575	3	1.00	22422	0.4	0.5	1
G2	Pleiades	2.0	-228.5	5.6147	3	0.58	21524	0.3	0.5	2
G3	Sirius	-20.0	-256.5	4.9261	3	1.00	17285	0.3	0.5	1
G4	Coma Berenices	-0.5	-246.5	3.0140	3	0.72	19330	0.3	0.5	1
G5	Hercules II	24.5	-203.5	2.0481	3	1.00	7602	0.4	0.6	2
G6	Dehnen98-14	-54.0	-227.0	1.5017	3	1.00	6331	0.4	0.5	1
G7	Dehnen98-6	-30.5	-228.0	1.2290	3	1.00	10463	0.3	0.5	2
G8	γLeo	-63.5	-253.5	0.5571	3	0.96	3359	0.5	0.4	2
G9	ϵInd	71.0	-203.0	0.5357	3	1.00	2192	0.6	0.6	1
G10	Liang17-9	-16.5	-199.0	0.2773	3	1.00	3805	0.2	0.6	1
G11	Antoja12-GCSIII-13	70.0	-250.5	0.1813	3	0.84	1392	0.7	0.4	1
G12	GMG 1	66.0	-175.5	0.1510	3	0.98	900	0.7	0.7	0
G13	GMG 2	-6.5	-187.0	0.1266	3	0.52	2672	0.2	0.7	0
G14	Antoja12-12	-108.0	-228.5	0.1188	3	1.00	526	0.7	0.5	1
G15	Antoja12-16	106.5	-239.5	0.1119	3	1.00	376	0.9	0.5	1
G16	Bobylev16-22	47.5	-177.5	0.0928	3	0.66	1260	0.5	0.7	2
G17	GMG 3	88.5	-174.0	0.0699	3	0.77	428	0.7	0.7	0
G18	ηCep (Arct)	36.0	-153.0	0.0596	3	0.89	445	0.5	0.8	1
G19	GMG 4	-50.5	-290.5	0.0553	2	1.00	270	0.5	0.6	0
G20	Antoja12-17 (Arct)	-26.0	-149.5	0.0305	2	0.88	291	0.3	0.9	1
G21	GMG 5	-56.0	-176.0	0.0275	1	0.92	452	0.5	0.8	0
G22	GMG 6	106.5	-272.0	0.0248	3	0.99	69	1.1	0.6	0

n.	Name	V_R	V_ϕ	Wavelet	C.L.	P_{BS}	Stars	σ_{VR}	$\sigma_{V\phi}$	Matches
G23	GMG 7	-133.5	-225.5	0.0164	1	0.94	86	0.9	0.5	0
G24	GMG 8	129.0	-237.5	0.0155	2	0.98	72	1.0	0.5	0
G25	GMG 9	142.0	-216.5	0.0131	2	0.96	46	1.4	0.6	0
G26	GMG 10	-75.0	-285.5	0.0120	0	0.83	109	0.6	0.5	0
G27	GMG 11	73.5	-281.5	0.0110	0	0.88	145	0.7	0.5	0
G28	GMG 12	-108.0	-152.0	0.0107	2	0.76	41	0.8	1.0	0
G29	GMG 13	-77.5	-130.0	0.0101	1	0.81	52	0.6	1.0	0
G30	GMG 14	125.5	-174.5	0.0100	1	0.86	74	1.0	0.7	0
G31	GMG 15	-125.0	-266.0	0.0092	1	0.97	23	1.0	0.4	0
G32	GMG 16	-23.5	-90.5	0.0084	2	0.91	24	0.5	1.4	0
G33	GMG 17	-1.5	-120.0	0.0082	1	0.84	63	0.4	1.1	0
G34	GMG 18	70.5	-92.0	0.0067	2	0.85	19	0.9	1.9	0
G35	GMG 19	14.0	-81.5	0.0063	2	0.86	20	0.4	1.1	0
G36	GMG 20	122.5	-202.5	0.0060	0	0.86	94	0.9	0.5	0
G37	GMG 21	-105.0	-96.0	0.0057	2	0.72	15	1.1	1.6	0
G38	GMG 22	-42.0	-118.5	0.0055	0	0.89	53	0.4	1.2	0
G39	GMG 23	47.0	-55.5	0.0046	2	0.61	11	0.6	1.1	0
G40	GMG 24	-126.5	-108.5	0.0040	1	0.81	13	1.0	0.9	0
G41	GMG 25	-130.0	-128.0	0.0040	1	0.80	8	0.6	0.9	0
G42	GMG 26	47.5	-342.0	0.0013	2	0.64	1	2.0	2.2	0
G43	GMG 27	-109.0	-339.5	0.0013	2	0.57	1	1.0	1.1	0
G44	GMG 28	-56.5	-322.5	0.0009	0	0.84	2	1.0	1.1	0

Table 3: Groups detected at scale j=4 (continuation)

not high enough. However, four of the detected groups have CL$\geqslant$3 (GMG1-3 and GMG6), and, remarkably, we find four (GMG-1 to -4) with strength comparable to that of the known MGs. While some of them may very well be part of the already recognised kinematic structures (e.g. G12 (GMG1) and G17 (GMG3) related to Bobylev16-22 and structure 18 from Kushniruk et al. (2017), or G13 (GMG2) related to Liang2017-9, HR1614 and structure 19 from Kushniruk et al. (2017)), peak G19 (GMG4) is part of the newly characterised arch (A1).

Finally, we observe three peaks with 1 or 2 stars (G42 to 44) as a result of not applying any arbitrary cut to the number of stars. These latter peaks appear significant due to their isolation from the rest of the distribution, but in any case they would not correspond to kinematic groups, and therefore are of no interest for our study.

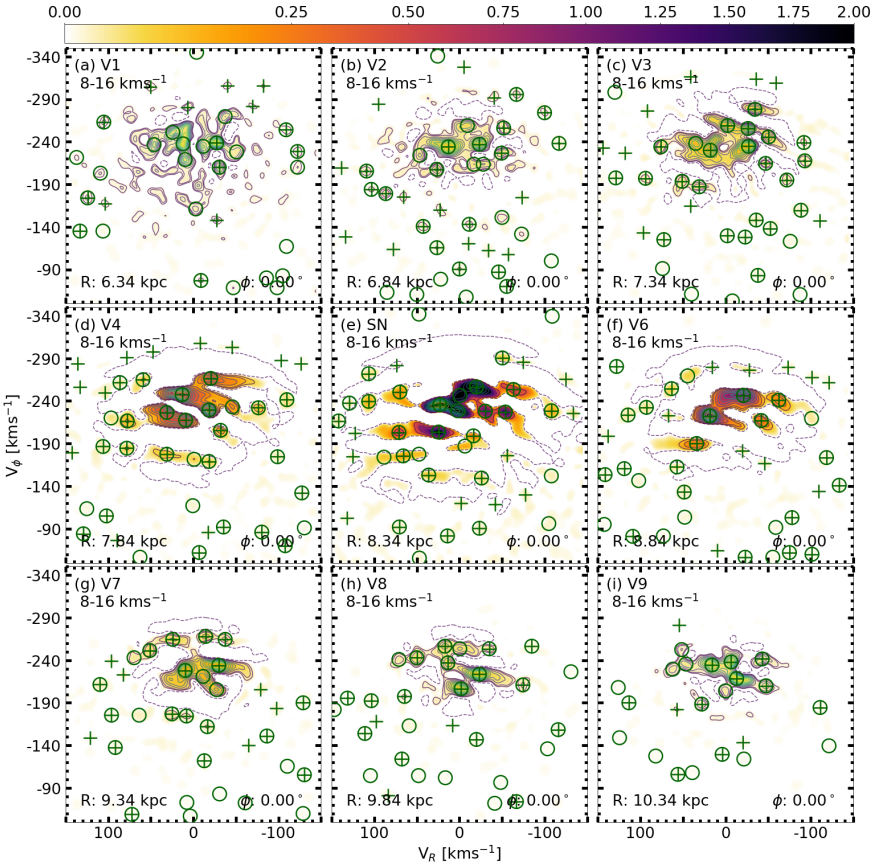

Figure 9: Wavelet planes of different Galactic neighbourhoods along the zero-azimuth line. Panels (a) to (i) correspond to the volumes V1 to V9 described in Table 1. We show the coefficients in a common colour bar with the significant peaks superposed and contours in the same manner as in Fig. 6. We notice the change in colour caused by the difference in number of stars of each sub-sample. Also, for the SN sample, the most crowded regions of the plane saturate (c.f. Fig.8).

2.5 EXPLORING OTHER GALACTIC NEIGHBOURHOODS

In this section, we focus on the abundant kinematic substructure that we find in different Galactic neighbourhoods and its variation with azimuth and radius. For this exploration we used the 216 sub-samples described in Sect. 2.2 (golden dots in Fig. 5). Most of our exploration in this section is based on the scale of 8-16 $\mathrm{km\,s^{-1}}$ since smaller scales appear noisier in the distant neighbourhoods for several reasons: the number of stars decreases as we move away from the Sun, the velocity uncertainties increase, and the velocity dispersion at inner Galactic radius is larger, effectively decreasing the density of stars in the velocity plane.

Figure 9 shows the wavelet plane at the scale of 8-16 $\mathrm{km\,s^{-1}}$ for a small sample of different Galactic neighbourhoods located at the the Solar azimuth ($\phi = 0\,\mathrm{deg}$) but at different radii, going from 6.34 (V1) to 10.34 kpc (V9). It is not necessary to move very far, though, to notice changes in the substructure of the velocity plane.

For example, Hercules, located at $V_\phi \sim -200$ $\mathrm{km\,s^{-1}}$ in the SN, appears to be shifted to -220 $\mathrm{km\,s^{-1}}$ in V4 and to -190 $\mathrm{km\,s^{-1}}$ in V6. In fact, we can trace this structure from V4 to V7, but in V3 it seems to have mixed with the central part of the velocity distribution. This shift is consistent with previous findings (e.g. Antoja et al., 2012) but now we trace it farther from the Sun than ever before. The same behaviour, shifting to smaller $|V_\phi|$ when increasing R, is also observed for other structures like Sirius and Hyades. In addition, a prominent arched structure at $V_\phi \sim -260$ $\mathrm{km\,s^{-1}}$ and positive V_R is observed at V6, then more strongly at the V7 and V8 volumes. At the SN, though, it appears quite weak and only represented by the two peaks that trace A1 from Fig. 7.

The changes of the velocity substructure and especially its smooth evolution with radius can be better seen in an animation (online animation 1, see Appendix B) which considers now the 51 neighbourhoods at different radii extending in R from ~6 kpc to ~ 11 kpc at steps of 100 pc. In this animation, the downwards movement of the different kinematic structures when increasing distance from the GC can be perfectly followed as continuous passages of kinematic waves. The equivalent animations at the scales of 4-8 (online animation 2) and 16-32 $\mathrm{km\,s^{-1}}$ (online animation 3) show a similar evolution.

To quantify the changes in the velocity distribution with Galactocentric radius, we collected all peaks detected in the WT at scale $j = 4$ with CL$\geqslant$2 in the 51 different volumes presented in Sect. 2.2, and plotted their V_ϕ as a function of R in Fig.10, colour-coding the symbols according to radial velocity. With the help of the colour code, we associated all peaks that seemed to follow a common trend (both in V_ϕ and V_R) and linked them with a continuous solid black line, each labelled with a number. While this association of peaks may seem

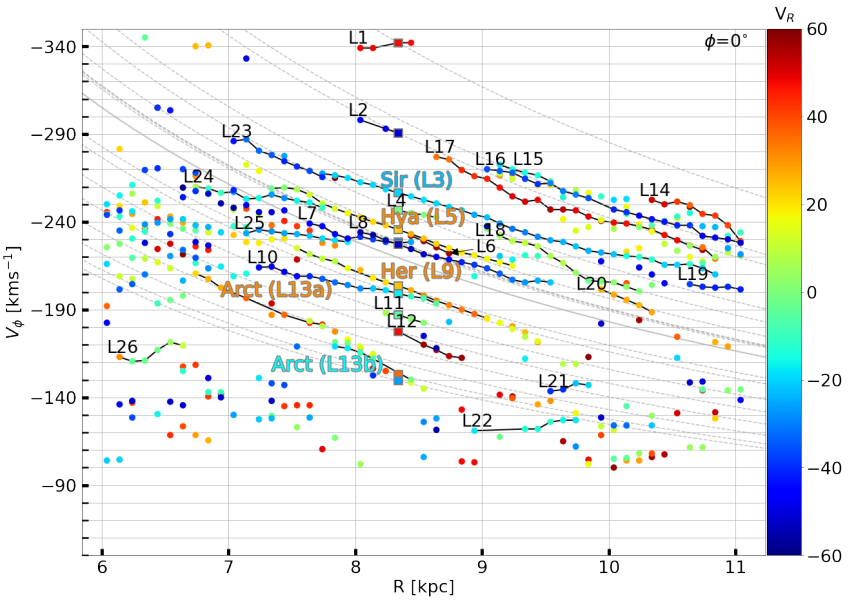

Figure 10: Evolution of the rotation velocity of the kinematic substructures as a function of the radius. From all the peaks at the 51 volumes along the Sun-GC line, only significant peaks according to Poisson (CL$\geqslant$2) with radial velocities in the range [+60,-60] km s^{-1} were considered. The peaks detected at Solar radius (8.34 kpc) are shown as squares; the remaining peaks are shown as circles, linked together through solid black lines when observed to belong to the same structure (except for L13, see text). The dashed grey lines correspond to constant angular momentum tracks.

rather subjective, the continuity in most of the cases is beyond doubt. A simple inspection of this figure reveals a wide variety of peaks forming a general trend downwards, consistent with a decreasing $|V_\phi|$ with R as mentioned above. The expected uncertainties in the location of the peaks along the vertical axis are negligible in front of the variations observed[3]. We note that lines span a wide range of Galactocentric radii, meaning that the peaks at the SN have their counterparts in many other Galactic neighbourhoods, but at a different azimuthal velocity. Table 4 lists all the prominent lines in Fig.10 where we also indicate the name of the kinematic arch or group that could be linked to each line, based on the peaks found at Solar radius (marked with squares instead of circles). Moreover, we used a linear regression to estimate the slope of the line, along with its associated uncertainty[4]

3 Even though the algorithm we use does not return an error associated to the location of the peak, this can be approximated by the error on the mean velocity of the N stars composing each group: we take the maximum between their standard deviation and their uncertainty in velocity, and then divide by the square root of N. These errors are between 0.04 and 1.06 km s^{-1} for 80% of the peaks in the SN and between ∼0.3 and 5.0 km s^{-1} on average for neighbourhoods at 1 kpc from the Sun, with the low $|V_\phi|$ region of the velocity plane being dominated by the larger errors.

4 In this calculation, the individual uncertainties of each peak have not been taken into account.

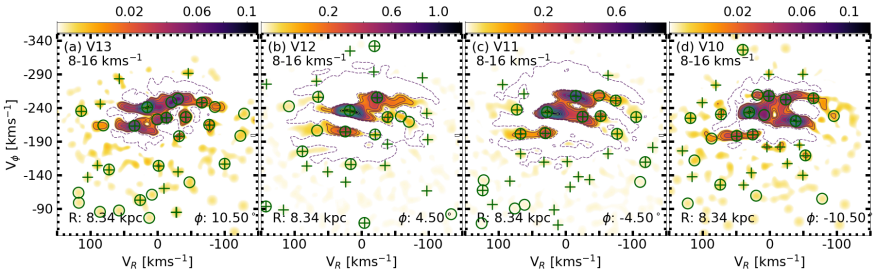

Figure 11: Wavelet planes of different Galactic neighbourhoods along the arc at Solar radius. Panels (a) to (d) correspond to the volumes V13 to V10 described in Table 1. The contour levels and the symbols are defined in the same manner as in Fig. 6.

(penultimate column in Table 4). Overall, excluding those lines that deviate from the main trend (L1,21,22,26), we observe a mean slope of 23 ± 2 kms^{-1}kpc^{-1}, in good agreement with the estimation by Quillen et al. (2018b).

By inspecting Table 4, we note some scatter in the measured slopes. Along with Fig.10, we see that there seems to be two different behaviours in the slope of the most prominent lines: L5 and L9 have slopes of ~25 kms^{-1}kpc^{-1}, while L3, 10, 24, and 25 have smaller slopes between 10 and 20 kms^{-1}kpc^{-1}. Developing on this, since the resonant effects of the bar and spiral arms are expected to create kinematic substructures[5] that, to first order approximation and for small epicyclic amplitudes, have an almost constant vertical angular momentum $L_Z = RV_\phi$ (Sellwood, 2010; Quillen et al., 2018b); we over-plot lines of constant L_Z (dashed grey lines) in Fig. 10. As a result, we see how L5 and L9 follow rather well the lines of constant L_Z, while other lines such as L3 and L10 do not. Moreover, the colour of the peaks reveals variations in radial velocity, which is one of the perquisites of using the WT compared to a direct plot of V_ϕ against R. For most of the lines, this gradient (or oscillation in some cases) might be related to noise but, as we shall see in the discussion, for some cases like Hercules, this extra information can help us understand the origin of such structure.

Focusing now on individual structures that traverse the Solar radius, L3 (Sirius) is the line with the largest reach, extending from R ~ 7.5 to R ~ 11 kpc. Other groups with large extensions are Hyades (L6), Dehnen98-6, and Dehnen98-14 (respectively, L7 and L8) or Hercules (L9). Next to Hercules in the SN, is the MG Liang17-9 (one of the several peaks linked to A9), represented here by L10. The evolution of this group with radius differs significantly from that of Hercules,

5 As Dehnen (2000) showed, gaps in the velocity distribution are easier to dynamically associate with resonances. Peaks on the other hand tend to be more unstable (Minchev et al., 2010). Nonetheless, those gaps naturally enhance the over-densities at each side of the separatrix and, as a consequence, the peaks approximately follow the gaps, which is in line with our focus on the peaks.

Table 4: Lines marked in Fig. 10. The first column contains the label of the Line, while the second refers to the name of the structure at Solar radius (if possible). Subsequently, columns 3 and 4 contain the Arches (Table 2) and Groups (Table 3) corresponding to the peak at Solar radius of the Line. The last three columns characterise the lines by, respectively, their number of points, the slope ($kms^{-1}kpc^{-1}$) obtained from the linear regression and the corresponding correlation coefficient, r.

n.	Name	Arch	Group	Points	Slope	r
L1			G42	4	-9.0±2.1	-0.95
L2	Arch 1	A1	G19	3	25.0±0.0	1.00
L3	Sirius	A4	G3	32	19.2±0.4	0.99
L4	Coma Berenices	A5	G4	4	13.0±0.7	1.00
L5	Hyades	A7	G1	20	24.9±0.5	1.00
L6				4	33.5±0.9	1.00
L7	Dehnen98-6	A5	G7	9	13.3±2.2	0.92
L8	Dehnen98-14	A6	G6	16	20.0±0.7	0.99
L9	Hercules II	A9	G5	15	26.5±0.2	1.00
L10	Liang17-9	A9	G10	15	14.3±0.5	0.99
L11	HR1614	A10	G13	4	19.0±2.1	0.99
L12	Bobylev16-22	A11	G16	5	31.0±2.7	0.99
L13a	Arcturus	A12		7	29.8±1.5	0.99
L13b	Arcturus	A12		5	32.9±3.4	0.98
L14				8	30.2±5.2	0.92
L15				5	22.5±1.7	0.99
L16				20	22.0±0.4	1.00
L17				24	23.4±0.8	0.99
L18				12	31.0±1.8	0.98
L19				5	6.0±1.9	0.88
L20				5	32.0±1.2	1.00
L21				4	-14.0±5.9	-0.86
L22				6	-8.5±2.5	-0.86
L23				8	31.4±2.0	0.99
L24				11	10.0±1.3	0.93
L25				8	7.9±1.2	0.92
L26				6	-20.4±6.8	-0.83

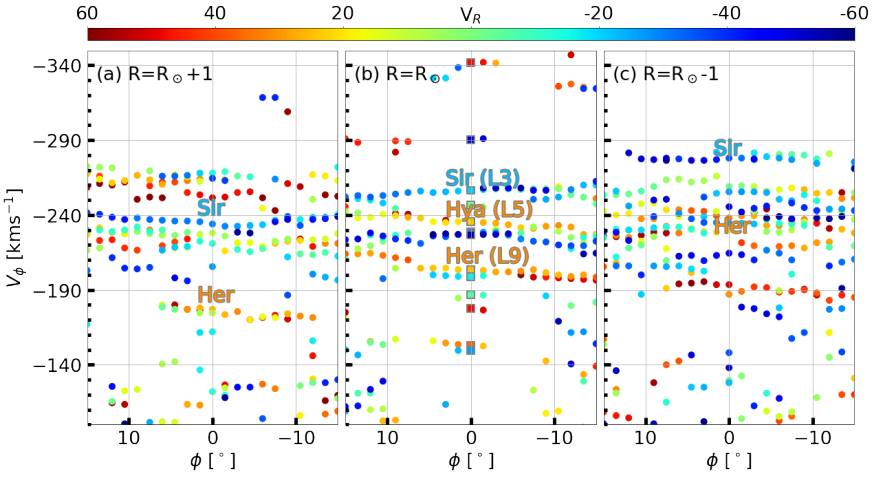

Figure 12: Evolution of the rotation velocity as a function of azimuth. Here, we show the peaks of the 63 volumes (21 at each radius) that fulfil the same conditions of Fig. 10. The central panel corresponds to the exploration at the Solar radius, while in the left panel we explore an outer radius and on the right we show the results for an inner radius.

suggesting that these two substructures are different entities, with a different origin. Finally, below those two structures, we have Arcturus which, as can be seen, has been split into two lines, L13a and L13b. This is because the elongated nature of this structure, as already mentioned, makes our algorithm detect the two ends of the structure separately. We notice that, even though we detected Pleiades at SN, we do not observe any continuity with radius for this group since its relation with L25 or L7 is unclear.

We also find clear lines that do not cross the Solar radius, that is, new peaks that are detected only in extrasolar volumes. The clearest examples in outer Galactic neighbourhoods are L15 to 17, which correspond to the prominent arch observed in panels (g) and (h) of Fig. 9. Their connection with L2 is only truncated at two volumes, yet is traceable in Fig. 9, and the splitting can be explained using the same argument as for Arcturus. Referring to L14 and L18, there is no clear link to any of the structures detected at SN, and nonetheless they evolve similarly to the lines between them. There are also prominent new structures at inner radii such as L23 or L24, which could be associated, by visual inspection of the animation (online animation 1), to Sirius and Hyades, respectively, and L25 which presents a significantly smaller slope and does not cross the Solar radius. Finally, there are other structures with smaller extension in R, such as L1, L19 to 22, and L26, which show some continuity, meaning they are unlikely to be sporadic peaks. They are present, however, in a small range of R and depict different shapes and trends compared to the prominent lines.

Changing to the variations along azimuth, Fig. 11 shows four different wavelet planes at scale $j = 4$, corresponding to the volumes centred at ϕ=10.5,4.5,-4.5,-10.5 deg. As in previous works (Antoja et al., 2012), we do not see much variation, with only more subtle changes in the substructure compared to their evolution with R. We do observe a drift of Hercules, which moves to higher $|V_\phi|$ and becomes more prominent when increasing ϕ. There is also a structure that at V13 appears as a single, almost isolated peak around V_ϕ ~-230, V_R ~-40 km s^{-1}, which corresponds to the mixture of Dehnen98-6 and Dehnen98-14, that for negative azimuth gains strength and forms an elongated structure.

In an analogous way to Fig. 10, in Fig. 12 we now plot V_ϕ against ϕ of the peaks found in each of the 21 different Galactic neighbourhoods that cover different azimuths ϕ, for three different radii. Focusing on the middle panel, corresponding to the Solar radius, we confirm that most of the structures do not present significant variation with ϕ, except for L5 and L9 corresponding to Hyades and Hercules, respectively. The variation in azimuthal velocity in these cases is of about 13 km s^{-1}in 30 deg, or equivalently, ~0.43 km s^{-1}deg^{-1}, which at Solar radius means ~3 km s^{-1}kpc^{-1}, and is thus much smaller than the average 23 km s^{-1}kpc^{-1} in the radial direction. As for the variations in radial velocity revealed by the colours, we see a slight shift of the peak towards larger positive V_R at ϕ=7.5 deg for Hercules. In contrast, Sirius (L3) remains relatively unchanged.

In the left and right panels of Fig. 12, we show the azimuthal evolution in two different radii, where we see all peaks moving to larger or smaller V_ϕ, in agreement with previous figures. In panel (a), corresponding to outer radius, at V_ϕ ~-175 km s^{-1}, the slope of Hercules with azimuth is still appreciable. In the same panel, among all the peaks at $\phi \geqslant 7.5^\circ$, we distinguish a new feature at ~-205 km s^{-1}, worth investigating because it seems to be related to Dehnen98-14 when inspecting the animations.

2.6 DISCUSSION

Although other studies have proposed links of rounded kinematic groups in the shape of a few diagonal branches (Skuljan et al., 1999; Antoja et al., 2008), ripple-like structures (Xia et al., 2015) or elongations (Kushniruk et al., 2017), the arched distribution depicted by the WT of the *Gaia* data is radically distinctive and clear.

ARCHES OF ALMOST CONSTANT ENERGY. We have seen that some arches appearing in the SN velocity distribution have the same kinetic energy at all its points in the velocity plane. This matches the models of Minchev et al. (2009) and Gómez et al. (2012) who showed how a phase-mixing process after a perturbation of the potential, possibly

due to a satellite passage, naturally leads to arches in the velocity plane of nearly constant energy.

Instead, some other arches that we detect do not follow lines of constant energy and are not symmetric in their Galactocentric radial velocity. In these lines, Antoja et al. (2009) showed with simulations that a barred potential acting on a disk suffering from phase mixing will make the arches deviate from symmetry. Also, a non-axisymmetric potential (i.e. with bar and/or spiral arms) by itself can create similar arches not centred with respect to the Galactocentric radial velocity. For instance, the studies by Fux (2001); Quillen & Minchev (2005); Antoja (2010); Monari (2014); Hattori et al. (2018) demonstrated that periodic orbits in the velocity plane have mostly an elongated locus with a peculiar arched shape. Nevertheless, while these are mostly theoretical studies analysing the regularity of the orbits, simulations of orbit integrations with realistic phase space distributions fail to distinctively populate many of these arches with particles (e.g. Antoja et al., 2011; Hattori et al., 2018), especially for spiral arms. Instead, some simulations with bars show few yet clear overdensities (and gaps) in the shape of arches (e.g. Dehnen, 2000; Fux, 2001). Quillen et al. (2011, 2018a) observed arches in the velocity distribution varying with position in the galaxy, which they attributed to the spiral arms.

DECREASE OF $|V_\phi|$ WITH R. We also note that most of the peaks detected by the WT decrease their azimuthal velocity with Galactocentric radius, that is, they have a negative $\frac{\partial |V_\phi|}{\partial R}$. Since the peaks that we detect are overdensities in phase space, their change in R is consistent with the diagonal ridges found in the R-V_ϕ projection of the recent study by Antoja et al. (2018) (their Fig. 3). We also confirm the large gradient measured by Quillen et al. (2018b) in the velocity of the peaks, and the extension of some of them hinted by their study.

Moreover, we find that the change in R of some of the peaks, such as Hercules and Hyades for example, is consistent with them being structures of roughly constant angular momentum (L_Z), i.e. following lines of constant L_Z in the R-V_ϕ plane, in contrast to, for instance, Sirius. This is to be expected in a resonance (Sellwood, 2010; Quillen et al., 2018b) since resonant features are composed of stars following similar orbits (roughly the same eccentricity) but at different amplitudes and phases. Given that not all of the arches found in the velocity plane of the SN evolve in the same manner, this could indicate that some are due to resonances and some to a phase-mixing event. In turn, this would reduce the number of phase-mixing "waves" and, thus, increase their velocity separation. A larger separation would reduce the estimated time of perturbation of ~2 Gyr in Minchev et al. (2009), potentially reconciling their assessment and the one by Ant-

oja et al. (2018) from the curling of the "snail shell" in the vertical projection of phase space.

THE HERCULES STREAM. Other authors have observed a correlation between the azimuthal velocity of Hercules and R, which was used in Antoja et al. (2014) and Monari et al. (2017b) to constrain the pattern speed of the bar. Our analysis returns a slope in the $V_\phi - R$ plane for Hercules of 26.5 ± 0.2 $kms^{-1}kpc^{-1}$, compatible with those studies. Nonetheless, we traced this trend for ~2 kpc as opposed to the ~0.6 kpc from previous studies. Additionally, we observe changes in the radial velocity V_R of Hercules with Galactocentric distance and azimuth, which varies from ~0 $km\,s^{-1}$ ($R \sim 7.5$ kpc) to ~40 $km\,s^{-1}$ ($R \sim 9$ kpc). This gradient is in agreement with the behaviour predicted by Dehnen (2000), where a structure caused by the OLR of the bar evolves from zero radial velocity towards smaller $|V_\phi|$ and positive V_R with increasing radius. This model also predicts an increase of the azimuthal velocity with ϕ, which we also observe in the *Gaia* data. Therefore, assuming that the gap between L5 and L9 in Fig. 10 is caused by the OLR, a direct application of Eq. (6) from Quillen et al. (2018b) using the average L_Z of Hercules and Hyades yields a rough estimate of the bar pattern speed of Ω_b ~54 $kms^{-1}kpc^{-1}$. In contrast, Hunt & Bovy (2018) recently explained the Hercules MG with the 4:1 OLR of a slow bar. We note that the elongated feature in their Fig.7 could also explain some of the arches that we found in the upper part of the velocity distribution. In parallel, Hattori et al. (2018) explored different models and, to our knowledge, the one that best reproduces the curvature of the gap above Hercules is their fast-bar-only. Moreover, their exploration of where in the disk the bi-modality is observed (their Fig. 10) is more consistent with our azimuthal exploration in the case of their fast-bar-only model: both data and model show an increase of strength in Hercules with positive azimuths. Bienaymé (2018) also studied the evolution of Hercules in different Galactic neighbourhoods, but in this case our range of exploration does not allow for a comparison of the key features in his simulations. In any case, further study of the Hercules structure is necessary to settle the debate over its origin and the controversy of the bar being slow or fast, first explored by (Pérez-Villegas et al., 2017).

OTHER KINEMATIC SUBSTRUCTURES. Another structure with unclear origin is Arcturus, which has been linked to accreted stars from a satellite Galaxy (Navarro et al., 2004) but also to a resonance of the bar (Williams et al., 2009; Antoja et al., 2009). Here we observe that Arcturus evolves with R similarly to Hercules, pointing to a dynamical origin. We also observed other peaks that show a distinct evolution with R compared to the main groups, that is, flat, oscillating, or

even increasing V_ϕ. Most of these have low angular momentum and therefore could have a different origin, perhaps related to accreted structures or groups in the nearby halo (Helmi et al., 1999; Koppelman et al., 2018), although their significance needs to be explored further. Finally, we recreated Figs. 10 and 12 using Bayesian distances from McMillan (2018) and observed that the differences were negligible, except for lines 21, 22, and 26 (see Table 4). With this sample we could not reconstruct any of the three, suggesting a spurious nature.

POTENTIAL BIASES. As can be appreciated from the strips in Fig. 5, our sample is affected by extinction. This erases the density oscillations expected in configuration space as a consequence of the conservation of number of stars and the collisionless Boltzmann equation, if we neglect minor effects from stellar birth and evolution (see this idea developed in Quillen et al. (2018b)). Apart from that, as mentioned in Sect. 2.2, our sample is more and more dominated by giants as we move away from the Sun. Therefore, the mean age of the population can change when increasing heliocentric distances and, accordingly, our data may suffer a change in the mean velocity dispersion that can influence the detected structures in the kinematic space. In both cases, our velocity distribution could be altered, yet further work is required to fully quantify these effects.

IMPROVEMENTS OVER PREVIOUS WORK. Previous studies with orders-of-magnitude less stars used the WT to reveal substructure in the SN that we now see by eye in the histogram (Antoja et al., 2008; Bobylev & Bajkova, 2016; Kushniruk et al., 2017), making it clear that this transformation is useful in terms of detecting the substructure hidden in a poorly populated histogram. In consequence, this allows us to explore the *Gaia* data in depth. This exploration is inspired by, but unquestionably improves over, previous ones such as Antoja et al. (2012, 2014), who focused mostly on Hercules and for a short range of R, and Quillen et al. (2018b), who explored mostly changes in Galactic longitude but at very close distances. In comparison with other analyses (e.g. Monari et al., 2017b; Antoja et al., 2018; Kawata et al., 2018), we decompose each volume independently with the WT which grants us the sensitivity necessary to explore the farthest neighbourhoods and allows us to detect more and better defined ridges. Also, it introduces a third variable (V_R), which in the case of Monari et al. (2017b) is done through cuts in the data at the cost of reducing the number of stars.

2.7 CONCLUSIONS

We have studied the velocity plane in cylindrical coordinates for a *Gaia* sample of stars with six-dimensional phase space coordinates

both in the SN, with 435,801 stars, and other Galactic neighbourhoods up to Heliocentric distances of $\sim$ 2.5 kpc. With the unprecedented number of stars and the small uncertainties in the observables, with median velocity errors of $\tilde{\sigma}_{vel} \leqslant 1$ km s^{-1} in the vicinity of the Sun and $\leqslant 3$ km s^{-1} for the rest of volumes, the kinematic substructures unveiled by the WT show a remarkable sharpness. We have characterised these structures, and followed their evolution with Galactocentric radius and azimuth.

The WT reveals conspicuous, thin kinematic arches with various morphologies that were not observed prior to *Gaia* due to resolution limitations. We find at least six long arches in the SN with a nearly constant azimuthal velocity and wide range of radial Galactocentric velocities, plus six additional shorter segments of arch. Based on the scale in the WT where they are better detected, we find that they have a width of 2-8 km s^{-1}. Thanks to the superb isotropy of the *Gaia* survey and the capabilities of the WT for unveiling structures, the exploration of the substructure in the velocity distribution can now be carried out in many different Galactic neighbourhoods, that is in all directions and spanning an astonishing range of 5 kpc in Galactocentric distance. In our analysis, we see that the azimuthal velocity of the peaks detected changes strongly with Galactocentric distance at an average rate of $\sim$23 kms^{-1}kpc^{-1}. We also see clear differences in their radial range, as some structures rapidly fade, while others can be identified in Galactic neighbourhoods 3 kpc apart.

When explored as a function of Galactic azimuthal angle, most of the substructures remain constant and some present little change of the order of 3 kms^{-1}kpc^{-1}, an order of magnitude smaller than the changes in Galactic radius. This is qualitatively in agreement with expectations from models of resonant structures (Antoja et al., 2011; Quillen et al., 2011) and of phase mixing (Gómez et al., 2012). Also, and although we can only explore a small portion of the MW, our results are in line with the findings of, for example, Quillen et al. (2011); Hattori et al. (2018), who proposed, based on their simulations, the existence of streaks and gaps in the velocity distribution throughout the entire Galaxy. Overall, when looking at the evolution of the velocity plane, most of the structures shift in the vertical axis (V_ϕ) at a similar rate, producing the illusion that we are indeed riding kinematic waves in the MW disk.

With the fine characterisation of the arches and ridges done in this work, we see that some of the kinematic substructures follow lines of nearly constant energy at a given volume and could be related to phase-mixing processes (Minchev et al., 2009; Gómez et al., 2012) induced, for example, by the close passage of the satellite dwarf. These coincide with the structures showing less variations in azimuthal angle, like Sirius. Others, such as Hyades or Hercules, seem to follow lines of constant angular momentum, similar to what is expected

in case of resonant kinematic substructure (Sellwood, 2010; Quillen et al., 2018b) induced by the bar and/or the spiral arms of our Galaxy, and also show variations with azimuthal angle. We could therefore be witnessing several mechanisms acting on the disk, as recently suggested in Antoja et al. (2018), who compared the ridges with different toy models of phase mixing and resonances, and in Trick et al. (2018) in their study of the *Gaia* data in action space. Here we provide additional evidence of the different dynamical characteristics of the kinematic substructures and a tentative way to differentiate between structures of different origin.

We have also shown the evolution of V_ϕ for Hercules both with radius and azimuth, which is consistent with the OLR models of the Galactic bar, reaching distances of ~1 kpc from the Sun in each direction. Moreover, we have quantified the changes in radial velocity, for the first time, at each volume along both directions. The trends seen remain consistent with the predictions for a fast bar.

Our exploration has lead also to the first unambiguous extrasolar kinematic structures, that is, MGs and arches not observed (or very weak) at Solar radius. Some of these new substructures follow similar trends with Galactocentric radius and azimuth as the substructure crossing the local volume, whereas others evolve distinctively.

The *Gaia* mission has still some years ahead to deliver even better data, yet with the results already available it is an exciting time for both observational and theoretical research on Galactic dynamics. As an example, the structures analysed in this work and their evolution can be used to experiment with numerical and theoretical models in the context of coexisting and interacting dynamical processes.

APPENDIX

A *The proper use of parallaxes*

Here we briefly discuss the recommendations given on the use of the *Gaia* parallaxes. For a more detailed study, we refer the reader to Luri et al. (2018). The problem of inverting the parallax is that it generates an asymmetric and biased distribution of probability for the true distance given the evidence (observations). In other words, the most probable distance is not the **true** distance of the star. Therefore, using summary statistics like, for instance, the mode or the mean, causes a bias in the distances derived for each star. Moreover, the simple $1/\varpi$, which in a Bayesian context is equivalent to select the most likely value given a uniform *prior*, has been shown to be a relatively poor estimator (Brown et al., 1997; Arenou & Luri, 1999; Luri et al., 2018). In addition, as shown in Luri et al. (2018), cutting in parallax relative error, σ_ϖ/ϖ is actually far from beneficial; it can introduce an even deeper bias depending on the characteristics of the sample. In

contrast, the recommendation given by the *Gaia* team is to work fully Bayesian, that is, not to use summary statistics and, instead, drag the *Posterior* probability distributions up to the quantities of interest. The results will then not be a value, but a whole probability density function filled with information. In general, though, it is enough to use the simple and biased estimator $1/\varpi$ to explore the data, always taking into account the effects it can introduce if the sample is not very close to the Sun and has large uncertainties.

Our sample, as described in Sect. 2.2, is for the most part made up of bright nearby stars, precisely those with the smallest mean uncertainties in the DR2 catalogue. Moreover, for nearby stars with fractional errors smaller than 0.2, the dependence on the *prior* is highly attenuated and the bias of using the inverse of the parallax as a distance estimator becomes negligible (e.g. Bailer-Jones 2015; Astraatmadja & Bailer-Jones 2016). Beyond that, our science case and conclusions do not rely heavily on the distance determination, and the potentially small bias does not affect the overall picture of the substructure in the kinematic plane.

As a side note, we notice that by using the Jacobian to propagate and calculate the uncertainties in the velocities, we are implicitly modelling the errors as Gaussian which is known to be false. As already mentioned, the inversion of the parallax results in an asymmetric probability distribution, also for the observed V_R and V_ϕ. We do not impose any threshold or sigma-clipping based on this errors. In this sense, since we already selected only stars with "good" parallax, the assumption of Normality is unimportant.

B *Online material*

The online data material includes a table and five animations. Table B.1 (available at the CDS) contains all the significant peaks in the SN sample at the scale 4-8 $\mathrm{km\,s^{-1}}$(j=3, see Fig. 7.a), with the columns being the same as in Table 3. The animations are composed of the snapshots at different Galactocentric radius and azimuth of the WT planes, which makes it possible to visualize the evolution of the velocity distribution at a particular scale. Figures 13 to 17 show the previews of each animations and, in the corresponding captions, the details of the scale and exploration.

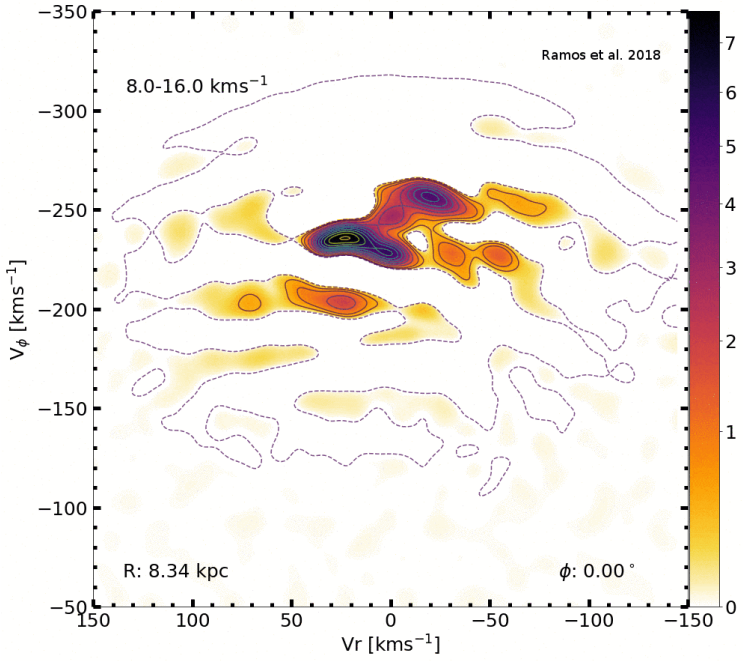

Figure 13: Preview of animation 1. WT at the scale 8-16 km s^{-1} of the velocity plane at different Galactocentric distances along the GC-Sun line ($\phi = 0$).

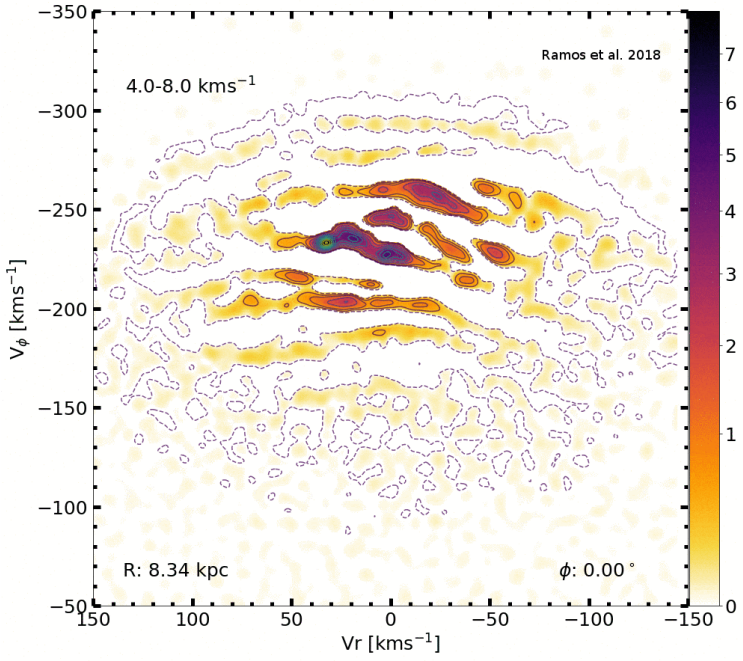

Figure 14: Preview of animation 2. WT at the scale 4-8 km s^{-1} of the velocity plane at different Galactocentric distances along the GC-Sun line ($\phi = 0$).

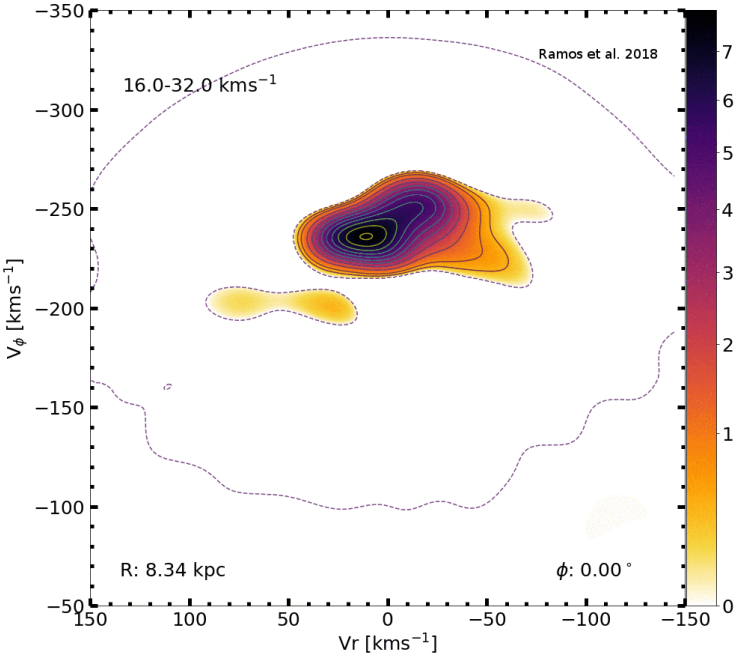

Figure 15: Preview of animation 3. WT at the scale 16-32 km s^{-1} of the velocity plane at different Galactocentric distances along the GC-Sun line ($\phi = 0$).

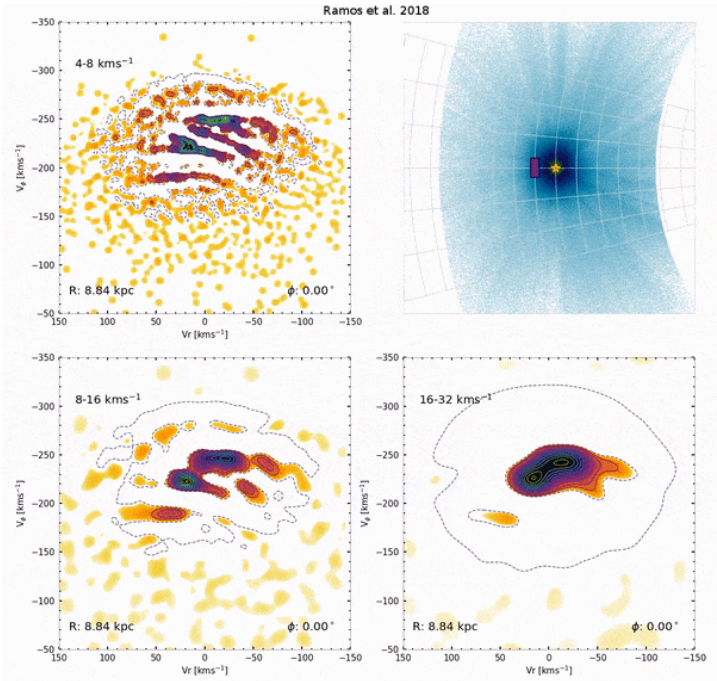

Figure 16: Preview of animation 4. All three scales (j=3,4,5) evolving simultaneously with Galactocentric distance at the GC-Sun line ($\phi = 0$).

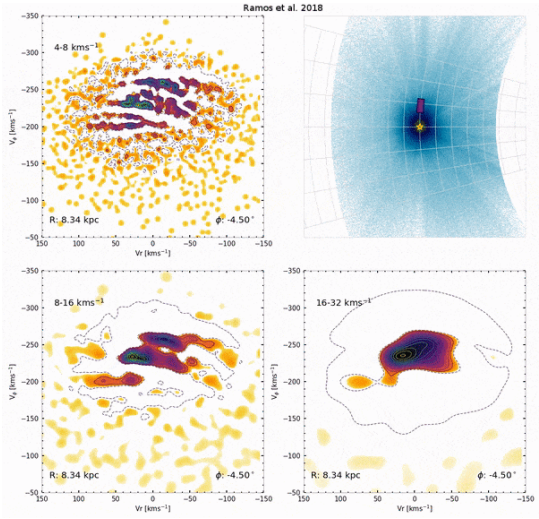

Figure 17: Preview of animation 5. All three scales (j=3,4,5) evolving simultaneously with azimuth at Solar radius ($R = R_{\odot}$).

C *List of moving groups*

We compiled a list of MGs from the corresponding tables of Dehnen (1998); Antoja et al. (2012); Xia et al. (2015); Bobylev & Bajkova (2016); Liang et al. (2017); Kushniruk et al. (2017) and list them in Table 5. We transformed their Heliocentric velocities into Galactocentric cylindrical coordinates following the recipe given in Sect. 2.2. Some MGs, like Hyades or Sirius, have more than one entry since each author independently derived a different location in velocity space.

For Kushniruk et al. (2017) we only took the new unnamed objects (at scales 3 and 4, see Kushniruk et al. 2017) in order to reduce the scatter in our table since in their study the same structure appears several times in their tables. Their newly found objects are label here including the scale they were found (since their notation and definition of the scales coincides with the one we used for this work). Regarding the elongated structures described by Xia et al. (2015), where just the start and end points are given, we did not include them to avoid mismatches, but we considered them for the discussion. The rest of new or unnamed objects found in each author's table are labelled as **{First Author} + {Year} + {Number in source table}**.

The names of the objects in our Table 3 are given according to the following criteria: first, we cross-matched the position of the peak detected in our data with the coordinates in the literature using a circle of radius $\Delta 2^j$ km s^{-1}. Since we may have several entries for a single object, we grouped the candidates by name and counted their frequency. In cases where multiple groups were obtained, we selected the one with more counts. If we had a draw, we selected the closest one to the peak.

Table 5: Compilation of MGs from different authors (see text). The first column contains the author and the year of publication, whereas the second one shows the name of the object and the fourth, the corresponding number in the author's original table. The source of the astrometry is shown in column three. Finally, the cylindrical velocities (columns 5 and 6) are derived using the parameters for the Sun and LSR described in Sect. 2.2. Those MGs detected by other means different from the WT are signalled with an asterisk next to their name.

Author	Name	Source	Original number	V_R [km s^{-1}]	V_ϕ [km s^{-1}]
Antoja2012	Antoja12-12	RAVE	12	-103	-229
Antoja2012	Antoja12-13	RAVE	13	92	-211
Antoja2012	Antoja12-GCSIII-13	GCSIII	-	69	-260
Antoja2012	Antoja12-15	RAVE	15	-71	-180
Antoja2012	Antoja12-16	RAVE	16	111	-233
Antoja2012	Antoja12-17	RAVE	17	-23	-144
Antoja2012	Antoja12-18	RAVE	18	-120	-220
Antoja2012	Antoja12-19	RAVE	19	-38	-132
Dehnen1998	Arcturus*	Hipparcos	10	-11	-142
Xia2015	Arifyantoo5*	LAMOST-RAVE	8	53	-172
Bobylev2016	Bobylev16-14	RAVE DR4	14	-41	-212
Bobylev2016	Bobylev16-15	RAVE DR4	15	85	-242
Bobylev2016	Bobylev16-17	RAVE DR4	17	-82	-217
Bobylev2016	Bobylev16-19	RAVE DR4	19	-46	-153
Bobylev2016	Bobylev16-20	RAVE DR4	20	-45	-178
Bobylev2016	Bobylev16-21	RAVE DR4	21	-1	-170
Bobylev2016	Bobylev16-22	RAVE DR4	22	50	-180
Bobylev2016	Bobylev16-23	RAVE DR4	23	-95	-178
Antoja2012	Coma Berenices	RAVE	1	-4	-246
Bobylev2016	Coma Berenices	RAVE DR4	1	-4	-246
Dehnen1998	Coma Berenices*	Hipparcos	4	-1	-247
Xia2015	Coma Berenices*	LAMOST-RAVE	4	0	-245

Table 5: Compilation of MGs from different authors (continuation).

Author	Name	Source	Original number	V_R [km s^{-1}]	V_ϕ [km s^{-1}]
Dehnen1998	Dehnen98-11*	Hipparcos	11	59	-242
Dehnen1998	Dehnen98-12*	Hipparcos	12	59	-202
Dehnen1998	Dehnen98-13*	Hipparcos	13	-61	-252
Liang2017	Dehnen98-14*	LAMOST-TGAS	5	-62	-224
Dehnen1998	Dehnen98-14*	Hipparcos	14	-61	-227
Antoja2012	Dehnen98-14	RAVE	7	-59	-228
Bobylev2016	Dehnen98-14	RAVE DR4	7	-54	-228
Dehnen1998	Dehnen98-6*	Hipparcos	6	-31	-232
Bobylev2016	Dehnen98-6	RAVE DR4	12	-31	-230
Dehnen1998	Dehnen98-8*	Hipparcos	8	29	-202
Dehnen1998	Dehnen98-9*	Hipparcos	9	14	-202
Antoja2012	ϵInd	RAVE	10	70	-210
Liang2017	ϵInd	LAMOST-TGAS	8	72	-213
Bobylev2016	ϵInd	RAVE DR4	10	79	-203
Antoja2012	ηCep	RAVE	14	16	-157
Bobylev2016	ηCep	RAVE DR4	11	31	-151
Liang2017	γLeo	LAMOST-TGAS	10	-81	-246
Antoja2012	γLeo	RAVE	11	-79	-253
Bobylev2016	γLeo	RAVE DR4	9	-76	-253
Antoja2012	γLeo	RAVE	9	-67	-254
Liang2017	γLeo	LAMOST-TGAS	7	-61	-255

Table 5: Compilation of MGs from different authors (continuation).

Author	Name	Source	Original number	V_R [km s^{-1}]	V_ϕ [km s^{-1}]
Liang2017	Hercules I	LAMOST-TGAS	6	41	-211
Antoja2012	Hercules I	RAVE	6	46	-204
Bobylev2016	Hercules I	RAVE DR4	8	46	-204
Liang2017	Hercules II	LAMOST-TGAS	4	17	-204
Antoja2012	Hercules II	RAVE	8	17	-202
Bobylev2016	Hercules II	RAVE DR4	5	24	-202
Liang2017	HR1614	LAMOST-TGAS	11	-32	-188
Dehnen1998	HR1614*	Hipparcos	7	-26	-192
Bobylev2016	HR1614	RAVE DR4	13	-25	-194
Antoja2012	Hyades	RAVE	2	19	-239
Bobylev2016	Hyades	RAVE DR4	2	19	-237
Liang2017	Hyades	LAMOST-TGAS	0	19	-236
Dehnen1998	Hyades*	Hipparcos	2	29	-232
Xia2015	Hyades-Pleiades*	LAMOST-RAVE	5	7	-234
Kushniruk2017	Kushniruk17-J4-2	RAVE-TGAS	2	-49	-259
Kushniruk2017	Kushniruk17-J3-13	RAVE-TGAS	13	-48	-260
Kushniruk2017	Kushniruk17-J3-18	RAVE-TGAS	18	75	-176
Kushniruk2017	Kushniruk17-J3-19	RAVE-TGAS	19	7	-185
Liang2017	Liang17-12	LAMOST-TGAS	12	11	-185
Liang2017	Liang17-13	LAMOST-TGAS	13	41	-265
Liang2017	Liang17-14	LAMOST-TGAS	14	25	-281
Liang2017	Liang17-9	LAMOST-TGAS	9	-19	-201

Table 5: Compilation of MGs from different authors (continuation).

Author	Name	Source	Original number	V_R [km s^{-1}]	V_ϕ [km s^{-1}]
Dehnen1998	NGC1901*	Hipparcos	5	14	-242
Liang2017	Pleiades	LAMOST-TGAS	1	-5	-229
Dehnen1998	Pleiades*	Hipparcos	1	1	-230
Bobylev2016	Pleiades	RAVE DR4	4	2	-228
Antoja2012	Pleiades	RAVE	4	5	-230
Liang2017	Sirius	LAMOST-TGAS	2	-27	-256
Xia2015	Sirius*	LAMOST-RAVE	3	-22	-251
Bobylev2016	Sirius	RAVE DR4	3	-21	-253
Dehnen1998	Sirius*	Hipparcos	3	-20	-255
Antoja2012	Sirius	RAVE	3	-15	-256
Bobylev2016	Wolf 630	RAVE DR4	6	-40	-231
Antoja2012	Wolf 630	RAVE	5	-39	-231
Liang2017	Wolf 630	LAMOST-TGAS	3	-34	-230

SUBSTRUCTURE IN THE HALO AND DISC EDGE

3

Abstract

Context: The astrometric sample provided by *Gaia* allows us to study the disc far from the Sun, in the halo and at their interface. It is at the very edge of the disc where the effects of external perturbations is most noticeable, but also where there could be the remnants of accreted satellites.

Aims: Our goal is to characterise the kinematic substructure present in the halo and at the edge of the Milky Way (MW) disc to provide observational constrains that can help us identify their origin.

Methods: We download, one HEALpix at the time, the proper motion histogram of distant stars selected with *Gaia* photometry and parallax, to which we apply the Wavelet Transformation to reveal the significant overdensities. Some of the peaks detected in different HEALpix form large coherent structures in the sky.

Results: We reveal a complex anticentre dominated by Monoceros and the Anticentre stream (ACS), which we find with an intensity comparable to the Magellanic clouds and the Sagittarius (Sgr) stream. The sharp picture obtained with our method allows us to perform a morphological analysis of both structures, which have an arch-like shape spanning more than 100° in longitude. Their kinematics obtain with our method are disc-like and the colour-magnitude diagram of the stars that populate them is consistent with an extended structure at ~11 kpc. By removing the foreground stars efficiently with our algorithm, we determine that Monoceros extends to latitudes at least as low as ~5°.

Conclusions: We present the most precise characterisation of Monoceros and Anticentre stream (ACS), detected for the first time exclusively in phase-space, without limiting ourselves to a particular stellar type. Our results allow future works to model their orbital parameters, chemistry and star formation history, to establish their origin and, ultimately, understand the most influential processes that shaped the MW over its history.

To be submitted: P. Ramos, T. Antoja, C. Mateu, F. Anders et al.

3.1 INTRODUCTION

With the publication of the *Gaia* (Gaia Collaboration et al., 2016b) second data release (DR2, Gaia Collaboration et al., 2018b), there has been a huge advance in the study of the Milky Way (MW) kinematics. For instance, it was possible to identify a large group of stars accreted ~10 Gyr ago in the last major merger event (Gaia Collaboration et al., 2018a; Belokurov et al., 2018; Haywood et al., 2018; Helmi et al., 2018). Another example is the advance in the study of the *moving groups* and the possibility to now visualise the kinematic substructure directly in the plane of Galactocentric radii against rotational velocity in the form of ridges (e.g., Antoja et al., 2018; Ramos et al., 2018; Khanna et al., 2019). The latter has been applied directly to the characterisation of the non-axisymmetric components of the Galaxy like the bar (e.g., Monari et al., 2019a,b).

All these studies made use of the 6D data (positions and velocities) provided by *Gaia*. Nevertheless, this sample is limited to G< 13 mag approximately[1], restricting the studies to a bubble of ~3 kpc radius from the Sun. Despite some attempts to extend the kinematic maps to further distances either by using statistical corrections to the parallax (López-Corredoira & Sylos Labini, 2019; López-Corredoira et al., 2020) or by adding spectroscopic information (Liu et al., 2017; Wang et al., 2019), these only have a significant amount of stars up to Galactocentric radii of ~16 kpc. Nonetheless, the 5D data (only astrometry and no radial velocity) contains valuable information and its power is exemplified by the work of, for instance, Castro-Ginard et al. (2018, 2019, 2020) applying Big Data algorithms to discover hundreds of new Open Clusters throughout the disc. Another example is Malhan et al. (2018b) and Ibata et al. (2019) where, by applying the STREAMFINDER algorithm (Malhan & Ibata, 2018; Malhan et al., 2018a), they are able to discover several new tidal streams, or the recent work by Koppelman & Helmi (2020) that provides a large sample of halo stars selected using the reduced proper motions (Jones, 1972).

The astrometric sample contains orders of magnitude more stars than the 6D and reaches down to G ~21 mag, implying that we should be capable of tracing kinematic structures up to distances of roughly 100 kpc from the Sun using Red Clump (RC) stars. Within this extended bubble of 100 kpc there are dozens of Globular clusters, some known since the XIX century, but also many structures that have been discovered in the last decades thanks to deep photometric surveys. One example is the identification by Ibata et al. (1994) of a dwarf spheroidal galaxy undergoing full tidal disruption just some ~25 kpc away from us. This system, named Sagittarius (Sgr), supposed a major break-through in the study of the halo and its assembly history, and it has been extensively used to constrain the shape and mass of the MW

1 Above that, the completeness drops significantly.

potential (Helmi, 2004; Johnston et al., 2005; Law & Majewski, 2010b; Fardal et al., 2019), mostly by exploiting the information contained in its tidal tails that wrap around the entire sky and probe different regions of the MW halo (Majewski et al., 2003; Belokurov et al., 2014; Hernitschek et al., 2017). Afterwards, with better detectors and telescopes, came the discovery of many more streams (e.g., Belokurov et al., 2006) and even other type of systems like the Ultra Faint Dwarf galaxies (e.g., Willman et al., 2005; Belokurov et al., 2007), showing that the halo is far from smooth in good agreement with the cosmological simulations.

Towards the anticentre, Newberg et al. (2002) reported, almost two decades ago, the presence of a peculiar population bluer than the thick disc and clearly appreciable as an overdensity of Main Sequence Turn Off (MSTO) stars above the mid-plane at a distance of ~10 kpc from the Sun. Known as Monoceros, this structure was observed to span several degrees in longitude ($100° < l < 270°$, see Rocha-Pinto et al., 2004) both in the north and south hemispheres. It was originally associated with the tidal debris of an accreted satellite based on its metallicity and kinematics (Yanny et al., 2003; Crane et al., 2003), partially supported by the simulations of Helmi et al. (2003). Nevertheless, Ibata et al. (2003) proposed several other mechanisms like a perturbation induced by the close passage of Sgr. Such interaction with a dwarf galaxy could cause some of the disc material to move to more inclined and eccentric orbits, and produce a stream of stars consistent with the observations. The simulations by Laporte et al. (2018, 2019a) have shown that, indeed, tidal feathers resembling Monoceros can appear in the disc as a response to Sgr. The idea is further reinforced by the detection of a vertical wave-like pattern in the disc (Widrow et al., 2012) that propagates almost radially (Xu et al., 2015; Schönrich & Dehnen, 2018), in good agreement with the simulations of Gómez et al. (2013). In their work, they demonstrate that corrugations like these can appear on a self-gravitating disc as a response to an external perturber hitting the MW disc. With the discovery of the phase-space spiral and consequent confirmation that our Galaxy is undergoing phase-mixing (Antoja et al., 2018), the interaction with Sgr is currently a great candidate to explain Monoceros.

Nevertheless, Monoceros is not the only structure present in the anticentre, as there is also the Anticentre stream (ACS) and the Easter Band Structure (Grillmair, 2006). Recently, Laporte et al. (2020) studied these structures with *Gaia* and confirmed that Monoceros and ACS have different populations (age and metallicities) and kinematics (see also de Boer et al., 2018). In their study, guided by their previous simulations of a MW interacting with Sgr, the authors intercede in favour of the perturbative origin for Monoceros and ACS, each one associated with a different pericentre passage of Sgr, and show that both have a conspicuous RC, in constrast with previous studies that

focused on the Main Sequence (MS) or the MSTO. However, the actual morphology of these structures is still blurry and their kinematics remain hard to reproduce analytically, which complicates any quantitative modelling of the interaction with Sgr. A deeper understanding of the events that lead to the observed stellar distribution in the anticentre could be used to constrain the orbit and mass of Sgr, as well as its effect on the gas and stars of our Galaxy.

Some years before DR2, Antoja et al. (2015b) devised a strategy to detect new kinematic and spatial coherent structures in the halo with *Gaia* data. It was specifically designed to detect new Ultra Faint Dwarf galaxies using the fact that these should create, simultaneously, an overdensity in proper motion space and in the sky. In this work, we use the first half of the methodology, that is, its application in proper motion space only, to study the kinematic substructure at large heliocentric distances. This approach allows us to scan the whole Celestial sphere systematically, homogeneously and using a statically robust technique that can distinguish subtle changes in the proper motion maps as we move with Galactic longitude and latitude. As a result, our maps are dominated by three large structures: the Magellanic clouds, the Sgr stream, and Monoceros-ACS. Our goal is to study the morphology and kinematics of these structures, taking advantage that our methodology allows us to obtain a large selection of members with almost no prior information. In this Chapter, we focus on the anticentre of the MW, while we study the Sgr stream in more detail in Chapter 4. In Sect. 3.2 we describe the strategy used to process the large amount of data available with *Gaia*. Section 3.3 then enumerates the different systems detected with our method and, in Sect. 3.4, we focus on characterising the complex kinematics of the anticentre, specially in the north where we observe Monoceros and ACS. We discuss the implications of our findings in Sect. 3.5, and finally present our conclusions in Sect. 3.6.

3.2 DATA AND METHODS

3.2.1 *Gaia data*

Thanks to the second data release (Gaia Collaboration et al., 2018b) of the *Gaia* mission, we have now access to the proper motions of more than a thousand million stars brighter than G $\sim$21 mag throughout the whole sky. However, most of these are actually close to the Sun, and can become a hustle when trying to observe the stars that lie behind. To study the halo and the outskirts of the MW we must first set aside the nearby stars which we do by cutting in parallax such that we only preserve sources that fulfil

$$\varpi - \sigma_{\varpi} < 0.1\,\mathrm{mas}. \tag{1}$$

With this filter we are selecting almost every star beyond 10 kpc independently of their parallax error[2]. The probability of *not* removing a source that is closer than 10 kpc depends on the quality of its parallax which, in turn, depends on its apparent magnitude. In other words, very close to the Sun most stars are bright and their measured parallax is large, and thus the probability that $\varpi < 0.1 + \sigma_\varpi$ tends to be low. Still, for stars with a $\varpi/\sigma_\varpi < 1$ this probability is larger than 50%, but the amount of stars with such large relative error diminish as we approach the Sun. On the other hand, as we move away from the Sun it is more likely to encounter stars with worse astrometry, which, combined with the reduction of the parallax itself, increases the chances that the source can pass the filter. The actual distribution of true distances resulting from our selection cannot be known with exactitude as it would require perfect knowledge of the actual stellar distribution in the MW. It should be possible to construct an analytical estimate by assuming a density profile, luminosity function and error model but, instead, we decide to observe the effects of our filter with a mock catalogue of the Galaxy (see Appendix C). The result is that most of the stars farther than 10 kpc are preserved while closer to the Sun the rejection ratio is significantly larger, but due to the increase in density the mode of the (true) distance distribution is at ~4 kpc.

Additionally, we also include a cut in the *Gaia* colour ($G_{BP} - G_{RP}$) to keep only stars redder than 0.2 mag. Since we do not expect young stars in the halo, removing the blue part of the colour-magnitude diagram (CMD) mostly reduces the amount of foreground stars in the disc that our previous cut in parallax did not remove. Nevertheless, we have confirmed that this second filter reduces the sample size by just a small fraction.

Our sample contains 700 412 152 sources. Properly processing and analysing such large data set is obviously impractical to do with a regular desktop computer. Usually, it would require a Big Data infrastructure. Nevertheless, given that we want to study changes in the velocity planes (similarly to the study performed in Chapter 2) but we do not have reliable distances for the majority of the stars, our observables are the proper motion histograms themselves. Due to the impracticality of downloading all the stars that fulfil the cuts imposed, we process in parallel each HEALpix downloading from the *Gaia* Archive[3] directly the proper-motion histograms. The HEALpix tessellation of the Celestial Sphere is encoded inside the `source_id` of each star, the basic identifier in the *Gaia* catalogue, allowing for a fast way to isolate patches in the sky by just selecting ranges of this indexed column with the following query:

2 The stars whose *true* distances is 10 kpc have a probability of passing the cut of ~84%. This is because our filter at that distance corresponds to the upper 1σ of a Gaussian distribution centred on the *true* parallax (0.1 mas) and a dispersion equal to σ_ϖ. Stars that are farther away have a larger probability of being selected.

3 Hosted at the *Gaia* Archive: https://gea.esac.esa.int/archive/

```
SELECT COUNT(*) as N, pmra\_index*binsize as pmra
   , pmdec\_index*binsize as pmdec FROM (SELECT
   source\_id, FLOOR(pmra/binsize) AS pmra\_index
   , FLOOR(pmdec/binsize) AS pmdec\_index FROM
   gaiadr2.gaia\_source WHERE source\_id BETWEEN
    hpnum*2**35*4**(12-level)  AND  (hpnum+1)
   *2**35*4**(12-level) AND parallax-parallax\_
   error < 0.1 AND bp\_rp >= 0.2 AND pmra IS NOT
   Null AND pmdec IS NOT NULL) as sub GROUP BY
   pmra\_index, pmdec\_index
```

where one should replace *hpnum*, *level* and *binsize* by the number of the HEALpix, the level of the HEALpix grid (here 5) used, and the size of the bin for the histogram (here 0.24 $\mathrm{mas\,yr^{-1}}$). This results in fast queries that return easy to handle small size files to each of which we then apply the methodology described in the next section. With a regular computer and eight CPU cores running, the whole sky execution takes on the order of 12h.

3.2.2 *Peak detection algorithm*

The peak detection algorithm is a simplified version of the method presented in Antoja et al. (2015b). Here we summarise the algorithm but more technical details and recent applications can be found in Starck & Murtagh (2002); Antoja et al. (2015b); Ramos et al. (2018).

The main piece of the algorithm is the *a trous* ('with holes') variant of the wavelet transform (WT, Starck & Murtagh 2002), which computes a discrete set of scale-related 'views' of a 2D image, where substructure at a particular scale is highlighted. We use the implementation in the MultiResolution software[4]. For each HEALpix, our initial image is the 2D histogram in proper motion space with bin size of 0.24 $\mathrm{mas\,yr^{-1}}$and range of [-12, 12] $\mathrm{mas\,yr^{-1}}$. We explore a set of three logarithmically spaced scales in proper motion of 0.48, 0.96 and 1.92 $\mathrm{mas\,yr^{-1}}$, that we denote 1, 2 and 3. An example of the WT application is presented in Fig. 18, where the WT coefficients are shown in a blue (red) colour scale corresponding to over-dense (under-dense) regions, for the three different scales (columns) and for two different sky positions as explained in the labels (rows).

Then we search for local peaks in the WT plane at each scale, using `peak_local_max` from the *Python* package `Scikit-image` (van der Walt et al., 2014). The WT also gives the significance of the coefficients based on a model for the Poisson noise. From all the peaks detected, we select only those with WT coefficient with significance[5] $\geqslant 3$, which

4 `http://www.multiresolutions.com/mr/`

5 This is equivalent to $WP \geqslant 99.7$ in the notation of Antoja et al. (2015b) and to $\mathrm{CL} = 3$ in Ramos et al. (2018).

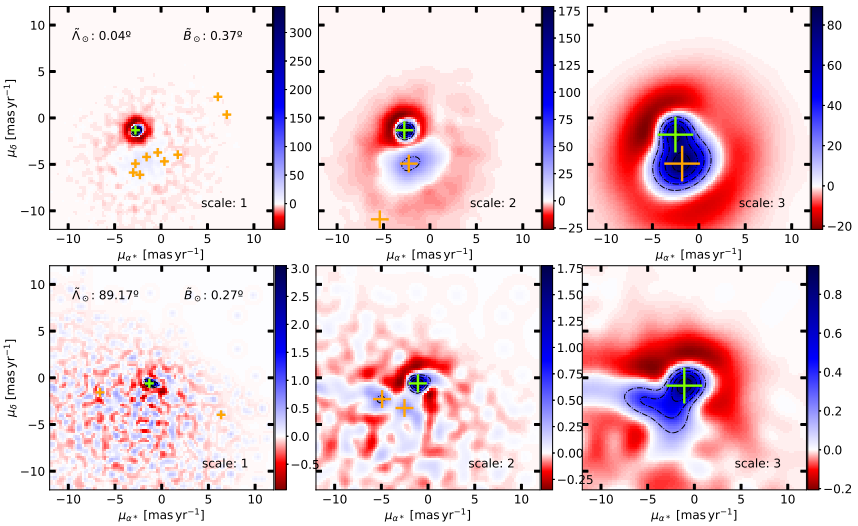

Figure 18: Example of WT planes in two different HEALpix fields corresponding to the Sgr core (top row) and the middle part of the leading arm (bottom) at the three different scales analysed here (three columns, from left to right for small to large). The colour indicates the value of the WT coefficients, where darker blue means higher WT, i.e. higher intensity of the substructure, while red colours are for under-dense regions. Crosses are peaks detected in these WT planes. The peak of the Sgr stream/dwarf is marked in green and appears well separated from the general field.

corresponds to $\sigma \geqslant 3$ in the Gaussian-equivalent case. The peaks detected in each scale are marked with crosses in Fig. 18. In these plots, which correspond to a HEALpix centred close to the Sgr dwarf (top) and the leading arm (bottom), respectively, a prominent peak is found (green cross), corresponding to Sgr as we discuss in more detail in Chapter 4.

Finally, the method yields the list of significant peaks in proper motion at each HEALpix with their associated quantities such as the location of the peak in $\mu_{\alpha*}$ and μ_δ, the WT coefficient, which can be thought of as the intensity of the peak, the scale where it was detected (1, 2 or 3), and the number of stars belonging to the peak. The latter is calculated by counting the sources within a circle centred at the position of the peak with a radius equal to 0.24×2^j mas, where j corresponds to the scale of the peak (see Chapter 2 for more details). A measure of the relative intensity of a peak can be computed as:

$$\frac{WT}{N_{hp}} \times 1000, \tag{2}$$

where N_{hp} is the total number of stars in the HEALpix and the 1000 factor is used to convert to more usable numbers (in this case, typical relative peak intensities will be of the order of 1).

3.3 GLOBAL MAP OF THE SUBSTRUCTURES

Figure 19 shows the Mollweide projection of the sky in Galactic coordinates coloured by the relative intensity (Eq. 2) of the highest peak in the proper motion histogram. By selecting only the overdensity with the largest intensity present at each proper motion histogram, we can focus on the dominant kinematic structure of the HEALpix (in some cases, the dominant peak might not be the peak in the proper motion plane with the largest amount of stars inside it). The normalisation used in Eq. 2 compensates the density gradient of the Galaxy and gives more contrast to the structures at higher latitudes. This figure reveals a wealth of substructure that cannot be seen with a simple density map of our sample. Figure 20 contains the number of sources that pass our filters at each HEALpix (top panel) where we can only identify the Magellanic clouds, some Globular clusters and the imprints of the extinction (which is shown in the middle panel for comparison) and the scanning law (shown in the bottom panel of the same figure) of *Gaia*.

With Fig. 19 we have been able to detect:

- The Magellanic clouds: this pair of satellite galaxies, known since ancient times, appear as large red patches in the bottom left part of the figure. Their angular size, in contrast with their size in the top panel of Fig. 20, is larger and shows the true extent of this systems as already noted in, e.g. Gaia Collaboration et al. (2018c). We also detect substructure within them, and we are able to recover some of the Globular clusters that orbit the Large Magellanic cloud.

- The Sgr stream: the core of the dwarf galaxy discovered by Ibata et al. (1994) is also clearly visible close to the Galactic centre (GC). Interestingly enough, we do not observe it in the top panel of Fig. 20, which highlights the difficulty, even in the *Gaia* era, to detect this structure with just stellar counts. A tidal tail can be seen sprouting from the core of the progenitor in the south hemisphere and wrapping around the sky until it hides behind the disc at the anitcentre ($l \sim 180°$). The other arm of the stream appears in the north hemisphere, following the same orbital plane.

- Almost vertically mirrored to the Sgr stream, we note a feature with a stream-like shape. Its proper motion is always centred on zero, implying a large heliocentric distance.

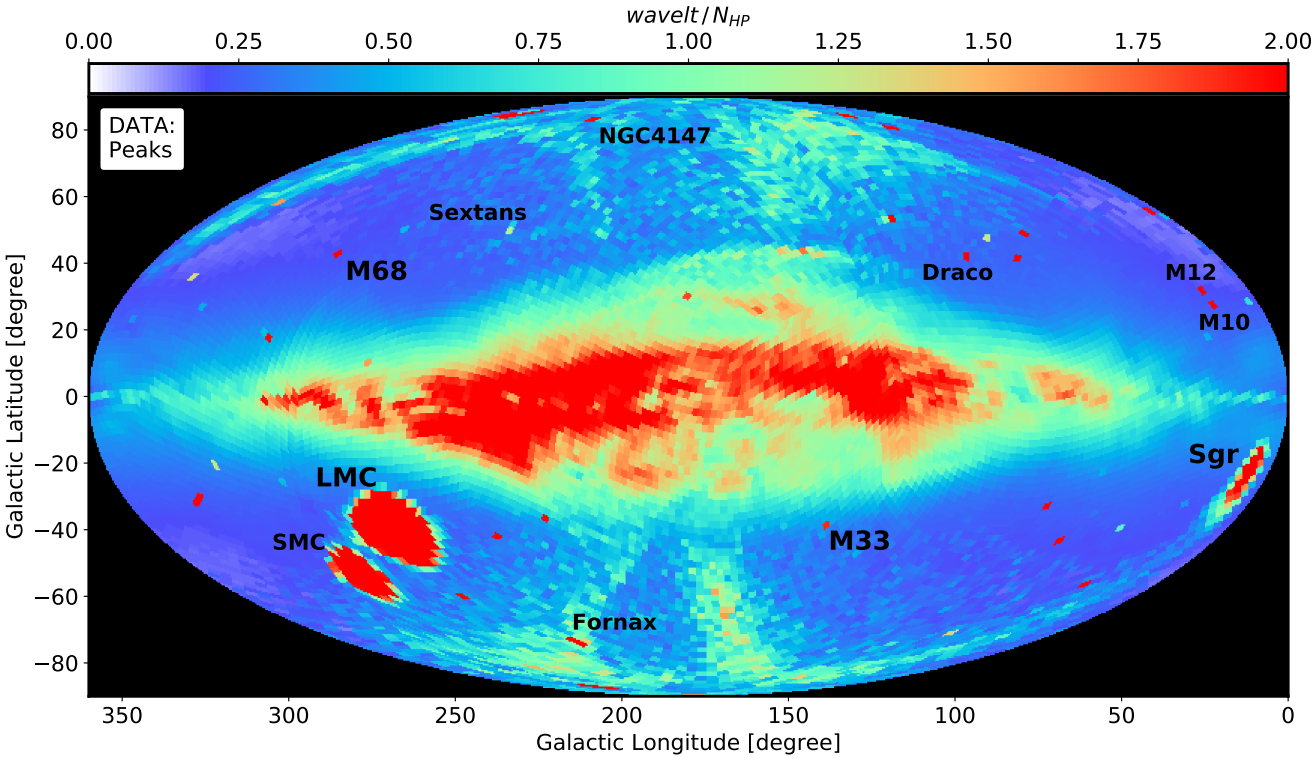

Figure 19: Mollweide projection of the relative intensity of the dominant structure in the proper motion plane at each HEALpix. By showing only the most significant kinematic overdensity and normalising to the number of stars in the HEALpix, a large number of structures become visible: the Sgr stream, tens of Globular Clusters and an intricate anticentre. We have label some of most relevant ones.

Nevertheless, after analysing the distribution of the sources that produce these peaks in the plane of colour against excess flux, we conclude that they are actually quasars because their excess flux is well above the cut defined in Evans et al. (2018, see their Eq. 1)[6] and because their proper motions are always normally distributed around the origin, as one would expect from the population of quasars observed by *Gaia*. Although these objects are ubiquitous and should not produce a band in the sky, the scanning law of *Gaia* favours certain regions of the sky as can be seen in the bottom panel of Fig. 20 with the `astrometric_gof_al`[7] that quantifies the quality of the astrometric solution. In this parts, the astrometric uncertainties of the quasars diminish enough so that they become more relevant than the diffuse halo population of stars. Since we did not expect to obtain such a clear signal from the quasars, we did not remove them beforehand. Nevertheless, our results are not affected by their presence. With the list of extended objects that will be published in *Gaia* DR3, we will be able to remove this objects up-front within the queries directly.

- Nearby galaxies: apart from the Magellanic clouds, we also detect M31 and M33, the latter clearly visible in Fig. 19 at $(l, b) \sim (133^\circ, -31^\circ)$.
- Dwarf spheroidals: Our method is able to detect several Dwarf spheroidals, like Fornax, Sextans or Sculptor, as well as fainter ones like Draco.
- Globular clusters: We recover 51 Globular clusters from the Bica et al. (2019) catalogue. From their 200 objects confirmed as Globular clusters, more than half are in the bulge where we do not detect any either because the contrast with the foreground is too low or due to the cut in parallax applied.
- Ultra Faint Dwarf galaxies: We do not recover any of the known Ultra Faint Dwarfs galaxies based solely on their kinematic signature. Their proper motion uncertainties are too large and there are too few members (see Massari & Helmi, 2018) to produce a significant overdensity. Nevertheless, we note that the application of the full methodology described in Antoja et al. (2015b), that includes the search of peaks in the sky and not only in proper motion as here, can effectively recover most of them.
- Anti-centre: Apart from all the substructure we find in the halo, our methodology reveals us a complex kinematic structure to-

6 They could be still be stars affected by Zodiacal light but we note that the structure we are detecting does not align with the ecliptic plane (c.f. Fig. 18 from Evans et al., 2018).

7 Other indicators are `astrometric_excess_noise` or `astrometric_n_good_obs_al`.

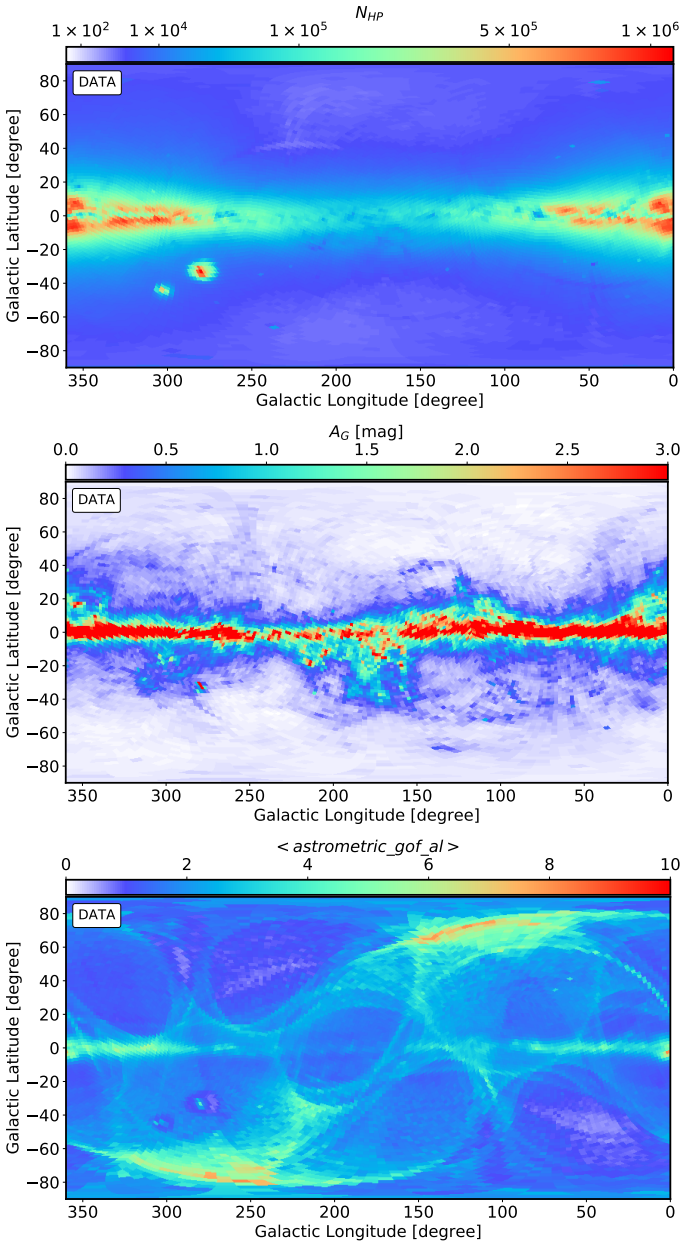

Figure 20: Top: Number of stars in each HEALpix that fulfil the selection described in Sect. 3.2. Middle: Absorption at infinite in the G band at each HEALpix. The extinction is computed using the Schlegel et al. (1998) maps with the re-calibration by Schlafly & Finkbeiner (2011), which is later transformed into absorption in the *Gaia* band with the procedure described in Appendix A. The colour used for this transformation is the average $G_{BP} - G_{RP}$ of the sources in the HEALpix. Bottom: Average `astrometric_gof_al` at each HEALpix. To obtain this map, we query the *Gaia* Archive with the cuts in parallax and colour described in Sect. 3.2 and download the mean *goodness-of-fit* (Lindegren et al., 2018) as described in Appendix B.

wards the anticentre of the MW, dominated by two arch-like features in the north Galactic hemisphere. After comparing with the extinction map shown in the middle panel of Fig. 20 obtained from Schlegel et al. (1998), using the mean colour in the HEALpix and the transformations described in Appendix A, we confirm that these features are not aligned with regions of high absorption. We have also checked that these do not align either with the scanning law, pointing to a physical origin instead.

We note that some of these structure also appear in Fig. 21, where we colour the sky according to the proper motion of the highest peak (the one used to colour Fig. 19). For instance, the Sgr stream is easily appreciable and we note that its proper motions vary along the tidal tails, especially the $\mu_{\alpha*}$ component (top panel). For its importance and impact on our Galaxy, we explore its kinematic detection in depth in Chapter 4. Also the structure at latitude b$\sim$35° ($140° < l < 200°$), appears as a conspicuous structure in the proper motion map. The rest of this Chapter is devoted to the analysis and characterisation of the anticentre given that our method has been able to produce the sharpest picture to date, focusing mostly in the north where we observe these two conspicuous arches in Fig. 19.

3.4 KINEMATIC FEATURES IN THE ANTICENTRE

To test the signal that we would expect to see in a galaxy without substructure, we run our whole method to the proper motion histograms obtained from a mock catalogue. For that, we select the Rybizki et al. (2018) *Gaia* DR2 mock since it allows for easy access via TAP query, which can be automated with the *Python* package `PyVo`. After applying the observational errors to the true proper motions, parallaxes and colours, we repeat the strategy described in Sect. 3.2 to obtain the maps of Appendix C. The first thing we note is that there is far less substructure, and that the warp dominates the shape of the plane. More importantly, though, is the difference in the recovered size of the disc towards the anticentre: while the mock is showing a disc that does not go beyond $|b| \sim 25°$ and transitions sharply into the halo, the data is revealing a slightly thicker disc (especially in the north hemisphere) with clumps and arches that blurs the frontier with the halo. We also note, from the analysis of the mock data, that we should not expect any kinematic features in this region apart from the solar reflex and the signature of the rotation curve. Again, this is not the case for the data where we observe that the proper motion of the peaks (Fig. 21) are different from the average proper motion (Fig. 30), which are dominated by the rotation of the disc and the peculiar velocity of the Sun.

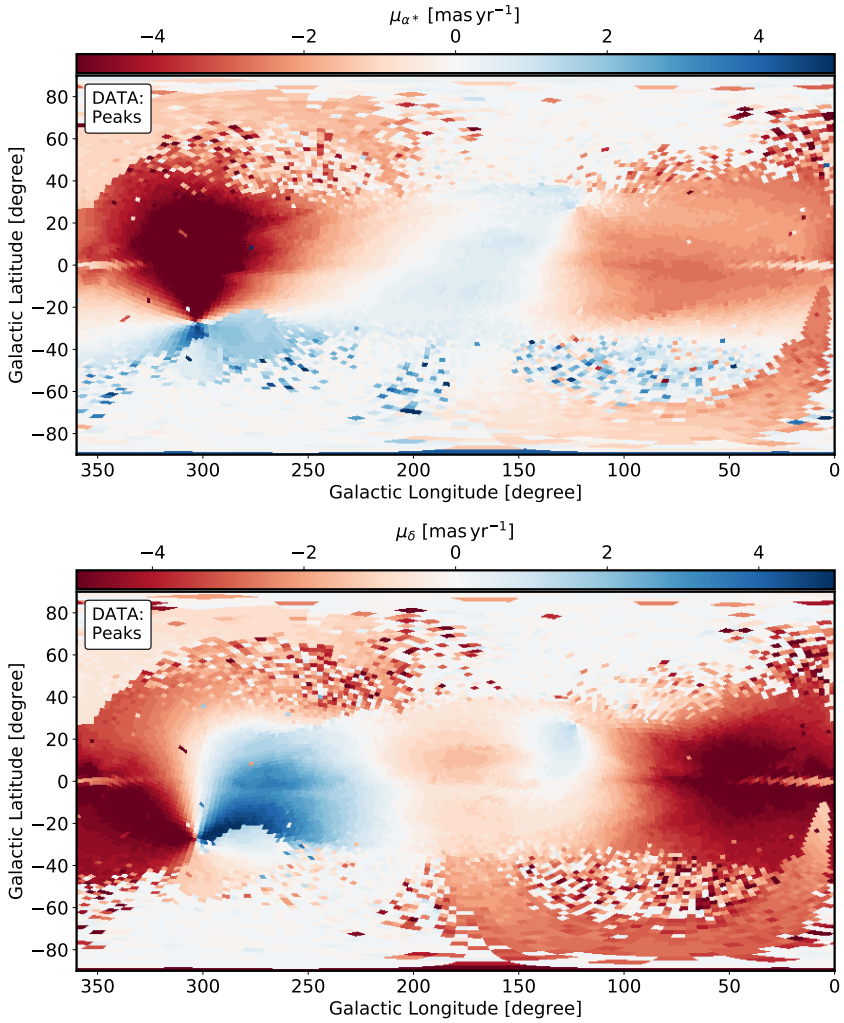

Figure 21: Proper motion coordinates of the dominant peak at each HEALpix. Top: Proper motion in right ascension. Bottom: Same but in declination. Conspicuous stream-like patterns crossing the entire Celestial sphere can be appreciated, one of which is Sgr (bottom right to top left) and the other corresponds to the quasars (bottom left to top right).

3.4.1 *Monoceros and ACS*

In Fig. 22 we present a zoom-in of Fig. 19 towards the anticentre and show our selection of the two structures that appear after colouring the sky according to the relative intensity of the dominant structure in proper motion. To build this selection in an objective manner, first, we apply a Gaussian softening (two sigmas) of the 2D image to erase the HEALpix limits, and then apply a bi-directional *Sobel* filter[8] used to reveal edges. By doing so, the two arches are cleanly separated at all longitudes. The final step is to select only the HEALpix whose *Sobel* intensity is above a certain threshold (0.0035 for the bottom arch,

8 Included in the *Python* package `Scikit-image` (van der Walt S et al., 2014)

0.0040 for the top one). However, if we applied this selection to all the region we would obtain a mixed list of HEALpix belonging to both structures as well as the border caused by the disc (long arch at b~10° in Fig. 22). Instead, we first draw a rectangle around each arch in an appropriate coordinate system. This coordinate system, different for the bottom and top arch, is obtained by rotating the Celestial sphere with respect to the Galactic reference frame until the structure is roughly flat at zero latitude. The resulting final selections are the contours shown in the bottom plot of Fig. 22. The structures can be seen to continue beyond the contours defined, especially for the feature at lower latitudes, but we focus on the regions where they are the most intense. We add three horizontal lines that represent an approximated latitude limit of each structure at l ~180°.

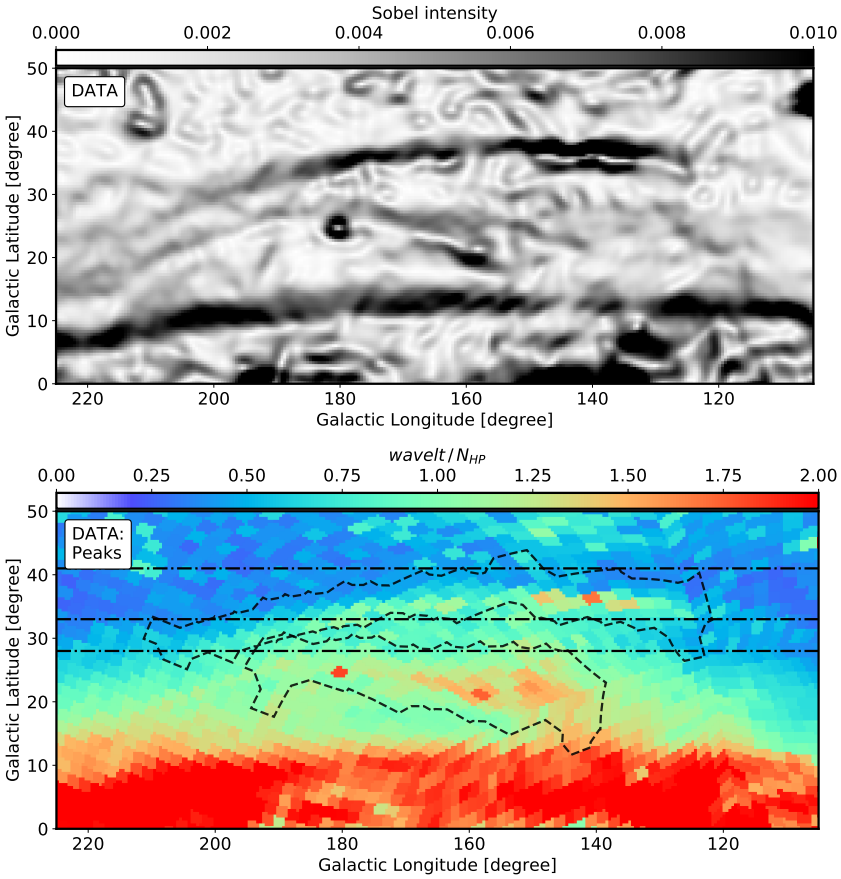

Figure 22: Zoom towards the anticentre region and definition of the patches. Top: Result of applying a Gaussian smoothing plus Sobel filter to Fig. 19 in the region: 110°< l <220°, -50°< b <50°. We use this map to isolate ACS and Monoceros. Bottom: $wavelet/N_{HP}$ (relative peak intensity) of the same region. The black contours delineate the regions that we have isolated according to the upper panel (Monoceros and below ACS), while the dashed horizontal lines (b = [28°,33°,41°]) give an approximate limit for the structures in latitude at l~180°.

By comparing the shape and location of these structures we note that they match with the Monoceros ring (bottom) and ACS (top) (Newberg et al., 2002; Grillmair, 2006). The patches we obtain are also in good agreement with the regions delineated by Laporte et al. (2020) but are much more thin and concise. In contrast to previous works, though, since we are not relying on counts but instead we detect these structures in relative intensity (Eq. 2), their morphology appears sharper and well defined. For instance, we observe a Monoceros structure that has a clear arch like shape[9] extending from ~120° to ~230° in longitude, where it meets the disc at a latitude of ~10°. The ACS is thinner, stays above Monoceros for the ranges of longitudes where we detect it and has its strongest signal at l ~140°, when Monoceros has already almost merged with the disc. This is the most precise picture of the anticentre available to date, mostly thanks to the introduction of kinematic information for the detection of these structures.

Once we have identified the Monoceros and ACS regions, we explore their kinematics and CMDs in more detail in Fig. 23. Each row contains the results for different regions: the first row is Monoceros, the second corresponds to the list of HEALpix that fall between Monoceros and ACS (hereafter, the bridge), then the third is ACS and, finally, the fourth is a region above ACS. The last row is an example obtained with the mock catalogue as we explain below. By doing so, we can evaluate the continuity of these structures and compare their characteristics with nearby regions in the sky where we do not see an enhancement in relative intensity (c.f. Fig. 22). In the first column of this plot we have aggregated all the stars that, in their respective HEALpix, fall within the highest intensity proper motion peak. We refer to such stars as *peak stars*. To show what we would see if we had not done this kinematic selection, the grey contours on top represent the CMD of all the stars of the region. The second and third columns contain, respectively, the trends of μ_l and μ_b with Galactic longitude for all the stars within the region. Here the black line encircles the stars selected kinematically, that is, the zero-contour of the peak stars. To provide some contrast with a fiduciary galaxy, in the bottom row we repeat the same process for the the particles in the mock catalogue that fall within the ACS footprint. In this case, the peak stars are selected according to the position and size of the peaks detected in the data, which is why the contours of panels h (i) and n (o) are so similar.

The first thing that we note is the presence of a Giant branch all the way from Monoceros to ACS, that disappears once we explore latitudes larger than ~40°. The fact that we see a well defined RC means that these stars share a similar distance which,

9 The strong red HEALpix at (l, b) ~$(140°, 25°)$ is the Globular cluster NGC 2419 which is far beyond Monoceros at a distance of ~83 kpc (Forbes et al., 2008).

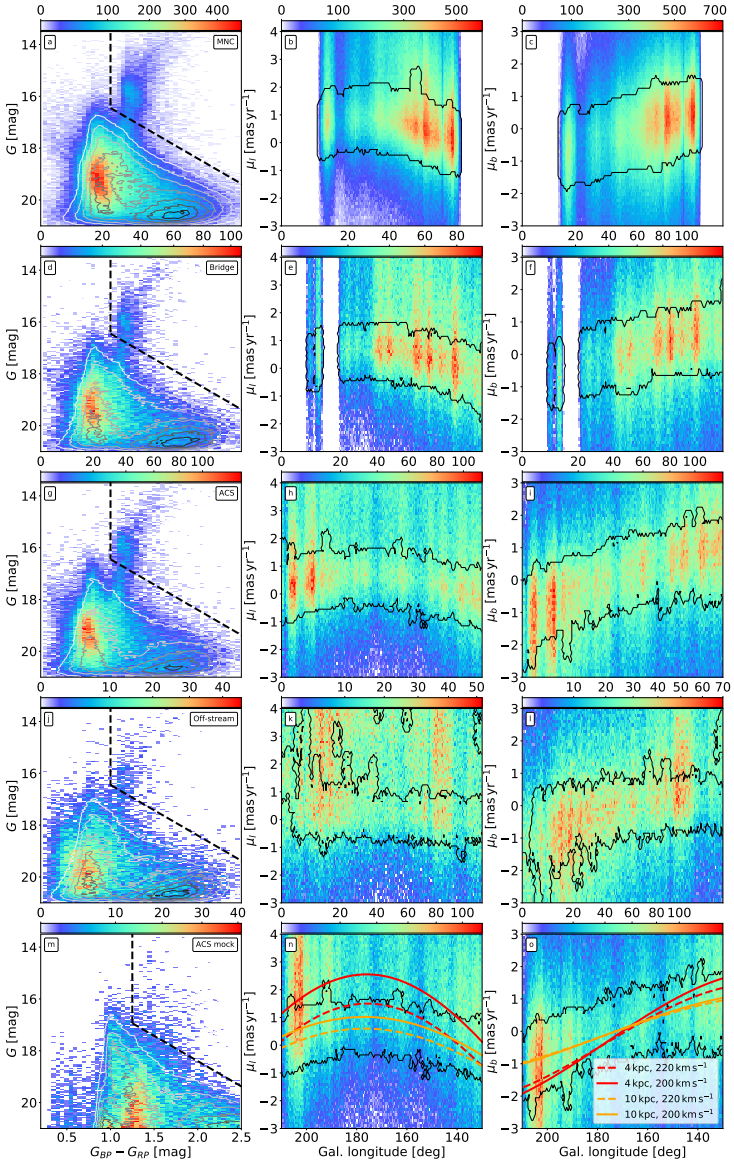

Figure 23: CMD (left) and proper motion trends with Galactic longitude in μ_l (middle) and μ_b (right) of each structure. The CMDs contain the histogram of the stars within the highest intensity proper motion peaks (peak stars) with grey contours on top that represent the CMDs of all the stars in the region. The black dashed lines represent our selection of Giant stars. The proper motion maps contain all the stars in the region, and the black line is the zero-contour of the peak stars, that is, the stars that fall within the highest intensity proper motion peak of their HEALpix. First row: Monoceros. Second row: Bridge between Monoceros and ACS. Third row: ACS. Forth row: above ACS. Fifth row: Same region as ACS but for the mock particles, selecting the stars for the CMD according to the contours of panels *h* and *i*. In the bottom panel we also include the proper motions expected from a structure 30° above the plane at a given distance, 4 (red) or 10 (orange) kpc, rotating at a given velocity, 200 (solid) or 220 (dashed) km s^{-1}, but with no radial or vertical velocity.

based on their magnitudes (~15.5 mag) and Galactic latitudes ($b > 15°$), puts them well above the mid-plane of the Galaxy ($z > 2$ kpc) at a height larger than the scale height of even the thick disc. If we compare with the CMDs of the data with the CMD of the mock catalogue, we do not expect many stars in this region of the diagram as the nearby Giants have been already removed with the cut in parallax (these are bright enough to have a reliable parallax) and there are not many stars at such heights/distances.

We also note, accompanying the Giant branch, a dense clump of stars appearing in red colours in panels a-d-g which is bluer than the Main Sequence (MS) of the disc seen in the mock. Newberg et al. (2002) already reported that the main sequence turn off of Monoceros was bluer than the thick disc and we detect the same behaviour for the stars in the peaks found within Monoceros and ACS. This group of stars is consistent with being the MS of an isochrone containing the RC discussed above. The rest of the stars that fall outside said isocrhone seem to follow the contours of the CMD obtained with all the stars (no kinematic selection, grey contours in those panels), and are most likely nearby, dwarf field stars that overlap with these structures in the proper motion plane. In contrast to previous works (e.g. Newberg et al., 2002; Ivezić et al., 2008; Xu et al., 2015; Laporte et al., 2020), where they detect an overdensity in counts for a given population, MS, MSTO or RC, here we have unveiled the whole sequence in the CMD by performing a blind kinematic selection of the stars instead.

In the bottom row of Fig. 23 we have included a few curves that represent the proper motion that *Gaia* would measure for a star at given distance if it only had azimuthal velocity[10]. In orange (red), this distance is 10 kpc (4 kpc) and in solid (dashed) the rotation velocity is $200\,\mathrm{km\,s^{-1}}$ ($220\,\mathrm{km\,s^{-1}}$). A structure that is too near, like the brown curve, does not match the contour delineated by the peak stars (black contours), while a structure that does not rotate, as could be the halo, would have to be at a distance larger than 50 kpc in average to fall within the black lines. And even then, its shape would not be compatible with the data. While we note that other combinations of distances and velocities could produce a similar shape (even if the result is not physically supported), the dashed red line shows a good agreement with our observations and corresponds to a structure at ~10 kpc rotating slightly slower than the disc. In other words, the peak stars in ACS (the same applies to Monoceros) have proper mo-

10 Here, we simply used the analytical expressions that transform the velocity of a star at a given position (l, b and distance) and that has only rotational velocity to proper motions in μ_l and μ_b. For the position and velocity of the Sun with respect to the GC we have used $R_\odot = 8.178$ kpc (Gravity Collaboration et al., 2019) and $V_\odot = [11.1, 248.5, 7.25]\,\mathrm{km\,s^{-1}}$ (Schönrich et al., 2010; Reid & Brunthaler, 2020). In all the cases we keep the latitude constant to 30° since the lines are used to compare with the tracks obtained in the ACS region, but we obtain similar results for the Monoceros region.

tions that change with Galactic longitude in a way that is compatible with a structure at a distance of ~10 kpc rotating at a speed similar to the disc or slower, in agreement with the analysis by de Boer et al. (2018).

By comparing the CMDs inside and outside the patches defined in Fig. 22, it is clear that, even though the MS of these structures is the dominant fraction, by focusing only on the Giants we can gain contrast with the MW foreground. Therefore, we introduce another tag, apart from the one that we have already been using to separate stars inside and outside the proper motion peaks. The stars will be called Giants whenever they are redder than $G_{BP} - G_{RP} > 1$ mag and their apparent magnitude smaller (brighter) than the line:

$$G < 1.95(G_{BP} - G_{RP}) + 14.50, \tag{3}$$

where we have used the slope calculated in Romero-Gómez et al. (2019) to follow the extinction arrow, and the zero-point is adjusted by eye to reduce the contamination from the disc while preserving the RC as much as possible. We note, however, that we are still selecting some faint and red dwarfs at all latitudes, the great majority of which are not classified as peak stars. This means that the Giants tagged also as peak stars are more likely to be true Giants, whereas field stars tagged as Giants have a larger probability of being nearby brown dwarfs.

Figure 24 shows the fraction of Giants inside the peaks (i.e., stars tagged as Giants and peak stars simultaneously) with respect to all

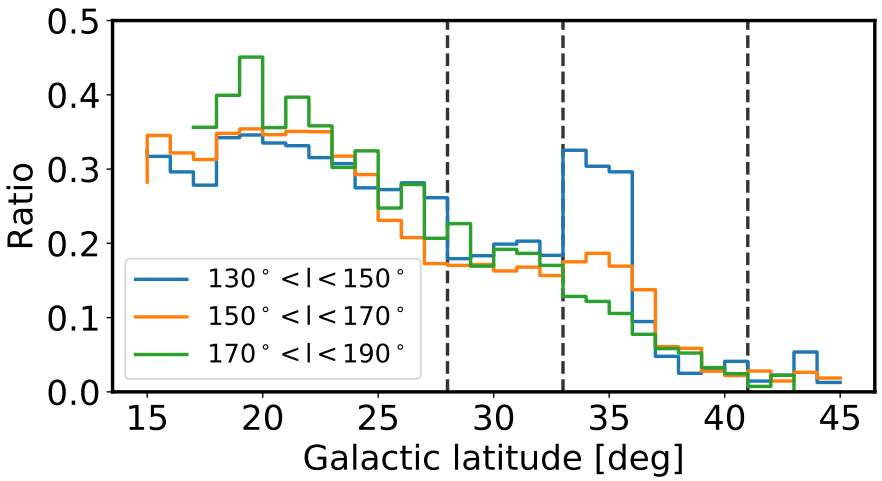

Figure 24: Ratio of Giants in the peak compared to all the Giants as a function of Galactic latitude for three different ranges in longitude: 130° < l < 150° (blue), 150° < l < 170° (orange), and 170° < l < 190° (green). The vertical lines give an orientation of the end of each structure with Galactic latitude (c.f. Fig 22). A sudden increase of the ratio can be seen in the part where ACS is the more intense.

the stars tagged as Giants as a function of latitude. Given that our classification is rather rough, we should treat these as simple estimates and focus on the trends instead. What we observe is that the parts where Monoceros and ACS have the strongest signal in relative intensity (c.f. Fig. 22) coincide with the regions where this ratio is the highest. We have already seen that the relative intensity of ACS decreases with with longitude, and here we note that the ratio of Giants also diminishes moving from one curve to the other. We also observe that the bridge keeps a constant ratio, in the range $130° < l < 150°$, showing that it is just the region where the tail of the two structures overlap. Finally, we note that our patch around ACS is too broad, as the ratio drops abruptly at $b \sim 37°$, coinciding with the place where we observe a discontinuity in the kinematics[11].

3.4.2 *Anticentre region: North vs South*

Above, we have proven that our methodology can detect the kinematic substructure and isolate it effectively from the rest of the disc. Also, the Giants that are inside the proper motion peaks are good tracers of Monoceros and ACS since the contamination in that region of the CMD is expected to be very low once we have filtered by parallax and kinematics. Therefore, we can use the location of the RC to trace the structures in physical space. To do so, we now explore the changes in apparent magnitude of the stars that we have tagged as peak stars, for different ranges of longitude, both in the north and south hemispheres.

Figure 25 shows the distribution of apparent magnitudes of peak stars with respect to the Galactic latitude using a histogram normalised by bins of b, for the range $130° < l < 150°$. This figure confronts the data (top) with the expectations from the mock (bottom). In this case, the particles selected in the mock correspond to the peaks that are detected with the mock itself (in contrast to panel m of Fig. 23 where we used the peaks detected in the data). We find an overdensity of stars in the north at a magnitude ~16 that corresponds to the RC seen in Fig. 23. It is most intense at $b \sim 35°$ and corresponds to the ACS (c.f. Fig. 22). We see it extending rather continuously down to $b \sim 20°$ where it merges with the disc, following an arch that is compatible with the increase in extinction.

We also observe a trace of overdensity in the south at bright magnitudes, where the mock predicts less particles, between latitudes of 15° and 25°. We do not see it the north either, and its origin at this point is not clear, as in that region of the map of relative intensity (Fig. 19) we see a decrease rather than the contrary (also compared to the mock, see Fig. 32). Right below it, there is a clump of stars

11 We have check that, indeed, the trends in proper motion as a function of latitude also suffer a sudden change at around $\sim 37°$, as can be seen in Fig. 21.

at apparent magnitude ~17. This second structure seems to coincide with the detection by Ibata et al. (2003) of a peculiar population, similar to Monoceros, near the disc in the M31 field of the Isaac Newton Telescope Wide Field Camera, at distances between 15 kpc and 20 kpc (RC apparent magnitudes between ~16.4 and ~17.0, assuming no extinction).

In Fig. 26 we now present the difference between the data and the mock in the same plane of apparent magnitude against Galactic latitude, for different bins in longitude from top to bottom: $130° < l < 150°$, $150° < l < 170°$, $170° < l < 190°$, and $190° < l < 210°$. In the first row we see the subtraction of the top panels of Fig. 25 from the bottom panels. In this case, the results are the same that we have already mentioned but we can now appreciate them with better contrast. However, we can now explore how these structures evolve with longitude. In the south we do not observe any relevant feature until the last row, where a diffuse overdensity appears again (latitudes

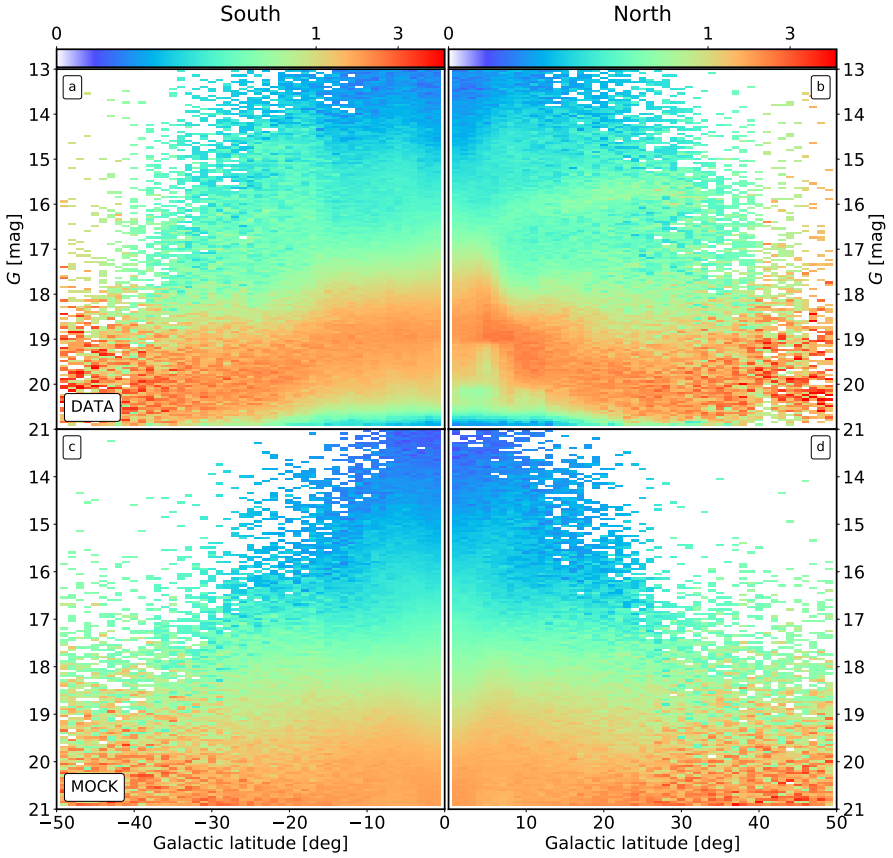

Figure 25: Apparent magnitude as a function of Galactic latitude for the stars in the peaks with $130° < l < 150°$. The histograms are normalised such the sum of all pixels in a given bin of b adds up to unity. A conspicuous overdensity of stars can be clearly seen appearing at G ~16 mag and extending from $15° < b < 40°$. Top: Data. Bottom: Mock.

between ~20° and ~30°, brighter than ~17 mag). Whether we do not observe this in the middle panels due to the increase in extinction is something worth investigating. Perhaps this overdensity in the south is part of the corrugation in the disc observed by Xu et al. (2015) at ~4-6 kpc from the Sun, and we can only detect it with our method

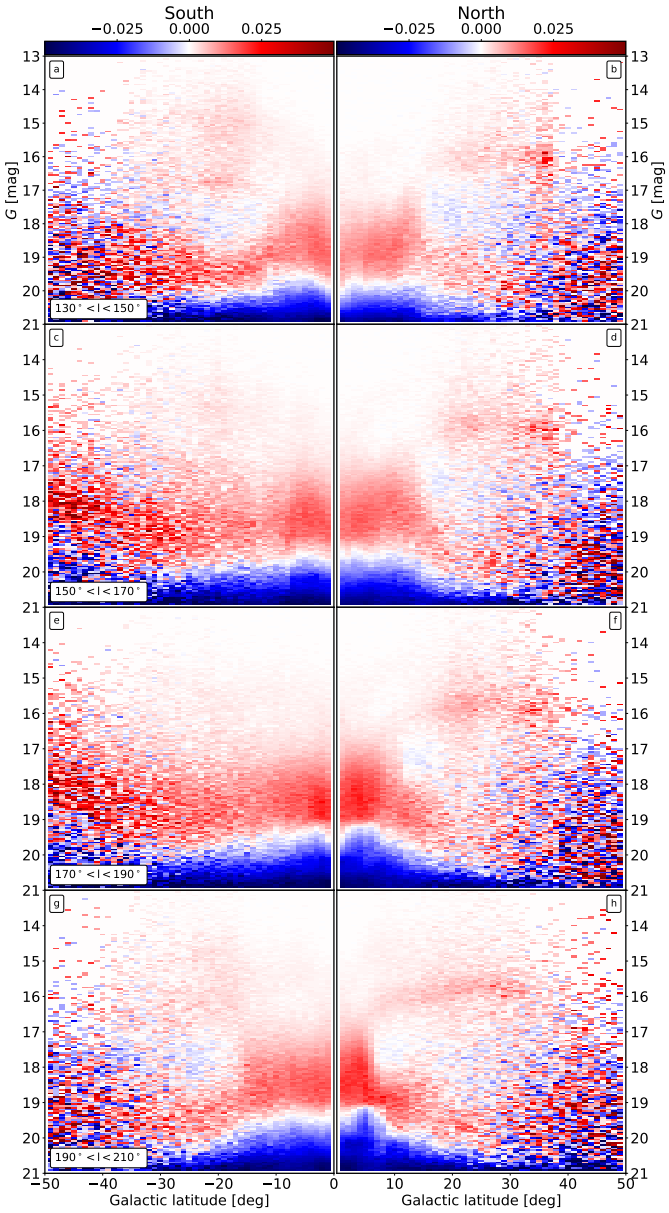

Figure 26: Differences between the data and the mock in the plane of apparent magnitude against Galactic latitude of counts in the peak stars, for different bins in longitude. The plots are obtained by subtracting the counts from the top and bottoms panels of Fig. 25, and similar panels for the other ranges of longitude, which had been previously normalised by bins of latitude. From top to bottom: 130° < l < 150°, 150° < l < 170°, 170° < l < 190°, and 190° < l < 210°.

where the extinction is low enough. In the north, we note that ACS decreases its intensity and shifts to lower latitudes when we move towards the third quadrant of the Galaxy, as we see also in Fig. 22. In the intermediate panels (d and f) we observe two concentrations at different latitudes, but similar apparent magnitudes, corresponding to Monoceros and ACS, whose tails overlap forming the bridge that we mentioned above. More importantly, we see the track of Monoceros extending more and more to lower latitudes, keeping roughly the same apparent magnitude throughout, until in the last row it can be traced down to very low latitudes. This is interesting as Monoceros is usually hard to trace so deep into the disc due to the foreground stars. And yet, using our kinematic selection we are able to detect its RC down to $\sim 5^\circ$ in latitude.

By measuring the median G for the Giant stars only, selected according to Eq. 3, we can investigate the relative distance of these structures. To do so, however, since the latitudes probed by Monoceros and ACS change with longitude, we focus only in the range $130^\circ < l < 170^\circ$ where they remain rather flat and the bridge quite wide (see Fig. 22). The median of the G magnitude and the associated one sigma interval of confidence, for the Giant stars in the peaks is shown in Fig. 27 as a function of latitude. To compensate for the effects of extinction, we have first corrected the apparent magnitude using the $G_{BP} - G_{RP}$ colour of each source and the prescription detailed in Appendix A. What we observe is that, below $b \sim 28^\circ$ where we identify Monoceros, the RC is brighter than above $b \sim 31^\circ$ where ACS begins. Since we have used the integrated extinction up to infinity (Schlegel et al., 1998), the separation that we observe is an upper limit: if we assume that the extinction applied to ACS is correct, since it is at a higher latitude, then Monoceros could actually be less extincted than assumed, and therefore be intrinsically fainter than the value we are recovering. Nevertheless, since both structures are quite far, this effect should be small and we can safely conclude that ACS is farther away than Monoceros.

To be more quantitative, we measure the median G, corrected for extinction, for the peak stars classified as Giants inside the portion of Monoceros and ACS that we find in the range $130^\circ < l < 170^\circ$. The result is the shaded areas shown in Fig. 27 where we can clearly see that ACS is, once we convert the difference in magnitude to distance, roughly 1 kpc farther away than Monoceros, with a discrepancy of more than 3σ. Moreover, we have estimated the median distance to each of the two structures. In doing so, we assume that the median apparent magnitude measured (horizontal lines in Fig. 27) corresponds to the magnitude of the RC. By imposing that the absolute magnitude

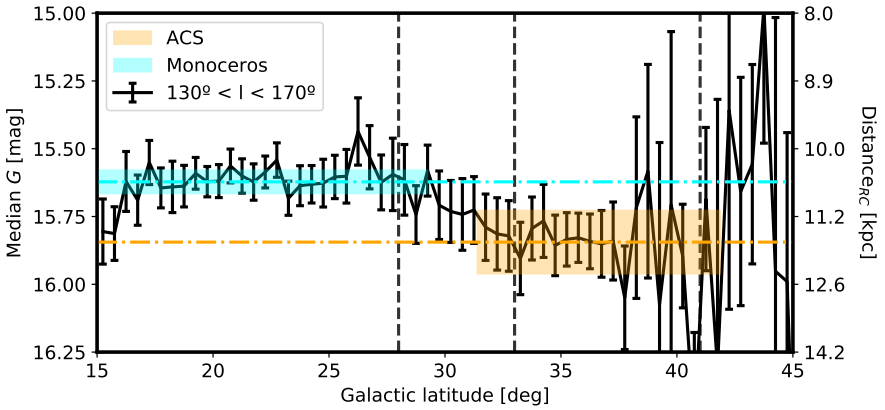

Figure 27: Apparent magnitude of Giants peak stars in the anticentre region ($130° < l < 170°$) as a function of Galactic latitude, after correcting for extinction (see text). The error bars denote the 1σ uncertainty on the median computed as $\sigma\sqrt{\frac{\pi}{2N}}$, where σ is the standard deviation of the apparent magnitude in the bin. Vertical lines represent the approximate limits of each structure in that range of Galactic longitudes (see Fig. 22), and the right axis represents the distance to a RC star with the apparent magnitude shown in the left axis. The horizontal lines correspond to the median G magnitude for the Giants peak stars within Monoceros (cyan) and ACS (orange). The shaded areas contain the $\pm 3\sigma$ interval of uncertainty and they extend from the minimum to the maximum latitude of the peak stars within each patch (the vertical dashed lines serve only as an orientation). As can be seen, the ACS is fainter than Monoceros and this translates to a difference in distance of ~1 kpc.

of a RC stars is M_G=0.495 mag (Ruiz-Dern et al., 2018), we obtain the following values[12]: $D_{MNC} \sim 10.6$ kpc, and $D_{ACS} \sim 11.7$ kpc.

Nevertheless, without a precise calibration of each individual star, and its extinction, we cannot investigate the changes in distance with longitude and latitude which is key to reveal the 3D shape of these structures. We make a first attempt to study the distribution of the arches along the line of sight by cross-matching the peak stars with the StarHorse catalogue (Anders et al., 2019). We download all the stars in the anticentre ($100° < l < 260°$ and $-60° < b < 60°$) with `SH_OUTFLAG` equal to "00000" and with a distance (50th percentile) less than 20 kpc. From the 13 098 038 stars in the north, we find 429 565 in StarHorse. In the south, the cross-match returns 514 167 stars out of the 13 669 647 that we have identified as peak stars. Most of them, however, are faint dwarfs found at low latitudes, closer than 10 kpc,

12 Here the dominant source of uncertainty is the systematic errors: the assumption that the median magnitude is the magnitude of the RC, and not using 3D extinction maps but instead correcting with the integrated extinction to infinity. Other sources of uncertainty are the error on the absolute magnitude of the RC, contamination from stars that are not Giants, or errors in the extinction map.

whose parallax quality is not good enough to discard them with the filter presented in Sect. 3.2. If instead we restrict ourselves to the Giants, then we find 378 955 (out of 1 449 250) in the north and 458 403 (out of 1 286 132) in the south. Not surprisingly, most of the stars remaining in StarHorse are classified as Giants since these are the ones that are more likely to converge to a satisfactory solution (see Anders et al., 2019) at such distances from the Sun.

Figure 28 shows the distribution of StarHorse distances as a function of Galactic latitude for the four ranges of longitude explored above. The first thing we note is the effect of our selection function as the nearby Giants are missing and a wall of stars at a distance of ~6 kpc is formed. The tails extend up to ~15 kpc, point beyond which StarHorse has trouble producing reliable estimates. Compared with the corresponding figure for the mock (Fig. 34), where we see the

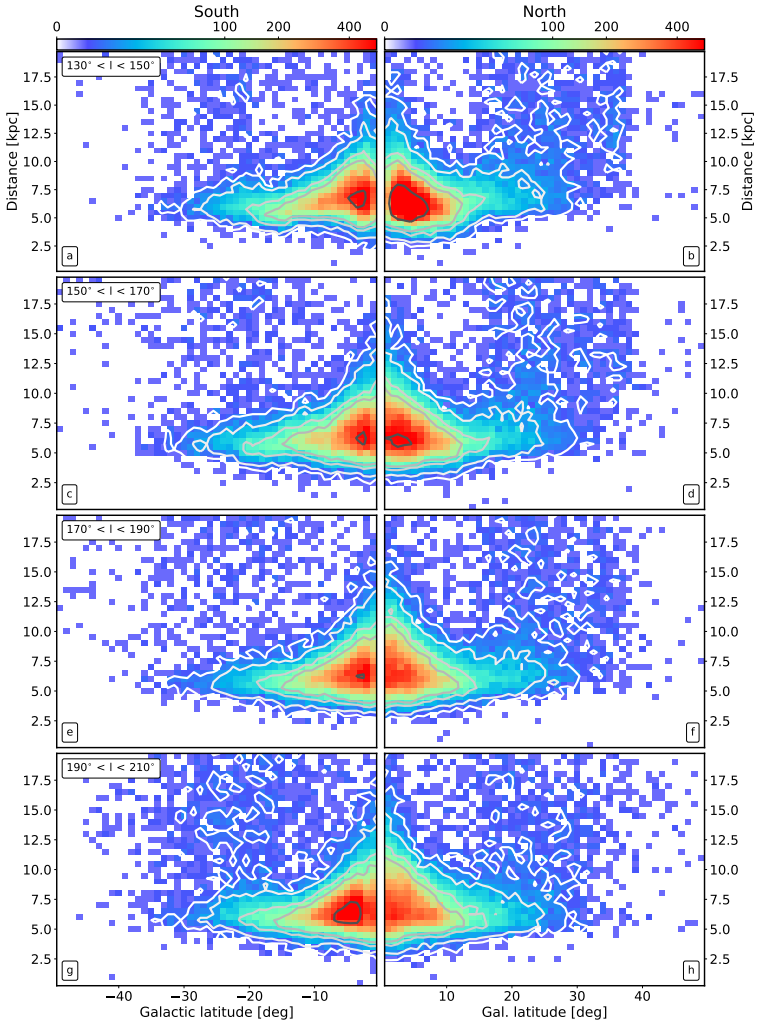

Figure 28: Distance from StarHorse as a function of Galactic latitude for different slices in Galactic longitude, only for the Giants stars within the peak. From top to bottom, $130° < l < 150°$, $150° < l < 170°$, $170° < l < 190°$, and $190° < l < 210°$.

disc extending much farther away, we note a clear excess of stars in the data at latitudes larger than 20° and at a distance of >7 kpc. We associate these to Monoceros and ACS. In the first row, in the range of longitudes where ACS is more intense, we see it clearly separated from Monoceros and slightly farther away. As we shift our view towards the third Galactic quadrant, these structures recede, becoming less prominent and shifting to lower latitudes (as we showed above). Monoceros covers a large range of latitudes and connects smoothly with the disc, but the lack of stars and the uncertainties prevent us from determining if there is a distance gradient with latitude or not.

The south does not show the same structures as the north but we note that, at least for panels c and e, the extinction is higher than in the north, which could block our line of sight. We note that we do not recover the structure detected in panel a of Fig. 25, probably due to low statistics. However, we do observe an increase of stars in panel g in the form of a diffuse distribution of distant stars at latitudes between -20° and -30°, coinciding with the location of the structure S200-24-19.8 reported in Newberg et al. (2002) and also the detection by Xu et al. (2015) that they associate with TriAnd (a different feature than the one discussed above and farther from the Sun, c.f. their Fig. 12).

3.5 DISCUSSION

The advantage of the methodology presented here is that we can trace the substructure in the MW using only their kinematics, that is, without having to do any selection by population or binning (other than the HEALpix). We have been able to reveal a clear arch-like shape for both Monoceros and ACS, tracing them in a continuous manner from $l \sim 120°$ to $l \sim 230°$ (Fig. 22). Not only that but we have also measured the kinematics of the structure using the changes in the proper motion of the peaks, which reduce the noise introduced by the measurement uncertainties, and tagged the stars that fall within said peaks, which can be used to generate a list of candidate members to Monoceros and ACS.

Although the recent works seem to favour a disc origin for these structures, this is still debated and the alternative, that they are the tidal debris of an accreted satellite, is not entirely ruled out. Based solely on the morphology that our method allows to observe, both Monoceros and ACS could very well be different wraps of the same tidal stream. If that was the case then we should be able to see at least a hint of continuity in the south, unless the tails only emerges from behind the disc at Galactic longitudes where the disc is already too dense for our method to detect them. Peñarrubia et al. (2005) presented an N-body model fitted to the observations of Monoceros available at the time, which was later used by Slater et al. (2014) to show

that there is a broad agreement with the PanSTARRS-1 (Chambers et al., 2016) data. We find that the arch described by the debris generated with their model is too wide to explain Monoceros but we note the presence of a tail (top right panel of Fig. 5 from Slater et al. 2014) that resembles ACS. Comparing the morphology now with the model of Laporte et al. (2019a)[13], where these "feathers" appear as a result of the interaction with Sgr, we note that the overall agreement is good (top left panel of their Fig. 1). For instance, the difference in latitude between the two structures and the fact that the one on top stops abruptly at a given longitude. Nonetheless, the "feather" corresponding to ACS obtained with their N-body simulations is thicker than the observed one and does not present a higher density of stars close to the turning point of the vertical oscillation (the highest point in latitude) as we see in the data. The fact that we observe a pile-up of stars at the turn-about is somewhat expected, and the sudden decrease that we observe afterwards is coherent with the simulations of Laporte et al. (2019a). In the case of an accreted satellite, though, this would require a large distance gradient to explain why we suddenly stop detecting it. Therefore, based on the shape that we observe for Monoceros and ACS, we favour a perturbative origin for these structures in spite of the fact that we are not able to fully discard the extragalactic origin (either with one or two progenitors).

When we explore the kinematic information obtained with the proper motion of the peaks, we see that these structures rotate slightly slower than the disc, in agreement with de Boer et al. (2018). Nevertheless, this alone does not probe that these structures were once part of the disc. The other option is to study their chemistry. Laporte et al. (2020) used the cross-match between *Gaia* and APOGEE (Majewski et al., 2017) to locate a few stars in the magnesium abundance versus metallicity plane. Again, their location in this plane is not entirely decisive as they fall at the low-metallicity tip of the chemical thin disc, where one expects the stars at the outskirts of the Galaxy to be (Hayden et al., 2015), but also where some metal rich dwarf spheroidal might be found. Nevertheless, the abundance ratios of elements like oxygen or sodium expected for such dwarf galaxies does not match with the measurements (Bergemann et al., 2018, , where their A13 seems to corresponds to our ACS). Confirming that the stars that form Monoceros and ACS were born in the disc is of great relevance since we can use them as chemical fossils. After they were kicked out of the disc, the stellar formation most likely came to a halt as any gas that initially accompanied the stars quickly settled back to the disc thanks to the efficient dissipation of energy. As a result, their current population became a frozen relic of the outskirts of the MW at the time when

13 We tried to compare also with the model of Kazantzidis et al. (2008, , Fig. 5) and Gómez et al. (2016, , Fig. 4) but there are too few particles to make a good assessment given the level of detail that the data is providing.

the perturbation occurred. If we had spectroscopic abundances for a large sample of stars belonging to these structures, for which our list of peak stars can be used an input catalogue, we could learn about the gas that dwelled at the edge of our Galaxy some Gigayears ago and use that information to constrain the chemo-dynamical models of the MW.

With all the information provided in this work it is now possible to fit an orbital model with precision using, for instance, the equations provided in Laporte et al. (2019a), or the method described in Peñarrubia et al. (2005). Such exercise is crucial as it would allow us to predict where the continuation of these structures should appear, both in Galactic coordinates as well as in distance, providing a way to search for them actively. Also, it would provide a quantitative characterisation of the orbits composing these structures, which can be used to compare models and, in the case of the perturbative one, quantify the mass of the perturber and the time of impact. Going one step further, as mentioned in Laporte et al. (2019a), by analysing the frequencies of the orbits we could even constrain the Galactic potential: the rotation curve at this distances, its slope, the shape of the Dark Matter halo, etc.

Another option to compare models is to add by hand simulated particles to a mock catalogue of the Galaxy. In this work we have used the Rybizki et al. (2018) catalogue which we now know that it was not so representative of the MW and, also, underestimated the observational errors (Rybizki et al., 2020). Nevertheless, the recent Rybizki et al. (2020) catalogue has fixed much of these issues and provides a great mock catalogue to use with the up-coming *Gaia* EDR3 (Brown, 2019). By adding particles generated with N-body models that can reproduce the observed Monoceros and ACS, we can improve our comparisons (e.g., Fig. 26), taking into account the nuances of our methodology, and attempt a quantitative comparison of the different mechanisms proposed. One of the key parameters here would be the stellar mass contained inside these structures, which is currently poorly measured. We have attempted to quantify the fraction of the disc that is within Monoceros and ACS in Fig. 24, yet it is not sufficient. A throughout study of their CMDs is necessary to obtain a reliable estimate that can be used in a forward modelling of the anticentre.

3.6 CONCLUSIONS

The application of the WT to the proper motion space has proven extremely useful to reveal the kinematic substructure of the halo. By removing most of the foreground with a naive cut in parallax, our method is able to efficiently detect kinematic substructure in the halo and detect external galaxies like M33 and the Magellanic clouds, several Dwarf spheroidals and dozens of Globular clusters, as well as

the Sgr stream. It has also revealed the sharpest picture of the anti-centre, with Monoceros and ACS appearing as the third most prominent structures in the distant sky (after the Magellanic clouds and Sgr), and containing a significant fraction of the Giant stars in the regions of the sky that they occupy.

We have been able to blindly detect the whole Monoceros north as well as the ACS from $l \sim 120°$ to $l \sim 230°$. Our findings are in good agreement with previous studies like Laporte et al. (2020), who also used DR2 data to investigate these structures. Nevertheless, we have been able to characterise their morphology with great detail, which is crucial for obtaining the orbital parameters of these groups of stars. We observe Monoceros with a clear arch-like shape, broader at small longitudes and becoming thinner towards larger longitudes. While we note a hint of substructure within Monoceros, a detailed study of the selection function and the extinction is needed to confirm that is not an artefact. ACS remains always on top of Monoceros and has a maximum of relative intensity when it reaches the highest latitude at $l \sim 140°$ (consistent with a pile up of stars at the maximum height in the orbit), and stops abruptly at a longitudes of $\sim 110°$. This behaviour, added to the fact that we do not observe a clear continuity in the south, favours the perturbative scenario proposed by Ibata et al. (2003), later supported by the simulations of many other authors (Kazantzidis et al., 2008; Gómez et al., 2016; Laporte et al., 2019a, e.g.,). Moreover, the kinematics of these features, which differ from the bulk motion of the disc stars that lay in front, are compatible with a low eccentricity orbit at ~10 kpc that rotates similarly to the disc (probably slower).

By analysing the apparent magnitude of the RC stars selected by proper motion we have been able to trace Monoceros down to a latitude of ~5°, closer to the disc than ever before. Also, by measuring the median apparent magnitude of the RC stars of each structure and converting to Heliocentric distance, we have determined that ACS (~11.7 kpc) is roughly 1 kpc farther away from the Sun the Monoceros (~10.6 kpc). This actually means that both structures are at roughly the same Galactocentric radius (but at heights above the disc of, respectively, ~6.5 kpc and ~4.5 kpc). Also, we have shown that Monoceros and ACS, despite being different structures, are extended in distance and in the sky, and their tails overlap both in the 3D physical space as well as in kinematic space.

In the south, for the range of longitudes explored, the dominant structure in proper motion belongs to the disc. Still, we have found a diffuse population of Giants at $130° < l < 150°$ and $190° < l < 210°$, coinciding with the regions of low extinction, that we do not observe in the mock catalogue nor in the north. Their apparent magnitudes span the range $14 < G < 15.5$ mag which implies distances for a RC star (not affected by extinction) between 5 and 10 kpc. These could be

related with the vertical wave described in Xu et al. (2015). On the other hand, in the longitude range $130^\circ < l < 150^\circ$ we have observed a faint trace of RC that matches the position of the detection by Ibata et al. (2003) of a population similar to Monoceros. Nevertheless, we do not observe a clear morphological connection between this structure and Monoceros north.

The data that we have obtained, being precise, continuous and covering a large range of longitudes, can be used for describing Monoceros and ACS with analytical/semi-analytical models and compare the goodness of fit of the different hypothesis available in the literature. For the "accreted satellite" model, one would obtain the mass of the satellite and a prediction of the current location of the progenitor (Peñarrubia et al., 2005). For the "Sgr interacting with the disc" model, one can use our data to estimate the mass of this satellite and constrain the time of its pericentre passages (Laporte et al., 2019a), as well as study the chemical composition of the stars that form Monoceros and ACS to constrain the chemo-dynamical models of our Galaxy (since in this scenario, both structures would be chemical fossils representative of the composition of the outer disc in the past). In both cases, a measure of the natural frequencies of the MW at large Galactocentric radii are obtained.

Studies like this will benefit the most from the next *Gaia* release (EDR3) which is expected to reduce the proper motion uncertainties on average by half, and increase the number of stars at the faintest magnitudes. As a result, the structures that we detect will become more concentrated in the proper motion space, and will produce stronger signals in our maps of relative intensity. This means that we will be able to trace them more clearly and deeper, and obtain less contaminated samples with which we can examine their CMDs, and other properties, for structures like Monoceros and ACS.

APPENDIX

A *Reddening to absorption transformations*

The reddening maps provided by Schlafly & Finkbeiner (2011) return a value of the colour excess, E(B-V), for each pair of celestial coordinates. To obtain the absorption we then assume a proportionality constant, R_V, of 3.1 (Cardelli et al., 1989). However, this yields the absorption in the V-band, A_V, and so we still need a conversion to the absorption in the G-band, A_G. For that, we use a fitted relationship between the ratio $\frac{A_G}{A_V}$ and the *Gaia* photometry (see Fig. 29).

The $\frac{A_G}{A_V}$ ratio is fitted against the $G_{BP} - G_{RP}$ colour using simulations derived from BaSeL-3.1 (Westera et al., 2002) spectral energy distributions using the same methodology as in Jordi et al. (2010).

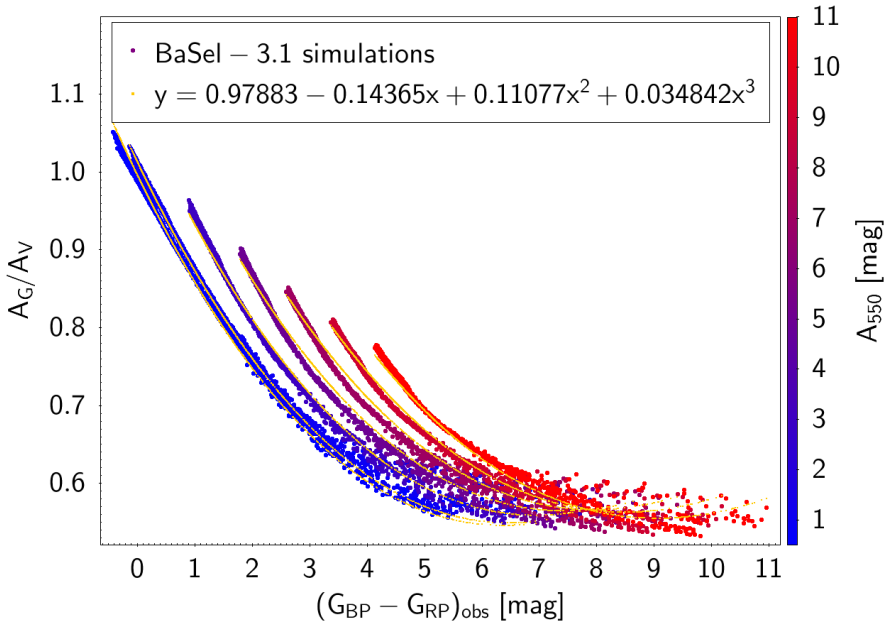

Figure 29: Fitted relationship between $\frac{A_G}{A_V}$ and the observed $G_{BP} - G_{RP}$ colour (affected by reddening) derived from simulations using BaSeL-3.1 synthetic spectral energy distributions (Westera et al., 2002) and *Gaia* DR2 passbands from Maíz Apellániz & Weiler (2018)

We used the *Gaia* passbands derived by Maíz Apellániz & Weiler (2018) as according to the *Gaia* team[14] they are more representative of the *Gaia* DR2 data. Among the two BP passbands provided in Maíz Apellániz & Weiler (2018) we chose the one that is valid at the faint regime ($G > 10.87$ mag) which is appropriate for a distant object like ones studied in this work. Nevertheless, only very small differences are present when considering the passband at the bright regime. For the Johnson V passbands, we used the response curve provided by Bessell & Murphy (2012).

To simulate reddened sources in the range $0 < A_{550} = 11$ mag, we use the Cardelli et al. (1989) extinction law and $R_V = 3.1$, A_{550} being the magnitude of the extinction at a wavelength equal to 550 nm.

To achieve a better fitting on $\frac{A_G}{A_V}$ we consider a second-degree dependency with the reddened $G_{BP} - G_{RP}$ colour (the observed one) plus two terms depending on the interstellar absorption in the V passband (A_V) as well as a crossed term. The obtained relationship is the following:

$$\begin{aligned} \frac{A_G}{A_V} &= 0.97883 - 0.14365\,(G_{BP} - G_{RP})_{obs} \\ &+ 0.011077\,(G_{BP} - G_{RP})^2_{obs} + 0.034842\,A_V \\ &- 0.0041448\,A_V \cdot (G_{BP} - G_{RP})_{obs}. \end{aligned} \tag{4}$$

14 https://www.cosmos.esa.int/web/gaia/dr2-known-issues

B *Queries to the Gaia archive*

To obtain the mean quantities used in this work all around the sky and in a single file, we use the following query to the *Gaia* Archive:

```
SELECT gaia_healpix_index(5, source_id) AS
   healpix_5, count(*) as N, avg(astrometric_n_
   good_obs_al) AS avg_n_good_al, avg(astrometric
   _gof_al) AS avg_gof_al, avg(astrometric_excess
   _noise) as, avg_excess_noise, avg(bp_rp) as
   avg_bprp, avg(phot_g_mean_mag) as avg_g, avg(
   pmra) as avg_pmra, avg(pmdec) as avg_pmdec,
   avg(pmra_error) as avg_pmra_error, avg(pmdec_
   error) as avg_pmdec_error
FROM gaiadr2.gaia_source WHERE parallax-parallax_
   error < 0.1 AND BP_RP>0.2 GROUP BY healpix_5
```

Computing the standard deviations is not so straight forward, though, as there is no implemented function to do so in ADQL. Instead, we repeat the same query but this time using the average *squared* of the quantities. A simple subtraction of both tables returns the standard deviations:

$$\sigma = \sqrt{E[X^2] - (E[X])^2} \tag{5}$$

where $E[X]$ is the mean of a vector X.

Figures 30 and 31 contain, respectively, the average proper motion and its dispersion for both components, right ascension and declination. With the mean proper motions we basically see a kinematic field dominated by the combination of the solar peculiar motion and the rotation of the Galaxy. Given the large amount of nearby stars that our filter (Eq. 1) cannot remove, only the very dense structures can be seen here: the Magellanic clouds, some Globular clusters and, although very faint, the Sgr stream. To understand better the extent of the disc in our sample, we use the relation between the kinematic dispersion and the kinetic temperature of each population (disc vs halo). We note a transition at $\sim 30^\circ$ in latitude from a rather cold population (disc) to a hotter one (halo). The oscillations with Galactic longitude, being different for each component of the proper motion, are most likely related to the singularity introduced by the apex and antapex of the Solar motion.

C *Gaia DR2 mock catalogue*

We query the Rybizki et al. (2018) catalogue and download, for each HEALpix, up to 2 000 000 stars. Among the quantities available to download, we select all the astrometry and photometry, as well as the age of the stars which we then use to separate the stars in thin

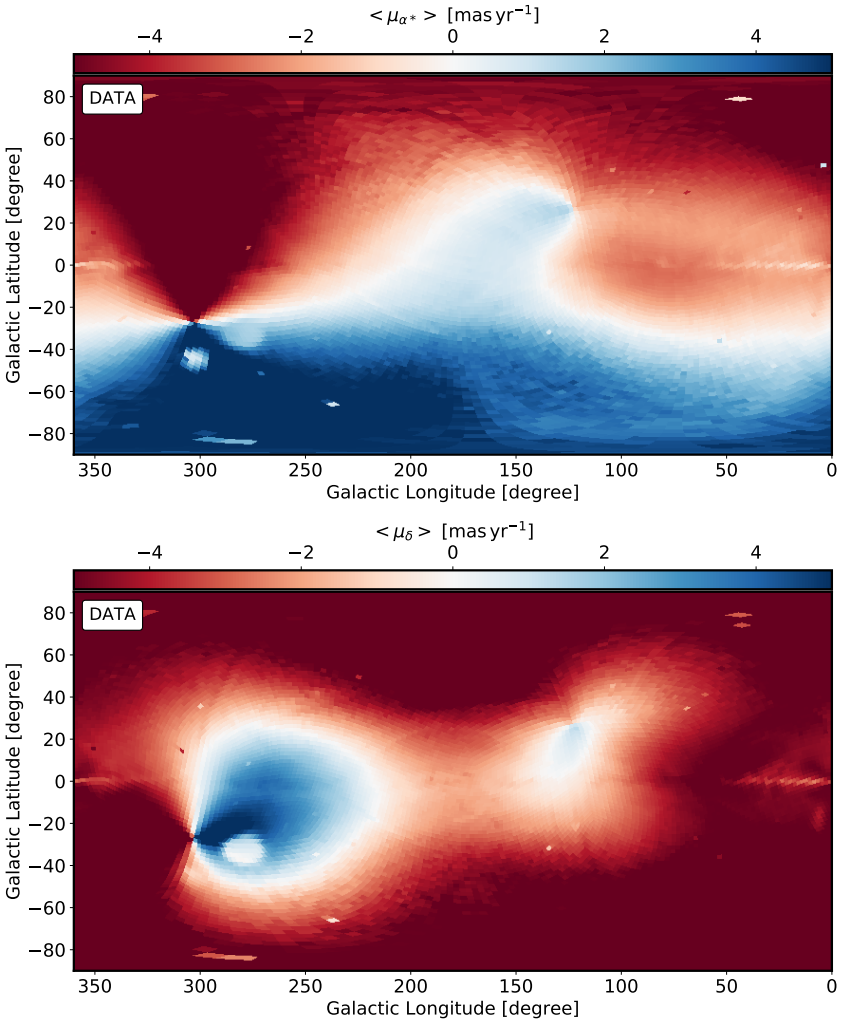

Figure 30: Average proper motion of the stars selected according to the criteria set in Sect. 3.2 as a function of position in the sky. Top: Proper motion in right ascension. Bottom: Same but in declination. Only a few Globular clusters and the Large Magellanic cloud are noticeable, as the rest of the field is dominated by the solar reflex (peculiar motion of the Sun and rotation of the local standard of rest (LSR)).

disc, thick disc and halo. Then, we draw for each star one realisation from a normal distribution centred on the true values and with a dispersion equal to the provided observational uncertainties to produce the mock particles. In the case of the colours, we apply the errors to the fluxes and then convert the observed fluxes to magnitudes using the equations published in the *Gaia* web-page[15] (Maíz Apellániz & Weiler, 2018). We note that these are meant to be used with synthetic fluxes derived using the same pass-bands, which is not the case here, but since we only use the photometry for reference (the cut in colour has little impact), we do not need a perfect match with reality.

15 https://www.cosmos.esa.int/web/gaia/dr2-known-issues

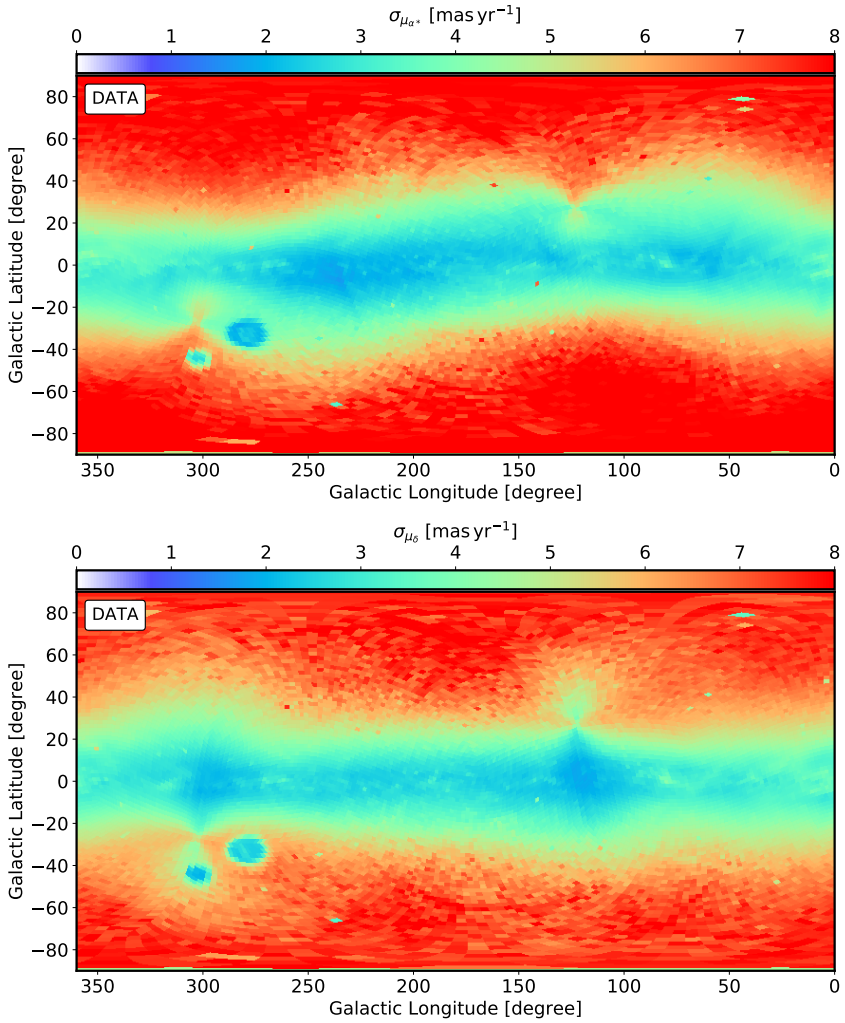

Figure 31: Dispersion in proper motion of the stars selected according to the criteria set in Sect. 3.2 as a function of position in the sky. Top: Proper motion in right ascension. Bottom: Same but in declination.

Once we have the mock particles, we apply the cuts in parallax and colour described in Sect. 3.2, generate the proper motion histograms and analyse them with the WT in the same manner as we did for the data (Sect. 3.2.2). The value of the WT coefficient is sensitive to the absolute number of counts and, in consequence, we scale the histograms such that the sum of all the bins equals the number of stars observed in that same HEALpix with *Gaia*. No substructure is added in this way since a scaling of the histogram does not bias the centroid and, whenever we show the coefficients we do it after normalising by the number of stars in the HEALpix.

Figure 32 shows the result of applying our methodology to the mock catalogue. The only structure present is the geometrical warp introduced in the underlying model of the galaxy. Apart from that, we note a sharp transition between the disc and the halo, noticeable

as a drastic change in the relative intensity. There is also a change between the thin disc that dominates the anticentre, and the thick disc that dominates the central parts of the mock MW. If we analyse the proper motions of the peaks obtained (Fig. 33) we recover the reflex of the solar motion, with the location of the appex and antapex clearly visible as singular points, and the perspective effect caused by the rotation, which introduces a gradient in the proper motions with Galatic longitude and latitude. This is the reason why the transition to the halo is so sharp: once the dominant structure in the proper motion plane is the halo, we observe the reflex of a non-rotating stellar system which only has 4 lobes instead of 8 as in the case of the disc.

In some of the figures, e.g. Figs 23 or 34, we select the particles not according to the peak obtained with the mock but with coordinates of the peaks detected in the data. In doing so we can check what is distribution in the CMD or in distance of the particles that have the observed kinematics.

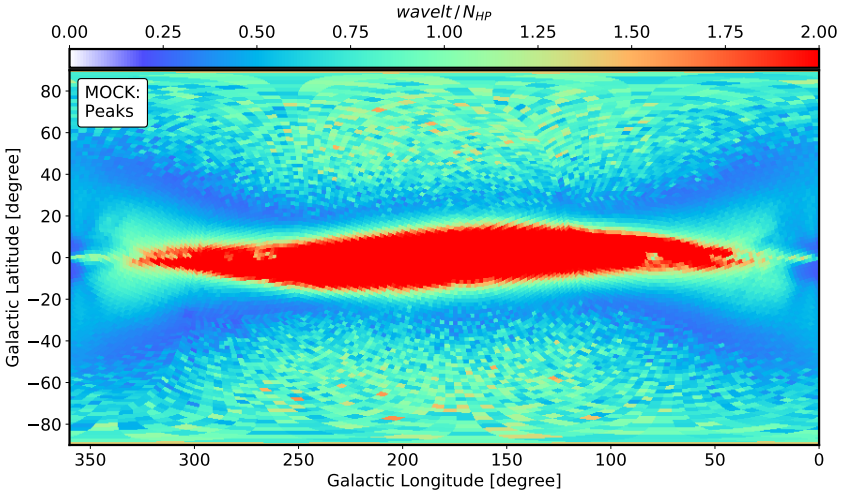

Figure 32: Relative intensity of the dominant structure in the proper motion plane of each HEALpix for the mock catalogue.

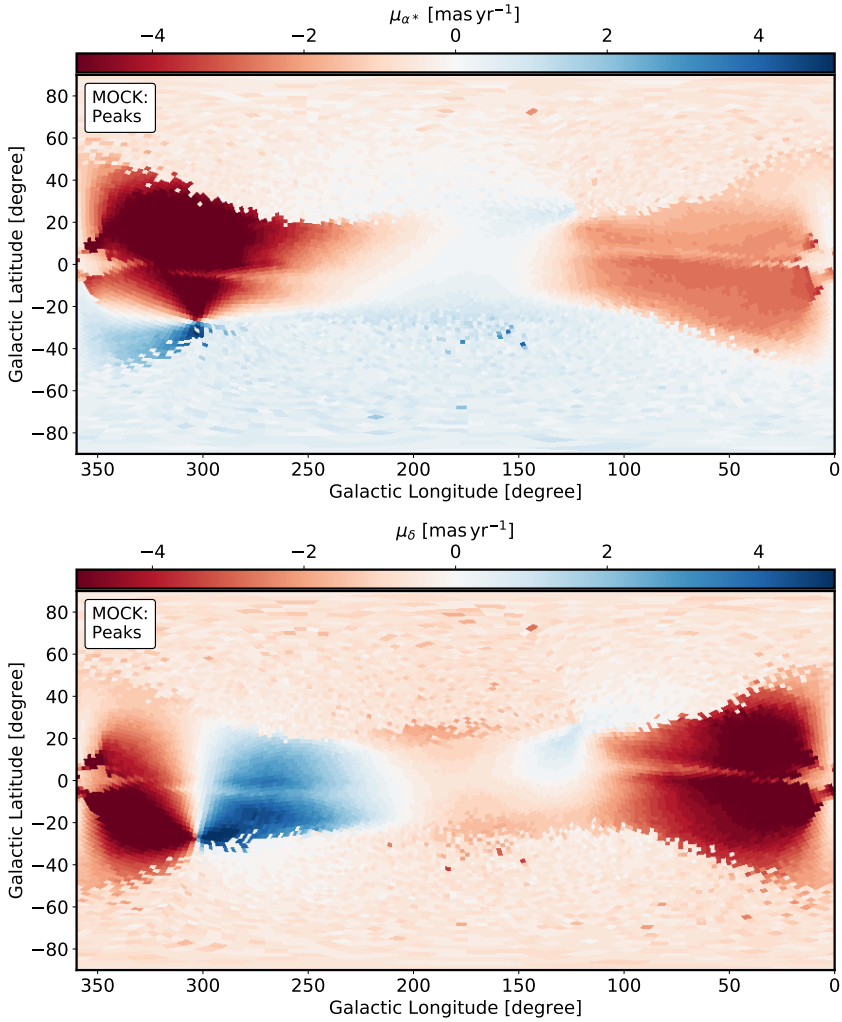

Figure 33: Same as Fig. 21 but for the mock.

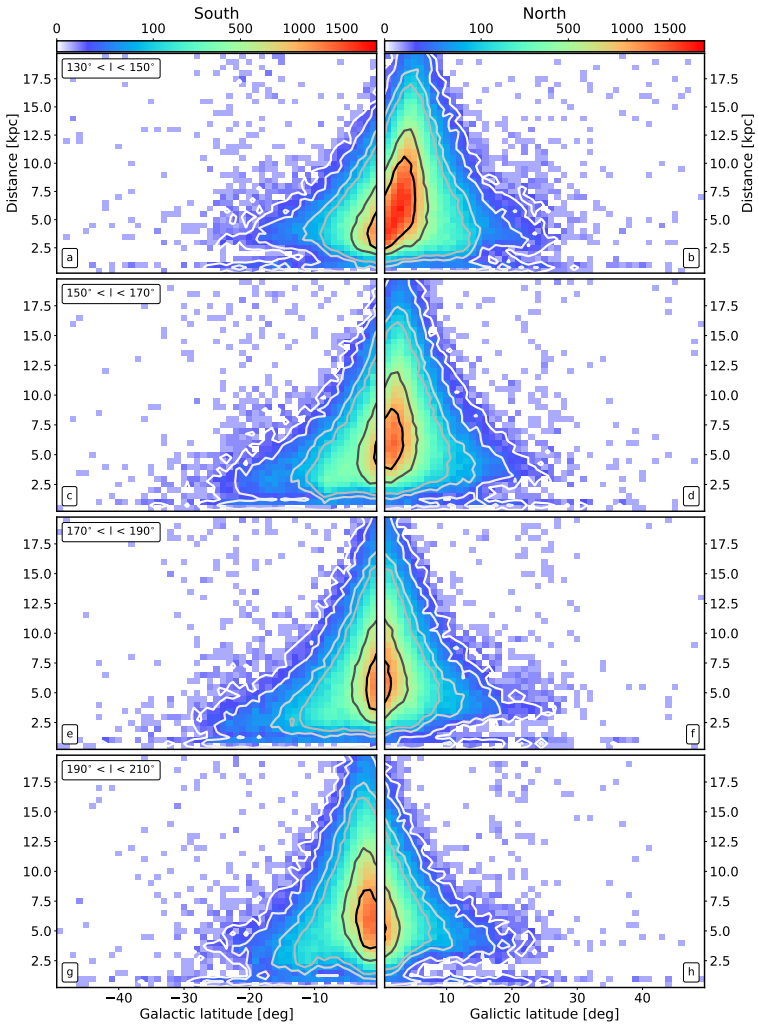

Figure 34: Same as Fig. 28 but for the particles in the mock catalogue that fall inside the peaks detected in the data.

DETECTION OF THE SAGITTARIUS STREAM USING PROPER MOTIONS

4

Abstract

Context: We aim to measure the proper motion along the Sagittarius stream, which is the missing piece in determining its full 6D phase space coordinates.

Aims: We conduct a blind search of over-densities in proper motion from the *Gaia* second data release (DR2) in a broad region around the Sagittarius stream by applying wavelet transform techniques.

Methods: We conduct a blind search of over-densities in proper motion from the *Gaia* second data release (DR2) in a broad region around the Sagittarius stream by applying wavelet transform techniques.

Results: We find that for most of the sky patches, the highest intensity peaks delineate the path of the Sagittarius stream. The 1500 peaks identified depict a continuous sequence spanning almost 2π in the sky, only obscured when the stream crosses the Galactic disk. Altogether, around 100 000 stars potentially belong to the stream as indicated by a coarse inspection of the color-magnitude diagrams. From these stars, we determine the proper motion along the Sagittarius stream, making it the proper-motion sequence with the largest span and continuity ever measured for a stream. A first comparison with existing N-body models of the stream reveals some discrepancies, especially near the pericenter of the trailing arm and an underestimation of the total proper motion for the leading arm.

Conclusions: Our study provides a starting point for determining the variation of the population of stars along the stream, the distance to the stream from the red clump stars, and the solar motion. It also permits much more accurate measurement of the Milky Way potential.

This chapter has been published as: T. Antoja, P. Ramos, C. Mateu, et al. 2020, A&A, 635, L3

4.1 INTRODUCTION

Research into tidal streams in the Milky Way (MW) has already benefited immensely from the *Gaia* mission (Gaia Collaboration et al., 2016b). The outstanding and precise proper motions of the second data release (DR2, Gaia Collaboration et al., 2018b) fostered the discovery of many new streams, both with known (Ibata et al., 2019; Palau & Miralda-Escudé, 2019) and unknown (Ibata et al., 2018; Malhan & Ibata, 2018; Malhan et al., 2018b) progenitors, and mapping over larger portions of the sky (Price-Whelan & Bonaca, 2018; Koposov et al., 2019). *Gaia* has also been crucial for the detection of peculiarities in streams, such as diffuse components and gaps, which could provide information about the structure of the progenitor and of the MW halo, and about the dark subhalos that could have interacted with the stream stars (e.g., Bonaca et al., 2019b; Malhan et al., 2018a, 2019; Bonaca et al., 2019a; Price-Whelan & Bonaca, 2018). The *Gaia* DR2 has also revealed evidence of misaligned proper motions, which seem to be a telltale sign of the gravitational effects of other MW massive satellites (Koposov et al., 2019; Erkal et al., 2019; Shipp et al., 2019).

The stream of the Sagittarius dwarf (Sgr, Ibata et al. 1994) discovered by e.g. Mateo et al. (1996) and Totten & Irwin (1998) is the most prominent stream in the MW halo and has served in multiple studies as a prototype of ongoing tidal disruption and hierarchical formation of the Galaxy, and to constrain the MW potential (Law & Majewski, 2016, and references therein). Nevertheless, reproducing the spatial structure simultaneously with the radial velocities remains a challenge. No single model has succeeded in reproducing all observational data, with the best so far being the triaxial halo by Law & Majewski (2010b, hereafter LM10) and Deg & Widrow (2013), which takes the form of a nearly oblate halo but with a minor axis oriented along the Galactic plane. This configuration is infrequent in **LCDM!** (LCDM!) and is dynamically unstable, but might be avoided by considering the effect of the Large Magellanic Cloud (Vera-Ciro & Helmi, 2013) or a rising MW rotation curve (Ibata et al., 2013). Even so, none of these models can account for other features of the Sgr stream like the bifurcations (Belokurov et al., 2006; Koposov et al., 2012) and substructure near the apocentres (Sesar et al., 2017b). However, the modelling efforts (Fellhauer et al., 2006; Peñarrubia et al., 2010; Dierickx & Loeb, 2017) that have managed to reproduce these still suffer from the radial velocity miss-match in the leading arm.

A precise measurement of the proper motion along the Sgr stream could be the observational piece that is missing to solve these long-standing puzzles. So far, determinations of the Sgr proper motion have been very limited: they have only been obtained in small patches along the stream and are based on a small number of selected mem-

ber stars (Carlin et al., 2012; Koposov et al., 2013; Sohn et al., 2015, 2016). Recently, Li et al. (2019) measured the proper motion of 164 stars from the Large Sky Area Multi-Object Fiber Spectroscopic Telescope (LAMOST) survey (Cui et al., 2012) along the trailing and leading arms with *Gaia* DR2. Yang et al. (2019) detected substructure with a few hundred members related mostly to the leading arm of the stream in a sample of LAMOST stars with proper motions from *Gaia* DR2.

Here we determine the proper motion along the Sgr stream using a completely different approach. We use *Gaia* DR2 astrometry and wavelet transformation (WT) techniques to conduct a blind detection of over-densities in the proper-motion plane for regions selected broadly in the plane of the stream (Sect. 4.2). We find, in an unforeseen way, that Sgr accounts for the peak of highest intensity in most of the probed fields (Sect. 4.3). From this we measure the continuous proper motion along the path of the stream (Sect. 4.4). By selecting all stars associated to the detected peaks, we explore their *Gaia* colour-magnitude diagram (CMD) and reconstruct the largest sample of candidate members of the Sgr stream (Sect. 4.5). We discuss the many avenues opened by our findings in Sect. 4.6.

4.2 DATA AND METHODS

We select stars from *Gaia* DR2 (Gaia Collaboration et al., 2018b) with parallax satisfying $\varpi - \sigma_\varpi < 0.1\,\mathrm{mas}$ and $\mathrm{BP} - \mathrm{RP} > 0.2\,\mathrm{mag}$. The first cut ensures that we keep stars farther than 10 kpc given their uncertainties and discards most of the foreground. The second cut eliminates blue foreground main sequence stars, while only removing a small fraction of blue horizontal branch stars.

We then look for over-densities in the proper motion covering the whole sky by applying a peak-detection algorithm in the proper-motion plane $(\mu_{\alpha*}, \mu_\delta)$ of each *Gaia* HEALpix of level 5. The peak detection algorithm is a simplified version of the method presented in Antoja et al. (2015) based on the WT, as we described earlier in Sect. 3.2.2. In summary, for the proper-motion plane of each HEALpix, the algorithm finds peaks and determines their proper-motion coordinates, their significance, their width or scale, their intensity or height, and the number of stars that belong to the peak. The algorithm detects peaks of a set of discrete widths, which are referred to as scales. Here we explore three logarithmically spaced scales in proper motion of 0.48, 0.96, and 1.92 $\mathrm{mas\,yr^{-1}}$, that we denote 1, 2, and 3. The peak associated to the Sgr stream is often detected at more than one scale in each HEALpix (see Fig. 18). However, the peak will have highest relative intensity at the scale that is closer to its actual size (typically, for Sgr, this occurs at scale 1, that is 0.48 $\mathrm{mas\,yr^{-1}}$). We select only the peaks with the highest relative intensity for each

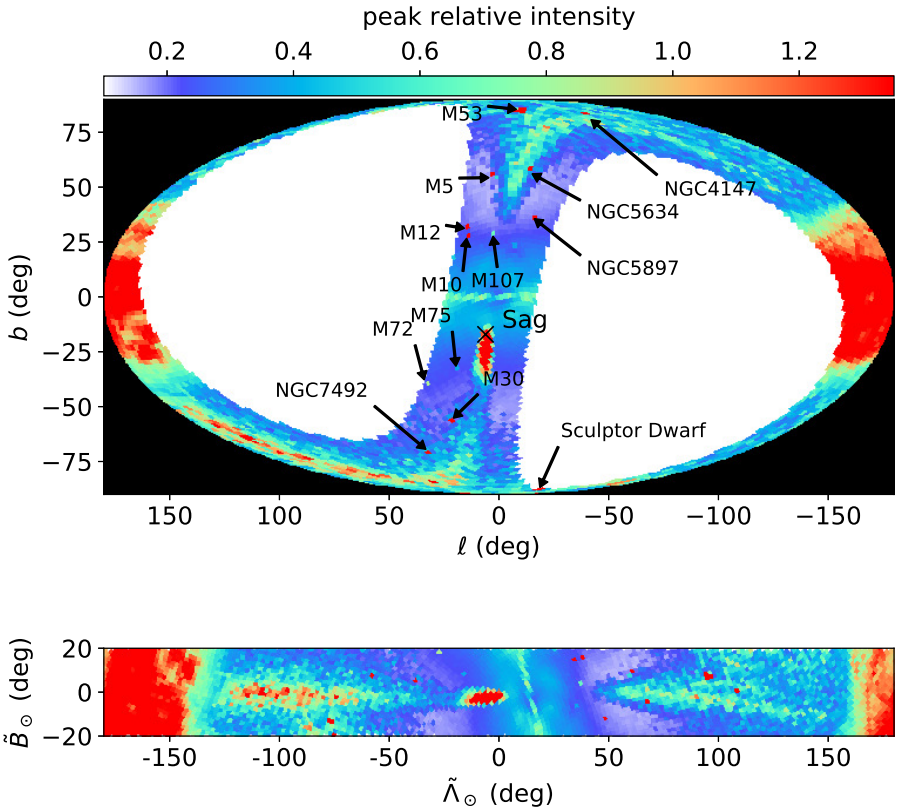

Figure 35: All sky view of the Sgr stream with Gaia data in Galactic coordinates (*top*) and in the coordinates of the orbital plane of Sgr (*bottom*). These HEALpix maps are coloured according to the relative intensity of the most prominent peak detected in the corresponding HEALpix(see text). Known objects such as globular clusters and dwarf galaxies show high relative intensities in their corresponding HEALpix and are marked with arrows. The location of the Sgr dwarf is shown with a black cross with position taken from Karachentsev et al. 2004.

HEALpix, which naturally removes redundant peaks. Finally, we select only the peaks with significance $\geqslant 3$ and we keep only the ones with the highest relative intensity in each HEALpix, that is, the peak with the largest height in each sky patch.

In several HEALpix, we found peaks at $(\mu_{\alpha*}, \mu_\delta) \approx (0, 0)$. These are triggered by quasars: in several regions of the sky, especially where the *Gaia* coverage has been larger (large `visibility_periods_used`), quasars are observed more easily and appear as concentrations of sources with almost zero proper motion.Those peaks have been removed by selecting only peaks with $\mu_{tot} \equiv \sqrt{\mu_{\alpha*}^2 + \mu_\delta^2} > 0.6$ mas yr^{-1}. Although this could be hindering the detection of the parts of the stream with small proper motions, most of these occur in areas that appear to be strongly contaminated by the foreground and would not have entered our selection (see Sect. 4.4). We also note that the LM10 model predicts very few stars ($< 2\%$) with $\mu_{tot} < 0.6$ mas yr^{-1}.

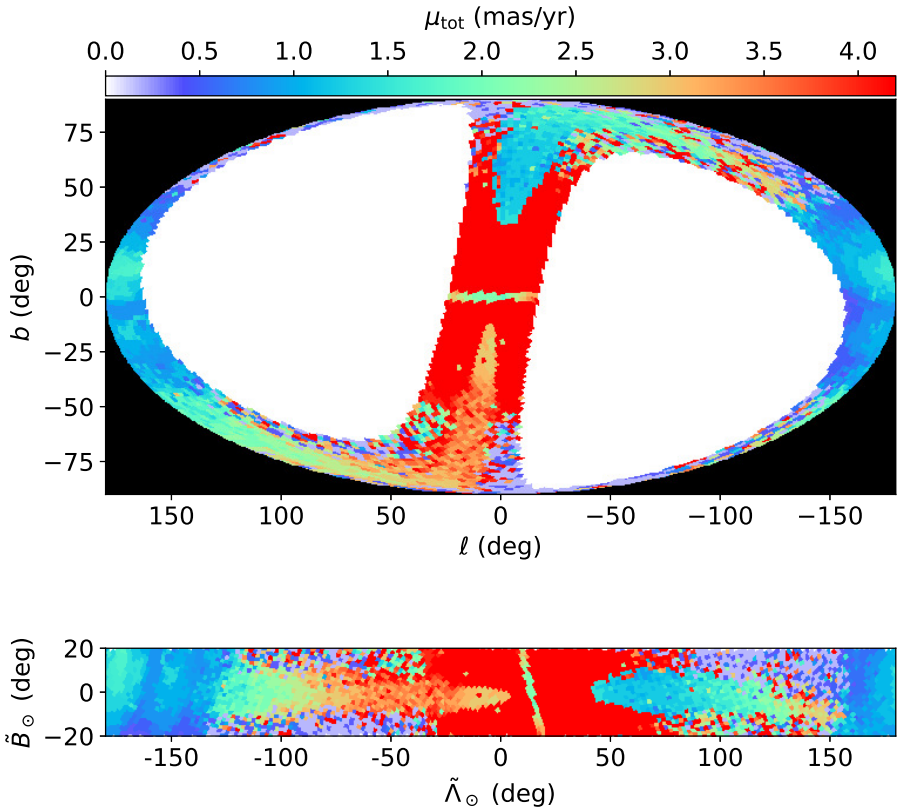

Figure 36: Same as Fig. 35 but coloured as a function of the total proper motion μ_{tot}. In all panels, the trace of the Sgr stream is clearly observed in an almost full circle on the sky, with the leading arm at positive Galactic latitude b (positive $\tilde{\Lambda}_\odot$) and the trailing at negative b (negative $\tilde{\Lambda}_\odot$).

4.3 A GAIA FULL SKY VISION OF THE SGR STREAM

Figures 35 and 36 show four HEALpix maps of our results. We plot only HEALpix fields with $|\tilde{B}_\odot| \leqslant 20°$, where $\tilde{B}_\odot$ is the latitude from the coordinate system of the Sgr stream $(\tilde{\Lambda}_\odot, \tilde{B}_\odot)$ defined in Majewski et al. (2003) with the orientation adopted in Belokurov et al. (2014). In the top-left panel, each HEALpix is coloured as a function of the relative intensity of the highest peak. This map clearly shows the stream emerging from the Sgr dwarf galaxy. The Sgr dwarf appears as a very strong concentration (red HEALpix) at approximately the centre of the map, marked with a black cross. The leading arm ($b > 0$) is seen in turquoise, while the trailing arm ($b < 0$), which has higher relative intensity, is seen in orange-red. This shows that in most of the sky around the Sgr stream the highest peak detected by our algorithm corresponds to the stream itself. Only where the stream crosses the Galactic plane, i.e., at $\ell \sim 0$ and $\sim 180°$, is another dominant structure apparent, which is probably related to the MW disk. We also see many other HEALpix with prominent peaks that correspond to known objects, mainly globular clusters and dwarf galaxies (some are indicated

with black arrows). Their detection corroborates the reliability of our method.

The HEALpix map in the top panel of Fig. 36 is coloured by total proper motion $\mu_{tot}$of the highest intensity peaks. Again, the Sgr stream appears as a river of HEALpix fields that gradually change their colour when moving from the Sgr dwarf towards the leading (blue-green colours) and trailing (orange-green colours) arms. This is the first all-sky view of the Sgr stream in proper motion ever produced.

In the bottom panels, the same HEALpix maps are shown but in the coordinates of the Sgr orbital plane as defined above. A clear bifurcation in the leading arm can be seen in the bottom-left panel from $\tilde{\Lambda}_\odot \approx 90°$ to $\approx 140°$, confirming that the discovery by Belokurov et al. (2006) is observed also with *Gaia* data. However, we do not see the bifurcation in the trailing arm (Koposov et al., 2012), nor do we a signature that the bright and faint parts of the leading arm have different proper motion (bottom right panel).

4.4 PROPER MOTION SEQUENCE OF THE SGR STREAM

The proper motion of the peaks with the highest intensity is shown in Fig. 37 as a function of $\tilde{\Lambda}_\odot$, only for $|\tilde{B}_\odot| \leqslant 10\,°$ instead of $|\tilde{B}_\odot| \leqslant 20\,°$ as in Fig. 35 in order to be more restrictive. Figure 37a shows the detected peaks in the planes of $\tilde{\Lambda}_\odot$-$\mu_{\ell*}$ (top), $\tilde{\Lambda}_\odot$-μ_b (middle), and $\tilde{\Lambda}_\odot$-μ_{tot}(bottom) colour coded by μ_b (top), by $\mu_{\ell*}$ (middle), and by the WT scale (bottom). Figure 37b is the same as Figure 37a but for the LM10 model of the Sgr stream, in which we have selected only particles that roughly correspond to the observed parts of the stream[1]. We note that the data panels show the peaks detected in proper-motion space (each one composed of hundreds to thousands of stars), while the panels for the model correspond to particles in the simulation. In the bottom panel of Figure 37b we colour-code them by distance to the Sun. Figure 37c shows a 2D histogram of the data peaks. We overplot the LM10 model with black curves obtained by computing the median proper motion in bins of $\tilde{\Lambda}_\odot$ and subsequently smoothing with a Gaussian filter. The data show a continuous sequence of proper motion along $\tilde{\Lambda}_\odot$ that strikingly resembles that of the LM10 model. We identify the first wrap of the trailing and leading arms of the Sgr stream. In addition, a few peaks seem to coincide with the expected position of the trailing arm at $\tilde{\Lambda}_\odot \approx 180°$. The continuity of the sequence is only broken where the stream crosses the Galactic disk and is hard to detect.

In the data, there is a set of peaks at $\tilde{\Lambda}_\odot \approx [-50, 50]°$ organised along a triangular shape in the top and bottom panels of Fig. 37a and Fig. 37c that do not belong to Sgr. An analysis of a *Gaia* mock

1 Particles in `http://faculty.virginia.edu/srm4n/Sgr/` with $P_{col} \leqslant 3$, i.e. that became unbound recently.

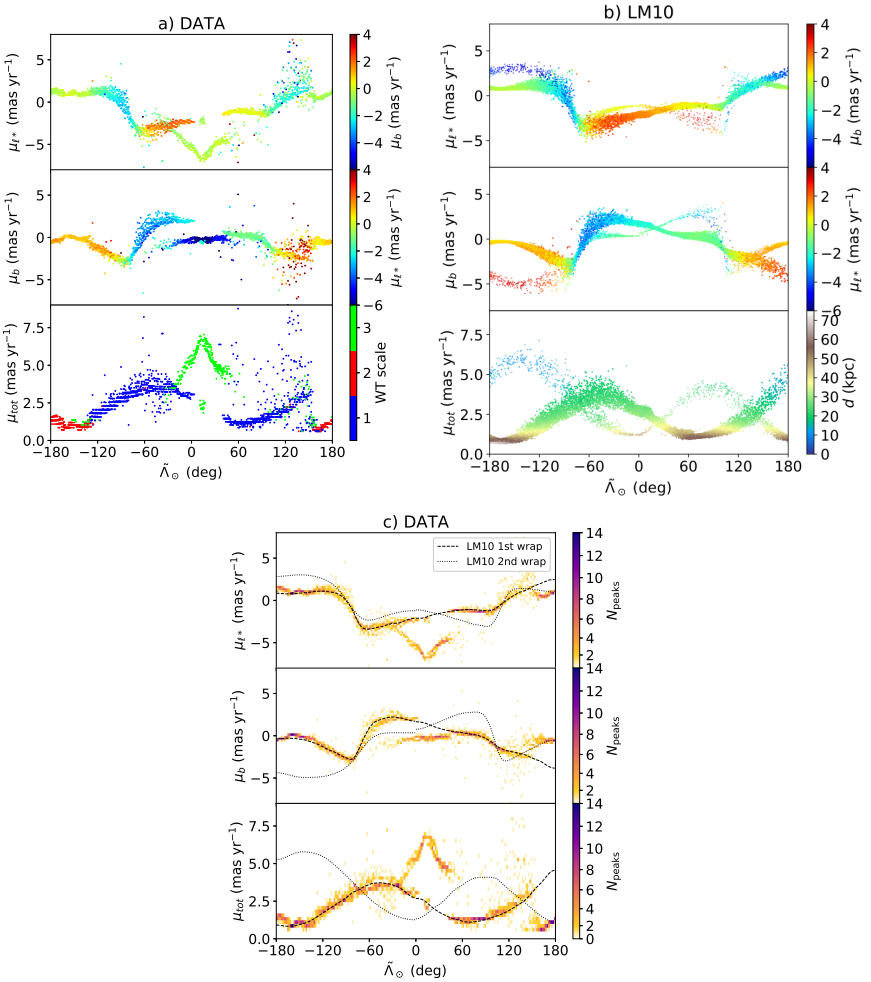

Figure 37: Proper motion of the Sgr stream from the *Gaia* data and comparison with the LM10 model. All panels show the proper motion in Galactic longitude in the top, in latitude in the middle, and total in the bottom, as a function of $\tilde{\Lambda}_\odot$. (a) Proper motions of the detected peaks colour coded by proper motion in latitude (top), in longitude (middle), and in WT scale (bottom). (b) Same but for the model and the bottom panel colored by distance to the Sun. The second wrap of the model has been given more transparency to enhance the contrast of the first wrap. (c) Same as (a) but represented by a 2D histogram with the trace of the model superposed in black dashed (first wrap) and dotted (second wrap) lines.

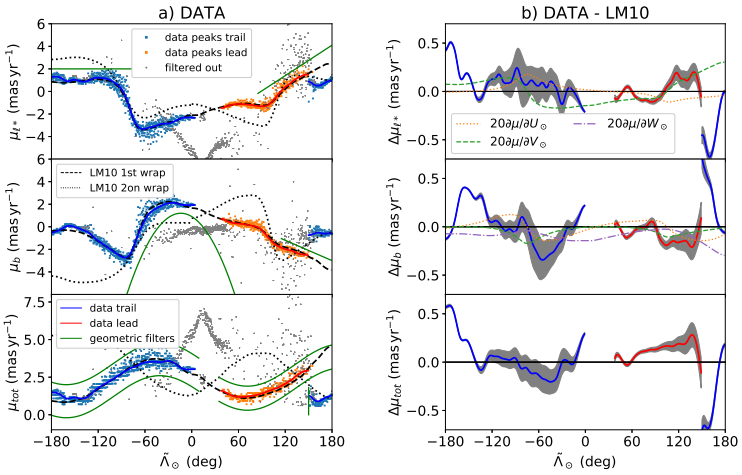

Figure 38: Proper motion of the Sgr stream from the *Gaia* data and comparison with the LM10 model (part 2). The top, middle, and bottom panels are organized as in Fig 37. (a) Proper motions of the peaks finally selected to belong to the Sgr stream colored with blue (trailing) and orange (leading). A smooth version of the median proper motion of the *Gaia* DR2 stars belonging to the detected peaks (see text) is shown in blue and red, together with the model in black. The green lines indicate the geometric filters that we apply to select the peaks that belong to the main sequences. (b) Differences in the median proper motions between data and model with the shaded areas indicating the statistical error. The rest of the curves indicate the values of a potential discrepancy due to an inappropriate assumption of the solar motion values in LM10 by 20 km s^{-1} (see text).

catalogue without the Sgr stream (Appendix A, Fig. 41) reveals a similar structure. We therefore conclude that this is caused by contamination from the stellar foreground. We filtered out these peaks by removing all peaks of scale 3 (green colours in the bottom panel of Fig. 37a). Additionally, we see peaks that fall outside the sequence around $\tilde{\Lambda}_\odot \approx 150°$. These do not appear in the mock catalogue but appear in an off-stream sky band selected in the range $15 < |\tilde{B}_\odot| \leqslant 20°$ (Appendix A, Fig. 42). Their origin at this point is not clear but we note that their location on the sky is similar to that of the Virgo overdensity and there is some overlap in proper motion according to the values reported by Yang et al. (2019).

For a more quantitative comparison between the data and the model, we refine the selection of peaks by applying simple geometric filters in the three planes ($\tilde{\Lambda}_\odot$-μ_{l*}, $\tilde{\Lambda}_\odot$-μ_b, $\tilde{\Lambda}_\odot$-μ_{tot}), intending only to remove peaks that are clearly off the proper-motion sequence. These filters are detailed in Appendix B and the region where peaks are selected is shown with green lines in Fig. 38a. We finally end up with 1540 peaks which are shown in blue and orange for the trailing and leading arms, respectively. We then retrieve from the *Gaia* archive the

stars associated to each peak by selecting those inside a circle centred on each peak with a radius equal to the corresponding WT scale. From this set of stars we have removed stars from globular clusters as detailed in Appendix C. Our final sample has 2 168 723 stars.

We then compute the stars median $\mu_{\ell*}$, μ_b and μ_{tot} in bins of $\tilde{\Lambda}_\odot$, which we then smooth with a Gaussian filter, as done previously for the model. We compute the statistical error on the median using the approximation $\sqrt{\frac{\pi}{2}}\frac{\sigma}{\sqrt{N}}$, where $\frac{\sigma}{\sqrt{N}}$ is the standard error on the mean. The curve obtained is shown in Fig. 38a with blue (trailing) and red (leading) solid lines. The error is <0.03 mas yr^{-1} for 75% of the points in the smoothed curves. Again, the black lines correspond to the LM10 model.

Finally, Fig. 38b shows the $\Delta\mu_{\ell*}$, $\Delta\mu_b$ and $\Delta\mu_{tot}$ residuals, defined as $\Delta \equiv$ (data)-(model) with the grey area showing the combined errors on the median added in quadrature (thus, 1σ). The differences are < 0.2 mas yr^{-1} for 75% of the bins along the evaluated sequences. For the leading arm, we see systematic differences $\lessapprox 0.2$ mas yr^{-1} in $\mu_{\ell*}$ and μ_b well above the statistical error and a larger total proper motion than for the model. However, the biggest differences are for the trailing arm at $\tilde{\Lambda}_\odot < -120°$ (including its prolongation at $\tilde{\Lambda}_\odot \approx 180°$). These discrepancies could be due to strong contamination from the foreground (see Appendix A). Indeed, the CMDs analyzed in Sect. 4.5 appear very contaminated in this range. There are also significant discrepancies near $\tilde{\Lambda}_\odot \approx -50°$ in μ_b that are ~ 0.3 mas yr^{-1}. This is close to pericenter of the orbit (small distances; see bottom panel of Fig. 37b). This position is also where the contribution of the solar motion is larger. In Fig. 38b we plot the derivative of the contribution of solar motion with respect to the individual components $(U_\odot, V_\odot, W_\odot)$. A distance needs to be assumed for this calculation, so we take this distance from the LM10 model. We see that the shape of $\frac{\partial \mu_{\ell*}}{\partial U_\odot}$ and $\frac{\partial \mu_b}{\partial U_\odot}$ is similar to that of the differences between data and model for the trailing arm, but not for the leading arm. However, all the derivatives are very small (at most of 0.01 mas yr^{-1} km s^{-1}). Therefore, the solar motion assumed in the LM10 would have to differ by more than 20 km s^{-1} in order to explain the observed differences. This could be plausible for $V_\odot$ (for instance $V_\odot = 232$ km s^{-1} in LM10 but $V_\odot = 255$ km s^{-1} from Reid et al. 2014) and therefore at this point we cannot discard the possibility that a combination of a different $V_\odot$ together with a distance difference is the cause of part (but not all) of the proper-motion discrepancies.

The systematic errors in the *Gaia* proper motions cannot account for the observed residuals since they are much smaller (of the order of 0.028 mas yr^{-1} at the scales of $\sim$ 14–20°; see Table 4 in Lindegren et al. 2018).

4.5 300 000 STARS IN THE SGR STREAM AND SGR DWARF

In Fig. 39 we plot the CMDs of the stars that belong to the detected peaks of Sgr in bins of 15° in $\tilde{\Lambda}_\odot$. We have organised the panels so that the detection of the trailing arm at $\tilde{\Lambda}_\odot = 180°$ is connected to that at $\tilde{\Lambda}_\odot = -180°$. In the direction of the Galactic centre, there were no selected peaks, hence the blank panel. Except for the panels of the first row that are close to the Galactic plane in the anti-centre direction (see discussion below), the signature of Sgr is clear, with prominent Red Clump (RC), red giant branch, extended horizontal branch, and turn-off stars. The Sgr dwarf itself has a high density of stars in the range $\tilde{\Lambda}_\odot = [-15, 15]°$ (second and third panels of the third row).

In Fig. 39 we observe the position of the RC moving continuously in G magnitude as a function of $\tilde{\Lambda}_\odot$ due to the varying distance of the stream. This is better seen in Fig. 40 where we show the apparent distance modulus versus $\tilde{\Lambda}_\odot$, computed as if all stars were RC stars, assuming a RC absolute magnitude of $M_G = 0.495$ (Ruiz-Dern et al., 2018) and neglecting effects of extinction and of the metallicity gradient along the stream (e.g., Keller et al., 2010; Hayes et al., 2019). The distance trend shows general good agreement with the LM10 model (blue curves, right axis). The leading arm appears to be ~ 5 kpc closer than predicted by the model at $\tilde{\Lambda}_\odot \approx 100°$, which cannot be caused by extinction since this would produce the contrary effect, and we see a shift in the angular position of the apocenter at around $\tilde{\Lambda}_\odot \approx 70°$. A more thorough comparison of the distances from the data and model is the subject of another work (see Chapter 5).

We note that an incorrect distance in the LM10 model would also cause a discrepancy in the proper motions. For instance, an overestimation of the model distance for the leading arm by 10% will cause an overall underestimation of the proper motion by 10%, which is similar to what we observe.

It is hard to identify the Sgr trailing stream in the CMDs of the first row of Fig. 39 where there is strong contamination. The RC of the trailing arm should be quite faint here given the distances of this part of the stream (~ 50 kpc according to LM10) and is probably hidden inside the big blob of contaminating stars. We only see the emerging tip of the giant branch at $\tilde{\Lambda}_\odot = [150, 180]°$ (plume of stars at $G_{BP} - G_{RP} \approx 1.75$) and some hints of it at $\tilde{\Lambda}_\odot = [-150, -120]°$. It is very unlikely that the RC that we see in the first five panels of Fig. 39 belongs to the leading arm in its second wrap: their distance inferred from their magnitude could be compatible with this second wrap but not their proper motion[2]. The structure seen in these panels could alternatively be due to contamination of the disk or disks, the

2 Indeed, the proper-motion difference of the two branches is about 5 mas yr^{-1} according to the LM10 model, which is much larger than the expected dispersion of the stream considering the intrinsic dispersion and also the dispersion produced by errors.

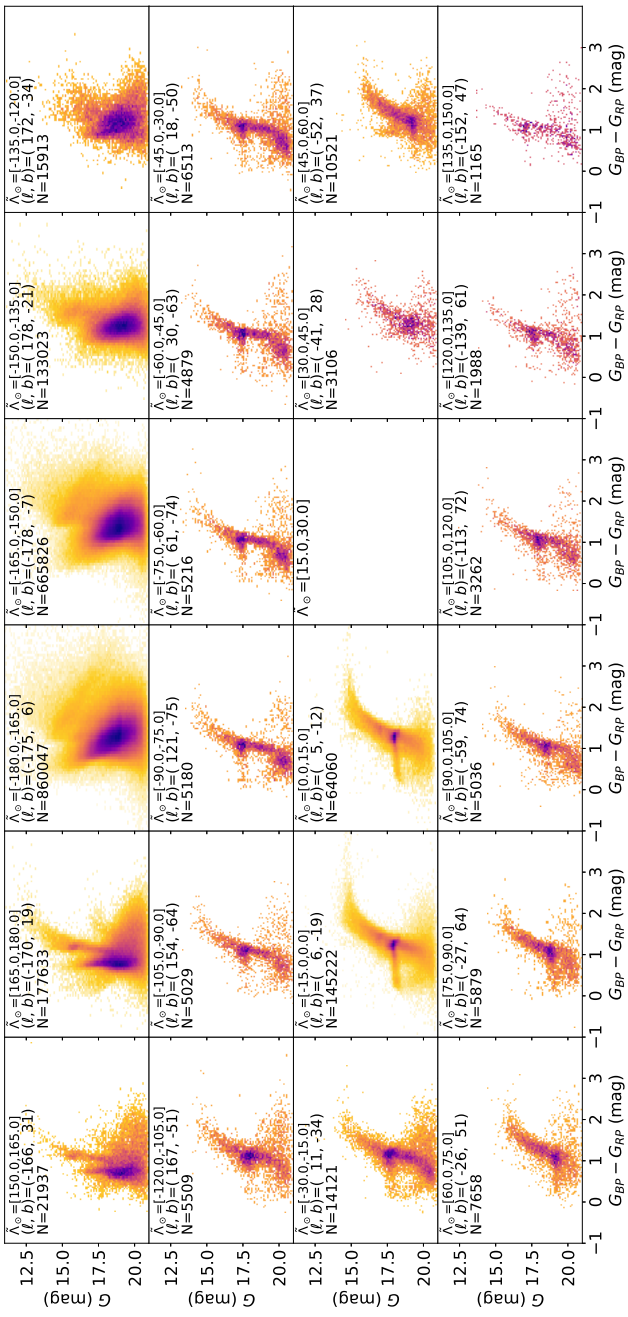

Figure 39: Colour-magnitude diagrams of the stars belonging to the proper motion peaks classified as Sgr peaks for different bins in $\tilde{\Lambda}_\odot$ as indicated in the legend. The corresponding means in Galactic coordinates of the stars are also shown. The CMDs at higher Galactic latitudes are dominated by the Sgr population.

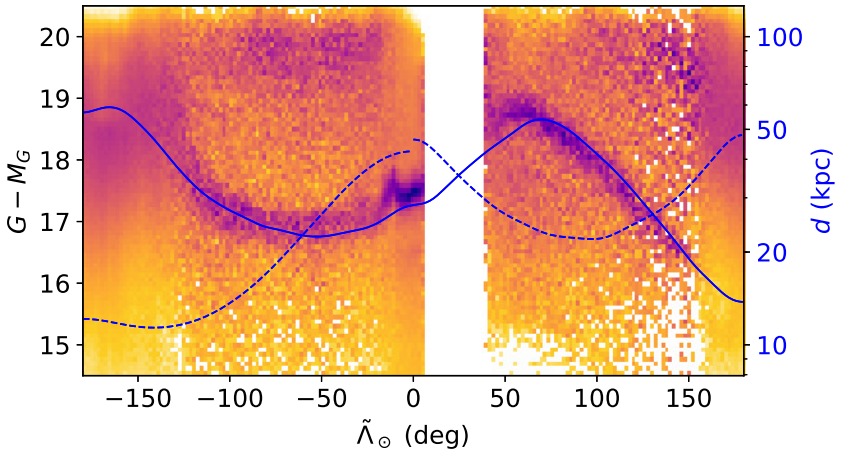

Figure 40: Apparent distance modulus as a function of $\tilde{\Lambda}_\odot$ for the stars belonging to the Sgr stream and Sgr dwarf. The data are shown as a histogram normalised by column. The stars belonging to the RC depict a well-defined sequence. In a secondary axis, the distance of the particles in the LM10 model is superposed in blue. In the absence of extinction and with our assumed calibration of the RC, the two would be directly comparable. The data show general good agreement with the model with discrepancies for example in the apocentre of the leading arm.

flare, the warp, or other outer disk substructures (Xu et al., 2015) such as the Monoceros ring (Newberg et al., 2002) or TriAnd overdensity (Rocha-Pinto et al., 2004; Sheffield et al., 2014; Price-Whelan et al., 2015).

We note that our selection of member stars is contaminated in certain areas and that the completeness resulting from our methodology is yet to be determined. While we plan to deal with these in the future, here we build a list of member candidates by selecting stars in the ranges of $\tilde{\Lambda}_\odot \in [-120, -10]^\circ$ (trailing arm) and of $\tilde{\Lambda}_\odot \in [30, 150]^\circ$ (leading arm) where the contamination is minimal. We count 61 937 and 38 615 stars, in the trailing and leading arms, respectively, making a total of 100 552 stars of different stellar types along the stream of Sgr. We also find 193 792 stars in the approximate region of the Sgr dwarf ($\tilde{\Lambda}_\odot = [-10, 10]^\circ$), given an apparent size of 15 ° (e.g., Giuffrida et al., 2010).

The list of member candidates (see Table 6), the median proper motions of the data, the interpolation used to obtain the smooth curves given as a pickle *Python* object, and additional material will be made publicly available at services.fqa.ub.edu/sagittarius and through CDS.

4.6 DISCUSSION AND CONCLUSIONS

Here, we present a measurement of the proper motion of the Sgr stream with *Gaia* DR2 data. Compared to previous studies based on a small number of stars located in a few particular fields (Carlin et al., 2013; Koposov et al., 2013; Sohn et al., 2015, 2016), our determination is substantially better because: i) it is based on a much greater number of stars (around 100 000 stars in the stream) and covers different stellar types; and ii) is, for the first time, a continuous determination that extends, except for the regions behind the Galactic plane, 2π in the sky. This makes it the proper motion determination with the largest span for any stream to date. We also clearly detect the bifurcation of the leading arm. The whole sky coverage and precision of the proper motions given by *Gaia* are key to the success of the present study.

Our determination comes directly from the detection of peaks of stars in the proper-motion plane covering the sky continuously. That is, we do not use a previous selection of Sgr members, but the member candidates are rather a by-product of our study. In this sense, it is the first time that the stream is detected based on a proper-motion search. Moreover, our search is a blind one, meaning that the peaks corresponding to the over-density of the stream stand out naturally as the peaks with highest intensity in the proper-motion distribution of each sky patch. We note that such a continuous determination would be hard to achieve using match filtering techniques since the distance to the stream changes across the sky. Moreover, our method does not require any assumptions, contrary to other methods that also use proper-motion information for the stream detection, such as for example in *STREAMFINDER* (Malhan & Ibata, 2018), where the authors look for trajectories coherent with a stream shape in a given gravitational potential. In fact, in the final stages of this work we found out that a simultaneous study by Ibata et al. (private communication) has also detected the Sgr stream with Gaia data using this completely different methodology and it will be extremely interesting to compare their results with ours in the near future. However, we note that our ability to detect new streams, as done with *STREAMFINDER*, has still to be confirmed.

We note that we detected several globular clusters along the path of the Sgr stream that also fall in the same proper-motion sequence as Sgr. From these, there is consensus about the likely relation of Pal 12, Arp 2, M 54, Ter 7, and Ter 8 with Sgr (e.g., Law & Majewski, 2010a; Massari et al., 2019), and more recently of NGC 2419 (Belokurov et al., 2014; Massari et al., 2017; Sohn et al., 2018) that we confirm here, while not for NGC 5053 and NGC 5024 (Sohn et al., 2018; Tang et al., 2018).

Our list of member candidates contains about 100 000 stars in the stream and 200 000 stars in the Sgr dwarf itself and opens up many

possibilities for further investigations, such as on the population of stars along the stream, the distance to the stream using RC stars, the width of the stream in the sky and its velocity dispersion, the determination of the solar motion (Hayes et al., 2018), and the possible detection gaps and spurs which are expected (Amorisco, 2015) and seen in other streams (Price-Whelan & Bonaca, 2018; Erkal et al., 2019).

The continuity and span in the sky of our proper-motion measurement allows for determination of the 3D kinematics of the Sgr stream along its first $2\pi^\circ$, which could hold valuable information for an improvement of the models of the gravitational potential of the Galaxy and companions such as the LMC influencing the Sgr orbit (Vera-Ciro & Helmi, 2013).

APPENDIX

A *Tests with mock Gaia DR2 data and fields off-stream*

Figure 41 shows the peaks detected in a mock sample that does not contain the Sgr stream. To built this simulated catalogue we took the mock data from Rybizki et al. (2018) and added Gaussian errors to colour, magnitude, parallax, and proper motions ($\mu_{\alpha*}$, μ_δ) with the uncertainties quoted. We select stars in the same manner as for the real DR2 data and we apply the same method to detect peaks in proper motion.

The mock data presents a sequence of peaks evolving with $\tilde{\Lambda}_\odot$ which most likely correspond to the centre of the main component/s of the distribution (mostly foreground stars) that changes with sky position due to differences in the true mean motion of the stars and to the projection in equatorial proper motions of the solar motion. In general, we see that the sequence in the mock catalogue and in the data do not match, confirming that the peaks that we assign to Sgr do not belong to the distribution of foreground stars. The exception is the group of peaks organised in a triangular shape at middle $\tilde{\Lambda}_\odot$, which as explained in the main text, have been removed for our analysis.

We also note that around $\tilde{\Lambda}_\odot \approx -180^\circ$ there are mock peaks that are very close to the LM10 model in all three components ($\mu_{\ell*}$, μ_b, μ_{tot}). This is unfortunate since in this position the stream crosses the Galactic plane and therefore we expect the contamination to be very important. This means that the peak corresponding to the stream will be hardly distinguishable from the one for the foreground population. At $\tilde{\Lambda}_\odot \approx 180^\circ$ the mock data also show coincidence with the model for the first wrap but only for $\mu_{\ell*}$, which means that the stream could be distinguished unambiguously from the other component μ_b. However, the second wrap of the trailing arm does have a proper motion similar to that of the field.

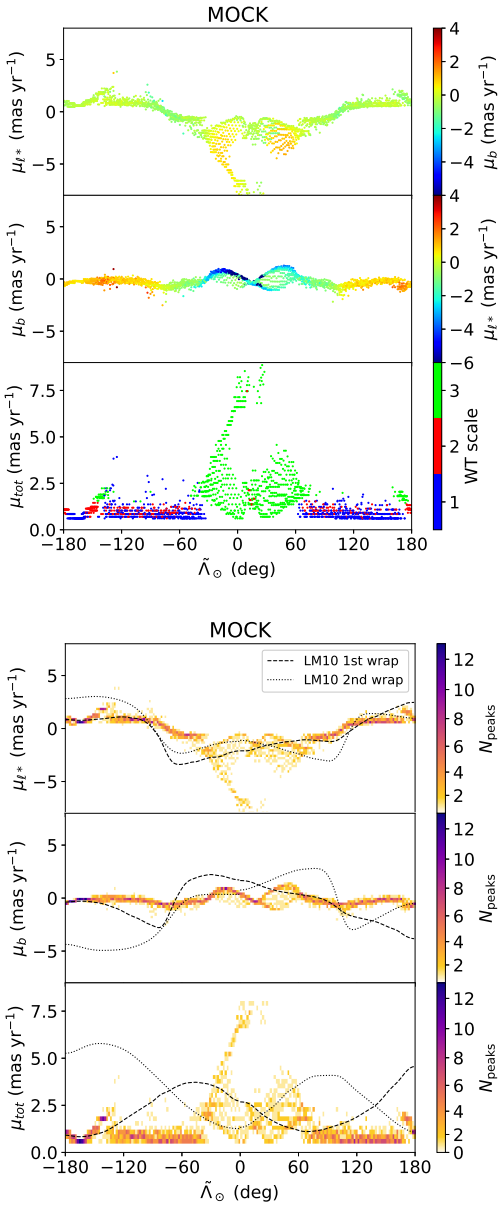

Figure 41: Peaks detected in the mock *Gaia* catalogue with no Sgr stream. Left: Proper motions of the peaks as a function of $\tilde{\Lambda}_\odot$ (top: proper motion in Galactic longitude, middle: in latitude, bottom: total proper motion) colour coded by proper motion in latitude (top), in longitude (middle), and by WT scale (bottom). Right: Same as in the left panel but in a 2D histogram with the LM10 model superposed with black lines.

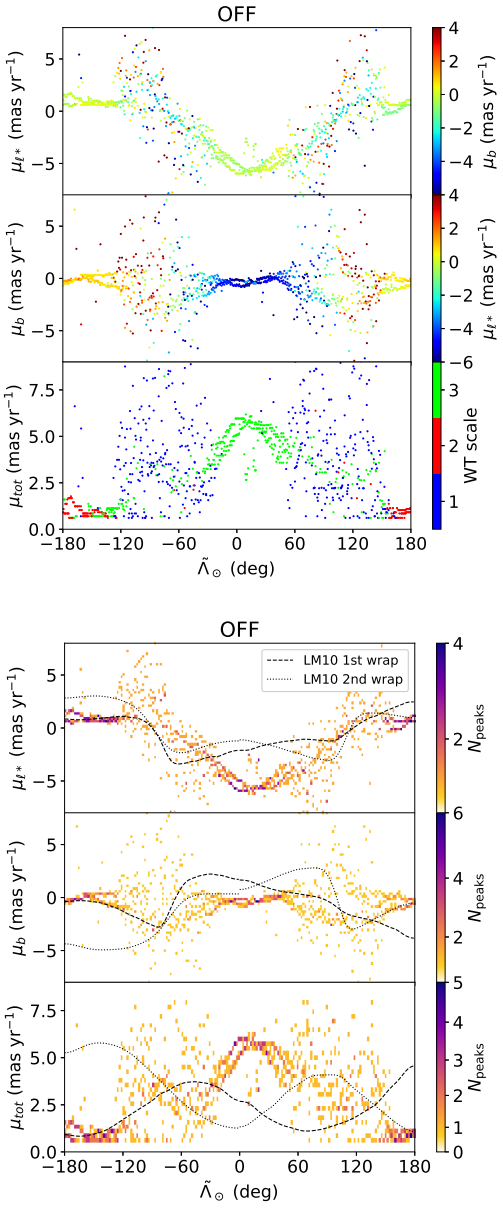

Figure 42: Same as Fig. 41 but for the fields off-stream in the *Gaia* DR2 data.

We have also run our method on a sample of stars off-stream defined as stars with $15 < |\tilde{B}_\odot| \leqslant 20°$. The corresponding plot of peaks is shown in Fig. 42. We note again the coincidence of peaks that are not Sgr but have the same proper motion at $\tilde{\Lambda}_\odot \pm 180°$, further evidencing the contamination when the stream crosses the Galactic plane. We note again the central triangular distribution of peaks that clearly do not belong to Sgr.

B *Selection of the Sagittarius peaks*

The selection of peaks of the different parts of the stream is done following the following empirical prescriptions. We first define the following lines, where proper motions are given in $\mathrm{mas\,yr^{-1}}$:

$$\begin{aligned}
\mu_{tot1} &= 2.3 - 1.4\sin(1.5\tilde{\Lambda}_\odot(\mathrm{rad}) - 0.5)\\
\mu_{tot2} &= 2.5 - 1.4\sin(1.5\tilde{\Lambda}_\odot(\mathrm{rad}) - 0.3)\\
\mu_{\ell*3} &= 2.4\\
\mu_{\ell*4} &= -4. + 0.045\tilde{\Lambda}_\odot\\
\mu_{b5} &= 1.2 - (1./4. \times 0.006)(\tilde{\Lambda}_\odot + 14.)^2\\
\mu_{\ell*6} &= 2.4 - 0.03\tilde{\Lambda}_\odot
\end{aligned} \tag{6}$$

We then select only peaks satisfying the following criteria for the first part of the trailing arm ($\tilde{\Lambda}_\odot < 0°$):

$$\begin{aligned}
|\mu_{tot} - \mu_{tot1}| &< 1.1\\
\mu_{\ell*} &< \mu_{\ell*3}\\
\mu_b &< \mu_{b5},
\end{aligned} \tag{7}$$

for the trailing small part at $\tilde{\Lambda}_\odot > 150°$:

$$|\mu_{tot} - \mu_{tot2}| < -1., \tag{8}$$

and for the leading part ($\tilde{\Lambda}_\odot > 0°$):

$$\begin{aligned}
|\mu_{tot} - \mu_{tot2}| &< 0.7\\
\mu_{\ell*} &< \mu_{\ell*4} \text{ for } \tilde{\Lambda}_\odot < 85°\\
\mu_b &< \mu_{b6} \text{ for } \tilde{\Lambda}_\odot > 115°.
\end{aligned} \tag{9}$$

After applying the above geometric filters and examining the proper motion in equatorial coordinates of the selected peaks, there is a peak that is clearly off the Sgr track in $\mu_{\alpha*}$ (while our selection is done in $\mu_{\ell*}$-μ_b). This is caused by an abrupt change of proper motion on certain parts of the celestial sphere related to the coordinate transformation. Thus, we further remove this peak (HEALpix 4491, ICRS level 5).

C *Removing stars from globular clusters*

From the peaks of high relative intensities, the ones for the globular clusters Pal 12, Terzan 7, Terzan 8, Arp 2, M 54, NGC 2419, M 53 (NGC 5024) and NGC 5053 coincide with the projected path of the Sgr stream and, more importantly, with the proper-motion sequence shown in the Fig. 3. We remove the mentioned globular clusters in Fig. 39 and from the list of candidate members by filtering out stars in these clusters. For this we consider the positions, tidal radius and distance from Baumgardt & Hilker (2018), and take the apparent size of the clusters as 5 times the tidal radius, except for NGC5024 and NGC6715 for which we use factors of 10 and 25, respectively.

D *Candidate members table*

Table 6 (available at the CDS) contains the data of the candidate members of the Sgr stream and dwarf delivered in this study in the range $-120° < \tilde{\Lambda}_\odot < 150°$, i.e. avoiding the region of the Galactic plane. We note that these members have been selected based on proper motion only and that a certain fraction of contamination is expected. Here we show an excerpt from the table with the first five rows.

Table 6: First five rows of the table provided in CDS with the list of candidate members of the Sgr stream and dwarf (precision has been reduced here).

Gaia source_id	α	δ	$\mu_{\alpha*}$	μ_δ	G	$G_{BP} - G_{RP}$
1192282922396	45.2822276579	0.3093182817	0.5029273104	-1.6911386321	18.21442	1.3065739
1340029814232	45.0983817638	0.2573337519	0.5391000357	-1.7131457615	17.18689	0.8256264
1687063232012 8	45.1122641436	0.3793731413	-0.0038042018	-1.8952268886	16.70960	0.9880648
2202459236416 0	44.7397533562	0.2424985998	-0.0589970570	-1.9336723389	18.68879	1.0945892
4666052473254 4	45.6057094408	0.5823213123	0.3125358412	-1.5970907824	18.31924	1.2143192

5D CHARACTERISATION OF THE SAGITTARIUS STREAM WITH RR LYRAE

5

Abstract

Context: The Sagittarius stream is one of the best tools that we currently have to estimate the mass and shape of our Galaxy. However, assigning membership and obtaining the phase-space distribution of the stars that form the tails is quite challenging.

Aims: Our goal is to produce a catalogue of RR Lyrae stars of Sagittarius and obtain an empiric measurement of the trends along the stream in sky position, distance and tangential velocities.

Methods: We generate two initial samples from the *Gaia* DR2 RR Lyrae catalogue: one, selecting only the stars within $\pm 20^\circ$ of the orbital plane of Sagittarius (Strip) and the other, the result of applying the Pole Count Map (nGC3) algorithm. We then remove most of the contamination by detecting and isolating the stream in distance and proper motions with a tailored model-independent method.

Results: The output is two empiric catalogues: the Strip sample (higher-completeness, lower-purity) which contains 11 677 stars, and the nGC3 sample (higher-purity, lower-completeness) with 6 608 stars. We characterise the changes along the stream in all the available dimensions, the 5 astrometric ones plus the metallicity, covering more than 2π rad in the sky and obtain new estimates for the apocentres and the mean [Fe/H] of the RR Lyrae population. Also, we show the first map of the two components of the tangential velocity, thanks to the combination of distances and proper motions. Finally, we detect the bifurcation in the leading arm and report no significant difference between the two branches, either in metallicity, kinematics or distance.

Conclusions: We provide the largest sample of RR Lyrae candidates of Sagittarius, which can be used as an input for a spectroscopic follow-up or as a reference for the new generation of models of the stream through the interpolators in distance and velocity that we have constructed.

This chapter has been accepted for publication in A&A: P. Ramos, C. Mateu, T. Antoja et al. 2020.

5.1 INTRODUCTION

The Sagittarius (Sgr) dwarf galaxy (Ibata et al., 1994) is the first detected and most conspicuous relic of an accretion and tidal destruction event in our Galaxy. Since its discovery (Mateo et al., 1996; Totten & Irwin, 1998), the stream has been studied extensively using different tracers and techniques in order to map its full extent and various wraps around the Galaxy, which, combined with kinematic information, can be used to understand the dynamics of its tidal disruption and to infer properties of the Galactic dark matter halo (Law & Majewski, 2010b; Deg & Widrow, 2013; Fardal et al., 2019).

Compared to simpler and thinner streams, such as for example GD-1, Pal 5, or Orphan, among dozens now known in our Galaxy (see Grillmair & Carlin, 2016; Mateu et al., 2018; Shipp et al., 2018; Ibata et al., 2019), the Sgr stream has several main characteristics that make it interesting but also challenging to observe and model. The stream is luminous and abundantly populated with stars; it is roughly planar and wraps around the Galaxy at least twice (Martínez-Delgado et al., 2004); and its (observed) debris spans distances from 20 to over 100 kpc (Sesar et al., 2017a). The extended star formation history (de Boer et al., 2015) of its luminous and massive progenitor has produced complex stellar population and metallicity gradients along the stream and, because the debris is all around the sky and spans such a large distance range, it is observationally demanding to trace in a continuous manner. Despite having a high surface brightness and a stellar population that is clearly different from that of the halo, which should in principle facilitate its detection, we still lack a model that can convincingly reproduce the stream. The long-standing problem is the lack of kinematic data and the reproducibility of features such as the bifurcation observed in both tails or the angular separation between apocentres (Belokurov et al., 2006; Koposov et al., 2012; Navarrete et al., 2017; Belokurov et al., 2014; Gibbons et al., 2016).

One of the key elements needed to properly model the infall of Sgr is the characterisation of the spatial distribution and kinematics of its different populations throughout the sky, in a continuous and homogeneous way. Majewski et al. (2003) made the first all-sky map of the tails using 2MASS M-giants, and were followed by many later studies that obtained radial velocities for red giants, blue horizontal branch stars, and other tracers, usually in small patches along the stream (e.g. Li et al., 2019, and references in Belokurov et al. 2014). Recently, Antoja et al. (2020), hereafter A20, used the precise astrometry of the *Gaia* second data release (DR2, Gaia Collaboration et al., 2018b) to detect the Sgr stream from proper motion alone, without having to select a specific stellar type, and determined for the first time its proper motion along the path of the full stream. However, these latter authors did not obtain distance estimates since the parallaxes at such faint

magnitudes provide little information and would require a thorough study of the astrometric systematic errors (global and local). In any case, this would only allow distance estimates out to a few tens of kiloparsecs. Tracers for which photometric distances can be obtained are therefore more useful when studying the stream to its full extent in a comprehensive way.

Before the publication of *Gaia* DR2, Hernitschek et al. (2017) used PanSTARRS-1 (PS1; Chambers et al. 2016) RR Lyrae stars to measure distances to the Sgr tails and were able to trace both arms, the leading (i.e. the stars that orbit ahead of the progenitor) and the trailing (those that lag behind), all around the sky while characterising its distance and line-of-sight depth. Later, Sesar et al. (2017a) identified new Sgr features at distances over 100 kpc using the same sample. The advantage of using RR Lyrae stars is that they are excellent as standard candles, their photometric distance errors being $\sim 7\%$ in the optical (Mateu et al., 2012) or as good as $\sim 3\%$ in the infrared (Sesar et al., 2017b) even without prior knowledge of their metallicity. This is an order of magnitude more precise than the $\sim 20-30\%$ errors that can be achieved with K and M giants (Liu et al., 2014), as these are far more sensitive to metallicity. For these reasons, RR Lyrae have become a standard used in studies of the halo structure (for a review see Table 4 in Mateu & Vivas, 2018) and substructure, serving to identify new streams and overdensities (Vivas et al., 2001; Duffau et al., 2006; Sesar et al., 2010; Mateu et al., 2018); to extend and find the connection between seemingly different substructures, like the Orphan and Chenab streams (Koposov et al., 2019); and, combined with *Gaia* DR2 kinematics, to provide a comprehensive 5D view of the Orphan (Koposov et al., 2019) and Pal 5 streams (Price-Whelan et al., 2019). RR Lyrae, being old ($\gtrsim$ 10 Gyr) and metal-poor ([Fe/H] $\lesssim -0.5$) stars (Catelan & Smith, 2015), are expected to dominate the outskirts of dwarf galaxies (Koleva et al. 2011, and references therein) and are therefore the first to be stripped, tracing the ancient components of a stream and thus contributing to the dynamically oldest wraps.

However, an all-sky view of the kinematics of the Sgr stream with RR Lyrae is still limited because radial velocities are observationally demanding to obtain due to the stars' pulsations. Currently, these are only available for a few dozen RR Lyrae in selected fields along the Sgr stream (Vivas et al., 2005). In this work, we aim to provide a cohesive 5D view of the distance and proper motions of the Sgr stream using RR Lyrae stars. In Section 5.2 we describe the input catalogue — the RR Lyrae identified as such by the *Gaia* variability pipelines complemented with the PS1 catalogue. In Section 5.3 we derive distances for these RR Lyrae stars and describe our selection method based on sky coordinates, proper motions, and distances, and use no prior information. In Section 5.4 we present our results providing an entirely empirical characterisation of the stream including for example

its proper motion, Galactocentric distance, tangential velocities, and the bifurcation. Finally, we present our conclusions in Section 5.5.

5.2 RR LYRAE AND GAIA SAMPLE

The second data release (Gaia Collaboration et al., 2018b) of the *Gaia* mission (Gaia Collaboration et al., 2016b) has provided not only positions, magnitudes, and proper motions for more than a billion stars, but also a vast catalogue of variable sources (hereafter VC, see Holl et al., 2018). For a detailed description of the detection, classification, and post-processing pipelines we refer the reader to Eyer et al. (2017) and Rimoldini et al. (2019). Among those detected variable sources, there are 140 784 RR Lyrae that have at least 12 good G-band transits which have been validated by the Specific Objects Study (SOS) pipeline (Clementini et al., 2019). We have further increased the number to 228 904 sources by including those classified as RR Lyrae by Holl et al. (2018) and Rimoldini et al. (2019), but not processed by SOS due to the small number of observations available in DR2. We then apply the filter recommended in Rimoldini et al. (2019) to remove obvious contaminants: `phot_bp_rp_excess_factor > 2 OR NULL`, leaving 175 164 RR Lyrae. Finally, we include 11 318 stars identified as *bona fide* RR Lyrae in the PS1 catalogue (Sesar et al., 2017b), but not classified as such by the *Gaia* pipelines. We identify these stars in the DR2 `gaia_source` table by cross-matching their positions on the sky with a 1" tolerance, and retrieve their astrometric data.

After removing the stars with no proper motions we obtain a list of 182 495 stars, 122 745 of which have been processed by the SOS pipeline. For some of them, the SOS team has derived photometric metallicities and absorption in the G band. In particular, 39 129 of them have both quantities simultaneously, which we use in Sect. 5.3.2 to obtain a first measurement of the metallicity distribution along the stream. As stated in Holl et al. (2018), the *Gaia* catalogue of variable sources is not meant to be complete and we do not expect the completeness to be above 80% when taking only sources with more than 12 field-of-view (FoV) transits (see also Mateu et al., in prep.).

5.3 SELECTION OF RR LYRAE IN THE SAGITTARIUS STREAM

Our aim is to detect the RR Lyrae of the Sgr stream from scratch to produce a characterisation that is as empirical as possible. To do so, we select two sets of initial candidates from the list of stars with proper motions presented in the previous section: the Strip and the nGC3 selections (Sect. 5.3.1), later pruned to filter out contaminants based on distance (Sect. 5.3.3) and kinematic information (Sect. 5.3.4 and 5.3.5). We use these two different selections since they offer different

Table 7: Number of stars in each sample at each step of the selection process.

Stage	nGC3	Strip
Initial sample	13 004	76 872
Distance selection	7 953	18 045
$\mu_{\alpha*}$ selection	6 797	12 583
μ_δ selection	6 608	11 677

advantages as we shall see below. In Table 7 we show the number of stars remaining after each selection step.

5.3.1 *Initial selections: Strip and nGC3*

strip selection. A HIGH-COMPLETENESS, LOW-PURITY SAMPLE: A first straightforward list of candidates can be obtained by selecting stars within 20° of the orbital plane defined by the pole (l,b)=(273°.8; 13°.5) from Majewski et al. (2003). This is exactly equivalent to selecting stars with $|\tilde{B}_\odot| < 20°$ in the Sgr coordinate frame[1], a spherical heliocentric frame rotated to have the plane of the stream at $\tilde{B}_\odot = 0°$ and the Sgr dwarf remnant at $\tilde{\Lambda}_\odot = 0°$. The resulting selection contains 76 872 RR Lyrae (41% of the full catalogue).

This selection is expected to be highly complete, limited only by the completeness of the input catalogue itself, as no kinematic or additional information (e.g. metallicity) is required. However, precisely because no information other than sky position is used, a large fraction of contaminants is expected, mostly due to the thick disc and halo. This contamination will be reduced significantly after the following selection steps.

ngc3 selection. A LOW-COMPLETENESS, HIGH-PURITY SAMPLE: Great circle cell count methods grouped in the xGC3 family (Johnston et al., 1996; Mateu et al., 2011, 2017) are aimed at the detection of groups of stars that populate an orbital plane different from that of the Milky Way (MW) disc. In its most basic implementation, this approach relies on the fact that the stars in a stream lie approximately on a plane through the centre of symmetry of the Galactic potential. Geometrically, this implies that the stream is confined to a great circle uniquely defined by the normal vector (pole) of the orbital plane. Therefore, if we grid the sky[2] and, for each cell, count the number of stars in a wafer of a certain width perpendicular to it, we should detect an overdensity whenever we align this wafer with the

1 In this work, we use the convention by Belokurov et al. (2014).

2 For streams that are too close to the Sun, projecting their orbit onto the Celestial sphere might introduce projection effects, i.e. the Galactic parallax becomes non-negligible.

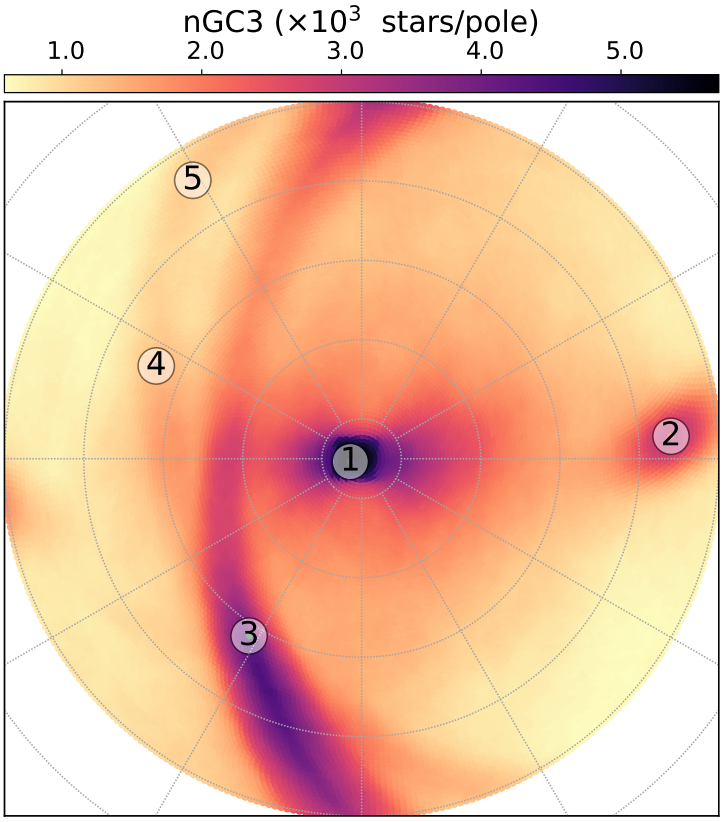

Figure 43: Pole Count Map of the RR Lyrae catalogue described in Sect. 5.2. The Galactic disc produces the large concentration at (1), while the peaks (3),(4), and (5) are related to the Large and Small Magellanic clouds. The prominent signal on the right, (2), is caused by the Sgr stream.

orbital plane of a stream. The result is a pole count map (PCM), which is a density map of the number of stars associated to each pole and, hence, great circle.

The nGC3 method introduced in Abedi et al. (2014) also requires proper motion information in the pole counting. In this method, the velocities of the stars are required to lie in the same great circle as their positions, within a certain tolerance. This helps to clean the sample of contaminant stars that lie in a given great circle band by chance. We cannot take this approach in the heliocentric frame because then the peculiar velocity of the Sun would dominate the PCM. Instead, the nGC3 pole counts are made in the galactocentric reference frame, for which we assume a distance from the Sun to the Galactic centre (GC) of $R_\odot$=8.0 kpc (Camarillo et al., 2018), a velocity of the Sun with respect to the local standard of rest (LSR) $[U_\odot, V_\odot, W_\odot]$ = [11.10, 12.24, 7.25] km s^{-1} (Schönrich et al., 2010), and V_{LSR} = 240 km s^{-1} (Reid et al., 2014). Obviously, we also require a distance to

each star which implies assuming a metallicity (see Sect. 5.3.2). We chose as a first value [Fe/H] = -1.7 dex. We find that the PCM does not change significantly within the range of metallicities typical for RR Lyrae in the halo: -1.5 dex $\leqslant$ [Fe/H] $\leqslant$ -1.7 dex.

Figure 43 shows the resulting PCM for the RR Lyrae, using a tolerance of 5° for both positional and velocity vectors. The method also returns a list of peaks, that is, local maxima, ordered by the number of counts contained within the corresponding pole. As expected, we observe a peak (label 1) at the centre caused by the disc. The second most dominant peak (label 2) is that produced by the Sgr stream. We also see signatures produced by the Large (label 3) and Small (labels 4 and 5) Magellanic clouds which, being concentrated on the sky, make trails instead of compact overdensities.

The nGC3 selection is made by extracting the RR Lyrae stars associated to the cells, or poles, around peak 2 within the 25th percentile of the maximum counts in that peak. This results in a preliminary list of candidates of 13 004 (7% of the full RR Lyrae catalogue). This sample is expected to be of lower completeness than the Strip selection because the method can introduce correlations between the spatial position and the proper motions and, more importantly, a dependence on the observational errors which can translate into kinematical biases. In particular, the method by construction selects against stars with significant motions perpendicular to the plane of the stream, making it unsuitable for the study of aspects such as velocity dispersion profiles, as we discuss in Sect. 5.4.6. By contrast, the nGC3 sample is expected to be of higher purity, and therefore better suited for purposes such as the selection of targets for spectroscopic follow-up.

Having a first list of candidates, we next look for trends in distances and proper motions to refine our selection. For the remainder of this section only, to avoid repetition, we use the nGC3 sample to show how our selection methodology works. This sample, by construction, is less contaminated than the Strip sample and allows us to more clearly illustrate the way we separate the candidate stars from the contamination. Wherever important differences with the Strip sample arise they are discussed in the text. The plots corresponding to the Strip selection can be found in Appendix B.

5.3.2 *Distance determination*

To determine the distances we begin by using the linear relation for the *Gaia* G band given in Muraveva et al. (2018):

$$M_G = 0.32^{+0.04}_{-0.04}[\mathrm{Fe/H}] + 1.11^{+0.06}_{-0.06}. \quad (10)$$

This relation returns the absolute magnitude of the RR Lyrae star given its metallicity in the Zinn & West (1984) scale (hereafter, ZW84). However, we note that the metallicity given by DPAC is calculated

from the Fourier parameters of the light curve (Clementini et al., 2019). In particular, in the case of RR Lyrae of type RRab, the metallicity is calibrated with the prescription of Nemec et al. (2013) which, for the range of periods and Fourier parameters of our sample (c.f. their Fig. 12), closely matches the Jurcsik & Kovacs (1996) metallicity scale. As noted in Gratton et al. (2004) and Di Fabrizio et al. (2005), there is a systematic difference of +0.3 dex between the metallicities derived from photometry in the Jurcsik & Kovacs (1996) scale and those calculated with spectroscopy[3]. Therefore, for our particular case, we subtract 0.3 dex from each RRab to convert the metallicities from DPAC into the ZW84 scale. This is not the case for the stars of type RRc, as their metallicity is given in a scale already similar enough to ZW84 (Nemec et al., 2013; Clementini et al., 2019).

Even though we have a way to compute the absolute magnitude for our stars, the metallicity is only available for a small fraction of them (~35%, see Clementini et al. 2019). Additionally, the Sgr stream presents a gradient in metallicity (e.g. Zhang et al. 2017; Hayes et al. 2019). Our approach is to first test whether there is a metallicity gradient for the RR Lyrae stars with measured metallicity. This is important because it could introduce a distance bias along $\tilde{\Lambda}_\odot$. However, we find that there is not (see below), and we assign an average metallicity to the rest of RR Lyrae.

To calculate the distances, we use the well-known relation for the apparent magnitude of a star,

$$d\,[\mathrm{pc}] = 10^{(m_G - M_G - A_G)/5+1}, \tag{11}$$

for all stars with reported metallicity and absorption in the nGC3 sample. In particular, we choose a sample of 884 stars between 20 kpc and 50 kpc from the Sun, i.e. preferentially selecting stars belonging to the stream (c.f. Fig. 4 of Hernitschek et al. 2017), all of which happen to be RRab according to the classification by SOS.

In Fig. 44 we study the dependence of the metallicity on $\tilde{\Lambda}_\odot$. The gradient we measure is (-1.5±0.4)×10^{-3} dex deg^{-1} and (0.9±3.7)×10^{-4} dex deg^{-1} for the leading and the trailing arms, respectively. While the latter is clearly compatible with zero, the former shows some sign of a gradient. Still, this gradient can be heavily influenced by the contamination, and the variations in metallicity that this would imply (0.15 dex every 100°) are smaller than the typical photometric metallicity precision (~0.2 dex). Therefore, we recover a mean metallicity $\overline{[\mathrm{Fe/H}]}_{ZW}$=-1.61 dex with no trace of a gradient, in good agreement with previous studies of the RR Lyrae population of Sgr (Cseresnjes, 2001). As for the statistical uncertainty on the mean, we find $\frac{\sigma_{[\mathrm{Fe/H}]}}{\sqrt{N}}$ = 0.02 dex. After repeating the measurement for the Strip sample,

3 The offset was calculated with respect to the Harris (1996) spectroscopic scale which has almost no shift compared to the ZW84 scale used in this work (Gratton et al., 2004).

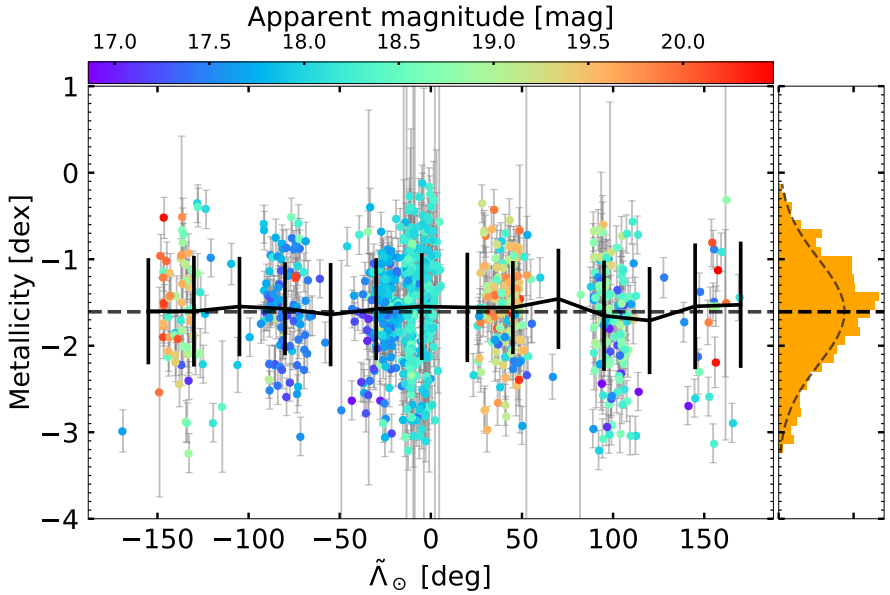

Figure 44: Metallicity dependence on $\tilde{\Lambda}_\odot$ for the stars selected by the *nGC3* method that have a measured metallicity and absorption. Only those stars between 20 kpc and 50 kpc are shown (884 RRab), coloured according to their apparent magnitude. The dashed line corresponds to the mean metallicity (-1.61 dex) whereas the solid line is the running median and 1σ interval within bins of 50° every 25°. On the right, we include the metallicity distribution and a Gaussian fit to the data: $\mu = -1.61$ dex and $\sigma = 0.61$ dex.

we obtain the same result but with a smaller uncertainty ($\frac{\sigma_{[Fe/H]}}{\sqrt{N}} = 0.01$ dex). We re-visit this determination in Sect. 5.4.4, after having selected a reliable sample of Sgr stars, and we obtain the same value within the uncertainties.

Given that there is no significant gradient, we impose the mean metallicity on all the candidate stars. We note that the distribution of apparent magnitude of the RR Lyrae type C is the same as that of the RRab. Assuming that there is no segregation between both types inside the stream, their distance distribution at any given $\tilde{\Lambda}_\odot$ should then be the same. Therefore, we can use the same metallicity for both as long as we apply the same calibration, i.e. Eq. 10.

In addition, to obtain a distance estimation for each star we need the absorption in the G band. For that, we use the Schlegel et al. (1998) dust maps with the Schlafly & Finkbeiner (2011) re-calibration and the relations that allow us to translate reddening to absorption (see Appendix A of Chapter 3). Having done that, we apply Eqs. 10 and 11 to the whole list of candidates and propagate the uncertainties

in metallicity, apparent magnitude, coefficients of Eq. 10, and absorption[4] using the Jacobian of the transformation.

Apart from the statistical uncertainties, we also have a systematic source of uncertainty: our metallicity zero point. As mentioned above, we subtracted 0.3 dex from the metallicities reported by SOS to obtain values in the ZW84 scale. Nevertheless, if that is not the right offset we would be biasing all distances by a fixed proportion:

$$\frac{D(\Delta Z)}{D_0} = 10^{-\frac{0.32}{5}\Delta Z}, \tag{12}$$

where ΔZ is the difference between the zero point that we assume and the true one. For instance, having no zero point in reality (ΔZ= +0.3 dex) and having a zero point that is double what we assumed (ΔZ= -0.3 dex), respectively, and for a distance of 25 kpc, we would obtain 23.92 kpc (-4.3%) and 26.13 kpc (+4.5%). We expect the true zero point to be closer to our value and therefore the systematic error to be much smaller than 4%.

5.3.3 *Distance selection*

In the top panel of Fig. 45 we present the resulting distribution of distances with $\tilde{\Lambda}_\odot$. A conspicuous pattern emerges as a result of selecting sources belonging to the Sgr orbital plane. Nevertheless, there is still a noticeable fraction of contamination even after applying the nGC3 PCM technique: thick disc, halo, and even the Sculptur dwarf Spheroidal at $\tilde{\Lambda}_\odot \sim$-75° (the latter is easily removed). Continuing with the aim of re-discovering the stream from scratch, we apply a method to select probable members that requires almost no assumptions and that we call Tailored Gaussian Mixture (TGM).

The idea of the TGM is to select the pattern formed by the Sgr stars with $\tilde{\Lambda}_\odot$ isolating it from both the foreground and the background contamination. For a given bin of $\tilde{\Lambda}_\odot$, we process the histogram of heliocentric distances and identify the different components (Sgr and contamination). A Gaussian is then fitted to each component to obtain their widths. The algorithm starts at the dwarf and uses it as an anchor since it is the dominant component at $\tilde{\Lambda}_\odot = 0°$. The component corresponding to Sgr in the contiguous bins is assigned by finding the one with the highest continuity in heliocentric distance. When none of the components found are close enough to the one in the previous bin, we skip the bin and try with the next one. The details of the method can be found in Appendix A.

With this algorithm we obtain a deterministic measurement of the centre of the pattern as well as a first estimation of its depth. The

4 We find that, when propagating the errors in colours to the transformations from A_V to A_G by Monte Carlo sampling, the uncertainty in absorption can be taken to be 0.02 dex.

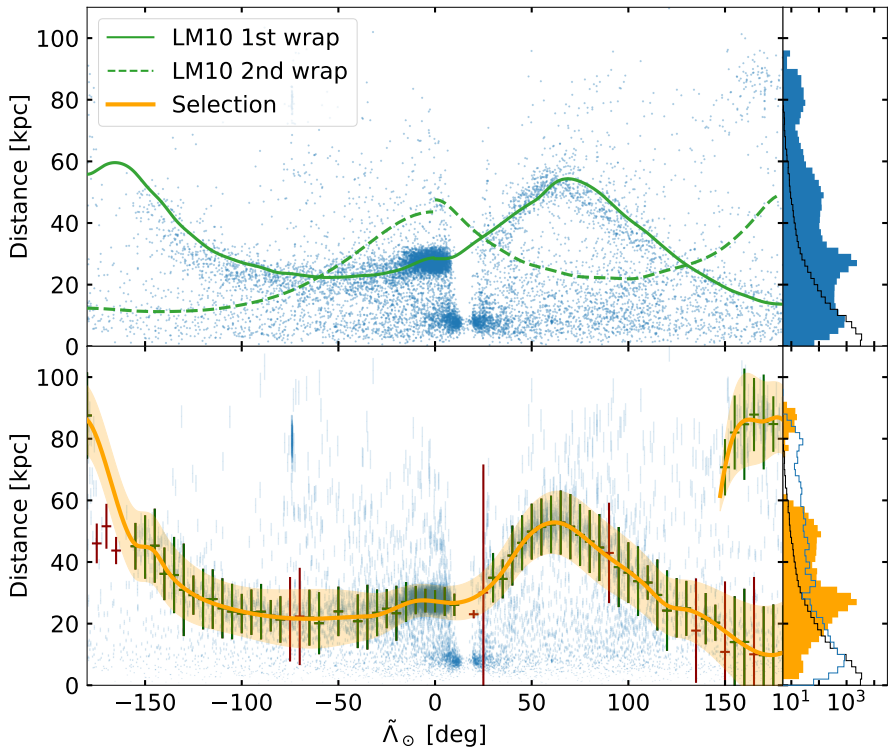

Figure 45: Distance as a function of $\tilde{\Lambda}_\odot$ for the stars in the Sgr stream. Top: All candidates selected by the *nGC3* method. The green lines represent the predictions of the LM10 model for the first (solid) and second (dashed) wrap. The blue bars on the right are the histogram of the same stars, while the black steps correspond to the predictions from the mock catalogue (see text). Bottom: Same stars, now with their associated uncertainties, with green (red) error bars representing the parameters extracted from the good (bad) fit to the kernel associated with Sgr (see text). We also show in orange the interpolation of the centres (dashed line) and the two-sigma interval (shaded area). The histogram on the right now shows the selected stars in orange, the remaining ones in blue, and the black one is the same as above.

result for the nGC3 sample is shown in the bottom panel of Fig. 45 as error bars located at the centre of each bin in $\tilde{\Lambda}_\odot$. The vertical extent of the error bars represents the 2σ interval of the dispersion recovered by the fit and the horizontal extent represents the size of the bin (barely visible). We note that using the same metallicity for all the stars increases the contamination because the foreground (thick disc) merges with the signal of the stream. Since the RR Lyrae in the thick disc tend to be more metal rich than those in Sgr, assigning an incorrectly smaller metallicity to these stars translates into larger distances and thus pushes its distribution towards that of the stream, hampering the separation. Finally, by visual inspection we find that in some of the bins the Gaussian fit has not converged to a good solution. The two main causes are i) too few sources and ii) the components are

too close to be resolved, resulting in an overestimated width. Those few cases (plotted in red in the bottom panel of Fig. 45) have been removed.

We finish by creating two splines with the good solutions (green error bars). The first passes through the centres and represents the change in the distance with $\tilde{\Lambda}_\odot$ (orange line). We use the second one to trace the changes in depth of the stream and produce a smooth $\sim 2\sigma$ confidence interval, as represented by the shaded orange area. We also show the smoothed median distance predicted by the Law & Majewski (2010b) model (hereafter, LM10[5]). These solid (first wrap) and dashed (second wrap) green lines can be seen to follow our orange track in some part of the stream. However, there are important differences which we comment on in Sect. 5.4. On the other hand, our results are in very good agreement with the recent determination of the pattern of Sgr obtained with RR Lyrae by Hernitschek et al. (2017) (see their Fig. 4).

The candidates are selected if they fall inside the orange shaded area, resulting in a set of 7 953 stars (61% of the initial nGC3 sample). In the case of the Strip sample (Fig. 54) the output of the TGM results in a selection of 18 045 stars (23%). Both samples contain field stars that require additional filters to be discarded, especially at $\tilde{\Lambda}_\odot \geqslant 120^\circ$ where the Sgr stars get closer to the Sun and merge with the Virgo overdensity (Jurić et al., 2008). In that region we also have the presence of Sgr stars at a distance of $\sim$90 kpc, which correspond to the apocentre of the trailing arm.

We also include a comparison with a mock catalogue. We query the mock *Gaia* catalogue by Rybizki et al. (2018) in HEALPix bins of level 4 ($\sim$14 square degrees) along the orbital plane of Sgr selecting 2 000 stars for each patch in the sky. We then compute the true distances by simply inverting the true parallaxes and produce the heliocentric distance histograms shown in black on the right of Fig. 45 (normalised to the number of stars in the nGC3 sample). The mock distribution presents a smooth exponential profile with no sign of bumps, in contrast with our data (blue filled histogram). With the mock as a reference, we gain an idea of the contamination that we expect at each portion of the stream, with the parts near pericentre being the most susceptible. This corresponds to the beginning of the trailing tail and the far end of the leading one ($\tilde{\Lambda}_\odot > 120^\circ$), this latter being particularly contaminated. After performing our selection (orange histogram at the bottom right panel of Fig.45) we see that what we have discarded, that is, what we consider contamination (blue line), resembles the mock distribution, except for two details: i) at short distances, the effect mentioned earlier of using an incorrect metallicity for the thick disc modifies the shape of the distribution and ii) the absolute value of counts at large distances is not the same.

5 Downloaded from http://faculty.virginia.edu/srm4n/Sgr/

The latter could be due either to a problem of normalisation between the thick disc and halo components of the mock or simply to the fact that the parameters of the model do not reproduce the observations accurately enough.

5.3.4 *Proper motion selection: Right Ascension*

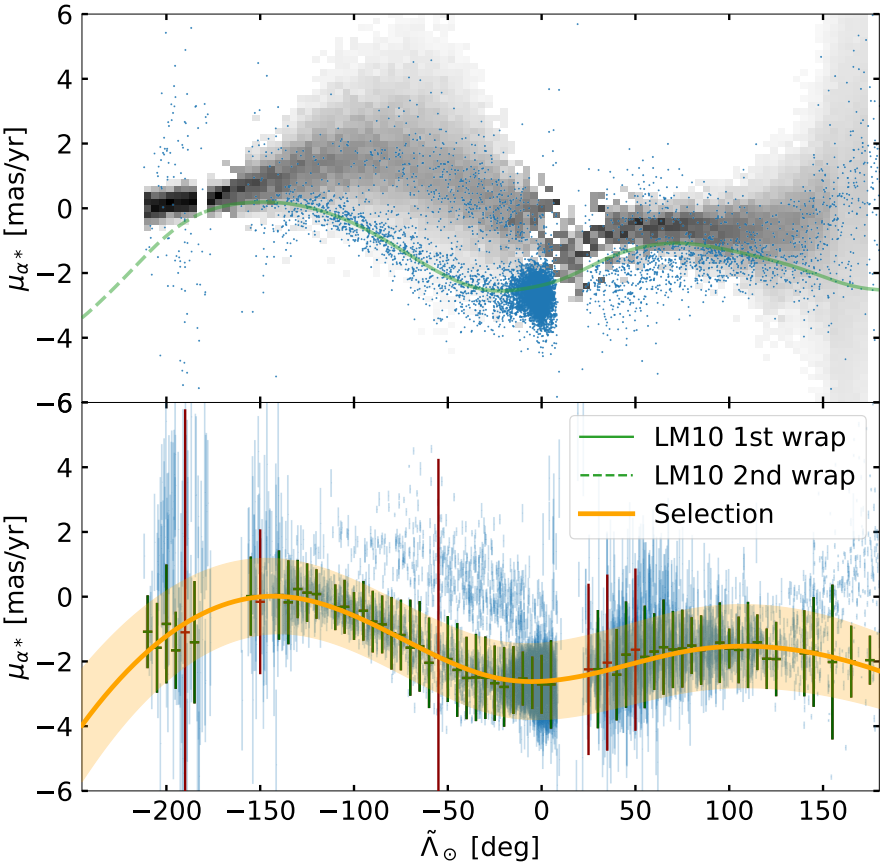

Figure 46: $\tilde{\Lambda}_\odot$ against proper motion in right ascension of the Sgr stream. Top: All stars selected by distance superimposed on the histogram obtained from the mock catalogue (see text). Bottom: Result of the TGM (green and red error bars) and the area that we use to further filter out the contamination (orange). Here we also show the prediction of the LM10 model with green lines. The stars at the trailing apocentre have been moved to the left of the plot by subtracting -360°.

We continue the selection of RR Lyrae candidates based now on their proper motion trends throughout the Sgr stream. In order to avoid overlap between the different wraps, we take those corresponding to the apocentre of the trailing arm and shift their location by -360°. Therefore, from here onwards the plots reach beyond -180°.

Taking the stars already selected according to their heliocentric distance, we now plot in Fig.46 the observed proper motion in right

ascension as a function of $\tilde{\Lambda}_\odot$ (blue dots). We observe a modulation of the dispersion which is dominated by the correlation between the uncertainty and the distance. This is especially noticeable in the Strip sample (Fig. 55), where the dispersion near the apocentres is significantly larger. Also, there are at least two clearly identifiable patterns, especially at the beginning of the trailing and the leading arms.

To understand the effects of the contamination, we resort once more to the mock MW catalogue described in Sect. 5.3.3. We use the orange area obtained in Sect. 5.3.2 to filter the particles in the model by distance, add the errors in proper motion provided with the mock catalogue and finally create the 2D histogram shown in the top panel of Fig. 46. As can be seen, it follows quite closely the trail of stars at higher $\mu_{\alpha*}$. We note that these mock sources are all labelled as halo stars, except for the small range of $\tilde{\Lambda}_\odot$ where the stream passes behind the GC, where it is dominated by thick disc stars with a small fraction of thin disc stars.

As done for the distance, we run our TGM with the parameters listed in Appendix A and skip any bin that contains less than five stars because we have fewer left after the previous selection. The results are shown in the bottom panel of Fig. 46, where we can already see that the prediction of the LM10 model shown in the upper panel (green line) is similar to the trend we detect (see Sect 5.4.1 for a discussion on the residuals). Again, after selecting only the stars within the orange shaded area, we are left with 6 797 RR Lyrae (52 %) stars in the nGC3 sample. In the case of the Strip sample, we find that we cannot recover the same trend beyond $\tilde{\Lambda}_\odot \geqslant 120°$ due to the predominance of the contamination. We tried different parameter combinations without any success. Finally, to avoid leaving that region void, we only select stars around the track of the LM10 model beyond $\tilde{\Lambda}_\odot = 120°$, choosing the ones with -3.5 mas yr^{-1} $\leqslant \mu_{\alpha*} \leqslant$ -0.5 mas yr^{-1} (orange box in Fig. 55). This results in a list of 12 583 stars (16 %).

5.3.5 *Proper motion selection: Declination*

We apply the TGM now to the proper motion in declination of the remaining stars with the same parameters as in Sect. 5.3.4 and recover a single component all along the stream, as can be seen in Fig. 47. We note that the halo stars from the mock catalogue present a proper motion that follows that of the Sgr stream closely but not exactly. This is likely due to the fact that μ_δ is roughly aligned with the motion perpendicular to the stream[6], and because the dominant contribution in this direction is the Solar reflex, it is natural that the stream cannot be cleanly separated from the field. In this step, we have therefore performed the equivalent to a two-sigma clipping.

6 The ICRS frame and the Sgr plane defined by Majewski et al. (2003) have similar poles.

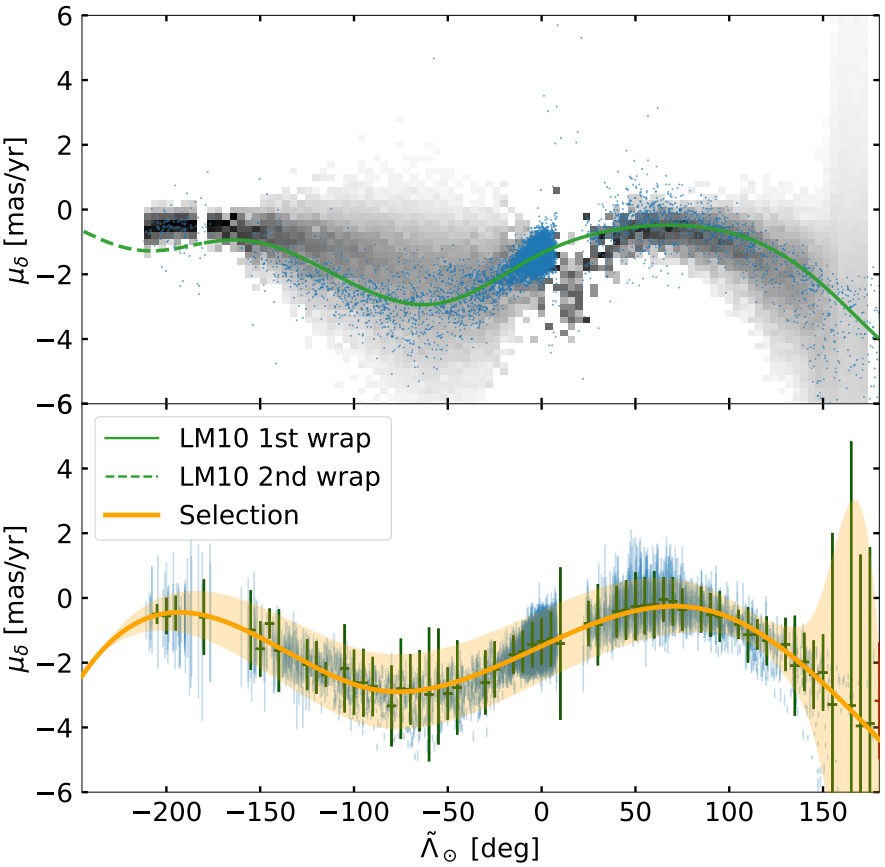

Figure 47: Same as Fig. 46 but with proper motion in declination. Now we only show the stars selected by distance and $\mu_{\alpha*}$.

After applying these selections we obtain our final list of candidates with 6 608 stars for the nGC3 sample and 11 677 for the Strip. The two catalogues are available as one table at CDS (see Appendix D), with a flag that describes whether the star was selected using one method, the other, or both.

5.4 RESULTS

Now that we have assembled a reliable list of stars belonging to the Sgr stream, we proceed on to examine its main characteristics. In this section, in contrast with the previous, we focus on the Strip sample because, as we discuss below, the nGC3 presents a kinematical bias induced by the PCM method. The corresponding figures and derived quantities for the nGC3 sample can be found in Appendix C.

5.4.1 *The missing dimensions: proper motions*

First, we want to determine the proper motion of the Sgr stream and examine the two samples looking for the presence of any kinematic bi-

ases. We do so by comparing the trends in proper motion of our stars with those obtained by A20 and the predictions of LM10. In Fig. 48 (Fig. 57) we present the proper motions in Galactic coordinates as a function of $\tilde{\Lambda}_\odot$ for the Strip (nGC3) sample. The colours of the panels (a), μ_l, and (b), μ_b, as indicated by the colour bars, are the same as in Fig.3a of A20 for ease of comparison. In panel (c) on the other hand, we show the total proper motion coloured according to the distance derived for each RR Lyrae star. In all three panels, we have added the smooth median obtained from A20 (black) and the predictions of the LM10 model (green). We note that the farthest stars (blue points in panel c) have approximately the proper motion that the model predicts for the second wrap, confirming that we are indeed detecting the apocentre of the trailing tail.

In panel (d) we plot the difference between the median of our sample and that of A20, both smoothed with a Gaussian filter, and the associated 1σ intervals. While the discrepancy is within 2σ in most parts of the stream, we note that the residuals start to grow again at $\tilde{\Lambda}_\odot$>120°, which is probably related to the degree of contamination being higher in this region due to our selection (see Sect. 5.3.4). In the trailing tail, the differences are within 1σ until $\tilde{\Lambda}_\odot$ ~-125°, at which point the A20 sample becomes heavily affected by the contamination of the disc. Remarkably, A20 find stars in the trailing apocentre amid all the contamination, and the median μ_{tot} found by these latter authors is compatible with ours (orange shaded area), even though the only criteria used in their selection was based on proper motions. Overall, the differences are of the order of ~0.3 mas yr^{-1} at most, and only with more accurate proper motions will we have the precision needed to decipher whether there is a kinematic separation between the different populations within the stream.

We also examined the residuals against LM10, which we show in Panel (e). The agreement is within 2σ in the range -150°<$\tilde{\Lambda}_\odot$<100° and is only broken near the trailing apocentre, which is expected given the differences between the predicted distances and the observed ones (c.f. Fig. 45), and beyond L $\geqslant$120°, the region where we already know that the Strip selection is poor.

5.4.2 *Galactocentric distance*

In Fig. 49, we show a decomposition of the Sgr stream into each of the available dimensions, with the first panel (a) containing the distribution of the candidate stars in the sky for reference. We begin by analysing the trend in Galactocentric distance with $\tilde{\Lambda}_\odot$ by converting the heliocentric distances derived in Sect. 5.3.2 with the parameters of the Sun described in Sect. 5.3.1. We are interested in the distribution of the tidal debris across the Galaxy since this gives us a direct insight into the actual orbit of the progenitor (Binney & Tremaine 2008, but

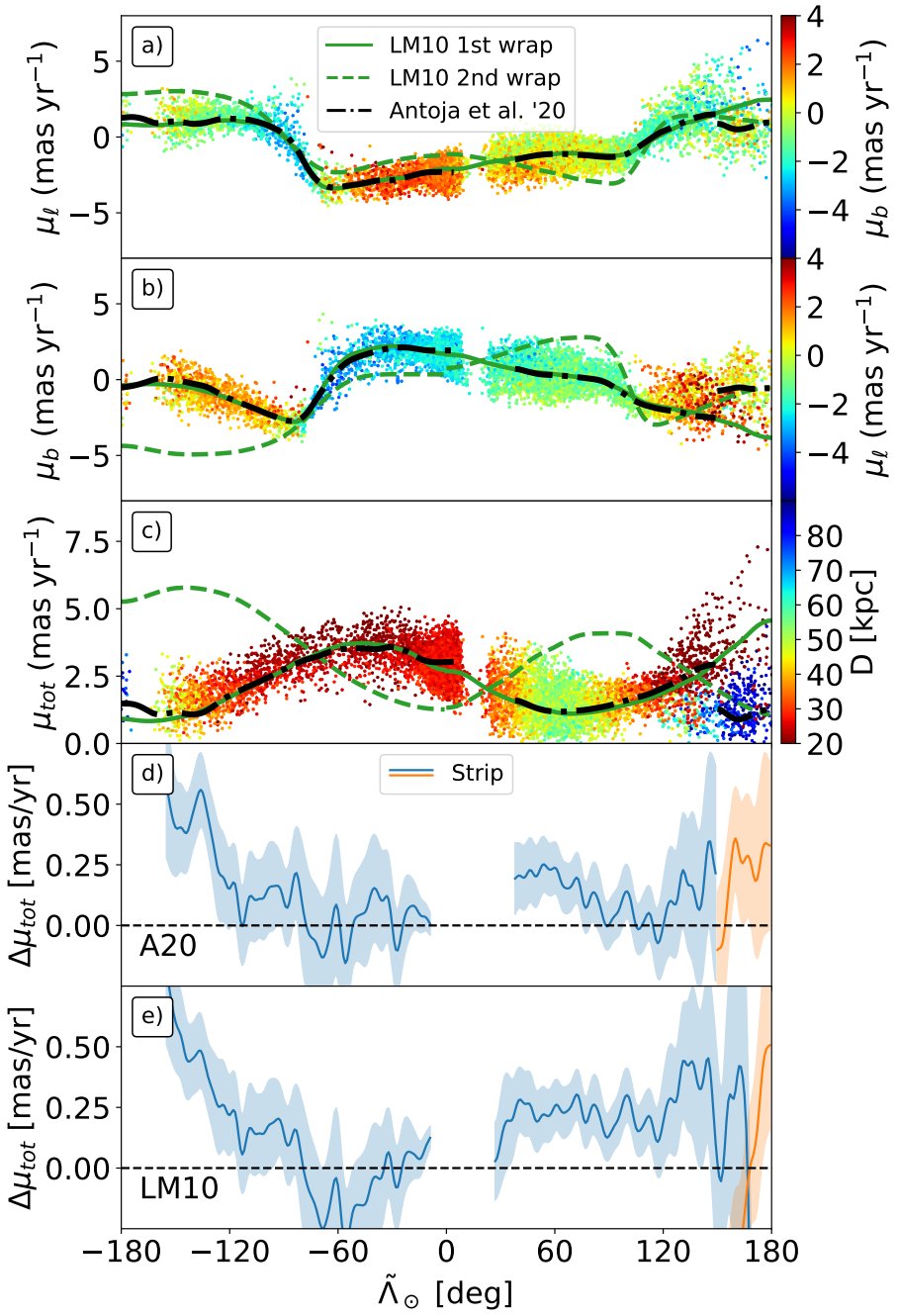

Figure 48: Proper motion trends with $\tilde{\Lambda}_\odot$ of the candidate RR Lyrae of the Sgr stream in the Strip sample. a) Proper motion in Galactic longitude coloured according to proper motion in Galactic latitude. b) Same as above but substituting longitude with latitude. c) Total proper motion coloured by distance. In all these panels, we show the predictions from the LM10 model with solid (first wrap) and dashed (second wrap) green lines, as well as the smoothed median from A20 (dashed-dotted black line). Panel (d) contains the residuals of the smoothed median of the total proper motion (blue - first wrap, orange - second wrap) minus that of A20. Panel (e), similarly, shows the residuals with respect to the LM10 model.

see Sanders & Binney 2013). Additionally, we also want to estimate the location of the apocentres and their angular separation, as these quantities can be used to characterise the stream and compare with independent determinations and models.

Panel (b) of Fig.49 shows the Galactocentric distance distribution of the stars in the Strip sample as a function of $\tilde{\Lambda}_\odot$. In orange we show the smoothed median in bins of 5°and its associated 1σ error. The green line corresponds to the prediction by LM10. We notice that the model does not follow our measurements, deferring more than 3σ in most parts of the stream, including the centre of the dwarf. These discrepancies cannot be due to the assumed metallicity zero point. We use Eqs. 10 and 11 to convert the residuals in distance observed in the leading arm into differences in metallicity and we find that there should be a change of ~1 dex in ~50° to account for it. This jump is much larger than the uncertainties in metallicity and would have been easily recognisable in Fig. 44. Moreover, the green and orange lines (model and data, respectively) cross at $\tilde{\Lambda}_\odot$ ~30° and again at $\tilde{\Lambda}_\odot$ ~80° implying a change of sign in the residuals. This would also require a shift in the sign of the offset (ΔZ defined in Sect. 5.3.2) to explain it, which by construction is not possible. Therefore, it is safe to conclude that the deviations from the model are indeed physical. The same applies to the trailing arm, where the discrepancy in metallicity is too large to be artificial. On the other hand, the pattern we find is compatible with the determination made by Hernitschek et al. (2017) although, compared to their work, we do not use any modelling of the halo and, as a result, the trend that we recover is smoother.

We tried to calculate the apocentres using the recipe described in Belokurov et al. (2014) and used again in Hernitschek et al. (2017), which consists of describing the apocentres of the debris as a Gaussian profile. We find that fitting a Gaussian to the leading arm does not accurately reproduce our observations and the results are highly dependent on the range of $\tilde{\Lambda}_\odot$ used. Instead, we construct a cubic spline (orange line in Fig. 49.b) to smooth the median and obtain a curve that can be evaluated at any point. We then use it to search for the local maximum. Due to the underlying binning, we use half the bin size in $\tilde{\Lambda}_\odot$ as the uncertainty in the angular position. In distance, we use the error in the median shown as an orange shaded area in Fig.49.b. Applying this strategy to the Strip samples leads to the following values (see Appendix C for the values estimated with nGC3):

- Trailing: $\tilde{\Lambda}_\odot = -193° \pm 2.^\circ5$ at $D_{GC} = (92.48 \pm 1.45)$ kpc
- Leading: $\tilde{\Lambda}_\odot = 64° \pm 2.^\circ5$ at $D_{GC} = (47.73 \pm 0.48)$ kpc,

with an angular distance between apocentres that implies a differential heliocentric orbital precession of $\omega_\odot = 360° + \tilde{\Lambda}^T_\odot - \tilde{\Lambda}^L_\odot = 103° \pm 3.^\circ5$.

We only show the statistical uncertainties but we stress again that an incorrect metallicity zero point would bias these estimates. Nevertheless, we expect the difference to be much smaller than 4% in distance (Sect. 5.3.2). On the other hand, the contribution of the uncertainty in the GC-Sun distance is negligible.

Our determination for the Strip, shown as vertical grey bands across the whole of Fig. 49, has to be compared with the values derived by Belokurov et al. (2014): $\tilde{\Lambda}_\odot = 71\overset{\circ}{.}3 \pm 3\overset{\circ}{.}5$ at D $= (47.8 \pm 0.5)$ kpc for the leading arm and $\tilde{\Lambda}_\odot = -189\overset{\circ}{.}5 \pm 1\overset{\circ}{.}0$ at D $= (102.5 \pm 2.5)$ kpc for the trailing arm ($\omega_\odot = 99\overset{\circ}{.}3 \pm 3\overset{\circ}{.}5$). We note that there is a $\sim 3.5\sigma$ discrepancy at the far apocentre, which cannot be reconciled by tuning ΔZ without creating tension in the near one. In contrast, the results of Hernitschek et al. (2017) using the RR Lyrae from PS1 are closer to ours: $\tilde{\Lambda}_\odot = 63\overset{\circ}{.}2 \pm 1\overset{\circ}{.}2$ at D $= (47.8 \pm 0.5)$ kpc for the leading tail and $\tilde{\Lambda}_\odot = -192\overset{\circ}{.}4 \pm 0\overset{\circ}{.}4$ at D $= (98.95 \pm 1.4)$ kpc for the trailing tail ($\omega_\odot = 104\overset{\circ}{.}4 \pm 1\overset{\circ}{.}3$). Nevertheless, the tension is still present. The major difference is that we have obtained our measurements in a model-independent way and using all the stars in our sample.

5.4.3 *A peek into the unknown: tangential velocities*

Finally, with all five dimensions together (position, proper motion, and distance) we can access an almost unexplored aspect of the stream: the tangential velocity. To do so, we make use of the *Python* package GALA (Price-Whelan, 2017; Price-Whelan et al., 2017) which provides a tool to correct for the solar reflex given the position and velocity of the Sun with respect to the GC. For that, we use the parameters described in Sect. 5.3. The resulting velocities for the Strip sample are shown in panels (c) and (d) of Fig. 49 for the velocity along ($v_{\tilde{\Lambda}_\odot}$) and across ($v_{\tilde{B}_\odot}$) the stream, respectively. In contrast with the previous section, here we smooth the median values in bins of 10°in $\tilde{\Lambda}_\odot$ with a Gaussian filter (similar to A20).

When looking at the velocity along the $\tilde{\Lambda}_\odot$ axis (orange line in Fig. 49.c) we note the general agreement with the LM10 model (green line). In most of the regions, both trends are compatible within 3σ except for i) the dwarf itself, where we find that our results are $\sim 20\,\mathrm{km\,s^{-1}}$ above the predictions; and ii) beyond $\tilde{\Lambda}_\odot > 80°$, where the differences exceed $70\,\mathrm{km\,s^{-1}}$ at some points. While the latter could be related to the contamination, it would need to bias both the distance by more than 5 kpc and the proper motions by more than $0.3\,\mathrm{mas\,yr^{-1}}$ to reconcile our observed $v_{\tilde{\Lambda}_\odot}$ with the model. A more likely scenario is that the orbit of the progenitor in LM10 is not accurately reproducing the observations, which is consistent with our findings of Sect. 5.4.2 and with the fact that we observe a significantly different tangential velocity for the dwarf.

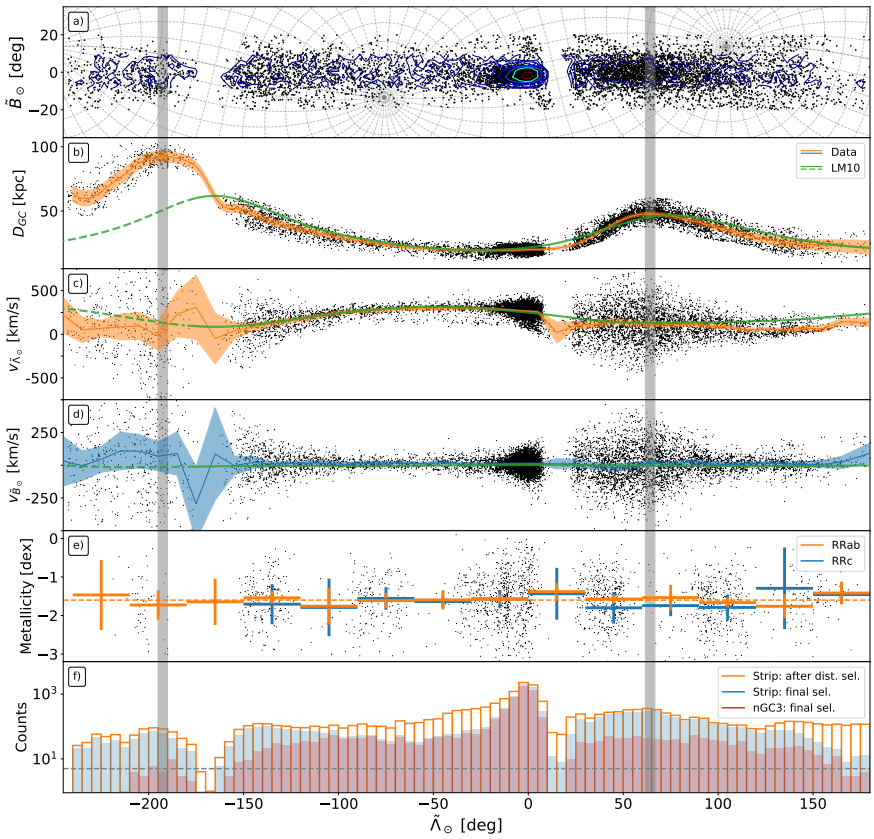

Figure 49: Position, distance, and velocity as a function of $\tilde{\Lambda}_\odot$ of the Sgr stream (Strip sample). a) Sky distribution with overlaid count contours. The dashed lines represents a regular grid in the Galactic coordinate frame. b) Smoothed median (orange line) and associated uncertainty (orange area) of the Galactocentric distance for the data (black dots) and LM10 (green line). c-d) Same as (b) but for the velocity in the $\tilde{\Lambda}_\odot$ (orange) and $\tilde{B}_\odot$ (blue) directions after correcting for the solar reflex. e) Median metallicity of the RR Lyrae types AB (orange) and C (blue). f) Histograms of $\tilde{\Lambda}_\odot$ for the Strip sample – but only after selecting by distance – (orange), for the final Strip sample (blue) and for the nGC3 sample (red). The dashed black line represents the threshold below which we do not compute the median used in the other panels. We also show the positions of the apocentres as two vertical grey stripes (see text).

The velocity perpendicular to the orbital plane of Sgr is also interesting since it is where the effects of other satellites like the Magellanic Clouds are expected to be more noticeable. This is the case of the Orphan stream, where the misalignment between the velocities of the stars and its orbit have been related to the Large Magellanic Cloud (Erkal et al., 2019). In panel (d) we show the changes in $v_{\tilde{B}_\odot}$ along the stream. We find no significant deviation from zero at the current level of precision but we notice the degeneracy with the velocities used to correct the solar reflex. Hayes et al. (2018) used a sample of Sgr stars to obtained an estimate of the Sun's velocity with respect to the GC by fitting the observations to the model of LM10. However, ideally we would like to obtain a global fit that can be used to quantify the deviations caused by the satellites and simultaneously estimate the solar parameters. While our sample can indeed be used for that purpose, this analysis is out of the scope of the present work.

We can also obtain a measure of the total velocity projected in the sky of the Sgr dwarf that can be used to initialise simulations from the present time, for example. We do so by summing in quadrature both components of velocity for all stars within a cone of 5° around the centre of the Globular Cluster M54 (Bellazzini et al., 2008). Then, the median tangential velocity is $V_\perp = 272.56 \pm 0.02\,\mathrm{km\,s^{-1}}$.

Our final output of this part is an interpolator for each component of the velocity for any $\tilde{\Lambda}_\odot$ along the stream. Despite the large uncertainties in proper motions, we can still recover a trend that can be used to test future models of Sgr. In Appendix D we explain how to download them, along with the rest of the interpolators used in this work, such as distance, proper motion, and so on.

5.4.4 *Metallicity*

Now that we have a reliable sample of candidates, we can check our initial assumption of a constant metallicity along the arms of Sgr (Sect. 5.3.2). The fifth panel of Fig. 49 shows the metallicity distribution for the stars for which this parameter has been measured. The error bars correspond to the median, with the associated error, in bins of 30° for both RRab (orange) and RRc (blue) RR Lyrae. The first thing we note is that the median oscillates around the dashed line that represents the mean value calculated in Sect. 5.3.2, with all stars in the range of distance between 20 kpc and 50 kpc: -1.6 dex.

With this we can already clearly see that there is no appreciable gradient. Nevertheless, we measure it by fitting a line to all RRab stars in the leading ($\tilde{\Lambda}_\odot$>0°) and the trailing ($\tilde{\Lambda}_\odot$<0°) arms. By doing so we obtain a slope of (-1.8±0.5) $\times 10^{-3}$ dex deg^{-1} and (0.3±0.4) $\times$ 10^{-3} dex deg^{-1} for the leading and trailing arms, respectively. While this could be easily disregarded as unimportant, we note that the current estimates of the metallicity gradient in the tails of Sgr are of

Table 8: Metallicity statistics of the nGC3 (Strip) final sample. For each type of RR Lyrae (first column) we show: the number of sources classified as such with reported metallicity (second column), their mean metallicity as given in the *Gaia* archive (third column), and the associated standard deviation (fourth column).

Type	N	<[Fe/H]> [dex]	$\sigma_{[Fe/H]}$ [dex]
RRab	997 (1 876)	-1.60 (-1.62)	0.63 (0.62)
RRc	89 (149)	-1.62 (-1.65)	0.45 (0.46)
RRd	1 (2)	-1.11 (-1.10)	- (0.02)

the order of $10^{-3}\,\mathrm{dex\,deg^{-1}}$ (Hayes et al., 2019). Nevertheless, considering the inhomogeneous coverage of the sky of the subsample of stars with metallicity and the possible contribution from contamination, it is hard to trust the variations that we measure. In the worst case scenario, this would cause a difference at the trailing apocentre of ~0.2 dex, which is of the order of the precision achievable with photometric metallicities. In turn, such a difference would imply that our measurement of the distance obtained in the previous section could be short by ~3%, that is, that the trailing apocentre could alternatively be at a distance of ~96 kpc instead of ~93 kpc. While this effect would bring our estimate closer to the values in the literature[7], it is still within its 2σ confidence interval. In summary, we can say that there is no measurable metallicity gradient at the current level of precision offered by the photometric metallicities.

Finally, we show the mean values of metallicity for each type of RR Lyrae star in Table 8 from which we can conclude that the metallicity of this sample is -1.61±0.01 dex.

5.4.5 *Completeness assessment*

Here, we inspect the distribution of the counts along the stream and the overlap between the different samples. The bottom panel of Fig. 49 shows the number of stars of the final Strip sample (blue bars) in 5° bins compared to the counts after the selection based on distance of Sect. 5.3.3 (orange step). Here, the dashed black line represents the imposed limit of five stars below which we do not compute the median used in panels (b), (c), and (d).

As expected, a significant fraction of the stars fall inside the dwarf itself: 4 730 (40%) in the region $\tilde{\Lambda}_\odot \in [-10°, 10°]$. The rest are spread rather uniformly except for the two parts where the stream crosses behind the MW disc, which are easily identifiable by a sudden drop

7 If we consider the gradient in both tails, then the estimate of the distance at the leading apocentre grows to ~48.5 kpc, departing from the values estimated by previous authors.

in the counts. We do observe a larger number of stars in the leading arm compared to the symmetric $\tilde{\Lambda}_\odot$ in the trailing arm, which is to be expected near apocentre where the stars in the stream slow down. Nevertheless, as explained in Sect. 5.3.4, the increase of the proper motion uncertainties near apocentre prevents us from effectively reducing the contamination there. That is why the orange (Strip sample after selecting only based on distance) and blue (final Strip sample) histograms are so close to each other in that region.

We also include the counts of the final nGC3 sample as red bars. In this case, the two distributions are similar for $\tilde{\Lambda}_\odot$<0° but are more different for the leading arm. The cross-match between both final samples tells us that all but 44 stars in the nGC3 sample are in the Strip sample. Thus, the missing stars in the leading tail are those that cause the difference in total proper motion seen in Fig. 48. Comparing both samples, we note that Cseresnjes (2001) estimated the total amount of RRab stars to be ~8 400. This value is almost exactly halfway between the number of stars in the nGC3 sample and the number in the Strip sample, reinforcing the idea that the former is pure but incomplete and the latter is complete but contaminated.

Regarding the cross-matched with A20, the first thing that is important to mention is that the sample of A20 contains only 3 476 RR Lyrae of the 182 495 from the list presented in Sect. 5.2. Compared to the Strip sample, the sample used in A20 contains 3 233 of the 11 677 selected in this work. If we restrict ourselves to the region where the contamination is lower (-120°<$\tilde{\Lambda}_\odot$<150°) then we find that out of the 3 145 RR Lyrae in A20, 3 033 are among the 10 431 of the Strip sample. This means that the recovery fraction is around 95%. If we now analyse the cross-match between the nGC3 and A20 samples, we see that the sample of A20 contains 2 712 stars of the 6 608 in the nGC3 sample; 2 661 out of 6 386 stars if we only consider the low contamination region defined in Sect. 5.4.5. The resulting recovery fraction is around 80% for the nGC3 sample. Since we obtained these estimates from low-contamination regions, we expect them to be similar to the true completeness but we stress that these percentages apply only to the true members among all the candidates (as if there was no contamination). In any case, the RR Lyrae in A20 that are *not* in any of our two samples can mostly be found in the dwarf, the tip of the tails (where we know that the contamination in A20 is higher), and, most interestingly, the leading apocentre. However, further investigation of the differences among the samples requires a fine characterisation of the different selection functions and we leave this for a future study. On the other hand, the recovery fraction for the RR Lyrae in A20 is roughly between 30% and 40% (we cannot extrapolate this estimates of completeness to stars with other colours and magnitudes). Nevertheless, expanding the list of A20 would require a good treatment of

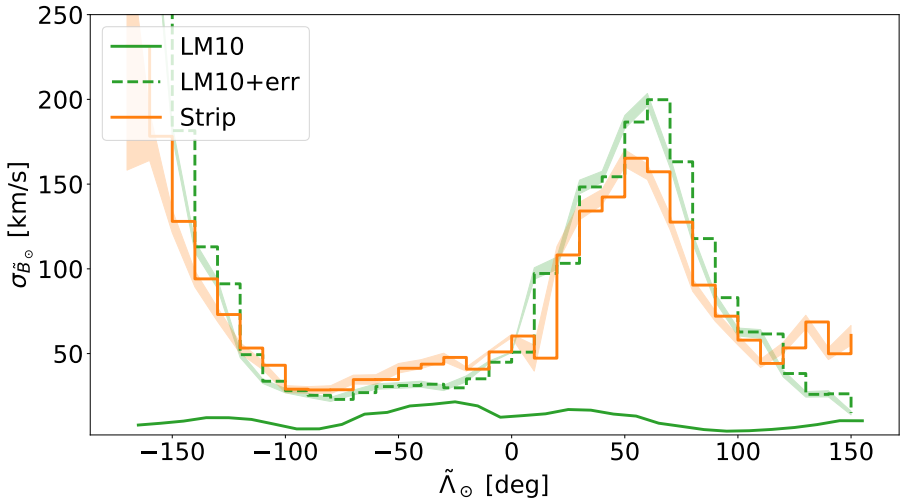

Figure 50: Velocity dispersion profile for $v_{\tilde{B}_\odot}$ as a function of $\tilde{\Lambda}_\odot$. The orange steps correspond to the velocity dispersion observed in the final Strip sample. The green lines are the LM10 model: the solid is for the model particles and the dashed for the model after introducing the observed errors in proper motion.

the contamination and probably the introduction of a model for the halo and thin/thick disc.

5.4.6 *Velocity dispersion*

As mentioned in Gibbons et al. (2014), the stars that escape through the Lagrange points do so with a dispersion in velocity inherited from the dispersion that the stars had at the outskirts of the dwarf, the latter being proportional to the total mass of the infalling satellite. Additionally, the stream can become kinematically heated by the continuous interaction with dark matter subhalos (Johnston et al., 2002). Therefore, learning about the velocity dispersion of the stream allows us to obtain a tighter constraint on the dynamical mass of the progenitor and potentially a test for dark matter models.

In Fig. 50 (Fig. 58) we show the velocity dispersion profile of $v_{\tilde{B}_\odot}$ for the Strip (nGC3) sample. We also include the profile of the LM10 model in green (solid line). We have been able to reproduce both curves easily with the LM10 particles by randomly assigning the uncertainties of the observed stars and subsequently applying only the initial selection (Sect. 5.3.1). The remaining differences between the observed profiles and the ones predicted by the model are mostly due to the fact that we did not apply the whole methodology described in Sects. 5.3.3 to 5.3.5. If we wanted to obtain an estimate of the deviations caused by possible subhalos, it would be necessary to build the selection function of our two samples and accurately model the observational errors.

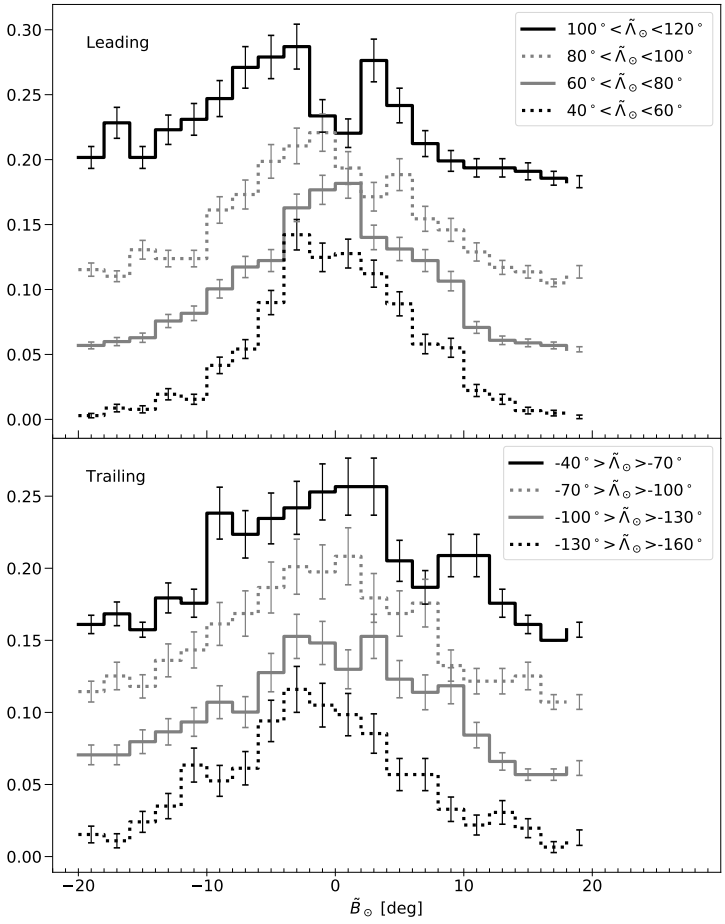

Figure 51: Histograms of $\tilde{B}_\odot$ normalised to the number count for different bins of $\tilde{\Lambda}_\odot$ for the Strip final sample. Top: Bins in the leading arm. Bottom: Bins in the trailing arm. We have added an arbitrary offset in the y-axis to each curve for visualisation purposes.

5.4.7 *The Bifurcation*

The bifurcation of the Sgr stream was observed for the first time by Belokurov et al. (2006) in the leading tail, and later detected in the trailing arm by Koposov et al. (2012) and Navarrete et al. (2017). This feature can be clearly seen with the M giants and shows the stream splitting into two branches creating a bi-modal distribution of $\tilde{B}_\odot$ in some portions of the tails. Although some models have been proposed to explain this feature with only one progenitor, for example Peñarrubia et al. (2010) (but see Peñarrubia et al. 2011), there is no consensus on its cause. Thus, it is important to provide additional observational evidence with different tracers to constrain the range of possibilities.

Figure 51 shows the histogram of $\tilde{B}_\odot$ of the final Strip sample for different bins in $\tilde{\Lambda}_\odot$ within the range -160°< $\tilde{\Lambda}_\odot$<120° (again, see Appendix C for the equivalent plot for the nGC3 sample). In some portions of the leading arm (top panel) a bi-modal distribution is evident.

The strongest signal is in the range $100^\circ<\tilde{\Lambda}_\odot<120^\circ$, where the two highest peaks are separated by $\sim 6^\circ$. We note the agreement between our findings and those in Belokurov et al. (2006), where these latter authors report the beginning of the bifurcation at $\tilde{\Lambda}_\odot \sim 80^\circ$ and the separation between the two branches growing from $\sim 7^\circ$ to $\sim 10^\circ$ at $\tilde{\Lambda}_\odot \sim 120^\circ$. In the trailing arm, there is no appreciable bifurcation. We have increased the bin width to compensate for the lower number of counts, but still we cannot see a significant signal (bottom panel of Fig. 51).

To investigate the possible differences between the two branches observed in the leading arm, we compute the weighted means for the distance and proper motions in four bins of $\tilde{\Lambda}_\odot$: 90° to 100°, 100° to 110°, 110° to 120°, and 120° to 130°. The weight assigned to each star represents the probability of belonging to one branch or the other based on their $\tilde{B}_\odot$. To obtain these two probability distribution functions, first we create a kernel of $\tilde{B}_\odot$ to have a continuous representation of the histogram. We then locate the only two local maxima that the kernel has and associate each one with either branch A (negative $\tilde{B}_\odot$) or branch B (positive $\tilde{B}_\odot$). After that, we restrict ourselves to $\pm 1.5^\circ$of one of the peaks, that is,, we only use the values of the kernel near the local maxima, and fit a parabola with which we can obtain a probability at every $\tilde{B}_\odot$ (wherever the parabola returns a negative probability we instead use zero). Finally, we repeat the procedure for the other peak to obtain the second probability distribution. Panels (a) to (d) of Figure 52 show the original histogram of $\tilde{B}_\odot$ at each bin in $\tilde{\Lambda}_\odot$ (black line) along with the resulting weighted histograms for branches A (blue) and B (orange). Panels (e) to (g) contain the corresponding weighted averages and their 1σ uncertainties in heliocentric distance, proper motion in right ascension, and proper motion in declination, respectively. To compute the uncertainty in this estimate, that is, the standard error of the weighted mean (SEM), we used the formalism of Cochran (1977)[8]. In order to cancel the gradients observed in the previous sections, we subtract the median value obtained from the stars within the bin.

The result is that the differences that we measure between the two sides of the bifurcation are always smaller than 2σ. Nevertheless, we note that the orange line in panel (e) is always below the blue one. This can be due to many factors, such as projection effects caused by the stream being a 3D structure, or contamination, since the faint branch (B) is more susceptible than the bright branch (A), or simply because one branch is actually more extincted than the other, which may not be well reproduced with the extinction map that we use. As an example, supposing that the latter is true, we would only need to

8 $(\mathrm{SEM}_w)^2 = \frac{n}{(n-1)\sum \omega_i}[\sum(\omega_i x_i - \bar{\omega}\bar{x}_w)^2 - 2\bar{x}_w \sum(\omega_i - \bar{\omega})(\omega_i x_i - \bar{\omega}\bar{x}_w) + \bar{x}_w^2 \sum(\omega_i - \bar{\omega})^2]$

add <0.1 mag of extinction to the mean distance of branch A to bring the blue line in panel (e) down to the orange line.

In contrast with the recent study of Yang et al. (2019), where these latter authors report differences in velocity and metallicity for Blue Horizontal Branch stars in the bifurcation, we conclude that there is no significant separation in either kinematics or distance between the two branches of the leading tail. Furthermore, if the branches were indeed different, their separation should be of the order of <1.5 kpc and <0.2 mas $^{-1}$. We have also looked at the metallicity and find no significant difference, but due to the small number of stars available and the measurement errors, we cannot give any meaningful upper limit. Finally, the fact that we do not observe the bifurcation in the trailing tail could be related either to our selection function or simply to a lack of stars.

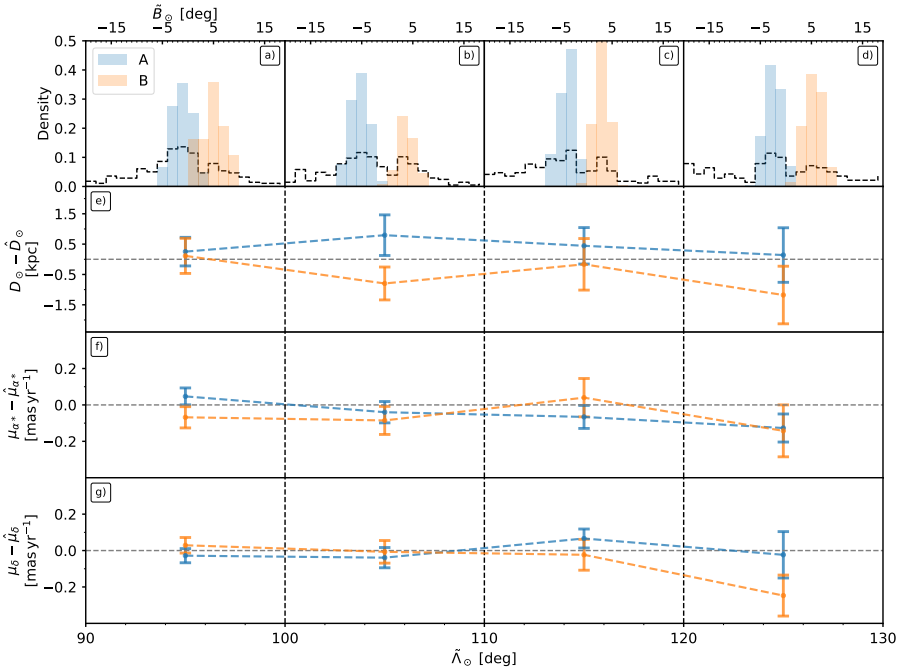

Figure 52: Comparison between the bright (A, blue) and faint (B, orange) branches of the bifurcation at different $\tilde{\Lambda}_\odot$>90° (Strip sample). The top panels (a) to (d) show the histogram of $\tilde{B}_\odot$ (black line) corresponding to the stars that fall in the range of $\tilde{\Lambda}_\odot$, from left to right, [90°-100°, 100°-110°, 110°-120°, 120°-130°]. We also show the weighted histograms for each branch, which highlight the stars that contribute to compute the means plotted in the panels below. In panel (e) we plot the weighted mean heliocentric distance, after subtracting the median distance, and the associated error. Panels (f) and (g) contain the weighted mean and its error for the proper motion in right ascension and in declination, respectively. Here we also subtract the median value of the bin to cancel the overall gradients.

5.5 CONCLUSIONS

Gaia has revolutionised the field of Galactic astronomy. With only 22 months of data, the scientific community has already been able to make numerous and quite significant discoveries. Furthermore, DR2 can produce novel results concerning areas that have already been thoroughly examined. The Sgr stream is a good example of this, and in this work, as well as in A20, we wanted to demonstrate what its discovery would have been like in the *Gaia* era, using only its kinematics.

We have produced two catalogues of probable RR Lyrae members of the Sgr dwarf and stream, starting with the most basic assumptions and exhausting the *Gaia* outputs to carefully select the list of candidates step by step. The two catalogues are produced by running this trimming process twice, each time from a different starting point. In the first case, we look for stars that are rotating coherently in a plane through the GC and end up with the nGC3 sample: a higher-purity but lower-completeness ($\approx 80\%$) sample. By demanding that the stars and their velocities do not deviate significantly from the mean orbital plane, we are able to efficiently discard most of the contamination at the cost of introducing kinematical biases. The second time, we select all stars in the sky that are within $\pm 20^\circ$ from the known midplane of the stream. In doing so, we obtain the Strip sample: a higher-completeness ($\approx 95\%$) but lower-purity sample. In this case, we rely on our data-driven selection schema based on distances and proper motions to get rid of most of the contamination. We have composed a list of 11 721 stars belonging to either the Strip (11 677 stars) or the nGC3 (6 608 stars) sample, and have made this list publicly available.

The main output of this work is the largest sample of RR Lyrae in the Sgr stream to date with both proper motions and distances together. This allows us to study, for the first time, the tangential velocities along the whole stream and provide a reference to compare against. Our results confirm the findings by A20 regarding the proper motion track along the stream. We observe more or less the same trends in proper motion, with differences of less than 0.3 mas/yr in most parts of the stream, with the only exception being those regions where either our sample or that of A20 are known to be contaminated. Also, we note that 93% of the RR Lyrae contained in A20 are inside our final sample, confirming that both are detecting the same structure. It will be interesting to compare our work with that of Ibata et al. (2020) in which, as we recently found out, they also provide a list of RR Lyrae obtained with *STREAMFINDER* (Malhan & Ibata, 2018). In doing so, we can produce an independent estimate of the completeness and quantify the possible biases. Of particular interest is the *Sagittarius Stream Selected Sample* of Bellazzini et al. (2020), composed of the 5 385 RR Lyrae from the `gaiadr2.vari_rrlyrae` catalogue that

pass a set of filters requiring that the stars are near the orbital plane of Sgr, rotate with it, and have a $\mu_{\tilde{\Lambda}_\odot}$ trend compatible with the fit obtained by Ibata et al. (2020). This sample is, by construction, very similar to our nGC3 since it requires that the stars must have their velocity vectors aligned with $\tilde{\Lambda}_\odot$. Nevertheless, apart from having less stars, we note from Fig. 1 of this latter-mentioned publication that there is no specific cut in distance. This means that on the one hand the nearby stars close to the bulge have not been removed, while on the other, features like the *fluff* (Sesar et al., 2017a) can be better preserved.

We compare the evolution of the different observables with $\tilde{\Lambda}_\odot$ against LM10, the reference model for most studies of Sgr. The residuals in proper motion are within the uncertainties, apart from the known issues discussed in Sect. 5.4. That is, that the Strip's mean $\mu_{\alpha*}$ is not reliable beyond $\tilde{\Lambda}_\odot$>120°and that the nGC3 sample is biased. When comparing the heliocentric distances, we find that the discrepancies are very much significant and not attributable to a gradient in metallicity or an incorrect calibration. Instead, we confirm the results of previous works (e.g. Belokurov et al. 2014; Hernitschek et al. 2017) which already pointed out that the apocentres in LM10 are inaccurate in terms of both $\tilde{\Lambda}_\odot$ and distance. More recent models are able to reproduce this, such as the one by Fardal et al. (2019), but how well their proper motions perform in light of the new observational constraints that we provide here is yet to be tested. We have also determined new apocentres based on the maximum Galactocentric distance of the tidal debris: $\tilde{\Lambda}_\odot = -193° \pm 2.^\circ5$ at $D_{GC} = (92.48 \pm 1.45)$ kpc for the trailing tail and $\tilde{\Lambda}_\odot = 64° \pm 2.^\circ5$ at $D_{GC} = (47.73 \pm 0.48)$ kpc for the leading. Our values are in some tension with those determined by Hernitschek et al. (2017) which cannot be explained by an incorrect metallicity zero point, and are most likely related to the fact that we used a completely empirical method to make our estimates.

With the Strip sample, we have been able to test the tangential velocities predicted by LM10. We find that the predictions agree within uncertainties in the trailing arm but fail to reproduce our observations at the location of the dwarf and at the leading arm. Moreover, we provide a measurement of the total velocity projected in the sky for the progenitor, $V_\perp$ = (274.18±0.02) $km\,s^{-1}$. Despite the complexity of our selection process, we can add that the velocity dispersion profiles of the model are also compatible with our observations.

Regarding the metallicity, we do not observe any meaningful gradient with $\tilde{\Lambda}_\odot$ at the current level of precision and the mean value we recover is -1.6 dex in the ZW84 scale. This is in contrast with other studies where differences are detected for most populations. In particular, Yang et al. (2019) reported a significant difference between the leading and the trailing arm for the Blue Horizontal Branch stars. Even though we use photometric metallicites instead of spectroscopic ones,

the former having larger uncertainties, and the hypothetical gradient has to be of the order of $10^{-3}\,\mathrm{dex\,deg^{-1}}$ at most in absolute value. Such small gradients would cause differences along the stream no larger than ~0.2 dex, which is similar to the typical precision for the photometric metallicities. However, we notice that the gradients that we have measured, which are compatible with the values obtained by Hayes et al. (2019), would imply that the trailing arm is on average slightly more metal rich than the leading arm, in agreement with previous works (e.g. Yang et al. 2019).

The nGC3 sample is a great starting point for a spectroscopic follow-up. Taking advantage of its high purity, the risk of measuring abundances and radial velocities for an off-stream star is minimised. The resulting catalogue would be the most extensive 6D+abundance sample of Sgr RR Lyrae to date, providing a more detailed picture of the metallicity of the stream and probing the full phase-space information for a single tracer.

We also searched for the bifurcation in our data and indeed observe it in both samples. We see a clear signal in the leading arm where it was originally discovered. We observe no significant separation in velocity, distance, or metallicity between the bright and faint branches. Also, we do not detect the bifurcation on the trailing arm where it was found by Koposov et al. (2012), perhaps because of the low number of stars we have in that region or because of the filters in distance and proper motion used to select the members. It will be interesting to obtain follow-up spectroscopic observations of the stars at each branch and study whether or not there is a separation in line of sight velocities as well.

Finally, we provide empiric trends (smoothed medians) in distance, proper motion, and tangential velocities of our final Strip sample (see Sect. D), along with the respective uncertainties. We also give these trends as interpolators that can be evaluated at any $\tilde{\Lambda}_\odot$, which can be very helpful when modelling the stream.

APPENDIX

A *Tailored Gaussian Mixture*

Here we explain the TGM algorithm in more detail. We use the particular case of the distance (see Sect. 5.3.3) to guide the exposition, but the steps are the same for any other quantity that varies as a function of $\tilde{\Lambda}_\odot$ ($\mu_{\alpha*}$ and μ_δ). We only tweak the parameters to obtain a better performance for each case: bin size, step size, threshold, maximum separation and kernel bin width.

First we take all the stars in the range $-2.5^\circ \leqslant \tilde{\Lambda}_\odot < 2.5^\circ$ and obtain a Gaussian kernel to the corresponding distance histogram. Having done that, we evaluate the kernel at 100 000 points and apply a

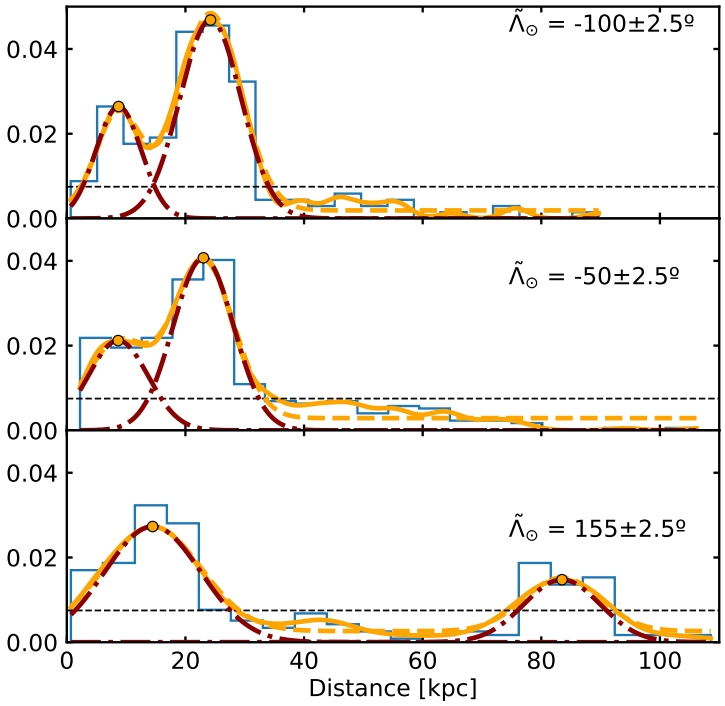

Figure 53: Example of the TGM applied to the distance distribution at selected bins of $\tilde{\Lambda}_\odot$=[-100°,-50°,155°] for the Strip sample. The blue steps show a histogram of the heliocentric distance of all stars with a bin size of 5°. The solid orange line is the kernel obtained with the parameters detailed in the text. The orange dots that appear on top of it are the peaks detected and the red lines the corresponding Gaussian distributions obtained from the fit. Finally, the orange dashed line is the reconstruction of the kernel with the individual Gaussians added together.

peak finder algorithm (`scipy.signal.find_peaks`) to locate all local maximum. We keep only those whose height are above a certain dimensionless threshold, set arbitrarily so that we can remove the small oscillations appearing on the tails of the distributions due to Poisson noise (0.0075 in this case). The remaining n peaks are then used as centres of n normal probability distributions. Finally, we fit the sum of a constant floor level (free parameter) and n Gaussians for which we set free their widths (σ [kpc]) and amplitudes. For that, we use the Least Square Minimisation algorithm implemented in `Scipy` and find the σ for each component that better reproduce the kernel. In order to avoid spending too much time at each bin, we limit the number of Gaussians to the four with highest height. Three examples of the fitting process are shown in Fig. 53.

Given that at $\tilde{\Lambda}_\odot$=0° the dominant component is that of the Sgr dwarf, we assign the Gaussian with the largest amplitude to the stream. Subsequently, we simply repeat this strategy every 5° in both directions, negative and positive $\tilde{\Lambda}_\odot$, but now associating to the stream the component most similar to the previous one. To define which

is the most similar we apply the following rule: rank the peaks by height, filter out those that are too far apart, and then chose the first one. In this case, we impose a maximum difference between two consecutive peaks of 10 kpc.

This method relies on the separation between the different components at any given $\tilde{\Lambda}_{\odot}$. If they are too close to each other, we need a smaller bin width when creating the kernel to resolve them at the expense of increasing the number of peaks created by simple Poisson noise. On the other hand, if we smooth the kernel too much in an effort to reduce the spurious peaks, the different components can interfere with each other, and therefore we obtain a biased position. Here, we have chosen a value of 0.15 (in the units given by the `Scipy` function) for both the Strip and the nGC3 samples.

In Sect. 5.3.4 and 5.3.5, we applied the same procedure but with the following parameters:

- Bin size: 2.5°
- Step size: 5°
- Bin width: 0.30
- Threshold: 0.10
- Separation: 1.5 mas yr^{-1}

As a final remark, it is also worth mentioning that we tried using the common clustering algorithms like DBSCAN, hierarchical DBSCAN or k-means. Nevertheless, most of this methods are based on density and, in our case, the Sgr stream presents significant gradients which result in suboptimal performance. We acknowledge that there could exist a combination of parameters and a coordinate transformation such that a clean separation between the contamination and the stream stars appears but, after some trial and error, we decided to apply the TGM.

B *Strip sample selection process*

Here we show the plots of each state of the filtering process starting from a Strip in the sky around the Sgr orbital plane (see Sect. 5.3.1). First, we apply the TGM to the heliocentric distance (Fig. 54) then on the proper motion in right ascension (Fig. 55) and finally, on the proper motion in declination (Fig. 56). The number of stars remaining after each step can be found in Table 7.

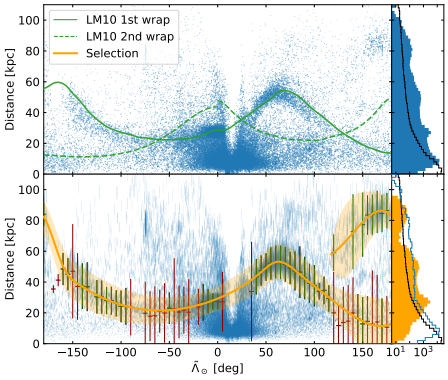

Figure 54: Same as Fig. 45 for the Strip sample.

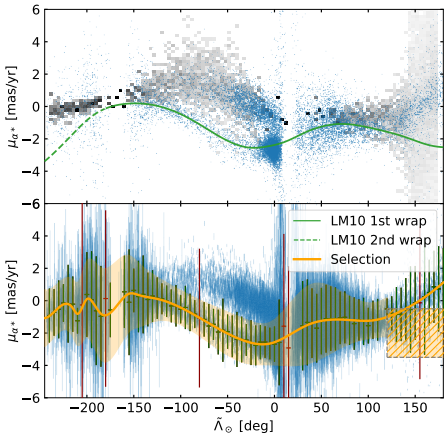

Figure 55: Same as Fig. 46 for the Strip sample.

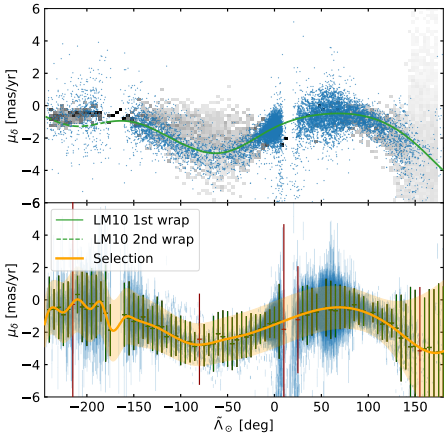

Figure 56: Same as Fig. 47 for the Strip sample.

C *Summary plots of the nGC3 sample*

In this Appendix we discuss the summary plots of the nGC3 sample, similar to what we have done for the Strip sample in Sect. 5.4.

Figure 57 contains the tracks in proper motion, equivalent to Fig. 48. With panels (a) to (c) it becomes obvious that, in the leading arm, the stars in the nGC3 sample are always on one side of the median predicted by LM10 and the observed by A20. This is confirmed with the residuals, shown in panel (d), where we plot the difference between the median of the nGC3 sample and A20 (computed in the same way), along with the 1σ intervals. This figure shows that even though the overall trends are similar, the discrepancy between A20 and the nGC3 sample exceeds 3σ in the leading arm, becoming smaller as $\tilde{\Lambda}_\odot$ increases. The difference between the nGC3 and the Strip sample in that region is also considerable, at the level of 2σ throughout the range $0<\tilde{\Lambda}_\odot<100°$. When compared to the model, additionally to the already mention bias in the leading arm (related to the lack of stars with small total proper motion) we also observe a large discrepancy in proper motions at $\tilde{\Lambda}_\odot \sim 40°$, as well as significant residuals in the trailing arm around $\tilde{\Lambda}_\odot \sim -120°$. All together, we suspect that the use of the PCM method has introduced some bias. Indeed, when we apply nGC3 algorithm to the LM10 particles we observe a similar behaviour in the residuals, thus confirming that the nGC3 sample is kinematically biased.

Regarding the trend in Galactocentric distance, we apply the same method described in Sect. 5.4.2 to this sample and obtain the following apocentres for the tidal debris:

- Trailing: $\tilde{\Lambda}_\odot = -188° \pm 2.^\circ5$ at $D_{GC} = (93.22 \pm 2.39)$ kpc
- Leading: $\tilde{\Lambda}_\odot = 66° \pm 2.^\circ5$ at $D_{GC} = (47.34 \pm 0.58)$ kpc.

The values we obtain for the nGC3 and Strip samples are compatible with one another, but we note that the angular positions in the trailing apocentre differ by one bin (i.e. 5°). Given that the nGC3 sample has few stars in that region, we expect the value inferred from the Strip to be more robust.

We have also calculated the total perpendicular velocity around M54, like we did in Sect. 5.4.3 for the Strip sample, resulting in a $V_\perp$ of 274.18±0.02 km s^{-1}. The (small) difference between both samples is most likely caused by the larger fraction of contamination present in the Strip sample.

Regarding the metallicity gradients, the difference is also small. In the case of the nGC3 sample, the result is (-2.3±0.7) $\times 10^{-3}$ dex deg^{-1} in the leading arm and (1.2±0.6) $\times 10^{-3}$ dex deg^{-1} in the trailing. The velocity dispersion profile, in contrast to the Strip sample, in this case is dominated by the initial selection method: the PCM nGC3 technique. This is illustrated in Fig 58 where we show the profile derived

from the nGC3 sample (red) along with the prediction of LM10 (solid green) and the result of adding realistic errors in proper motion and applying the PCM to the particles of the model (dotted-dashed line). Finally, regarding the bifurcation discussed in Sect. 5.4.7, it is also evident in the nGC3 sample as can be seen in Fig. 59.

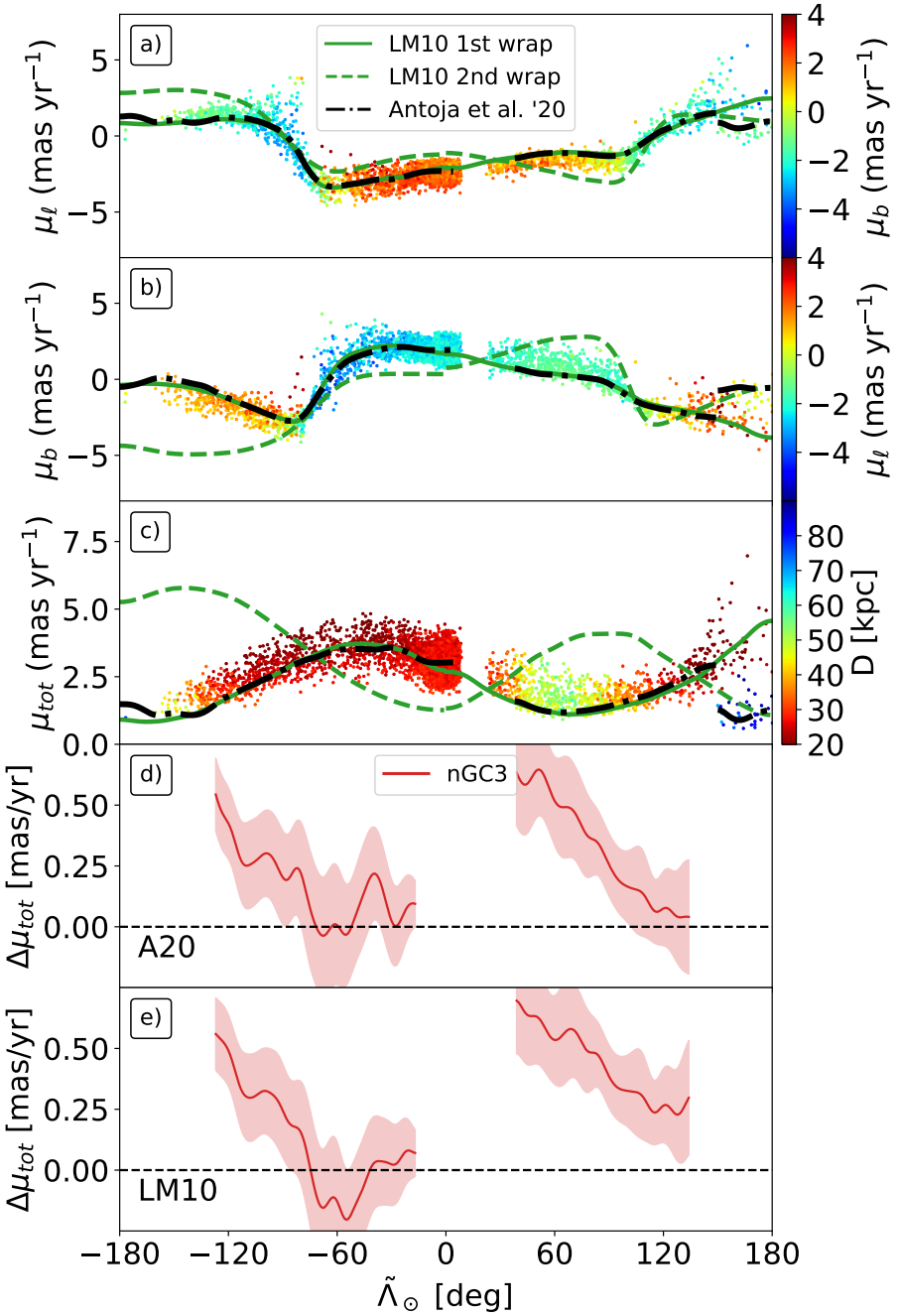

Figure 57: Same as Fig. 48 for the nGC3 sample.

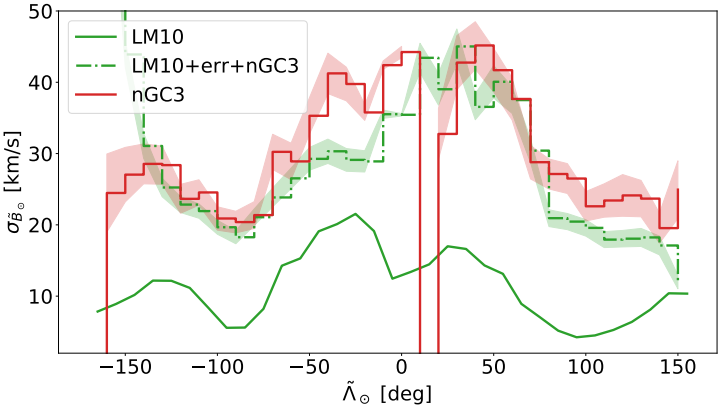

Figure 58: Same as Fig. 50 but for the nGC3 sample.

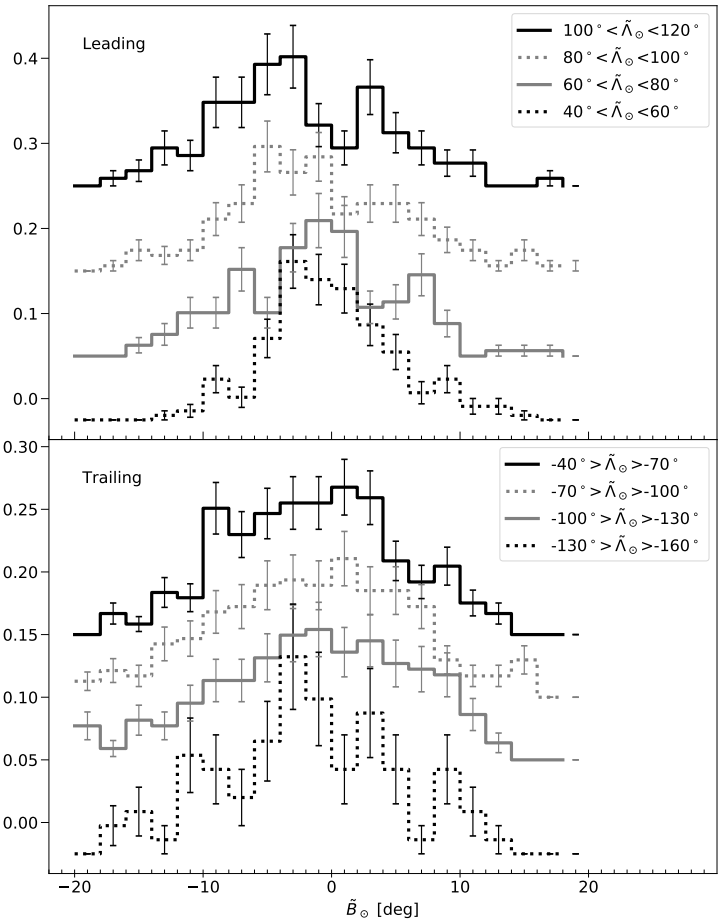

Figure 59: Same as Fig. 51 for the nGC3 sample.

D *Samples and interpolators*

Table 9 contains our final sample after the trimming process detailed in Sect. 5.3. Along with the `source_id` and apparent magnitude in the G band, which can be used to identify the star, we also provide the astrometry in three different Celestial coordinates: ICRS, Galactic

and Sagittarius (as defined in Sect. 5.3.1). Additionally, we include the quantities that have been calculated in this work: distance and velocity along ($v_{\tilde{\Lambda}_\odot}$) and across ($v_{\tilde{B}_\odot}$) the orbit. We have also added the type of star – either RRab, RRc or RRd – according to the SOS team, the PS1 classification and the VC table. Finally, we add two codes that can be used to filter the sources based on, respectively, their source catalogue (SOS, PS1 and/or VC) and our classification (nGC3 and/or Strip). In case of the latter, for instance, the first bit corresponds to the nGC3 sample, being 1 when the star is contained in that sample and 0 otherwise. Similarly for the Strip sample, which is represented by the second bit. As an example, a source with the code *'01'* on the last column (see caption of Table 9) has been found on the Strip sample but not on nGC3.

We also provide a series of interpolators that can be used to obtain the values of the heliocentric distance, proper motion in each reference frame (ICRS, Galactic or Sagittarius) and tangential velocities ($v_{\tilde{\Lambda}_\odot}$ and $v_{\tilde{B}_\odot}$). The interpolators are given as a table containing the median of the corresponding quantity in bins of $\tilde{\Lambda}_\odot$ and as a pickled *Python* function (a stream of bytes that represent said object). In the case of the later, we include instructions for loading them into *Python*. All this information, and more, can be found at https://services.fqa.ub.edu/sagittarius.

Table 9: First ten rows of the sample of RR Lyrae stars selected with our method as probable members of the Sgr stream and dwarf. For each star, we provide `source_id` (column 1), *G* apparent magnitude (column 2), distance (column 3) and its error (column 4) along with sky positions and proper motions, with the associated uncertainties, in three different reference systems (columns 5 to 22): ICRS, Galactic and Sagittarius in that order. We also provide in columns 23 to 26 the tangential velocities along and across the stream with its errors. Then, columns 27 to 29 contain the type of RR Lyrae according to, respectively, the SOS team, the PS1 classification or the VC table. Finally, column 30 contains a 3-bit code to specify in which source catalogue the source can be found: 1st bit, SOS table; 2nd bit, PS1; 3rd bit, VC. Similarly, the last column is a 2-bit code that can be used to separate between the nGC3 sample (first bit) and the Strip sample (second bit). The full table is available at the CDS.

source_id	G	D	σ_D	ra	dec	$\mu_{\alpha*}$	$\sigma_{\mu_{\alpha*}}$	$\mu_{\delta*}$	σ_{μ_δ}
	[mag]	[kpc]	[kpc]	[°]	[°]	[mas yr^{-1}]	[mas yr^{-1}]	[mas yr^{-1}]	[mas yr^{-1}]
1775711279448832	18.176125	29.74	1.25	46.055586	0.974464	-0.00100	0.337000	-1.456000	0.294000
2882438451930880	18.433370	34.04	1.44	44.322907	0.785228	0.44944	0.420931	-1.940657	0.344875
7820276453880320	17.942139	26.85	1.15	46.699115	2.303871	-0.27400	0.293000	-1.969000	0.339000
1035533795140608	17.633774	22.33	0.94	46.817211	3.026294	-0.24200	0.243000	-2.612000	0.234000
1407379179248512	17.636488	24.05	1.03	42.887455	1.805318	0.00500	0.221000	-2.736000	0.205000
1742622850845696	18.143019	29.20	1.25	45.233647	2.930012	0.38200	0.361000	-1.910000	0.353000
1889068351365504	18.687496	37.34	1.59	45.880614	3.615917	-0.75300	0.424000	-1.982000	0.388000
2018600269987200	18.124815	28.20	1.18	44.924684	3.642131	0.07200	0.299000	-2.260000	0.265000
2057461133775616	18.324300	31.47	1.32	44.046648	3.646809	0.19800	0.334000	-1.339000	0.337000
2345017784412032	17.838280	24.52	1.04	47.234054	2.984734	0.25200	0.228000	-2.590000	0.233000

Table 9: First ten rows of the sample of RR Lyrae stars selected with our method as probable members of the Sgr stream and dwarf (continuation).

l	b	μ_{l*}	$\sigma_{\mu_{l*}}$	μ_b	σ_{μ_b}	$\tilde{\Lambda}_\odot$	$\tilde{B}_\odot$	$\mu_{\tilde{\Lambda}_\odot *}$	$\sigma_{\mu_{\tilde{\Lambda}_\odot *}}$	$\mu_{\tilde{B}_\odot}$	$\sigma_{\mu_{\tilde{B}_\odot}}$
[°]	[°]	[mas yr^{-1}]	[mas yr^{-1}]	[mas yr^{-1}]	[mas yr^{-1}]	[°]	[°]	[mas yr^{-1}]	[mas yr^{-1}]	[mas yr^{-1}]	[mas yr^{-1}]
177.010893	-47.466387	1.048785	0.315392	-1.009944	0.317069	-118.292238	-5.411846	0.725345	0.326881	-1.262462	0.305211
175.393271	-48.834901	1.687999	0.382442	-1.057737	0.387117	-116.690091	-4.711547	0.581370	0.405304	-1.905297	0.363113
176.272049	-46.078912	1.215095	0.208588	-1.573398	0.396562	-119.515437	-4.577431	1.213980	0.377142	-1.574258	0.241937
175.653504	-45.487516	1.681556	0.238517	-2.013325	0.238568	-119.977084	-4.008319	1.503414	0.240825	-2.149617	0.236238
172.740556	-49.094217	1.864541	0.194024	-2.002301	0.230696	-115.956967	-3.109966	1.367416	0.232648	-2.369788	0.191679
174.126892	-46.666029	1.601207	0.334025	-1.109126	0.378626	-118.553571	-3.306850	0.619289	0.377788	-1.846755	0.334972
174.109970	-45.723944	0.835326	0.395506	-1.948734	0.417007	-119.456350	-3.032725	1.637522	0.424904	-1.346794	0.387010
173.088715	-46.362979	1.599826	0.261816	-1.597917	0.301792	-118.640657	-2.535687	1.062825	0.308080	-1.995792	0.254387
172.147907	-46.955375	1.050140	0.335371	-0.854008	0.335636	-117.882781	-2.094757	0.496883	0.334750	-1.259060	0.336255
176.111968	-45.220658	2.024245	0.194627	-1.635248	0.261522	-120.319169	-4.250378	1.061385	0.256281	-2.375935	0.201477

Table 9: First ten rows of the sample of RR Lyrae stars selected with our method as probable members of the Sgr stream and dwarf (continuation).

$v_{\hat{\Lambda}_\odot}$ [km s^{-1}]	$\sigma_{v_{\hat{\Lambda}_\odot}}$ [km s^{-1}]	$v_{\hat{B}_\odot}$ [km s^{-1}]	$\sigma_{v_{\hat{B}_\odot}}$ [km s^{-1}]	SOS	PS1	VC	Catalogue	Sample
156.23	46.55	63.64	43.11	-	RRab	-	010	01
147.25	65.70	-65.71	58.66	RRab	RRab	RRab	111	01
208.87	48.83	41.18	30.84	-	RRab	RRab	011	11
213.67	27.04	13.94	25.02	-	RRc	-	010	11
209.06	27.99	-28.47	21.89	-	RRab	RRab	011	11
139.78	52.64	-14.05	46.37	-	RRab	RRab	011	11
344.24	76.64	3.08	68.51	-	RRab	RRab	011	01
196.16	41.99	-25.29	34.02	RRc	RRc	RRc	111	11
127.96	50.22	53.63	50.21	-	RRc	-	010	01
177.98	30.74	-34.68	23.47	-	RRab	RRab	011	11

SUMMARY OF RESULTS, DISCUSSION AND CONCLUSIONS

6

In this thesis, we have looked into the kinematical substructure of the Milky Way (MW) across its different components, from the disc – either close to the Sun or its edge – up to the halo. Said substructure appears as a result of symmetry breaks in the gravitational potential like non-axisymmetric components (bar/spiral arms) or non-stationary phenomena (gravitational perturbations caused by external galaxies or the bar, stripped stars from an accreted satellite, etc.), which means that we can exploit the signatures in velocity space to learn about the complex history of our Galaxy. The global analysis performed in this thesis offers a detailed view of the state of the MW and provides a link between the disc and the halo through the orbit of the Sagittarius (Sgr) dwarf and its interaction with our Galaxy. In the following paragraphs, I comment on the main findings of each Chapter, then discuss on the recent developments in the field and propose possible avenues to take from here onward, before finally presenting my conclusions.

6.1 SUMMARY

As a result of the study presented in Chapter 2, where we analysed the substructure present in the velocity plane (v_R-v_ϕ) of the disc at different Galactocentric radius and azimuths, we have homogenised the list of known *moving groups* and expanded it with new ones both near and a few kiloparsecs away from the Sun. By tracking the changes of each moving group with position, we have found that all the structures shift towards lower azimuthal velocity with Galactocentric radius, but each one with a different slope. In fact, both components of the velocity change with radius, as well as with azimuth. In the case of the latter, they do so with much smaller gradients and without a coherent sign on their slopes, as some structures increase their angular momentum in the direction of the Galactic rotation while some others do the opposite. Measuring these changes is pivotal since many of the dynamical models proposed thus far to describe the disc predict significantly different behaviours for the kinematic substructure with both azimuth and radius. The precise characterisation and further quan-

tification of the morphology of the structures and their gradients allowed us to associate, tentatively, each one with a different dynamical mechanism based on the quantities that remain almost constant along the tracks: resonances roughly preserve the angular momentum perpendicular to the disc, while stars trapped in phase-mixing should have similar frequencies (thus, similar energies). In doing so, we have been able to reconcile the views of Minchev et al. (2009) and Gómez et al. (2012) (the velocity plane is dominated by arch-like structures induced by phase-mixing) with those of, e.g., Antoja et al. (2008) or Quillen et al. (2018a) (it is dominated by resonances with the bar and/or spiral arms). Given that the gravitational potential defines the gradients of the ridges, our study is a step towards constraining the shape and mass of the MW in an innovative manner using the kinematic substructure present across the disc.

In Chapter 3, we extended the search for kinematic substructure beyond the 6D sample used in the previous Chapter and focused instead in the full astrometic sample (positions, parallaxes and proper motions). In the halo, we recover the position and kinematics of external galaxies like M33, dozens of Galactic Globular clusters and even several dwarf spheroidal galaxies orbiting the MW. Our method has also revealed a complex and substructured Galactic anticentre, with Monoceros and the Anticentre stream (ACS) being the third and fourth most prominent features in the sky, only after the Magellanic clouds and the Sgr stream. The result of our analysis on the anticentre provides its sharpest picture to date and allows us to clearly observe Monoceros and ACS as two arches in the northen Galactic hemisphere spanning ~100° in longitude. By selecting, at each HEALpix, the stars that form the overdensity in the proper motion histogram, we obtain a large sample of kinematically selected stars that reveals a conspicuous colour-magnitude diagram (CMD) with a well defined Red Clump (RC) and its corresponding Main Sequence (MS). The ages and chemical abundances of these stars could provide us with crucial information about the state of our Galaxy prior to the hypothetical perturbation that detached them from the disc, if that were the case. We used the apparent magnitude of the RC stars to trace Monoceros down to latitudes ~5°, closer to the mid-plane than ever before, and to obtain a distance estimate to the centre of each structure: $D_{MNC} \sim 10.6$ kpc (R~18 kpc, z~4.5 kpc), and $D_{ACS} \sim 11.7$ kpc (R~18 kpc, z~6.5 kpc). Also, we noted that the Giants within Monoceros and ACS represent a significant fraction (up to ~40%, at some latitudes) of all the Giant stars in that region of the sky located between the Sun and ~20 kpc away from it. From the morphological and kinematic analysis of these two arches, and by comparing the fraction of Giants that compose each one, we conclude that they are different structures, extended in 3D space to the point of overlapping with each other, with proper motions compatible with a disc-like population. We are now at the point,

thanks to these results and the data we provide, to compare quantitatively and test the different dynamical mechanisms proposed to explain the origin of Monoceros and ACS (most notably, a perturbation on the disc by Sgr or the remnant of accreted dwarf/s satellite/s).

Building on the results of our all-sky search for kinematic substructure, in Chapter 4 we have focused on the Sgr stream. We have produced a vast sample of candidate stars, at least an order of magnitude larger than previous ones and covering the whole sky homogeneously thanks to *Gaia*, by carefully selecting the peaks in the proper motion histograms caused by the stream and isolating them from the ones caused by the MW disc. Since we did not selected any particular population, we have been able to show the most detailed CMD of this system all along its tidal tails. From our analysis it is clear that the model proposed by Law & Majewski (2010b) to predict the 6D distribution of the debris, one of the most successful, does not explain adequately the observed proper motion tracks along the stream, especially in the leading arm. This is not strange given that their fit only included distances and radial velocities, which were shown latter to also present similar discrepancies with the more recent observations. Still, this has been the first time that the proper motions predicted by a model have has been tested with enough data and for a large portion of the stream. We have also done a first comparison of the distribution of distances and, although a rigorous calibration of the RC stars in our sample is still needed, we have observed some significant discrepancies with the model. This sample represents a milestone in the study of Sgr and is intended to be used for both the modelling of its orbit as well as the analysis of its populations and star formation history.

Finally, in Chapter 5 we go one step forward and provide the largest 5D sample of RR Lyrae in the stream containing positions, proper motions and precise distances for more than ten thousand stars. This list of stars is made of two sub-samples, a purer (but more incomplete) one that is aimed to be used as input catalogue for future follow-up spectroscopic surveys, and another more complete (but less pure) with which we can study better the physics of the stream. We have derived new apocentres for the tidal debris, in tension ($>3\sigma$) with previous estimates, and to produce the first map of the tangential velocities along the stream, a result only possible thanks to the combination of proper motions and distances. Compared to the predictions by Law & Majewski (2010b), the tangential velocities agree within the uncertainties in the trailing arm but the differences become significant both at the dwarf and in the leading tail. It is precisely in the leading arm where we observe the stream bifurcating into two branches, a bright and a faint one (we do not detect a bifurcation in the trailing arm). After carefully comparing the two branches, we find that any difference in distance or proper motion has to be very small

given that we do not observe any significant separation at the current level of precision, which constrains the possible mechanisms that can create this still poorly understood feature.

6.2 DISCUSSION

Recent works have shown that the effect of Sgr on the disc is probably more significant than what it was previously thought. Up until now, Sgr has been used mostly to learn about the shape and mass of the halo. Nevertheless, we have already mentioned the work by Laporte et al. (2018, 2019a,b, 2020), in which the authors show (qualitatively) that the interaction with this dwarf spheroidal could explain several of the features seen in the disc, e.g., the creation of spiral arms, the v_R maps obtained with *Gaia* (Fig. 10 from Gaia Collaboration et al., 2018d), the phase-space spiral in the Z-v_Z plane and ridges in R-v_ϕ (Antoja et al., 2018), and the Monoceros and ACS structures (Newberg et al., 2002; Grillmair, 2006). One of their conclusions is that the orbit and mass of Sgr have a huge impact on the final state of the disc. This idea is reinforced by the study of several N-body simulations in Bland-Hawthorn et al. (2019), where they show that reasonable changes in the parameters of the dwarf spheroidal lead to dramatic changes in the shape of phase-space at the present time. Without a tight constraint on Sgr we cannot quantify its effects and understand the coupling with other dynamical mechanisms acting on the stars of our Galaxy, like the bar, spiral arms or even the speculated dark sub-halos (Chequers et al. 2018, but see Laporte et al. 2019a).

Very recently, Ruiz-Lara et al. (2020) argued that, in fact, the effects of this particular satellite are likely to be also noticeable in the star formation history of the MW (as hinted by Mor et al., 2019). They report three bursts of star formation that coincide with the different times when the core of Sgr was close to pericentre, at least according to some models, suggesting that the repeated passages of this dwarf galaxy might have significantly influenced the growth in mass of the MW disc. However, we still lack the theoretical framework to correctly predict the relation between the time when Sgr reaches pericentre and when the star formation in the disc is, as a consequence, at its maximum. It is therefore quite challenging to constrain the infall history of Sgr using the time when the bursts happened. Additionally, as pointed out in Ruiz-Lara et al. (2020), the complex mixture of populations observed inside Sgr contains useful information about its past too. The study of its star formation history has so far revealed a quenching of the star formation (de Boer et al., 2015) that coincides with the age of the oldest burst that they detect in the MW, most likely caused by the stripping of the gas from the dwarf as it plunged into the halo. Also, the ages derived from the two distinct turn-off sequences observed at the core the dwarf (Siegel et al., 2007) seem to agree with the times of

the last two star formation enhancements reported in Ruiz-Lara et al. (2020).

We have now provided a vast sample of Sgr stars which should allow us to test the causal relation between the stellar histories of both systems. On one hand, the new and abundant observations allow for a better orbital fit, and therefore a better dynamical determination of the times of pericentre passage. On the other, we can now try to measure the changes in the Herzprung-Russel diagram as a function of the angular distance to the core of Sgr, and quantify the relative fraction of the different populations within Sgr as a function of dynamical time (i.e., the time when the stars were stripped from the progenitor) to relate them with the different pericentre passages. In a sense, the analysis of the differences between the intermediate-age sample (Chapter 4) and an old-age sample (Chapter 5) is a simple way to test if there is a connection between the spatial distribution of the tidal debris and the star formation of the progenitor. In the future, this data can be complemented, for example, by the abundances and radial velocities provided by the WEAVE survey (Dalton et al., 2012) in the leading arm, and the corresponding sample of extremely metal poor stars from the PRISTINE survey (Starkenburg et al., 2017). Moreover, the Sgr sample will be significantly improved in size and quality once we apply our methodology to the early *Gaia* DR3, which is expected to contain astrometry for more stars all while reducing the proper motion uncertainties by a half, on average (Brown, 2019).

Apart from the long-lived and on-going interaction with Sgr, our Galaxy has another element that induces substructure in the disc: the bar. Fragkoudi et al. (2019) obtained several ridges in the plane R-v_ϕ similar to the ones observed in Antoja et al. (2018), but also to the tracks that we obtained in Chapter 2, with an N-body simulation of a MW-like galaxy hosting a fast bar. They also report differences in the mean radial velocity (v_R) among the ridges, just as we showed in Chapter 2 for the *moving groups*, confirming that ridges and *moving groups* are in fact two sides of the same coin representing the same physical phenomena. From the simulations of Antoja et al. (2018) and Fragkoudi et al. (2019) we can conclude that, even in a simplified scenario with only a bar, the ridges have a wide range of slopes. This complicates any attempt to associate a dynamical origin to the *moving groups* based on their gradients since these could coincide with the ones caused by a phase-mixing process. Even though the fast bar used by Fragkoudi et al. (2019) was the preferred model until some years ago, the recent works by Hunt & Bovy (2018) and Monari et al. (2019b) conclude, after re-analysing the kinematics at the SN, that the bar could also be slower, for instance with a pattern speed of $\sim 39\,\mathrm{km\,s^{-1}\,kpc^{-1}}$ in the case of the latter. This conclusion is further reinforced by the decrease in angular momentum of the Hercules *moving group* with azimuth, as seen in Chapter 2, in agree-

ment with the expectations of a structure caused by the co-rotation of the long and slow bar (Monari et al., 2019a). Even with all these convincing arguments in favour of a slow bar, added to the estimates obtained with other tracers (for a review, see Bland-Hawthorn & Gerhard, 2016), the fast bar cannot be completely ruled out yet. In part, this is because we still do not understand completely the coupling between a pertubation on the disc, like the one caused by Sgr, and a bar resonance, so it could be that the behaviour of the *moving groups* with azimuth that we observe is actually created by the Outer Lindblad Resonance (OLR) of a fast bar acting on a population undergoing phase-mixing. This scenario has not been properly explored and therefore the challenge now is to understand the combined effects of the interaction with Sgr and the resonance with a bar, all while taking into account that the pattern speed of the bar can oscillate with time due to periodic re-connection with the spiral arms (Hilmi et al., 2020). In this sense, it would be interesting to run an N-body model that simulates the interaction MW-Sgr while tracing the evolution in phase-space of the particles that participate on each of the different structures. Here, several scenarios are worth investigation like, for instance, the differences between a galaxy that had a bar (fast or slow) prior to the impact of the satellite and one that developed it as a result of the gravitational interaction between the two systems.

One of the predictions of the *slow* models for the bar is that the OLR should manifest itself as a *moving group* at high angular momentum in the SN. While we do have a candidate (Arch 1 from Chapter 2), its morphology and changes with Galactocentric radius with the current data are consistent with both a resonant structure or a phase-mixing one.We do note, nonetheless, that the associated ridge in the R-v_ϕ plane (see also Antoja et al., 2018; Khanna et al., 2019) is similar to the ridge caused by the OLR of a bar with a pattern speed of $\sim 39\,\mathrm{km\,s^{-1}\,kpc^{-1}}$ (see Fig. 6 of Monari et al., 2019b). In this regard, the combination of the next *Gaia* data release (Brown, 2019), and its ~70 million radial velocities, with complementary spectroscopic surveys like WEAVE (Chiappini et al., 2019) and 4MOST (de Jong et al., 2019) will shed light on this question by expanding the 6D sample significantly, and providing enough good quality data to study Arch 1 properly (as well as the interface between the disc an the bar towards the Galactic centre, where the effects of other inner resonances could be noted.).

Our study of the kinematic substructure in the disc (Chapter 2), the detailed characterisation of Monoceros and ACS (Chapter 3) together with the vast sample of stars in the Sgr stream compiled in this work (Chapter 4 and 5), provide the necessary ingredients to attempt for the first time a hybrid fit to characterise the Sgr infall, the evolution over time of the Galactic potential and its components (dark matter halo, bar, spiral arms, etc.), and their interaction. The

morphology of the *moving groups* in velocity space provide information on the dynamical mechanisms that cause them, and their gradients are governed by the gravitational potential. On the other hand, assuming that Monoceros and ACS were once part of the disc, they are a chemical fossil that can be used to improve the current chemo-dynamical models, apart of course from providing information on the events that lead to their current phase-space configuration: mass of Sgr, timing of the successive pericentre passages, and rotation curve of the MW at large radii. To finally close the circle, we have the Sgr dwarf galaxy whose phase-space distribution of the associated tidal debris is determined by its initial mass and velocity as well as the parameters of the Dark Matter halo. But at the same time, under the current hypothesis, this dwarf is the force responsible for some of the ridges that we observe as well as Monoceros and ACS. Linking all three pieces together (disc kinematics, structures in the anticentre and the Sgr stream) in a self-consistent manner is a complex task that requires a strong theoretical framework[1].

A good road-map to attain this goal beginnings by improving our understanding of each part of the puzzle individually. First, as we mentioned in Chapter 1, different authors have reached contradicting conclusions regarding the shape of the gravitational potential when trying to explain the orbit of Sgr using its observed stream. To be able to use it as a trustworthy constraint on the Dark Matter halo first we have to quantify the coupling between the combined effect of the dynamical friction and the mass loss, the influence of the Magellanic clouds both on Sgr (Vera-Ciro & Helmi, 2013) as well as on the centre of mass of the MW (Gómez et al., 2015; Petersen & Peñarrubia, 2020), and the impact that a halo with varying shape as a function of radius (Shao et al., 2020) can have on the stream. Secondly, we need to confirm that Monoceros and ACS were indeed caused by Sgr, which can be achieved by obtaining accurate ages and abundances for the stars in our sample. Then, with models of the extended phase-space distribution (e.g., Sanders & Binney, 2015; Sharma et al., 2020), we can calculate the likelihood of these stars to have been part of the disc, at its very edge, more than 2 Gyr ago, prior to the first pericentre passage of Sgr (e.g., Purcell et al., 2011). Finally, if we want to constrain the potential with the gradients of the *moving groups*, we need to comprehend the dynamical processes involved through, for instance, the analysis of self-consistent simulations of systems with different set-ups, aimed at reproducing the observed trends. The ideal output would be a (semi-)analytical expression describing the gradients that we can then apply to our observations to infer the properties of the MW. Additionally, there are other dynamical features of the disc that

1 As an example, projects like SEGAL (Secular Evolution of GALaxies, https://www.secular-evolution.org/) are trying to model the formation and evolution of self-gravitating systems with the most recent developments in Kinetic theory.

we have not discuss here in detail, but that could be related to the ones already mentioned: the nature of the spiral arms – their dynamics and origin still unknown to us –, the vertical wave like pattern that corrugates the disc, or the warp. With a deeper understanding of each one of these elements, we will be able to start joining the pieces of this Galactic jigsaw.

6.3 CONCLUSIONS

The main outputs of this thesis are:

- The velocity distribution of disc stars presents a high level of substructure at least up to ~3 kpc from the Sun.
- Each substructure has a unique morphology in the v_R-v_ϕ plane and a different gradient with Galactocentric radius and azimuth.
- We provide the largest list of *moving groups* with a detailed characterisation of their properties in velocity space.
- There is kinematic substructure in the anticentre (north Galactic hemisphere) formed by stars in prograde orbits at heights above the disc larger than 2 kpc, and up to approximately 7 kpc. These structures are not an artefact of the data or the method, an their intensity on our maps is only surpassed by the Magellanic clouds and the Sgr stream.
- The stars that populate the structures in the anticentre are grouped in, at least, two extended arches overlapping in configuration space that correspond to Monoceros and ACS.
- We can trace these structures to latitudes as low as ~5°, but we do not observe them continuing in the south.
- A significant fraction of the nearby halo belongs to the Sgr stream.
- We provide the first proper motion determination of this stream along its full first wrap, and a vast sample of candidate stars with positions, proper motions and, for the subset of RR Lyrae, also distances.
- The changes along the tidal tails in proper motion, and in tangential velocities if we add the distances, are not well reproduced by some of the models available.
- There is a bifurcation in the leading arm of the stream present in both the intermediate age population as well as in the old population, with no significant separation in distance or kinematics between the two branches at the current level of precision.

The main conclusions of this thesis are:

- To comprehend the complexity of phase-space in the MW we have to account for, at least, phase-mixing and resonances with the bar, as well as the interplay between the two mechanisms.
- The high intensity of Monoceros and ACS imply that these structures are relevant features of the MW, and thus that our observations contain crucial information about its past and the interface between the disc and the halo, whether they are accreted satellites or the response of the disc to an external perturbation.
- With the addition of the proper motions trends along the tidal tails of Sgr that we have measured, the models of the stream can be finally constructed to fit its full phase-space.
- The lack of theoretical background hampers our capability to compare our results in front of different hypothesis, which is why this thesis highlights the importance of pursuing the necessary modelling efforts to predict quantitatively the effects on the MW of a merger with a satellite of the mass of Sgr.

With the superb *Gaia* DR2 data, we have been able to collect a long list of new observational constrains on the substructure of the phase-space at various levels which, once combined with the theoretical and simulated studies necessary for their interpretation, will result in a significant advance on the knowledge of our Galaxy and its history.

BIBLIOGRAPHY

Abedi, H., Mateu, C., Aguilar, L. A., Figueras, F., & Romero-Gómez, M. 2014, MNRAS, 442, 3627

Amorisco, N. C. 2015, MNRAS, 450, 575

Anders, F., Khalatyan, A., Chiappini, C., et al. 2019, A&A, 628, A94

Antoja, T. 2010, PhD thesis, Universitat de Barcelona

Antoja, T., Figueras, F., Fernández, D., & Torra, J. 2008, A&A, 490, 135

Antoja, T., Figueras, F., Romero-Gómez, M., et al. 2011, MNRAS, 418, 1423

Antoja, T., Helmi, A., Bienayme, O., et al. 2012, MNRAS, 426, L1

Antoja, T., Helmi, A., Dehnen, W., et al. 2014, A&A, 563, A60

Antoja, T., Helmi, A., Romero-Gómez, M., et al. 2018, Nature, 561, 360

Antoja, T., Mateu, C., Aguilar, L., et al. 2015b, MNRAS, 453, 541

Antoja, T., Monari, G., Helmi, A., et al. 2015, ApJ, 800, L32

Antoja, T., Ramos, P., Mateu, C., et al. 2020, A&A, 635, L3

Antoja, T., Valenzuela, O., Pichardo, B., et al. 2009, ApJ, 700, L78

Arenou, F. & Luri, X. 1999, in Astronomical Society of the Pacific Conference Series, Vol. 167, Harmonizing Cosmic Distance Scales in a Post-HIPPARCOS Era, ed. D. Egret & A. Heck, 13–32

Astraatmadja, T. L. & Bailer-Jones, C. A. L. 2016, ApJ, 833, 119

Bailer-Jones, C. A. L. 2015, PASP, 127, 994

Battrick, B. 1994, Horizon 2000 Plus. European Space Science in the 21st Century

Baumgardt, H. & Hilker, M. 2018, MNRAS, 478, 1520

Bellazzini, M., Ibata, R., Malhan, K., et al. 2020, arXiv e-prints, arXiv:2003.07871

Bellazzini, M., Ibata, R. A., Chapman, S. C., et al. 2008, AJ, 136, 1147

Belokurov, V., Erkal, D., Evans, N. W., Koposov, S. E., & Deason, A. J. 2018, MNRAS, 478, 611

Belokurov, V., Koposov, S. E., Evans, N. W., et al. 2014, MNRAS, 437, 116

Belokurov, V., Zucker, D. B., Evans, N. W., et al. 2006, ApJ, 642, L137

Belokurov, V., Zucker, D. B., Evans, N. W., et al. 2007, The Astrophysical Journal, 654, 897

Bergemann, M., Sesar, B., Cohen, J. G., et al. 2018, Nature, 555, 334

Bessell, M. & Murphy, S. 2012, PASP, 124, 140

Bica, E., Pavani, D. B., Bonatto, C. J., & Lima, E. F. 2019, AJ, 157, 12

Bienaymé, O. 2018, A&A, 612, A75

Binney, J., Gerhard, O., & Spergel, D. 1997, MNRAS, 288, 365

Binney, J. & Tremaine, S. 2008, Galactic Dynamics: Second Edition

Bissantz, N. & Gerhard, O. 2002, MNRAS, 330, 591

Bland-Hawthorn, J. & Gerhard, O. 2016, ARA&A, 54, 529

Bland-Hawthorn, J., Sharma, S., Tepper-Garcia, T., et al. 2019, MNRAS, 486, 1167

Bobylev, V. V. & Bajkova, A. T. 2016, Astronomy Letters, 42, 90

Bonaca, A., Conroy, C., Price-Whelan, A. M., & Hogg, D. W. 2019a, arXiv e-prints, arXiv:1906.02748

Bonaca, A., Hogg, D. W., Price-Whelan, A. M., & Conroy, C. 2019b, ApJ, 880, 38

Bovy, J. 2010, ApJ, 725, 1676

Brown, A. G. A. 2019, in The Gaia Universe, 18

Brown, A. G. A., Arenou, F., van Leeuwen, F., Lindegren, L., & Luri, X. 1997, in ESA Special Publication, Vol. 402, Hipparcos - Venice '97, ed. R. M. Bonnet, E. Høg, P. L. Bernacca, L. Emiliani, A. Blaauw, C. Turon, J. Kovalevsky, L. Lindegren, H. Hassan, M. Bouffard, B. Strim, D. Heger, M. A. C. Perryman, & L. Woltjer, 63–68

Bullock, J. S. & Johnston, K. V. 2005, ApJ, 635, 931

Camarillo, T., Mathur, V., Mitchell, T., & Ratra, B. 2018, PASP, 130, 024101

Cardelli, J. A., Clayton, G. C., & Mathis, J. S. 1989, ApJ, 345, 245

Carlin, J. L., DeLaunay, J., Newberg, H. J., et al. 2013, ApJ, 777, L5

Carlin, J. L., Majewski, S. R., Casetti-Dinescu, D. I., et al. 2012, ApJ, 744, 25

Castro-Ginard, A., Jordi, C., Luri, X., et al. 2020, A&A, 635, A45

Castro-Ginard, A., Jordi, C., Luri, X., Cantat-Gaudin, T., & Balaguer-Núñez, L. 2019, A&A, 627, A35

Castro-Ginard, A., Jordi, C., Luri, X., et al. 2018, A&A, 618, A59

Catelan, M. & Smith, H. A. 2015, Pulsating Stars

Chambers, K. C., Magnier, E. A., Metcalfe, N., et al. 2016, arXiv e-prints, arXiv:1612.05560

Chequers, M. H., Widrow, L. M., & Darling, K. 2018, MNRAS, 480, 4244

Chiappini, C., Minchev, I., Starkenburg, E., et al. 2019, The Messenger, 175, 30

Clementini, G., Ripepi, V., Molinaro, R., et al. 2019, A&A, 622, A60

Cochran, W. G. 1977, Sampling Techniques, 3rd Edition. (John Wiley)

Crane, J. D., Majewski, S. R., Rocha-Pinto, H. J., et al. 2003, ApJ, 594, L119

Cropper, M., Katz, D., Sartoretti, P., et al. 2018, A&A, 616, A5

Cseresnjes, P. 2001, A&A, 375, 909

Cui, X.-Q., Zhao, Y.-H., Chu, Y.-Q., et al. 2012, Research in Astronomy and Astrophysics, 12, 1197

Dalton, G., Trager, S. C., Abrams, D. C., et al. 2012, Society of Photo-Optical Instrumentation Engineers (SPIE) Conference Series, Vol. 8446, WEAVE: the next generation wide-field spectroscopy facility for the William Herschel Telescope, 84460P

de Boer, T. J. L., Belokurov, V., & Koposov, S. 2015, MNRAS, 451, 3489

de Boer, T. J. L., Belokurov, V., & Koposov, S. E. 2018, MNRAS, 473, 647

de Jong, R. S., Agertz, O., Berbel, A. A., et al. 2019, The Messenger, 175, 3

De Lucia, G. & Blaizot, J. 2007, MNRAS, 375, 2

De Silva, G. M., Freeman, K. C., Bland-Hawthorn, J., et al. 2015, MNRAS, 449, 2604

De Simone, R., Wu, X., & Tremaine, S. 2004, MNRAS, 350, 627

Debattista, V. P., Roškar, R., Valluri, M., et al. 2013, MNRAS, 434, 2971

Deg, N. & Widrow, L. 2013, MNRAS, 428, 912

Dehnen, W. 1998, AJ, 115, 2384

Dehnen, W. 1999, AJ, 118, 1190

Dehnen, W. 2000, AJ, 119, 800

Di Fabrizio, L., Clementini, G., Maio, M., et al. 2005, A&A, 430, 603

Di Matteo, P., Haywood, M., Lehnert, M. D., et al. 2019, A&A, 632, A4

Dierickx, M. I. P. & Loeb, A. 2017, ApJ, 836, 92

Duffau, S., Zinn, R., Vivas, A. K., et al. 2006, ApJ, 636, L97

Eggen, O. J. 1958, MNRAS, 118, 560

Eggen, O. J. 1996, AJ, 112, 1595

Erkal, D., Belokurov, V., Laporte, C. F. P., et al. 2019, MNRAS, 487, 2685

ESA, ed. 1997, ESA Special Publication, Vol. 1200, The HIPPARCOS and TYCHO catalogues. Astrometric and photometric star catalogues derived from the ESA HIPPARCOS Space Astrometry Mission

Evans, D. W., Riello, M., De Angeli, F., et al. 2018, A&A, 616, A4

Eyer, L., Mowlavi, N., Evans, D. W., et al. 2017, ArXiv e-prints [[arXiv]1702.03295]

Eyre, A. & Binney, J. 2009, MNRAS, 400, 548

Famaey, B., Jorissen, A., Luri, X., et al. 2005, A&A, 430, 165

Fardal, M. A., van der Marel, R. P., Law, D. R., et al. 2019, MNRAS, 483, 4724

Fellhauer, M., Belokurov, V., Evans, N. W., et al. 2006, ApJ, 651, 167

Forbes, D. A., Lasky, P., Graham, A. W., & Spitler, L. 2008, MNRAS, 389, 1924

Fragkoudi, F., Katz, D., Trick, W., et al. 2019, MNRAS, 488, 3324

Freeman, K. & Bland-Hawthorn, J. 2002, ARA&A, 40, 487

Fux, R. 2001, A&A, 373, 511

Gaia Collaboration, Babusiaux, C., van Leeuwen, F., et al. 2018a, A&A, 616, A10

Gaia Collaboration, Brown, A. G. A., Vallenari, A., et al. 2018b, A&A, 616, A1

Gaia Collaboration, Brown, A. G. A., Vallenari, A., et al. 2016a, A&A, 595, A2

Gaia Collaboration, Helmi, A., van Leeuwen, F., et al. 2018c, A&A, 616, A12

Gaia Collaboration, Katz, D., Antoja, T., et al. 2018d, A&A, 616, A11

Gaia Collaboration, Prusti, T., de Bruijne, J. H. J., et al. 2016b, A&A, 595, A1

Gallart, C., Bernard, E. J., Brook, C. B., et al. 2019, Nature Astronomy, 3, 932

Gerhard, O. 2011, Memorie della Societa Astronomica Italiana Supplementi, 18, 185

Gibbons, S. L. J., Belokurov, V., Erkal, D., & Evans, N. W. 2016, MNRAS, 458, L64

Gibbons, S. L. J., Belokurov, V., & Evans, N. W. 2014, MNRAS, 445, 3788

Giuffrida, G., Sbordone, L., Zaggia, S., et al. 2010, A&A, 513, A62

Gómez, F. A., Besla, G., Carpintero, D. D., et al. 2015, ApJ, 802, 128

Gómez, F. A., Minchev, I., O'Shea, B. W., et al. 2013, MNRAS, 429, 159

Gómez, F. A., Minchev, I., Villalobos, Á., O'Shea, B. W., & Williams, M. E. K. 2012, MNRAS, 419, 2163

Gómez, F. A., White, S. D. M., Marinacci, F., et al. 2016, MNRAS, 456, 2779

Gratton, R. G., Bragaglia, A., Clementini, G., et al. 2004, A&A, 421, 937

Gravity Collaboration, Abuter, R., Amorim, A., et al. 2019, A&A, 625, L10

Grillmair, C. J. 2006, ApJ, 651, L29

Grillmair, C. J. & Carlin, J. L. 2016, in Astrophysics and Space Science Library, Vol. 420, Tidal Streams in the Local Group and Beyond, ed. H. J. Newberg & J. L. Carlin, 87

Harris, W. E. 1996, AJ, 112, 1487

Hattori, K., Gouda, N., Yano, T., et al. 2018, ArXiv e-prints [[arXiv]1804.01920]

Hayden, M. R., Bovy, J., Holtzman, J. A., et al. 2015, ApJ, 808, 132

Hayes, C. R., Law, D. R., & Majewski, S. R. 2018, ApJ, 867, L20

Hayes, C. R., Majewski, S. R., Hasselquist, S., et al. 2019, arXiv e-prints, arXiv:1912.06707

Haywood, M., Di Matteo, P., Lehnert, M. D., et al. 2018, ApJ, 863, 113

Helmi, A. 2004, ApJ, 610, L97

Helmi, A., Babusiaux, C., Koppelman, H. H., et al. 2018, Nature, 563, 85

Helmi, A., Navarro, J. F., Meza, A., Steinmetz, M., & Eke, V. R. 2003, ApJ, 592, L25

Helmi, A., Navarro, J. F., Nordström, B., et al. 2006, MNRAS, 365, 1309

Helmi, A., White, S. D. M., de Zeeuw, P. T., & Zhao, H. 1999, Nature, 402, 53

Hernitschek, N., Sesar, B., Rix, H.-W., et al. 2017, ApJ, 850, 96

Hilmi, T., Minchev, I., Buck, T., et al. 2020, arXiv e-prints, arXiv:2003.05457

Holl, B., Audard, M., Nienartowicz, K., et al. 2018, A&A, 618, A30

Hunt, J. A. S. & Bovy, J. 2018, MNRAS, 477, 3945

Ibata, R., Bellazzini, M., Thomas, G., et al. 2020, ApJ, 891, L19

Ibata, R., Lewis, G. F., Martin, N. F., Bellazzini, M., & Correnti, M. 2013, ApJ, 765, L15

Ibata, R. A., Gilmore, G., & Irwin, M. J. 1994, Nature, 370, 194

Ibata, R. A., Irwin, M. J., Lewis, G. F., Ferguson, A. M. N., & Tanvir, N. 2003, MNRAS, 340, L21

Ibata, R. A., Malhan, K., & Martin, N. F. 2019, ApJ, 872, 152

Ibata, R. A., Malhan, K., Martin, N. F., & Starkenburg, E. 2018, ApJ, 865, 85

Ivezić, Ž., Sesar, B., Jurić, M., et al. 2008, ApJ, 684, 287

Johnston, K. V., Hernquist, L., & Bolte, M. 1996, ApJ, 465, 278

Johnston, K. V., Law, D. R., & Majewski, S. R. 2005, ApJ, 619, 800

Johnston, K. V., Spergel, D. N., & Haydn, C. 2002, ApJ, 570, 656

Johnston, K. V., Zhao, H., Spergel, D. N., & Hernquist, L. 1999, ApJ, 512, L109

Jones, E. M. 1972, ApJ, 173, 671

Jordi, C., Gebran, M., Carrasco, J. M., et al. 2010, A&A, 523, A48

Jurcsik, J. & Kovacs, G. 1996, A&A, 312, 111

Jurić, M., Ivezić, Ž., Brooks, A., et al. 2008, ApJ, 673, 864

Kalnajs, A. J. 1991, in Dynamics of Disc Galaxies, ed. B. Sundelius, 323

Karachentsev, I. D., Karachentseva, V. E., Huchtmeier, W. K., & Makarov, D. I. 2004, AJ, 127, 2031

Katz, D., Sartoretti, P., Cropper, M., et al. 2019, A&A, 622, A205

Kawata, D., Baba, J., Ciuca, I., et al. 2018, MNRAS, 479, L108

Kazantzidis, S., Bullock, J. S., Zentner, A. R., Kravtsov, A. V., & Moustakas, L. A. 2008, ApJ, 688, 254

Keller, S. C., Yong, D., & Da Costa, G. S. 2010, ApJ, 720, 940

Khanna, S., Sharma, S., Tepper-Garcia, T., et al. 2019, MNRAS, 489, 4962

Khoperskov, S., Di Matteo, P., Gerhard, O., et al. 2019, A&A, 622, L6

Koleva, M., Prugniel, P., De Rijcke, S., & Zeilinger, W. W. 2011, MNRAS, 417, 1643

Koposov, S. E., Belokurov, V., & Evans, N. W. 2013, ApJ, 766, 79

Koposov, S. E., Belokurov, V., Evans, N. W., et al. 2012, ApJ, 750, 80

Koposov, S. E., Belokurov, V., Li, T. S., et al. 2019, MNRAS, 485, 4726

Koppelman, H., Helmi, A., & Veljanoski, J. 2018, ApJ, 860, L11

Koppelman, H. H. & Helmi, A. 2020, arXiv e-prints, arXiv:2004.07328

Kos, J., de Silva, G., Buder, S., et al. 2018, MNRAS, 480, 5242

Kushniruk, I., Schirmer, T., & Bensby, T. 2017, A&A, 608, A73

Laporte, C. F. P., Belokurov, V., Koposov, S. E., Smith, M. C., & Hill, V. 2020, MNRAS, 492, L61

Laporte, C. F. P., Johnston, K. V., Gómez, F. A., Garavito-Camargo, N., & Besla, G. 2018, MNRAS, 481, 286

Laporte, C. F. P., Johnston, K. V., & Tzanidakis, A. 2019a, MNRAS, 483, 1427

Laporte, C. F. P., Minchev, I., Johnston, K. V., & Gómez, F. A. 2019b, MNRAS, 485, 3134

Law, D. R. & Majewski, S. R. 2010a, ApJ, 718, 1128

Law, D. R. & Majewski, S. R. 2010b, ApJ, 714, 229

Law, D. R. & Majewski, S. R. 2016, Astrophysics and Space Science Library, Vol. 420, The Sagittarius Dwarf Tidal Stream(s), ed. H. J. Newberg & J. L. Carlin, 31

Li, J., FELLOW, L., Liu, C., et al. 2019, ApJ, 874, 138

Liang, X. L., Zhao, J. K., Oswalt, T. D., et al. 2017, ApJ, 844, 152

Lindegren, L., Hernández, J., Bombrun, A., et al. 2018, A&A, 616, A2

Lindegren, L., Lammers, U., Bastian, U., et al. 2016, A&A, 595, A4

Liu, C., Deng, L.-C., Carlin, J. L., et al. 2014, ApJ, 790, 110

Liu, C., Xu, Y., Wan, J.-C., et al. 2017, Research in Astronomy and Astrophysics, 17, 096

López-Corredoira, M., Garzón, F., Wang, H. F., et al. 2020, A&A, 634, A66

López-Corredoira, M. & Sylos Labini, F. 2019, A&A, 621, A48

Luri, X., Brown, A. G. A., Sarro, L. M., et al. 2018, A&A, 616, A9

Maíz Apellániz, J. & Weiler, M. 2018, A&A, 619, A180

Majewski, S. R., Schiavon, R. P., Frinchaboy, P. M., et al. 2017, AJ, 154, 94

Majewski, S. R., Skrutskie, M. F., Weinberg, M. D., & Ostheimer, J. C. 2003, ApJ, 599, 1082

Malhan, K. & Ibata, R. A. 2018, MNRAS, 477, 4063

Malhan, K., Ibata, R. A., Carlberg, R. G., Valluri, M., & Freese, K. 2019, arXiv e-prints, arXiv:1903.08141

Malhan, K., Ibata, R. A., Goldman, B., et al. 2018a, MNRAS, 478, 3862

Malhan, K., Ibata, R. A., & Martin, N. F. 2018b, MNRAS, 481, 3442

Martínez-Delgado, D., Gabany, R. J., Crawford, K., et al. 2010, AJ, 140, 962

Martínez-Delgado, D., Gómez-Flechoso, M. Á., Aparicio, A., & Carrera, R. 2004, ApJ, 601, 242

Massari, D. & Helmi, A. 2018, A&A, 620, A155

Massari, D., Koppelman, H. H., & Helmi, A. 2019, A&A, 630, L4

Massari, D., Posti, L., Helmi, A., Fiorentino, G., & Tolstoy, E. 2017, A&A, 598, L9

Mateo, M., Mirabal, N., Udalski, A., et al. 1996, ApJ, 458, L13

Mateu, C., Bruzual, G., Aguilar, L., et al. 2011, MNRAS, 415, 214

Mateu, C., Cooper, A. P., Font, A. S., et al. 2017, MNRAS, 469, 721

Mateu, C., Read, J. I., & Kawata, D. 2018, MNRAS, 474, 4112

Mateu, C. & Vivas, A. K. 2018, MNRAS, 479, 211

Mateu, C., Vivas, A. K., Downes, J. J., et al. 2012, MNRAS, 427, 3374

McMillan, P. J. 2013, MNRAS, 430, 3276

McMillan, P. J. 2018, Research Notes of the American Astronomical Society, 2, 51

Mihalas, D. & Binney, J. 1981, Galactic astronomy. Structure and kinematics

Minchev, I., Boily, C., Siebert, A., & Bienayme, O. 2010, MNRAS, 407, 2122

Minchev, I., Nordhaus, J., & Quillen, A. C. 2007, ApJ, 664, L31

Minchev, I., Quillen, A. C., Williams, M., et al. 2009, MNRAS, 396, L56

Monari, G. 2014, PhD thesis, Rijksuniversiteit Groningen

Monari, G., Famaey, B., Minchev, I., et al. 2018, Research Notes of the American Astronomical Society, 2, 32

Monari, G., Famaey, B., Siebert, A., et al. 2019a, A&A, 632, A107

Monari, G., Famaey, B., Siebert, A., et al. 2017a, MNRAS, 465, 1443

Monari, G., Famaey, B., Siebert, A., Wegg, C., & Gerhard, O. 2019b, A&A, 626, A41

Monari, G., Kawata, D., Hunt, J. A. S., & Famaey, B. 2017b, MNRAS, 466, L113

Mor, R., Robin, A. C., Figueras, F., Roca-Fàbrega, S., & Luri, X. 2019, A&A, 624, L1

Muraveva, T., Delgado, H. E., Clementini, G., Sarro, L. M., & Garofalo, A. 2018, MNRAS, 481, 1195

Navarrete, C., Belokurov, V., Koposov, S. E., et al. 2017, MNRAS, 467, 1329

Navarro, J. F., Helmi, A., & Freeman, K. C. 2004, ApJ, 601, L43

Nemec, J. M., Cohen, J. G., Ripepi, V., et al. 2013, ApJ, 773, 181

Newberg, H. J., Yanny, B., Rockosi, C., et al. 2002, ApJ, 569, 245

Noether, E. 1971, Transport Theory and Statistical Physics, 1, 186

Palau, C. G. & Miralda-Escudé, J. 2019, MNRAS, 488, 1535

Peñarrubia, J., Belokurov, V., Evans, N. W., et al. 2010, MNRAS, 408, L26

Peñarrubia, J., Martínez-Delgado, D., Rix, H. W., et al. 2005, ApJ, 626, 128

Peñarrubia, J., Zucker, D. B., Irwin, M. J., et al. 2011, ApJ, 727, L2

Pecaut, M. J. & Mamajek, E. E. 2013, ApJS, 208, 9

Pérez-Villegas, A., Portail, M., Wegg, C., & Gerhard, O. 2017, ApJ, 840, L2

Perryman, M. A. C., de Boer, K. S., Gilmore, G., et al. 2001, A&A, 369, 339

Petersen, M. S. & Peñarrubia, J. 2020, MNRAS, 494, L11

Press, W. H. & Schechter, P. 1974, ApJ, 187, 425

Price-Whelan, A., Sipocz, B., Major, S., & Oh, S. 2017, adrn/gala: v0.2.1

Price-Whelan, A. M. 2017, The Journal of Open Source Software, 2

Price-Whelan, A. M. & Bonaca, A. 2018, ApJ, 863, L20

Price-Whelan, A. M., Johnston, K. V., Sheffield, A. A., Laporte, C. F. P., & Sesar, B. 2015, MNRAS, 452, 676

Price-Whelan, A. M., Mateu, C., Iorio, G., et al. 2019, AJ, 158, 223

Proctor, R. A. 1869, Royal Society of London Proceedings Series I, 18, 169

Purcell, C. W., Bullock, J. S., Tollerud, E. J., Rocha, M., & Chakrabarti, S. 2011, Nature, 477, 301

Quillen, A. C., Carrillo, I., Anders, F., et al. 2018a, MNRAS, 480, 3132

Quillen, A. C., De Silva, G., Sharma, S., et al. 2018b, MNRAS

Quillen, A. C., Dougherty, J., Bagley, M. B., Minchev, I., & Comparetta, J. 2011, MNRAS, 417, 762

Quillen, A. C. & Minchev, I. 2005, AJ, 130, 576

Ramos, P., Antoja, T., & Figueras, F. 2018, A&A, 619, A72

Reid, M. J. & Brunthaler, A. 2020, ApJ, 892, 39

Reid, M. J., Menten, K. M., Brunthaler, A., et al. 2014, ApJ, 783, 130

Riello, M., De Angeli, F., Evans, D. W., et al. 2018, A&A, 616, A3

Rimoldini, L., Holl, B., Audard, M., et al. 2019, A&A, 625, A97

Rocha-Pinto, H. J., Majewski, S. R., Skrutskie, M. F., Crane, J. D., & Patterson, R. J. 2004, ApJ, 615, 732

Romero-Gómez, M., Mateu, C., Aguilar, L., Figueras, F., & Castro-Ginard, A. 2019, A&A, 627, A150

Ruiz-Dern, L., Babusiaux, C., Arenou, F., Turon, C., & Lallement, R. 2018, A&A, 609, A116

Ruiz-Lara, T., Gallart, C., Bernard, E. J., & Cassisi, S. 2020, arXiv e-prints, arXiv:2003.12577

Rybizki, J., Demleitner, M., Bailer-Jones, C., et al. 2020, arXiv e-prints, arXiv:2004.09991

Rybizki, J., Demleitner, M., Fouesneau, M., et al. 2018, PASP, 130, 074101

Sanders, J. L. & Binney, J. 2013, MNRAS, 433, 1826

Sanders, J. L. & Binney, J. 2015, MNRAS, 449, 3479

Schlafly, E. F. & Finkbeiner, D. P. 2011, ApJ, 737, 103

Schlegel, D. J., Finkbeiner, D. P., & Davis, M. 1998, ApJ, 500, 525

Schönrich, R., Binney, J., & Dehnen, W. 2010, MNRAS, 403, 1829

Schönrich, R. & Dehnen, W. 2018, MNRAS, 478, 3809

Schwarzschild, K. 1907, Nachrichten von der Gesellschaft der Wissenschaften zu Goettingen, Mathematisch-Physikalische Klasse, 5, 614

Sellwood, J. A. 2010, MNRAS, 409, 145

Sesar, B., Hernitschek, N., Dierickx, M. I. P., Fardal, M. A., & Rix, H.-W. 2017a, ApJ, 844, L4

Sesar, B., Hernitschek, N., Mitrović, S., et al. 2017b, AJ, 153, 204

Sesar, B., Vivas, A. K., Duffau, S., & Ivezić, Ž. 2010, ApJ, 717, 133

Shao, S., Cautun, M., Deason, A. J., & Frenk, C. S. 2020, arXiv e-prints, arXiv:2005.03025

Sharma, S., Hayden, M. R., & Bland-Hawthorn, J. 2020, arXiv e-prints, arXiv:2005.03646

Sheffield, A. A., Johnston, K. V., Majewski, S. R., et al. 2014, ApJ, 793, 62

Shipp, N., Drlica-Wagner, A., Balbinot, E., et al. 2018, ApJ, 862, 114

Shipp, N., Li, T. S., Pace, A. B., et al. 2019, arXiv e-prints, arXiv:1907.09488

Siegel, M. H., Dotter, A., Majewski, S. R., et al. 2007, ApJ, 667, L57

Simon, J. D. & Geha, M. 2007, ApJ, 670, 313

Skuljan, J., Hearnshaw, J. B., & Cottrell, P. L. 1999, MNRAS, 308, 731

Slater, C. T., Bell, E. F., Schlafly, E. F., et al. 2014, ApJ, 791, 9

Slezak, E., de Lapparent, V., & Bijaoui, A. 1993, ApJ, 409, 517

Sohn, S. T., van der Marel, R. P., Carlin, J. L., et al. 2015, ApJ, 803, 56

Sohn, S. T., van der Marel, R. P., Kallivayalil, N., et al. 2016, ApJ, 833, 235

Sohn, S. T., Watkins, L. L., Fardal, M. A., et al. 2018, ApJ, 862, 52

Soubiran, C., Jasniewicz, G., Chemin, L., et al. 2018, A&A, 616, A7

Springel, V., Frenk, C. S., & White, S. D. M. 2006, Nature, 440, 1137

Starck, J.-L. & Murtagh, F. 2002, Astronomical image and data analysis, ed. Starck, J.-L. and Murtagh, F. (Springer)

Starck, J.-L., Murtagh, F. D., & Bijaoui, A. 1998, Image Processing and Data Analysis, 297

Starkenburg, E., Martin, N., Youakim, K., et al. 2017, MNRAS, 471, 2587

Steinmetz, M., Zwitter, T., Siebert, A., et al. 2006, AJ, 132, 1645

Tang, B., Fernández-Trincado, J. G., Geisler, D., et al. 2018, ApJ, 855, 38

Totten, E. J. & Irwin, M. J. 1998, MNRAS, 294, 1

Trick, W. H., Coronado, J., & Rix, H.-W. 2018, ArXiv e-prints, arXiv:1805.03653

van der Walt, S., Schönberger, J. L., Nunez-Iglesias, J., et al. 2014, PeerJ, 2, e453

van der Walt S, Schönberger JL, t. s.-i. c. et al. 2014, scikit-image: image processing in Python, [PeerJ 2:e453]

Vera-Ciro, C. & Helmi, A. 2013, ApJ, 773, L4

Vivas, A. K. & Zinn, R. 2006, AJ, 132, 714

Vivas, A. K., Zinn, R., Andrews, P., et al. 2001, ApJ, 554, L33

Vivas, A. K., Zinn, R., & Gallart, C. 2005, AJ, 129, 189

Wang, H.-F., Carlin, J. L., Huang, Y., et al. 2019, ApJ, 884, 135

Westera, P., Lejeune, T., Buser, R., Cuisinier, F., & Bruzual, G. 2002, A&A, 381, 524

White, S. D. M. & Rees, M. J. 1978, MNRAS, 183, 341

Widrow, L. M., Gardner, S., Yanny, B., Dodelson, S., & Chen, H.-Y. 2012, ApJ, 750, L41

Williams, M. E. K., Freeman, K. C., Helmi, A., & the RAVE collaboration. 2009, in IAU Symposium, Vol. 254, IAU Symposium, ed. J. Andersen, J. Bland-Hawthorn, & B. Nordström, 139–144

Willman, B., Dalcanton, J. J., Martinez-Delgado, D., et al. 2005, ApJ, 626, L85

Wilson, G. A. 1990, PhD thesis

Xia, Q., Liu, C., Xu, Y., et al. 2015, MNRAS, 447, 2367

Xu, Y., Newberg, H. J., Carlin, J. L., et al. 2015, The Astrophysical Journal, Volume 801, Issue 2, article id. 105, 25 pp. (2015)., 801 [[arXiv]1503.00257]

Yang, C., Xue, X.-X., Li, J., et al. 2019, ApJ, 886, 154

Yanny, B., Newberg, H. J., Grebel, E. K., et al. 2003, ApJ, 588, 824

York, D. G., Adelman, J., Anderson, J. E. J., et al. 2000, AJ, 120, 1579

Zhang, X., Shi, W. B., Chen, Y. Q., et al. 2017, A&A, 597, A54

Zinn, R. & West, M. J. 1984, ApJS, 55, 45

LIST OF FIGURES

LIST OF TABLES

ACRONYMS

ACS	Anticentre stream
AGIS	Astrometric Global Iterative Solution
BS	bootstrap
CL	confidence level
CMD	colour-magnitude diagram
DF	Distribution function
ESA	European Space Agency
GC	Galactic centre
MS	Main Sequence
MSTO	Main Sequence Turn Off
MW	Milky Way
MG	moving group
LSR	local standard of rest
OLR	Outer Lindblad Resonance
PCM	pole count map
PS1	PanSTARRS-1
RC	Red Clump
Sgr	Sagittarius
SDSS	Sloan Digital Sky Survey
SN	Solar neighbourhood
TGM	Tailored Gaussian Mixture
WT	wavelet transformation

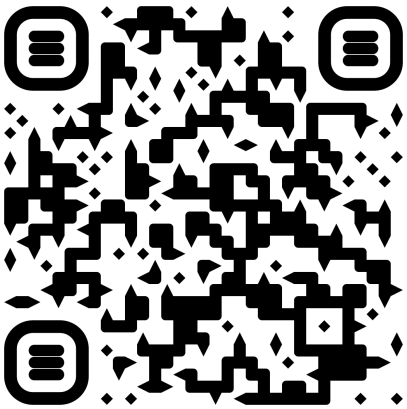

COLOPHON

This document was typeset using the typographical look-and-feel `classicthesis` developed by André Miede and Ivo Pletikosić. The style was inspired by Robert Bringhurst's seminal book on typography "*The Elements of Typographic Style*". `classicthesis` is available for both LaTeX and LyX:

`https://bitbucket.org/amiede/classicthesis/`

Happy users of `classicthesis` usually send a real postcard to the author, a collection of postcards received so far is featured here:

`http://postcards.miede.de/`

Thank you very much for your feedback and contribution.